



TAMPEREEN TEKNILLINEN YLIOPISTO
TAMPERE UNIVERSITY OF TECHNOLOGY

Mikko Närhi

**Measurements of Noise-seeded Dynamics in
Nonlinear Fiber Optics**



Julkaisu 1515 • Publication 1515

Tampere 2017

Tampereen teknillinen yliopisto. Julkaisu 1515
Tampere University of Technology. Publication 1515

Mikko Närhi

Measurements of Noise-seeded Dynamics in Nonlinear Fiber Optics

Thesis for the degree of Doctor of Science in Technology to be presented with due permission for public examination and criticism in Rakennustalo Building, Auditorium RG202, at Tampere University of Technology, on the 24th of November 2017, at 12 noon.

Tampereen teknillinen yliopisto - Tampere University of Technology
Tampere 2017

Doctoral candidate: Mikko Närhi
Photonics Laboratory
Faculty of Natural Sciences
Tampere University of Technology
Finland

Supervisor: Professor Goëry Genty
Photonics Laboratory
Faculty of Natural Sciences
Tampere University of Technology
Finland

Pre-examiners: Professor Dmitry Skryabin
Department of Physics
University of Bath
United Kingdom

Professor Morten Bache
Department of Photonics Engineering
Technical University of Denmark
Denmark

Opponent: Professor Jérôme Kasparian
GAP Nonlinearity and Climate
University of Genève
Switzerland

ISBN 978-952-15-4051-6 (printed)
ISBN 978-952-15-4060-8 (PDF)
ISSN 1459-2045

Abstract

Nonlinear physical systems are ubiquitous in nature - formation of sand dunes, currents occurring in a rapidly flowing river or a simple double rod pedulum are just a few examples from everyday life. Studying and understanding these systems has interested scientists for decades. Because these nonlinear systems might be chaotic, measurements of such systems need to be performed on a real-time basis and by statistical analysis methods.

The propagation of short and intense pulses in optical fibers are another well-known example of nonlinear systems. However, the rapid fluctuations of optical fields has prohibited studying these systems on a real-time basis, until recent years. This thesis demonstrates the use of state-of-the-art real-time measurement techniques to capture the stochastic dynamics of noise-seeded nonlinear processes in optical fibers allowing for novel insights and interpretation within analytical frameworks.

In particular, we characterize noisy picosecond pulse train emerging from spontaneous modulation instability using a time lens system. The experimental results are compared with analytical Akhmediev breather solutions showing remarkable agreement, allowing to understand the complex dynamics from an analytical viewpoint. An experimental demonstration of a high dynamic range real-time spectral measurement system for spontaneous modulation instability is also introduced to study the random breather structures in the spectral domain, paving the way for possible indirect optical rogue wave detection schemes.

By combining real-time temporal and spectral measurements unforeseen details of transition dynamics of a mode-locking of a fiber laser are also reported. The simultaneous spectro-temporal acquisition allows for complete electric field reconstruction with numerical algorithms, which has not been possible before at megahertz repetition rates with sub-picosecond and sub-nanometer resolutions demonstrated here.

Supercontinuum generation is one of the most well-known examples of nonlinear fiber optics that is also becoming widely spread in applications. The details of the complex and noise driven dynamics are now well-known, but the connection of the stability of such light sources with traditional coherence theory was only derived recently. Experimental measurement of supercontinuum stability in the framework of second-order coherence theory is demonstrated, filling a gap in characterization of non-stationary light sources.

Finally, an application of supercontinuum generation is proposed in terms of all-optical signal amplification. This is based on the inherently sensitive nature of the nonlinear process to any input fluctuations. The potential of such a highly nonlinear system for a practical application is demonstrated and the underlying dynamics leading to this sensitivity are explained.

Preface

The work of this thesis was carried out at the Ultrafast Fiber Optics group in the Photonics Laboratory of Tampere University of Technology (TUT) and at the FEMTO-ST institute of Université de Franche-Comté in France during my five month research visit there. I would like to acknowledge the TUT Graduate School for the main funding for my degree as well as Kaute-foundation, TES-foundation & Magnus Ehrnroth-foundation for making the international research visits possible.

I would like to express my sincere gratitude to my thesis supervisor Professor Goëry Genty for providing the opportunity to pursue my doctorate degree in an internationally acknowledged research environment. The level of scientific knowledge and never-ending ideas combined with the serious, but relaxed working atmosphere truly made the journey easier and certainly more malty and hoppy.

I'm also extremely grateful for Professor John M. Dudley for the chance to work with the outstanding research infrastructure at FEMTO-ST and his guidance in subjects ranging from Bowie's music to scientific practices and principles.

I would also like to thank Dr. Piotr Ryzkowski for the endless(!) discussions regarding all things from heaven to earth, including very supportive and insightful discussions related to work. I'm also grateful to Dr. Cyril Billet, who saw the effort of bringing me up-to-date with all of the experimental equipment and details at FEMTO-ST. Support from Dr. Benjamin Wetzell with the experimental and numerical work was also invaluable during my visit to FEMTO-ST. I would also like to thank Dr. Lasse Orsila for walking me through the experimental setup for the optical signal amplifier experiments.

Finally, I would like to thank all of the people that I've had the pleasure to work with in the (late) Optics lab of TUT. Professors Martti Kauranen and Juha Toivonen have kept the car running through the years. The UFO group meetings on Friday evenings with Caroline, Shanti, Jani & Lauri were a pleasure. I also enjoyed the Optics sports collective with Jan, Samu, Kim, Antti K., Tommi & Timo even though I did not win every time. Special thanks go also to Antti A., Johan, Mariusz and road-trippin' Léo for spectacular company during the on- and off-hours of work.

Contents

Abstract	iii
Preface	v
Acronyms	ix
Nomenclature	xi
List of Publications	xiii
1 Introduction	1
1.1 Aim and scope of this work	2
1.2 Structure of the thesis	3
1.3 Author's contribution	3
2 Light propagation in optical fibers	5
2.1 Linear light propagation in dielectric waveguides	5
2.2 Nonlinear effects and pulse propagation equation	10
2.3 Spectrogram representation	18
2.4 Modulation instability	20
2.5 Breather formalism	23
2.6 Supercontinuum generation	26
3 Real time measurement of noise initiated dynamics	33
3.1 Spatio-temporal duality in optics	35
3.2 Temporal breather structures in spontaneous modulation instability . . .	39
3.3 Spectral measurements of spontaneous modulation instability	44
3.4 Transient dynamics of fiber laser modelocking	52
3.5 Conclusions	63
4 Second order coherence measurement of supercontinuum	65
4.1 Coherence theory	66
4.2 Supercontinuum coherence measurement	70
4.3 Experimental results	72
4.4 Measuring the complex mean field	76
4.5 Conclusions	80
5 All-optical signal regeneration by supercontinuum generation	81
5.1 Proof-of-principle measurements	82
5.2 Physical mechanism of amplification	84

5.3	Effect of supercontinuum coherence on signal amplification	85
5.4	Conclusions	89
6	Summary and conclusions	91
	Bibliography	93
	Publications	105

Acronyms

AB	Akhmediev breather
APD	avalanche photodiode
AOM	acousto-optic modulator
CSD	cross spectral density
CW	continuous wave
DFT	dispersive Fourier transform
DMI	delayed Michelson interferometer
DW	dispersive wave
FWM	four-wave-mixing
FWHM	full width at half maximum
GNLSE	generalized nonlinear Schrödinger equation
GDD	group delay dispersion
GVD	group velocity dispersion
IST	inverse scattering transform
MCF	mutual coherence function
MI	modulation instability
NFT	nonlinear Fourier transform
NLSE	nonlinear Schrödinger equation
QML	Q-switched mode-locking
RSFS	Raman self-frequency shift
SBS	stimulated Brillouin scattering
SC	supercontinuum
SPM	self-phase modulation
SRS	stimulated Raman scattering

TL	time lens
ZDW	zero dispersion wavelength
XFROG	cross correlation frequency resolved optical gating
XPM	cross-phase modulation

Nomenclature

x, y, z	Cartesian coordinates
A_{eff}	Effective area of an optical fiber
A_c	coherence area
$A(z, t)$	complex electric field envelope
$A_0(z, t)$	amplitude of the complex electric field envelope
a	a-parameter of the Akhmediev breather solutions
\mathbf{B}	Magnetic field flux vector
b	b-parameter of the Akhmediev breather solutions
\mathbf{D}	Electric field displacement vector
D	Dispersion parameter
D_i	Group delay dispersion of component i
$\delta(t)$	delta-function response
\mathbf{E}	Electric field vector
$E(z, t)$	complex electric field amplitude
$F(x, y)$	electric field transverse profile
\mathcal{FT}	Fourier transform
f	focal length of a lens
f_R	fractional contribution of the Raman effect
$g(\Omega)$	Modulation instability gain profile
$g^{(2)}(\Delta t, \bar{t})$	Intensity correlation function
$g_{12}^{(1)}(t)$	First order coherence function for non-stationary light
\mathbf{H}	Magnetic field vector
$h_R(t)$	temporal response function of the Raman effect
$I(t)$	temporal intensity envelope
$I^{(M)}(t)$	temporal margin of a spectrogram
I_{RW}	rogue wave threshold intensity
\mathbf{J}	Current density
L_{fiss}	soliton fission length
\mathbf{M}	Magnetization of the material
M	magnification factor of a time lens
N	soliton order
n	refractive index of the material
n_g	group index of a waveguide
n_2	intensity dependent nonlinear refractive index
\mathbf{P}	Material total polarization
P_0, P_p	Peak power
$p(t)$	probe pulse shape in XFROG
$R(t)$	Delayed response function for nonlinear susceptibility

$S(\lambda), S(\omega)$	power spectral density
$S^{(M)}(\lambda)$	spectral margin of a spectrogram
t	time
T, τ	normalized time
T_0	hyperbolic secant pulse duration
Δt	difference time coordinate
\bar{t}	average time coordinate
$V(\omega)$	spectral fringe visibility function
v_g	group velocity
$W(\Delta\omega, \bar{\omega})$	cross spectral density
$X(\tau, \omega)$	XFROG spectrogram
χ_e	total electric susceptibility tensor
χ_e^i	electric susceptibility tensor of order i
χ_m	magnetic susceptibility tensor
∇	partial derivative with respect to all of the Cartesian coordinates
c	speed of light in vacuum
α	absorption/attenuation constant
$\beta(\omega)$	propagation constant
β_2	group velocity dispersion
$\phi(t), \varphi(\omega)$	phase function of the complex electric field envelope
$\Gamma(\Delta t, \bar{t})$	mutual coherence function
γ	nonlinear parameter
$\gamma^{(1)}(\tau)$	classical first order coherence function
$\gamma(\Delta t, \bar{t})$	normalized mutual coherence function
$\gamma_{cs}(\Delta t, \bar{t})$	coherent part of MCF
$\gamma_{qs}(\Delta t)$	quasi-stationary part of MCF
ϵ_0	vacuum electric permittivity
λ	wavelength
λ_0	center wavelength
μ_0	vacuum magnetic permeability
$\mu(\Delta\omega, \bar{\omega})$	normalized cross spectral density
$\mu_{cs}(\Delta\omega, \bar{\omega})$	coherent part of CSD
$\mu_{qs}(\Delta\omega)$	quasi-stationary part of CSD
$\psi(\xi, \tau)$	wavefunction in the nonlinear Schrödinger equation
ρ_f	free electric charge density
τ_c	coherence time
τ_{shock}	optical shock characteristic time
ξ	normalized position coordinate
Ω_M	modulation instability gain maximum frequency
ω	angular frequency
ω_0	center angular frequency
ω_a	omega parameter of Akhmediev breather solutions
$\Delta\omega/\Omega$	frequency detuning/difference frequency coordinate
$\bar{\omega}$	average frequency coordinate

List of Publications

- I Mikko Närhi, Benjamin Wetzel, Cyril Billet, Shanti Toenger, Thibaut Sylvestre, Jean-Marc Merolla, Roberto Morandotti, Frederic Dias, Goëry Genty, John M. Dudley, "Real-time measurements of spontaneous breathers and rogue wave events in optical fibre modulation instability," *Nature Communications*, vol 7, no. 13675, Dec. 2016.
- II Piotr Ryczkowski, Mikko Närhi, Cyril Billet, Goëry Genty, John M. Dudley, "Real-time measurements of dissipative solitons in a mode-locked fiber laser", arXiv:1706.08571
- III Mikko Närhi, Jari Turunen, Ari T. Friberg, Goëry Genty, "Experimental Measurement of the Second-Order Coherence of Supercontinuum," *Physical Review Letters*, vol 116, no. 24, June. 2016.
- IV Lasse Orsila, Johan Sand, Mikko Närhi, Günter Steinmeyer, Goëry Genty, "Supercontinuum generation as signal amplifier" *Optica*, vol 2, no. 757, Aug. 2015.

1 Introduction

Many advances in physics have arisen from our ability to measure physical quantities with higher accuracy. Measurements with better precision in turn allow us to refine models of physical phenomena and progress in the physical understanding of nature. Approximations are often made in the description of physical models that allow to simplify the problem and predict the behavior of the system at hand. One of the most common approach is to linearize the model by assuming that small perturbations do not affect the steady-state of the system and always remain relatively small. A classical example is the oscillation period of a pendulum which is independent from its amplitude provided the initial oscillation amplitude is initially small. This insensitivity to small perturbations of the oscillation amplitude is the reason why pendula are used as references to keep track of time.

Although many physical systems behave linearly when the input excitation or amplitude of a perturbation is small, the response may become nonlinear when the amplitude of the excitation of a perturbation is large. In the previous example of the pendulum, that implies that the pendulum oscillation period is not constant anymore if the initial oscillation amplitude is large. And indeed many systems in optics, electronics, fluid dynamics, solid state physics, classical mechanics etc. have been shown to exhibit a nonlinear behavior for initially large excitation amplitudes [1–7]. A typical characteristic of complex nonlinear systems is their sensitivity to input conditions, leading to chaotic behaviour sometimes described with the popular science term “butterfly effect”. In nonlinear fiber optics, this is manifested as modulation instability (MI), which describes the exponential amplification of an infinitesimally small perturbation to the optical field leading eventually to a break-up of the field into multiple sub-pulses [8, 9]. Modulation instability is one of the most ubiquitous nonlinear effects in physics and has been observed in many physical systems including deep water waves [6, 9, 10], plasma physics [11, 12] and Bose-Einstein condensates [13, 14].

Even though MI in optics has been studied extensively [15–22], direct experimental observation in real-time of the process and associated chaotic dynamics has not been previously possible due to the limitation of direct measurement methods using ultra-fast photodiodes. Advanced techniques such as frequency resolved optical gating [23] and spectral interferometry [24] are capable of measuring events at ultrafast time scales on the other hand but they are typically limited to averaged measurements due to measurement times that exceed the typical occurrence rate of the chaotic dynamics. More generally, the limitations of conventional techniques often prevent to study ultrafast dynamics in real time, and in particular nonlinear dynamics that are sensitive to tiny variations of the input parameters. Novel measurement techniques capable of real time temporal [25, 26] and spectral measurements [27–29] of ultrafast optical waveforms are central to advance the current understanding of many fundamental nonlinear phenomena in optics.

While from a fundamental research viewpoint it is important to characterize the output properties of a given physical system in real-time, from an applied perspective it is also important to quantify its average or statistical behavior. In the case of light sources, the average state or statistics can be described by the coherence properties. When propagating in a nonlinear medium, ultra-short pulses light can induce a wide range of nonlinear optical processes that, in turn, transform the spectrum and coherence of light. The supercontinuum generation process leading to the massive spectral broadening of intense narrowband laser light to a bandwidth that can span several optical octaves is certainly the most spectacular example of such nonlinear light sources [30–32]. When occurring inside an optical fiber, the spatial coherence is maintained, which makes supercontinuum laser sources ideal for numerous applications ranging from precision frequency metrology to imaging and spectroscopy [33–35]. Optimizing the performance of supercontinuum sources for practical applications requires detailed understanding of their coherence properties [36].

More generally, understanding the average behavior and real-time dynamics of nonlinear systems is the key to open possibilities for designing more cost-effective systems (e.g. by using fewer repeaters in fiber optic communications [37]) or predicting natural disasters such as extreme waves at deep seas [38, 39].

1.1 Aim and scope of this work

The aim of this thesis is to develop and utilize state-of-the-art real-time measurement techniques with picosecond (10^{-12} s) and nanometer (10^{-9} m) resolutions in the temporal and spectral domains, respectively, in order to understand the fundamental properties of noise seeded, stochastic physical processes of nonlinear fiber optics and their limitations in specific practical applications. The thesis work is mostly of experimental nature and the results are compared with theoretical models and numerical simulations.

A particular phenomenon of significant importance is modulation instability. The ability to measure the dynamics of modulation instability in real time, which has not been realized before, is therefore of fundamental interest and the result reported here bring new insight into a long standing problem.

Ultrafast lasers emitting short pulses of light are complex nonlinear systems which can be also be very sensitive to small noise perturbations. This is particularly true in the transient regime phase where the steady emission of light pulses builds up. Combining spectral and temporal domain measurements in real-time, we have for the first time measured the complete electric field associated with the mode-locking transition of a fiber laser, allowing to observe subtle nonlinear dissipative soliton dynamics not seen before.

Supercontinuum generation is one of the most spectacular development in the field of light sources in the past fifteen years. Not only because of the nonlinear physics involved in the formation of these broadband spectra, but also because of the major potential for practical applications in metrology, sensing, and imaging. Depending on the application at hand, a key property of supercontinuum light sources is their temporal and spectral coherence, which can be significantly affected by the presence of modulation instability. The ability of measuring and describing accurately the coherence properties of supercontinuum light is thus of high importance and this was achieved within the framework of this thesis by introducing a novel measurement approach which provides more complete information as compared to traditional techniques. We further expanded our study of the coherence

of supercontinuum sources to examine its implication in a novel method for all-optical signal amplification of weak modulation signals.

1.2 Structure of the thesis

The thesis consists of six chapters, starting with an introduction and theoretical background on light propagation in optical fibers covering all of the essential linear and nonlinear phenomena required to understand the physics behind the experiments reported in the following chapters.

Chapter 3 concentrates on measurement techniques capable of characterizing individual laser pulses at high acquisition rates. The importance of such measurements and a brief review of existing techniques and their principle of operation is given. This is followed by three separate sections, where various single-shot techniques are applied to experimentally study the evolution of noise driven nonlinear phenomena in fiber optics to obtain the necessary theoretical understanding of these effects.

Chapter 4 discusses the coherence properties of supercontinuum light when the massive spectral broadening process is triggered by noise. A theoretical background on the coherence properties is presented followed by experimental results introducing a technique based on average measurements and capable of resolving the underlying spectral and temporal correlations in the supercontinuum without the need for single-shot measurements.

Chapter 5 presents an application utilizing fiber nonlinearities for optical signal processing by supercontinuum generation. We focus on the competition between noise driven and deterministic dynamics that influence the applicability of the proposed amplification technique.

The thesis is concluded with a summary in chapter 6 discussing future perspectives.

1.3 Author's contribution

The thesis consists of four publications related to the experimental characterization of noise driven dynamics in optical fibers. The author contributed significantly to the writing of all the articles. A short description of the publications and the author's contribution is given below.

Paper I The paper demonstrates the measurement of chaotic picosecond pulses in real time originating from spontaneous modulation instability in a nonlinear fiber using a temporal magnification system. Numerical simulations complement the experimental results which can be understood in terms of the analytical Akhmediev breather theory. The author proposed and built the experimental setup with the help of the co-authors: C. Billet provided instructions on operating the time lens, J-M. Merolla provided consultation on the detection electronics and T. Sylvestre provided the amplifier system for the experiments. The author and B. Wetzel performed the actual measurements, numerical simulations and prepared the manuscript. F. Dias, S. Toenger, R. Morandotti, J.M. Dudley and G. Genty provided overall supervision and help for analysis of the obtained results.

Paper II This paper reports on the real-time measurements of mode-locking transition of a fiber laser with sub-nanometer and sub-picosecond resolutions at megahertz acquisition rates. The combined spectro-temporal measurements allow for phase-retrieval of the

complex electric field data. The author built the measurement setup and demonstrated the synchronization of the two signals. Experiments were performed by the author and P. Ryczkowski, who also performed the data analysis. J-M. Merolla and C. Billet provided support for using the experimental devices. The author wrote the numerical algorithm for the phase-retrieval and provided the first draft of the manuscript. J.M. Dudley, P. Ryczkowski and G. Genty finalised the manuscript.

Paper III The paper presents the first experimental characterization of second-order coherence functions of supercontinuum light. The measurements are performed on three cases with distinct coherence properties, demonstrating good agreement with numerical simulations. The author built the experimental setup and performed all the data analysis and numerical simulations for the paper. All authors contributed to the writing of the manuscript.

Paper IV Use of supercontinuum generation in an application for all-optical signal amplification is demonstrated in experiments. High signal amplification is shown to be associated with the sensitive soliton-dispersive wave coupling. The setup was designed by L. Orsila with the photodiode circuit provided by J. Sand. The author performed the measurements with L. Orsila and contributed to data analysis. G. Steinmeyer and G. Genty provided supervision and wrote the manuscript.

2 Light propagation in optical fibers

2.1 Linear light propagation in dielectric waveguides

Light can be described classically by simultaneous oscillations of electric and magnetic fields as first shown by James Clerk Maxwell in the 19th century [40]. The electric and magnetic fields are related by the famous Maxwell's equations (in their macroscopic form) that describe the behaviour of all electromagnetic waves:

$$\nabla \cdot \mathbf{D} = \rho_f \quad (2.1)$$

$$\nabla \cdot \mathbf{B} = 0 \quad (2.2)$$

$$\nabla \times \mathbf{E} = -\frac{\partial \mathbf{B}}{\partial t} \quad (2.3)$$

$$\nabla \times \mathbf{H} = \mathbf{J} + \frac{\partial \mathbf{D}}{\partial t}. \quad (2.4)$$

Here, \mathbf{E} and \mathbf{H} are the time and space dependent electric and magnetic fields, respectively. \mathbf{J} represents the electric current density flowing in the material and ρ_f corresponds to the free electric charge density in the material.

The material response to the electromagnetic field is described by the displacement \mathbf{D} and magnetic flux \mathbf{B} (so called material relations):

$$\mathbf{D} = \epsilon_0 \mathbf{E} + \mathbf{P} = \epsilon_0 \mathbf{E} + \epsilon_0 \chi_e \mathbf{E} \quad (2.5)$$

$$\mathbf{B} = \mu_0 \mathbf{H} + \mathbf{M} = \mu_0 \mathbf{H} + \mu_0 \chi_m \mathbf{H}. \quad (2.6)$$

Here ϵ_0 and μ_0 are the vacuum electric permittivity and magnetic permeability that describe what kind of electric charge distributions (displacement) and magnetic fluxes cause the corresponding electric and magnetic fields in vacuum. In a material these fields might also affect the material electric or magnetic dipoles resulting in an additional response to the total displacement and magnetic flux compared to vacuum. These are described by the electric polarizability $\mathbf{P} = \epsilon_0 \chi_e \mathbf{E}$ and magnetization $\mathbf{M} = \mu_0 \chi_m \mathbf{H}$, where χ_e and χ_m are the electric and magnetic susceptibilities that describe the strength of the material response and are equal to zero in vacuum.

Optical fibers are made of dielectric (insulating) materials, generally glasses and they do not conduct electricity or accumulate charges well as there are no free electrons. Therefore in the above equations we can set $\mathbf{J} = 0$ and $\rho_f = 0$. Furthermore, glasses are usually non-magnetic and no additional magnetic response from the material occurs ($\chi_m = 0$) and Maxwell's equations in a homogeneous dielectric material reduce to:

$$\nabla \cdot \mathbf{D} = 0 \quad (2.7)$$

$$\nabla \cdot \mathbf{B} = 0 \quad (2.8)$$

$$\nabla \times \mathbf{E} = -\mu_0 \frac{\partial \mathbf{H}}{\partial t} \quad (2.9)$$

$$\nabla \times \mathbf{H} = (\epsilon_0 + \epsilon_0 \chi_e) \frac{\partial \mathbf{E}}{\partial t}. \quad (2.10)$$

In order to describe light propagation in a material, these equations are combined into a single equation, where only the electric field is present. Taking the curl of Eq. 2.9 and inserting Eq. 2.10 one obtains the following:

$$\nabla \times \nabla \times \mathbf{E} = -\mu_0 \epsilon_0 \frac{\partial^2 \mathbf{E}}{\partial t^2} - \mu_0 \epsilon_0 \chi_e \frac{\partial^2 \mathbf{E}}{\partial t^2}. \quad (2.11)$$

Using the vector calculus identity $\nabla \times \nabla \times \mathbf{E} = \nabla(\nabla \cdot \mathbf{E}) - \nabla^2 \mathbf{E}$ and noting that $\nabla \cdot \mathbf{E} = 0$ Eq. 4.19 reduces to:

$$-\nabla^2 \mathbf{E} = -\mu_0 \epsilon_0 \frac{\partial^2 \mathbf{E}}{\partial t^2} - \mu_0 \epsilon_0 \chi_e \frac{\partial^2 \mathbf{E}}{\partial t^2}. \quad (2.12)$$

Using the relation between the speed of light in vacuum, electric permittivity and magnetic permeability in vacuum, $1/c^2 = \mu_0 \epsilon_0$, and using the definition of the induced polarization \mathbf{P} of Eq. 2.6 we obtain:

$$\nabla^2 \mathbf{E} = \mu_0 \epsilon_0 (1 + \chi_e) \frac{\partial^2 \mathbf{E}}{\partial t^2} \quad (2.13)$$

$$= \frac{1}{c^2} \frac{\partial^2 \mathbf{E}}{\partial t^2} + \mu_0 \frac{\partial^2 \mathbf{P}}{\partial t^2}. \quad (2.14)$$

These two forms are equivalent and useful in explaining some specific features. First of all, both of them are second order partial differential equations with respect to time and space, which means that they are wave equations. This point is particularly clear from Eq. 2.13, which has the form of a standard wave equation $\nabla^2 u(r, t) = k \frac{\partial^2 u(r, t)}{\partial t^2}$, where $k = \text{constant}$. Furthermore, we can see that the material response to the electric field is determined by the electric susceptibility χ_e .

The second form in Eq. 2.14 shows that the wave propagation is changed from free space propagation by the induced polarization in the material, that acts as an additional source term. This form will be more instructive later, when we discuss nonlinear propagation effects.

2.1.1 Linear effects in optical fibers

We first discuss linear propagation of light in materials, and in particular in optical fibers. Linear propagation effects in fibers results from changes in the phase velocity of light v in the material and losses (or attenuation/absorption). These are most instructively understood from inspecting Eq. 2.13. In general the electric susceptibility is a complex quantity. The real part can be associated with the refractive index $n = c/v$ while the

complex part corresponds to attenuation α . After some mathematical steps, one can show that they are related to the susceptibility by:

$$n = \text{Re}\{\sqrt{1 + \chi_e}\} \quad (2.15)$$

$$\alpha = \frac{\omega}{nc} \cdot \text{Im}\{\chi_e\}, \quad (2.16)$$

where ω is the angular frequency of the propagating field.

Refractive index & Material dispersion

The refractive index of materials depends on the frequency (or wavelength) of the light i.e. $n = n(\omega)$ - thts why the water droplets in air cause a rainbow. Full understanding of this dependence requires a quantum mechanical model, which is beyond the scope of the discussion here, but it can be intuitively understood from the fact, that electrons in a material react differently to electromagnetic waves of different frequencies (and hence different energies). In practice, this means that frequencies experience different velocities and are delayed in time by various amounts when propagating through the material, therefore leading to a temporal walkoff between the frequency components.

The frequency dependence of the refractive index of silica (SiO_2 the most common material for optical fibers) is shown in Fig. 2.1. This dependence is referred to as *material dispersion*.

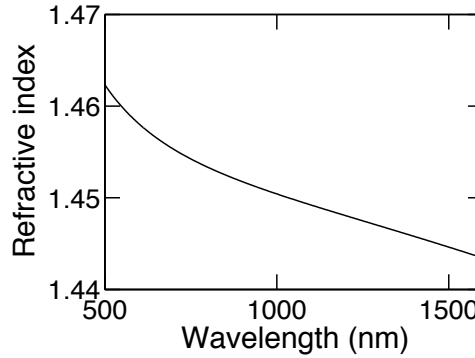


Figure 2.1: Typical refractive index profile of silica displaying the wavelength dependence.

The temporal walk-off becomes especially important in the case of ultrashort light pulses of 10 fs - 1 ps duration. Such pulses have spectral bandwidths varying between 1 nm - 100 nm at 1000 nm wavelength, resulting in a significant walkoff between the wavelengths and thus in temporal broadening of the pulses. This walkoff can be estimated from the propagation constant $\beta(\omega) = n(\omega)\omega/c$. (also known as the wavenumber or wavevector $k(\omega)$). Considering the propagation of an optical pulse, the group velocity v_g is often defined as:

$$v_g = \left(\frac{\partial \beta(\omega)}{\partial \omega} \right)^{-1} \bigg|_{\omega=\omega_0}, \quad (2.17)$$

representing the speed at which the optical field or pulse envelope centered at ω_0 propagates and has units of meters per second. The dispersion of the material leads also to frequency dependence of the group velocities in the material, causing delay between the different frequency components. This walkoff can be estimated from the change of the group velocity with respect to the center frequency by defining the group velocity dispersion (GVD) -parameter:

$$\beta_2 = \frac{\partial}{\partial \omega} \frac{1}{v_g} = \frac{\partial^2 \beta(\omega)}{\partial \omega^2}, \quad (2.18)$$

that has units of s^2/m , or equivalently $\frac{\text{s}}{\text{Hz}\cdot\text{m}}$ that can be viewed as the delay in seconds per one hertz bandwidth of the field per meter of propagation in the fiber.

While the above definition is extremely useful in the physical models discussed later, the GVD can be recast in a more practical dispersion parameter D ,

$$D = -\frac{2\pi c}{\lambda^2} \beta_2, \quad (2.19)$$

with units of $\text{ps}/\text{nm}/\text{km}$. The simplicity of use of the dispersion parameter can be understood from the following. The amount by which the two extreme wavelengths of a laser pulse with 1 nm bandwidth, propagating in 1 km of fiber is directly given by the value of D , resulting in an equivalent temporal broadening of the pulse.

Modal and waveguide dispersion in optical fibers

Conventional optical fibers consist of a cylindrical core of a few micrometers to tens of micrometers in diameter made of a material with a given refractive index and surrounded with by a cylindrical cladding made of material with lower refractive index. The difference in refractive index between the core and the cladding allows total internal reflection to keep the light trapped inside the fiber and enable guidance over long distances.

The core and the cladding are typically made of the same material and the increase in the refractive index in the core is, usually small $\Delta n \approx 0.01n$, is achieved by doping the core with small amounts of GeO_2 , P_2O_5 or Al_2O_3 . In photonic crystal fibers the guiding mechanism relies on the photonic bandgap effect achieved by adding a lattice of air holes around the core of the fiber [41]. In addition to the material dispersion, both types of fiber experience additional sources of dispersion resulting from the fiber geometry, referred to as modal and waveguide dispersion.

In order to explain the origin of modal and waveguide dispersion we need to introduce the concept of fiber modes, which correspond to possible transverse electric field distributions of light that is guided in the fiber. They are obtained by solving the Maxwell equations with boundary conditions set by the geometrical dimensions and the refractive indices of the materials in the fiber.

The electric field oscillating at a single frequency or wavelength can fulfill the boundary conditions for several different transversal distributions (see Fig. 2.2), depending on the fiber core diameter. Different modes experience different geometrical paths inside the fiber resulting in delay between these modes and this is referred to as *modal dispersion*.

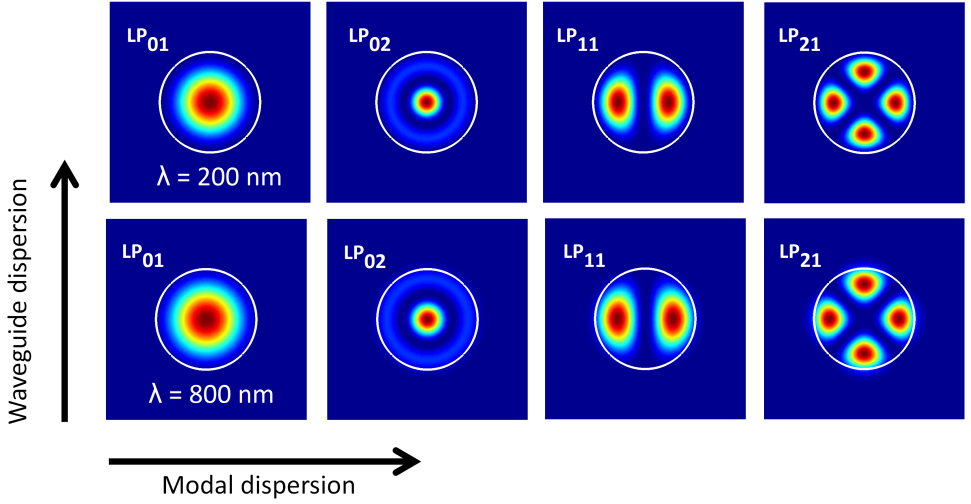


Figure 2.2: Example of transverse fiber modes with linearly polarized light. Top row and bottom row have been calculated with different wavelengths, illustrating the difference in the mode distributions leading to waveguide dispersion.

If the fiber core size is reduced such that only a single transverse mode can propagate at any frequency, the fiber is called a single-mode fiber. Although generally the mode distributions for the first allowed mode appear similar for different frequencies in Fig. 2.2, there will still be a delay between them, which results from the fact, that modes with higher frequency (shorter wavelength) are more confined into the core, and therefore effectively experience a higher refractive index than the lower frequency modes (compare Fig. 2.2 top and bottom row). This is called *waveguide dispersion*.

When using multimode fibers, all of these three dispersion sources contribute to the effective refractive index, or group index $n_g(\omega)$ at a given frequency. From an application viewpoint however, it is generally desired to use single mode fibers to avoid possible detrimental interference and cross-talk problems in applications. However, even with single mode fibers, waveguide dispersion needs to be accounted to the effective refractive index. Figure 2.3 illustrates the effect of waveguide dispersion on the total effective refractive index.

When describing the dispersion of optical waveguides one needs to account for all possible sources of dispersion to correctly model the system. This means that the propagation constant should be defined accounting for the effective refractive index frequency dependence $\beta(\omega) = n_g(\omega)\omega/c$. In practice, the exact knowledge of all the contributions are rarely exactly known at all wavelengths, and the propagation constant is expressed through a Taylor series expansion at the center wavelength ω_0 of the propagating light,

$$\beta(\omega) = \sum_{k \geq 0} \frac{1}{k!} \beta_k (\omega - \omega_0)^k, \quad (2.20)$$

where $\beta_k = \partial^k \beta(\omega) / \partial \omega^k$ are evaluated at ω_0 . We can immediately associate β_1 with the group velocity and β_2 with the GVD-parameter discussed earlier that are now accounting

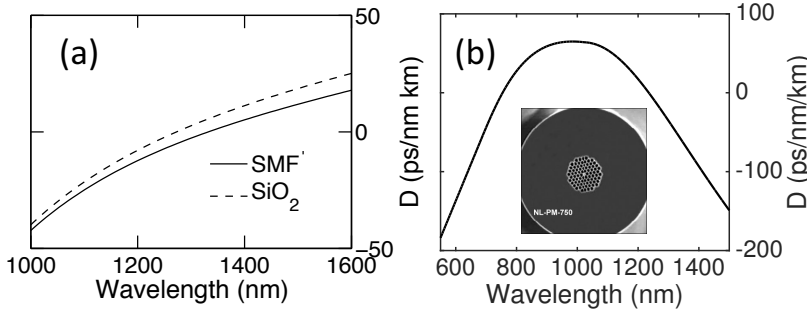


Figure 2.3: (a) The dashed line displays the dispersion parameter D resulting from the bulk material dispersion of silica as displayed in Fig. 2.1 and the solid line shows the effect of the waveguide dispersion in a standard single mode fiber on the total dispersion parameter. (b) Dispersion curve and microscope image of a photonic crystal fiber NL-PM-750 used in some of the experiments of this thesis. This fiber has two ZDW wavelengths at 750 nm and 1260 nm.

for all of the dispersive effects instead of only the material dispersion. When $k \geq 3$ the derivatives do not have any specific names and are just referred to as higher order dispersion parameters.

The dispersive properties can be divided into two regimes by the points where the dispersion parameter D in Fig 2.3 (a) passes through zero. Wavelengths, where D has positive values ($\beta_2 < 0$) are referred to as the anomalous dispersion regime, and wavelengths where D has negative values ($\beta_2 > 0$) are called normal dispersion regime. The difference between the two regimes is, that in normal dispersion long wavelengths travel faster than short wavelengths (as is usual for optical glasses in the visible wavelengths, hence the name normal), whereas the opposite occurs in anomalous dispersion. In the case of purely linear propagation of light, these two regimes only lead to temporal broadening. However, when coupled with nonlinear effects discussed next, the particular dispersion regime can dramatically impact the resulting physics.

The point where the D -parameter crosses zero is called the zero dispersion wavelength (ZDW) and is where dispersive broadening is minimum. As the waveguide dimensions affect the total dispersion some tunability of the ZDW can be achieved. This has been especially the case with the development of photonic crystal and microstructured fibers (see Fig. 2.1 (c)), that have allowed for single mode operation over very broad bandwidths while engineering the waveguide dispersion [41]. In particular, this has allowed to bring ZDW and anomalous dispersion regimes down to visible wavelengths, allowing the use of high power solid state lasers in combination with such fibers. Dispersion engineering has also been used to flatten the dispersion profile in order to minimize pulse broadening in telecommunication systems [42, 43].

2.2 Nonlinear effects and pulse propagation equation

We have seen that the response of material's electrons gives rise to the refractive index and losses via the electric susceptibility χ_e . This model is perfectly valid in most situations, when the electric field \mathbf{E} is relatively weak (for ambient sunlight the electric field amplitude is well below 10^3 V/m). However, the invention of the laser, has led to the emergence of light sources with extremely high intensities by focusing coherent laser light into tiny

spots with electric field values exceeding 10^{11} V/m, that is the characteristic electric field strength inside atoms $E_{at} \propto e/(\epsilon_0 a_0^2)$, where e is the electron charge and a_0 is the atomic radius. This value can be considered as the limit for *nonlinear optical interaction* of electrons with the electric field [1]. The complete picture would require quantum mechanical treatment, but the basic phenomena can be understood with the help of a simple model, whereby a single electron is bound by a spring to the core of the atoms that constitute the material. This model is known as the Lorentz model.

Under the action of the electric field, the electron feels a force that pulls the electron away from the atom (opposing the spring), and in the case of an electric field with weak amplitude, displaces it by some amount that is *linearly* proportional to the electric field amplitude, Fig. 2.4 (a). If the intensity of light increases and correspondingly the electric field amplitude, the electron feels an increased force from the electric field and the spring becomes fully extended Fig. 2.4 (b). In analogy with a mechanical spring, the further the electron spring is extended, the more force is required to extend it more. In this case the displacement is not only proportional to the electric field amplitude, but also its harmonics, in other words it is nonlinearly dependent on the electric field strength. This causes the electron to move out of synchronization with respect to the electric field, resulting in new frequencies being generated from the electron oscillations.

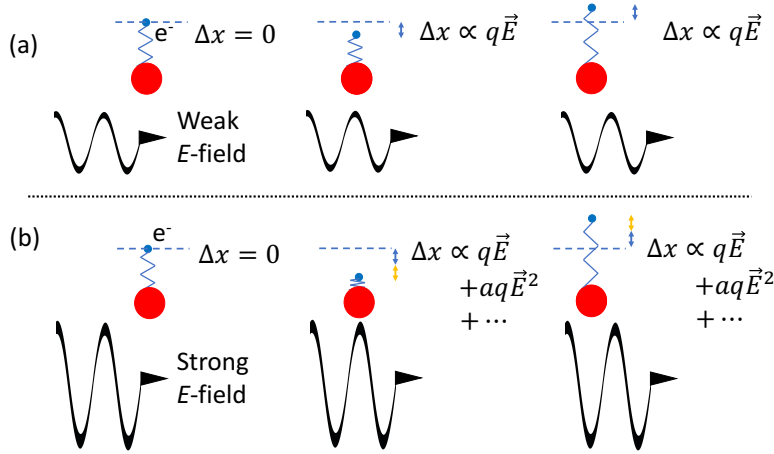


Figure 2.4: (a) Response of an electron with charge $q = e$ bound to an atom by an imaginary spring when a weak optical field E is applied. Displacement Δx of the electron due is linearly proportional to the applied electric field. (b) The electron is pulled further away when a strong electric field is applied. However the atom responds to this and the displacement is now proportional to the linear displacement and an additional term aqE^2 proportional to the square of the field appears. Here a is a proportionality constant.

Going back to the wave equation of 2.14, this nonlinear response can be modeled by taking into account that the electronic polarizability \mathbf{P} consists from a linear part \mathbf{P}_L (defined earlier) and an additional nonlinear part \mathbf{P}_{NL} dependent on the harmonics of the E-field:

$$\mathbf{P} = \mathbf{P}_L + \mathbf{P}_{NL} = \epsilon_0 \chi_e^{(1)} \mathbf{E} + \epsilon_0 \chi_e^{(2)} \mathbf{E}^2 + \epsilon_0 \chi_e^{(3)} \mathbf{E}^3 + \dots \quad (2.21)$$

Here, $\chi_e^{(k)}$ are the material electric susceptibilities, generally tensors of rank $k + 1$ to account for the vectorial nature of the electric field. The nonlinear susceptibilities ($k \geq 2$) describe the strength of the nonlinearity (or how strong our opposing electronic spring is) as well as the spatial dependency of the electronic response (hence the tensors that describe the dependence of the incoming light beam). In standard nonlinear optical experiments it is usually sufficient to consider only the square and cubic terms of the nonlinear response, as higher order terms have extremely low susceptibilities that make their contribution very weak [1]. Furthermore, the material structural properties can lead to simplifications of the tensor properties or vanishing terms in the expansion of Eq. 2.21. An important example is the silica glass used in optical fibers that possesses inversion symmetry leading to all of the even-order susceptibilities vanishing [1]. This means that from the point of view of nonlinear fiber optics, the total material polarization can be expressed as $\mathbf{P} = \epsilon_0 \chi_e^{(1)} \mathbf{E} + \epsilon_0 \chi_e^{(3)} \mathbf{E}^3$.

Furthermore, if one assumes a linear polarization in a single mode fiber, the transverse x-y-dependence of the electric field can be neglected and its amplitude can be written as $E(z, t) = A(z, t)e^{i(\beta_0 z - \omega_0 t)} + c.c.$, where $A(z, t) = A_0(z, t)e^{i\phi(t)} \equiv A$ is the pulse complex envelope (with phase information) and $|A|^2$ corresponds to the instantaneous power in Watts. Note, that we have chosen to present the real-electric field as a sum with its complex conjugate (c.c.) to simplify calculations. We first evaluate the contribution of the nonlinear polarization using this ansatz:

$$\begin{aligned} P_{\text{NL}} &= \epsilon_0 \chi_e^{(3)} [A(z, t)e^{i(\beta_0 z - \omega_0 t)} + c.c.]^3 \\ &= \epsilon_0 \chi_e^{(3)} A(z, t)^3 e^{i(3\beta_0 z - 3\omega_0 t)} + 3\epsilon_0 \chi_e^{(3)} |A(z, t)|^2 A(z, t) e^{i(\beta_0 z - \omega_0 t)} + c.c. \\ &\approx 3\epsilon_0 \chi_e^{(3)} |A(z, t)|^2 A(z, t) e^{i(\beta_0 z - \omega_0 t)} + c.c. \end{aligned} \quad (2.22)$$

The last approximation follows from that normally the field at the third harmonic frequency propagates at a different velocity in the waveguide than the fundamental field and is therefore not amplified significantly and can be neglected. Thus, it's said that the fields are not *phase-matched*, or momentum is not conserved. It is in general difficult to achieve phase-matching for multiple frequencies simultaneously in any material due to the material dispersion [1].

Next we consider the whole Eq. 2.14 with the above ansatz. We start by transferring equation 2.14 to the spectral domain, by Fourier transforming it:

$$\nabla^2 \tilde{E}(\omega) + \frac{\omega^2}{c^2} \tilde{E}(\omega) + \frac{\omega^2}{\epsilon_0 c^2} \tilde{P}_L(\omega) = \mathcal{FT} \left[\frac{\partial^2}{\partial t^2} P_{\text{NL}}(t) \right]. \quad (2.23)$$

Here we have used the fact that the derivatives can be replaced by $\frac{\partial}{\partial t} \rightarrow i\omega$ and $\tilde{E}(\omega)$ is the Fourier transform, \mathcal{FT} , of the field. We have also not explicitly written out the FT of the nonlinear polarization due to its complexity. The linear polarization part can be written out with the help of the first order electric susceptibility $\tilde{P}_L(\omega) = \epsilon_0 \chi^{(1)}(\omega) \tilde{E}(\omega)$ and it can be combined together using the frequency dependent refractive index, $n^2(\omega) = 1 + \chi^{(1)}(\omega)$ to obtain:

$$\nabla^2 \tilde{E}(\omega) + \frac{\omega^2 n^2(\omega)}{c^2} \tilde{E}(\omega) = \mathcal{FT} \left[\frac{\partial^2}{\partial t^2} P_{\text{NL}}(t) \right]. \quad (2.24)$$

Furthermore, as we are considering the propagation in a single mode fiber, the transverse profile properties can be omitted by setting $\nabla^2 \approx \frac{\partial^2}{\partial z^2}$. We can also use the propagation constant $\beta(\omega) = n(\omega)\omega/c$ to simplify the equation to:

$$\frac{\partial^2}{\partial z^2} \tilde{E}(\omega) + \beta^2(\omega) E(\omega) = \mathcal{FT}[\frac{\partial^2}{\partial t^2} P_{\text{NL}}(t)]. \quad (2.25)$$

Evaluating the derivative with respect to z by using our ansatz we obtain:

$$\frac{\partial^2}{\partial z^2} \tilde{E}(\omega) = \left(\frac{\partial^2 \tilde{A}(z, \omega)}{\partial z^2} + 2i\beta_0 \frac{\partial \tilde{A}(z, \omega)}{\partial z} - \beta_0^2 \tilde{A}(z, \omega) \right) e^{i\beta_0 z} + c.c. \quad (2.26)$$

Using the assumption that the pulse envelope $\tilde{A}(z, \omega)$ varies slowly compared the wavelength of light (slowly varying envelope approximation) one can neglect the second order derivative of the envelope with respect to z and we can write equation 2.25 as:

$$\left[2i\beta \frac{\partial \tilde{A}(z, \omega)}{\partial z} + (\beta^2(\omega) - \beta_0^2) \tilde{A}(z, \omega) \right] e^{i\beta_0 z} + c.c. = \mathcal{FT}[\frac{\partial^2}{\partial t^2} P_{\text{NL}}(t)]. \quad (2.27)$$

Finally, as the propagation constant change with respect to frequency in optical materials is usually moderate, one can approximate $\beta^2(\omega) - \beta_0^2 \approx 2\beta_0(\beta(\omega) - \beta_0)$, after which we perform an inverse Fourier transform back to time domain and re-arrange to obtain:

$$\begin{aligned} & \left[\frac{\partial A(z, t)}{\partial z} + \beta_1 \frac{\partial A(z, t)}{\partial t} + \sum_{k \geq 2} i^{k+1} \frac{\beta_k}{k!} \frac{\partial^k A(z, t)}{\partial t^k} \right] e^{i(\beta_0 z - \omega_0 t)} + c.c. \\ &= \frac{-i}{2\beta_0 \epsilon_0 c^2} \frac{\partial^2}{\partial t^2} P_{\text{NL}}(z, t). \end{aligned} \quad (2.28)$$

Here β_i are the Taylor series coefficients of the propagation constant that are used to simplify the Fourier transform, as an exact functional form of $\beta(\omega)$ is rarely known.

Performing the derivation twice on the nonlinear polarization part given by eq. 2.22 and assuming an instantaneous nonlinearity (i.e. $\chi^{(3)}(t) = \text{const.}$), one will obtain the following

$$\begin{aligned} & \frac{\partial^2}{\partial t^2} P_{\text{NL}}(z, t) = 3\epsilon_0 \chi^{(3)} e^{i(\beta_0 z - \omega_0 t)} \\ & \left(\frac{\partial^2 |A(z, t)|^2 A(z, t)}{\partial t^2} - 2i\omega_0 \frac{\partial |A(z, t)|^2 A(z, t)}{\partial t} - \omega_0^2 |A(z, t)|^2 A(z, t) \right) + c.c. \end{aligned} \quad (2.29)$$

Similarly as before, assuming that the temporal envelope $A(z, t)$ varies slowly with respect to time, one can neglect the first and second order derivatives (the first order derivative should be included in some cases as will be discussed later in higher order effects), and equation 2.28 reduces to:

$$\begin{aligned} & \left[\frac{\partial A(z, t)}{\partial z} + \beta_1 \frac{\partial A(z, t)}{\partial t} + \sum_{k \geq 2} i^{k+1} \frac{\beta_k}{k!} \frac{\partial^k A(z, t)}{\partial t^k} \right] e^{i(\beta_0 z - \omega_0 t)} + c.c. \\ &= i \frac{3\chi^{(3)} \omega_0}{2n_g(\omega_0)c} |A(z, t)|^2 A(z, t) + c.c. \end{aligned} \quad (2.30)$$

We define γ as the nonlinear parameter describing the strength of the nonlinear effects arising from the nonlinear polarization:

$$\gamma = \frac{3\omega_0}{2n(\omega_0)c}\chi^{(3)}. \quad (2.31)$$

The strength of the nonlinearity at ω_0 is determined by the third-order susceptibility, the group index $n_g(\omega_0)$ which is affected by the material and the fiber geometry. Smaller fiber core areas lead to higher confinement resulting in stronger electric field strengths and lead to enhanced nonlinear effects.

Furthermore, we can neglect the complex conjugates on both sides of equation 2.31 and simplify by multiplying with $e^{-i(\beta_0 z - \omega_0 t)}$. One can also introduce losses α by using the complex refractive index of Eq. 2.16 in the derivation to obtain:

$$\frac{\partial A}{\partial z} + \beta_1 \frac{\partial A}{\partial t} + \sum_{k \geq 2} i^{k+1} \frac{\beta_k}{k!} \frac{\partial^k A}{\partial t^k} + \frac{\alpha}{2} A = i\gamma |A|^2 A. \quad (2.32)$$

Finally, with a change of variable $T = t - z/v_g$ one can transform Eq. 2.32 into a co-moving frame with the pulse envelope:

$$\frac{\partial A}{\partial z} - \sum_{k \geq 2} i^{k+1} \frac{\beta_k}{k!} \frac{\partial^k A}{\partial T^k} + \frac{\alpha}{2} A = i\gamma |A|^2 A. \quad (2.33)$$

This equation is referred to as the basic nonlinear propagation equation.

2.2.1 Optical Kerr effect

One of the most important manifestations of the nonlinearity is the intensity dependent refractive index, or Kerr effect. The nonlinear term causes a local increase in the effective refractive index of the material $n_{\text{eff,NL}} = n_g + n_2 I$. Here, n_g is the group index resulting from material and waveguide dispersion, which is further modified by an intensity dependent term $n_2 I$ arising again from the nonlinear susceptibility. Often the nonlinear parameter γ of a material is experimentally determined by measuring the intensity dependent refractive index which are related by $\gamma = n_2 \omega_0 / (c A_{\text{eff}})$. In optical fibers, this intensity dependent refractive index gives rise to four-wave-mixing (FWM), self-phase modulation (SPM) and cross-phase modulation (XPM) which are special cases of the Kerr effect.

Briefly described, SPM is the additional phase shift/delay experienced by the electric field in the fiber caused by the increased effective refractive index. For laser pulses, the intensity dependence of the Kerr effect leads to a time-dependent phase-shift. In practice this means, that while the pulse temporal shape stays the same, the temporally varying phase generates new frequencies in the spectral domain and the pulse spectrum broadens.

XPM corresponds to the case when two fields with different center frequencies are injected into an optical fiber. Due to the Kerr effect, both will experience an increased refractive

index (and corresponding phase shift) dependent on the second field in addition to the increase due to SPM.

FWM refers to the interaction of four fields at different frequencies that interact with each other via the nonlinearity. As mentioned earlier, phase-matching of several frequencies simultaneously is difficult in normal materials. However, when the intensities of the constituent fields are increased and significantly large changes to the corresponding refractive indices due to the Kerr effect occur allowing for phase-matching to be fulfilled, significant energy transfer between the fields can occur.

2.2.2 Higher order nonlinear effects

Aside from the nonlinear effects rising from the instantaneous nonlinear polarization of the material, there are other nonlinear physical mechanisms that can become significant depending on the experimental conditions. These other nonlinearities arise from a coupling between the molecular structure and electric field in contrast to the purely electronic nature of the Kerr effect. Such examples are stimulated Brillouin scattering (SBS) arising from a periodic refractive index change caused by electrostriction, or stimulated Raman scattering (SRS) arising from energy transfer between the vibrational energy states of the molecules and the electric field [2].

SBS is significant only when using long pulses ($> \text{ns}$) or continuous wave (CW) fields as electrostriction takes time to build up in the material. Therefore SBS usually does not need to be considered for ultrafast pulses with durations below tens of picoseconds.

SRS on the other hand has a relatively short response time of tens of femtoseconds and becomes increasingly important as pulses become shorter, needing to be included in the pulse propagation model. The mathematical expression for Raman scattering can be derived by using a temporal response function $R(t)$ for the third-order susceptibility that includes the instantaneous response, $\delta(t)$, as well as a delayed response, $h_R(t)$, accounting for the Raman effect [2, 44]:

$$R(t) = (1 - f_R)\delta(t) + f_R h_R(t). \quad (2.34)$$

Here $f_R = 0.18$ is the fractional contribution of the Raman effect to the total nonlinearity and $h_R(t)$ is the delayed response function determined by using the Kramers-Kronig relations and experimentally measured Raman gain curve [45] or by using the nearly equivalent analytic form [44].

Using the response function $R(t)$ for the nonlinear susceptibility in equation 2.32 one can obtain, after some algebra, a more complete model for the propagation of short laser pulses in fibers in the co-moving time frame:

$$\frac{\partial A}{\partial z} - \sum_{k \geq 2} i^{k+1} \frac{\beta_k}{k!} \frac{\partial^k A}{\partial T^k} + \frac{\alpha}{2} A = i\gamma \left(1 + i\tau_{\text{shock}} \frac{\partial}{\partial T} \right) \times \left(A \int_{-\infty}^{\infty} R(t') |A(z, T - t')|^2 dt' \right) \quad (2.35)$$

This form is often referred to as the generalized nonlinear Schrödinger equation (GNLSE). The delayed response $R(t)$ of the third order susceptibility (i.e. SRS) is evaluated by the integral term.

In addition to the delayed nonlinear response, we observe the factor $(1 + i\tau_{\text{shock}} \frac{\partial}{\partial T})$ that results from accounting for the first order derivative of the nonlinear polarization in Eq. 2.30. This factor takes into account the frequency dependence (dispersion) of the nonlinear parameter γ with the time derivative term that causes effects at a characteristic time scale of $\tau_{\text{shock}} = 1/\omega_0$. These effects are usually associated with self-steepening and optical shock formation [1, 2, 31]. Even though the derivation of Eq. 2.33 assumed a slowly varying envelope, the inclusion of this frequency dependent nonlinearity is actually a key factor allowing the extension of using the GNLSE down to pulses with few femtosecond durations [31].

This model is non-integrable, but various finite-difference or pseudospectral numerical integration methods can be used to find approximate solutions (see chapter 2 of [2] and the references therein). One of the most successful and straightforward approaches is the split-step Fourier method that can be classified as a finite-difference method. Briefly described, it splits the fiber into shorter segments, where the nonlinear and dispersive effects can be evaluated independently. One then approximates the field evolution to the next segment by first taking a purely nonlinear evolution step followed by only the dispersive evolution calculated in the Fourier domain and giving the algorithm its name. This modelling approach has yielded excellent agreement with experimental results and is now widely used because of straightforward implementation using fast Fourier transform algorithms on PCs [31].

Raman self-frequency shift

As the Raman effect involves energy exchange, it implies a change in the frequency of the propagating light. While theoretically both increase and decrease in the frequency are possible, a simple thermodynamic argument shows, that only high frequency components can amplify the low frequency components such that Raman gain is strongly asymmetric with respect to the pump frequency [45]. For long pulses/CW fields in silica fibers, SRS will cause amplification of discrete frequency bands separated by 13.2 THz (maximum gain) from the pump. For short pulses, below 1 ps duration, the spectral bandwidth of the pulse is broad enough for the high frequency components of the pulse to amplify the low frequency components, a phenomenon referred to as intrapulse Raman scattering. This results in a continuous spectral shift of the pulse center frequency, which is known as the Raman self-frequency shift (RSFS). The magnitude of the frequency shift can be shown to be inversely proportional to the fourth power of pulse duration [2].

2.2.3 Optical solitons

When discussing pulse propagation in waveguides the term solitons cannot be avoided. They are light pulses that propagate undistorted in the waveguide. The effect of dispersion is balanced by the nonlinear phase shift induced by SPM. This implies that in order for solitons to exist, two conditions need to be fulfilled. Firstly, as the phase shift due to SPM has always a gradient to the same direction in time, dispersion has to be in the opposite direction. This means that bright solitons only exist in materials or waveguides with anomalous dispersion. Secondly, the input pulse power needs to be large enough to induce enough SPM to compensate for the dispersion.

Note that the term bright soliton is used here, which refers to a pulse of light on no background radiation. Dark solitons, that are observed as “missing light” in a background

pulse, also exist. Moreover, they can also exist in the normal dispersion regime [46]. As lasers generally produce bright soliton pulses, we concentrate on the dynamics of these.

The analytical pulse shape that fulfills this condition is the bright hyperbolic secant soliton:

$$A(z = 0, T) = \sqrt{P_0} \operatorname{sech}\left(\frac{T}{T_0}\right). \quad (2.36)$$

Here P_0 is the peak power of the soliton and T_0 is the pulse duration related to the full width at half maximum (FWHM) duration as $T_0 = T_{\text{FWHM}}/1.763$. The dispersive and nonlinear effects cancel each other out when $P_0 = |\beta_2|/(\gamma T_0^2)$.

If the peak power is increased in Eq. 2.36 we obtain what are referred to as *higher order solitons*. At $z = 0$, they have the same shape of the hyperbolic secant, where the peak power is set by the soliton condition $N = m$, where $m = 1, 2, 3, \dots$, and N is the soliton order defined by

$$N = \sqrt{\frac{\gamma P_0 T_0^2}{|\beta_2|}}. \quad (2.37)$$

In contrast to $N = 1$ solitons, higher order solitons do not propagate undistorted, but rather undergo periodic evolution, with complex expansion and compression cycles both in the temporal and spectral domains. Higher order soliton can in fact be considered as the nonlinear superposition of fundamental $N = 1$ solitons with different phases and amplitudes. Eventually they return to their original hyperbolic secant shape and the cycle starts again. Figure 2.5 compares the evolution of a $N = 1$ and $N = 3$ solitons in the temporal and spectral domains.

An interesting question is what happens if the pulse parameters T_0, P_0 do not match the condition $N = 1$, or the input pulse shape is not hyperbolic secant (though this holds true for most soliton-mode locked lasers). The soliton solution is in fact an analytical attractor state for pulse propagation in fibers such that, if a pulse does not fulfill the soliton condition, it will broaden or compress in time, and possibly shed excess energy, in order to adjust its properties fulfill a soliton solution. If the peak power is such that it does not fulfill the soliton condition $N = \text{integer}$, the pulse will adjust itself to the nearest integer soliton number. In the case when $N < 0.5$, the nonlinear effects are not strong enough, and the pulse will just undergo linear, dispersive broadening and not turn into a soliton.

Soliton fission

Even though solitons are attractor solutions of for pulse propagation in fibers and they propagate unchanged when only second-order dispersion and the Kerr effect are present, typical experimental conditions involve higher-order dispersion and nonlinearities such that one should consider the pulse propagation in the full GNLSE framework. Higher-order solitons are very sensitive to these perturbations and typically break up into its constituent fundamental solitons that subsequently propagate separately. This process is called *soliton fission* and it occurs approximately at a distance $L_{\text{fiss}} \approx N/(\gamma P_0)$, which

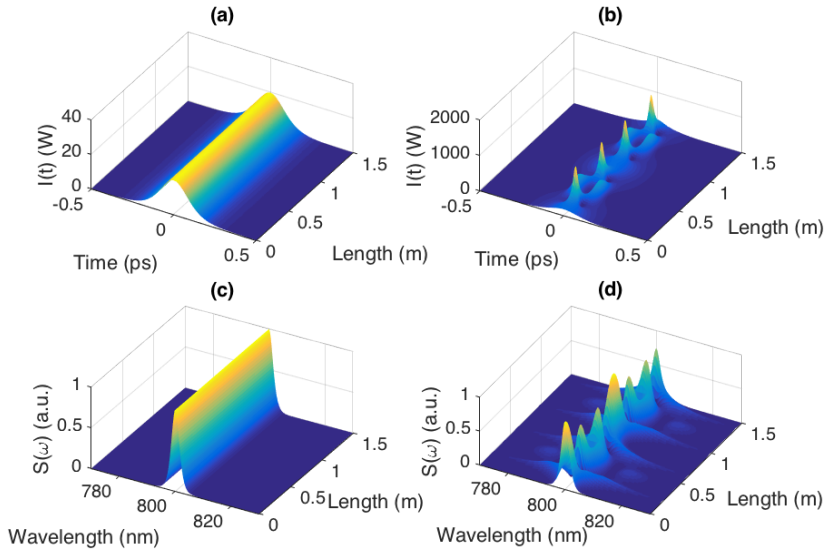


Figure 2.5: Evolution in time domain of a fundamental soliton propagating unchanged (a) and third order ($N = 3$) soliton (b) undergoing typical periodic evolution in a fiber with only second order dispersion and nonlinearity present. Corresponding evolution in spectral domains are also shown in (c) for the fundamental and (d) the third order soliton.

is around the same distance where the spectral broadening of the higher order soliton reaches its maximum for the first time and the perturbative effects are the strongest [31].

As each of the fundamental solitons have different durations and peak powers, the subsequent higher-order effects will also affect each of these in separate manners. One of the most prominent ones is the RSFS discussed earlier, that will start redshifting the solitons at different rates due to the shift rate dependence on the soliton duration.

Dispersive wave generation

When higher order dispersion terms cannot be neglected (as is usual for short pulses with large bandwidths) and a soliton propagates near the ZDW so that a part of its spectrum extends to the normal dispersion regime, a dispersive wave (DW) can be generated. The higher-order dispersion terms allow for phase-matching between the soliton center frequency and the dispersive wave, and resonant energy transfer occurs from the soliton to the dispersive wave wing [47]. The soliton will react to this with a spectral recoil away from the ZDW, which reduces the phase-matching until the resonance is lost and energy transfer stops. Furthermore, additional redshift from the RSFS will reduce the distance over which the DW and soliton are phase-matched further reducing the transferred energy amount [31]. Generally the amount of energy transferred is difficult to estimate analytically, but the frequency of the phase-matched dispersive wave can be estimated accurately.

2.3 Spectrogram representation

For the analysis of some of the results presented in this thesis, it can be useful to plot the spectrogram representation of the electric field. The spectrogram yields an intuitive

picture of the electric field of light in the temporal and spectral domains simultaneously and is convenient to visualize pulse propagation effects. Furthermore, it can be measured experimentally using a frequency resolved optical gating system [23].

The spectrogram $X(\tau, \omega)$ is a two-dimensional time-frequency distribution of the signal, in other words it tells which frequencies of a given electric field source arrive at which time. Mathematically it is defined as:

$$X(\tau, \omega) = \left| \int_{-\infty}^{\infty} E(t) p(t + \tau) e^{-i\omega t} dt \right|^2. \quad (2.38)$$

Here $p(t + \tau)$ is a known reference pulse that is shorter in time than $E(t)$ and narrower in spectral bandwidth. In this particular case, one can also observe, that the *margins of the spectrogram* (that are obtained by integrating the spectrogram over either the spectral or temporal axis) are a convolution of $p(t)$ and $E(t)$ in the corresponding domains. The spectrograms and their margins are shown in figure 2.6 illustrating some of the linear and nonlinear propagation effects discussed above:

- (a) a hyperbolic secant shaped pulse with $T_{\text{FWHM}} = 150$ fs, for which the time and bandwidth fulfill the minimum time-bandwidth product [2]
- (b) the same pulse as in (a) but which has undergone dispersive temporal broadening in a fiber with anomalous dispersion (also known as linear chirp)
- (c) same pulse as in (a), but which has experienced spectral broadening due to SPM.

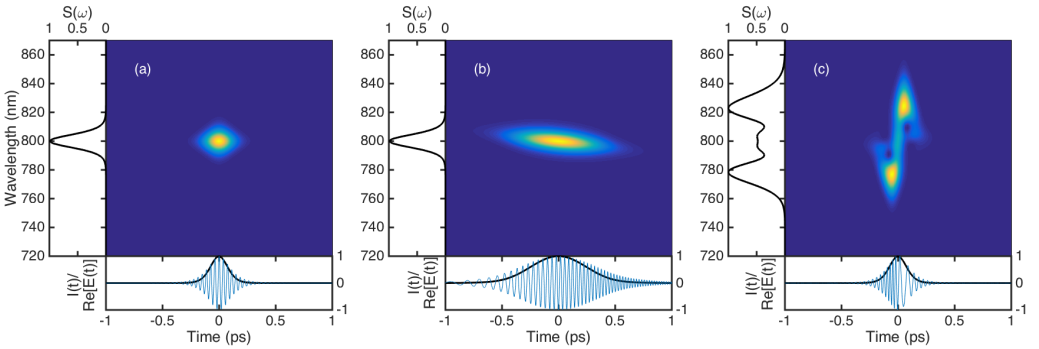


Figure 2.6: Examples of XFROG spectrograms and their margins for three different cases listed above with a gate pulse duration of $T_{\text{FWHM}} = 75$ fs. In addition to the integrated margins shown by the black lines, we illustrate an example of the actual electric field oscillations of the light, by the blue lines demonstrating the temporally varying instantaneous frequency for cases (b) and (c).

These simple examples illustrate the usefulness of the spectrogram representation. The change in the instantaneous frequency of the pulse caused by dispersion can be observed directly from the pulse tilt. The long wavelength contributions arrive earlier (due to the smaller effective refractive index in anomalous dispersion regime) compared to long wavelengths. For the pure SPM case, we can observe how the pulse has not broadened in time compared to (a) and (b), but the spectrum has undergone significant broadening.

Experimental measurement of the spectrogram can be performed for example by cross correlation frequency resolved optical gating (XFROG) whose setup is illustrated in figure 2.7.

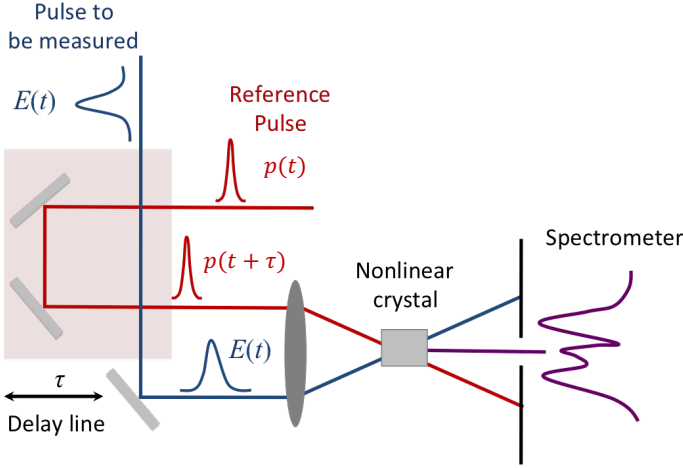


Figure 2.7: Simple schematic of the XFROG setup. The reference pulse and pulse under study are mixed together in a second order nonlinear crystal where a sum frequency generation (SFG) procedure occurs. This SFG signal is measured by a spectrometer at various delays in order to form the spectrogram.

There exist inversion algorithms that allow one to retrieve the full complex electric field $E(t)$ from the spectrogram $X(\tau, \omega)$, if the reference pulse complex field is known [23]. As XFROG measurements are usually averaged over multiple pulses, this retrieval requires the measured pulse train to be stable over this averaging. Single-shot versions of FROG measurements do exist, but they have significant limitations that hinder their usability for extremely complex pulses e.g. generated in supercontinuum generation discussed later.

2.4 Modulation instability

In what follows, we consider the special case of continuous wave fields (or long pulses with $A(z, T) \approx \text{const.}$, for periods longer than nanoseconds) propagating in the anomalous dispersion regime. Even though we limit our scope for the moment, the dynamics explained here can also play an important role for shorter pulses. This long pulse assumption however helps explaining the essential features of the dynamics with less complicated theory involved.

For continuous fields, the delayed response becomes irrelevant and SRS can be neglected. For moderate powers, SBS effects can also be neglected and thus the only nonlinearity arises from the Kerr effect. In silica optical fibers losses are generally small (0.18 dB/km @ 1550 nm) and we can neglect attenuation for short propagation lengths in the GNLSE of Eq. 2.33. As the bandwidth of CW fields is very narrow, dispersive effects can also be modeled with the simple inclusion of the GVD term β_2 . Using the above approximations, we obtain the nonlinear Schrödinger equation (NLSE):

$$\frac{\partial A}{\partial z} + \frac{i\beta_2}{2} \frac{\partial^2 A}{\partial T^2} = i\gamma|A|^2 A. \quad (2.39)$$

The NLSE can be considered as a special integrable case of the GNLSE, where analytical solutions do exist and can be obtained by the inverse scattering transform (IST) [48–50]. Aside from the fact that these analytical solutions can be used for insight into the evolution of quasi-CW fields in optical fibers, it has cross-disciplinary importance in physics. Indeed, the NLSE arises also in the context of wave propagation in deep water [6, 9, 10], in plasma physics [11, 12] or in Bose-Einstein condensates [13, 14].

One of the celebrated properties of the NLSE is the instability of a continuous wave against small perturbations in the anomalous dispersion regime. Any small perturbation is amplified exponentially with propagation and the continuous wave breaks up into substructures (pulses), whose characteristics are defined by the perturbation, the CW power and the fiber parameters β_2, γ . This exponential amplification is commonly referred to as modulation instability (MI). The classical example consists of a periodic and weak sinusoidal perturbation applied on top of a continuous wave field - as illustrated in figure 2.8.

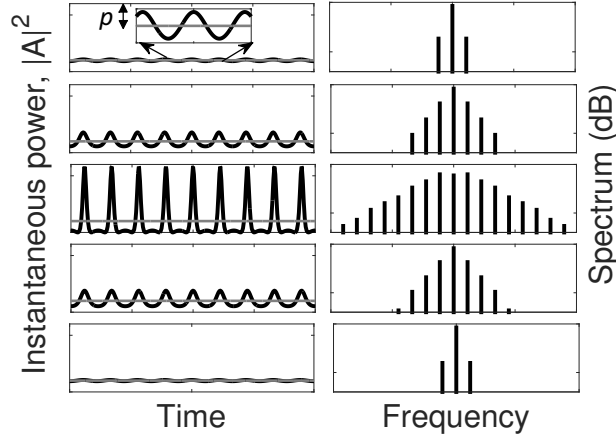


Figure 2.8: Schematic of the evolution of a continuous wave field with a weak sinusoidal perturbation, $P_0(1 + p \cdot \sin(\omega_{mod}t))$, in an NLSE system. Evolution in the temporal domain (left) and evolution in the spectral domain (right). The grey line illustrates the CW background with constant power.

It is instructive to study in detail the evolution of this sinusoidal modulation first. The initial modulation amplitude, set by $p \ll 1$ can be seen to be amplified in the temporal domain, resulting in pulse formation with nearly 100% contrast compared to the CW background. In the spectral domain (Fig. 2.8, right column, obtained by Fourier transform of the field), we see the DC component from the constant background as the strongest peak, accompanied by weak sidebands located symmetrically at ω_{mod} due to the sinusoidal modulation. With further propagation energy is transferred from the continuous wave component to the first sidebands, which in turn can further transfer the energy to new sidebands in a cascaded manner at integer multiples of the original modulation frequency. As the energy in the system is conserved, the energy flow to the sidebands reaches a

maximum, after which the energy starts flowing back to the pump and the original state will be restored (often other perturbations in experimental systems will prevent perfect restoration). This behavior is observed in many nonlinear systems, and is known as the Fermi-Pasta-Ulam recurrence, named after the physicists finding the phenomenon in studying vibrational modes in atomic lattices [51, 52].

The energy transfer is the result of the nonlinearity in the system that couples the different modes (or frequency components) together. From a fiber optics perspective, the nonlinearity arises from the third-order susceptibility and can be viewed as a degenerate FWM process [2] where two pump photons at ω_0 are simultaneously annihilated to create two photons at what are usually called the signal and idler frequencies so that energy is conserved, i.e. $\omega_0 + \omega_0 = \omega_i + \omega_s$ [1]. Such FWM process is only efficient only when a proper phase-matching condition is met.

The phase-matching condition can be derived from a perturbation analysis assuming an initial weak periodic modulation and injecting it into the NLSE [2]. Linearizing the resulting equation one finds a system of coupled equations that describe the evolution of the sidebands. The key results are: (i) exponential amplification of the perturbation can only occur in anomalous dispersion regime $\beta_2 < 0$ of the NLSE (higher order dispersion and nonlinear effects can relax this condition for the GNLSE [2]) and (ii) only the frequencies within the MI gain band defined by:

$$g(\Omega) = |\beta_2 \Omega| \sqrt{\frac{4\gamma P_0}{|\beta_2|} - \Omega^2}, \quad (2.40)$$

are phase-matched and thus amplified. Here $\Omega = \omega_0 - \omega$ is the frequency detuning from the pump and $P_0 = |A|^2$ is the instantaneous power. Figure 2.9 plots the gain curve for various input powers. MI can occur also in normal dispersion regime with two pumps that are phase matched by XPM [53, 54], but this phenomenon is not studied in this thesis. In the normal dispersion regime the system is stable to perturbations.

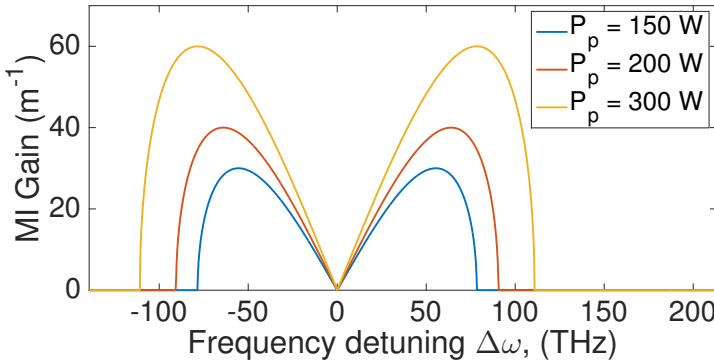


Figure 2.9: MI gain curve for NL-PM-750 fiber at 825 nm, with $\beta_2 = -9.8 \cdot 10^{-27} \text{ s}^2/\text{m}$, $\gamma = 0.1 (\text{Wm})^{-1}$ and various peak powers.

The maximum of the gain occurs for a perturbation with frequency detuning of $\Omega_M = \sqrt{2\gamma P_0/|\beta_2|}$. From an experimental viewpoint it is worth noting that the maximum of the gain can be tuned by adjusting the input pulse power or pump wavelength. The latter option will change the GVD-value and therefore affect the gain maximum. Even though the nonlinear parameter has also in principle a small frequency dependence, the change is relatively small within the tuning range of available lasers and therefore not very relevant.

Up to now we have only discussed the case where the perturbation is periodic with well defined shape. It is an obvious question to ask what happens when the perturbation is of some other form. At the extreme the perturbation can consist of entirely random fluctuations, or noise, on top of the continuous wave field. In such a case, all the frequency components of the noise falling within the MI gain curve will be amplified simultaneously by the pump. An illustration of the evolution of the noisy field in this case is shown in figure 2.10.

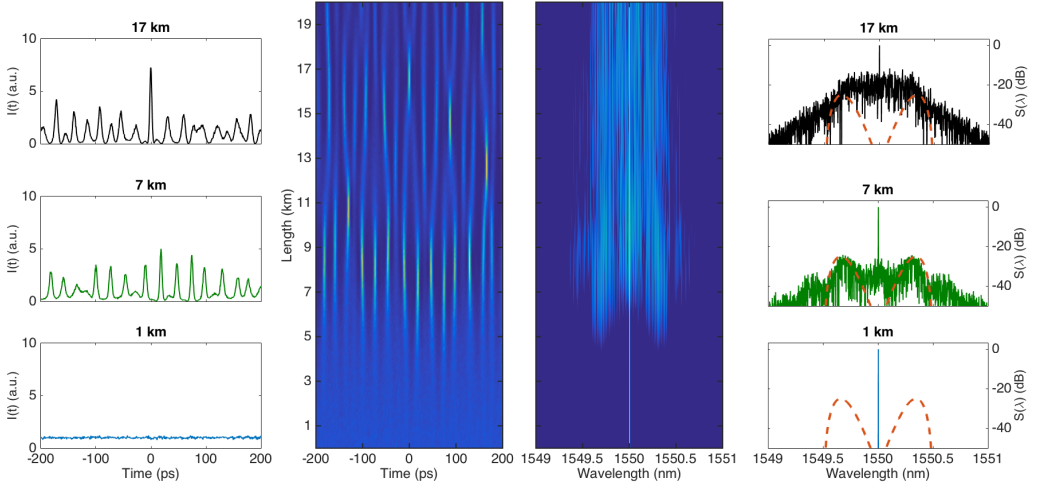


Figure 2.10: Simulated evolution of spontaneous MI originating from noise in the temporal (left) and spectral (right) domains. The fiber used for the simulation is SMF-28 fiber of 20 km length with a continuous wave field of 700 mW power at $\lambda_0 = 1550$ nm. The red curve in the spectral domain shows the theoretical MI gain curve calculated for these parameters from eq. 2.40.

This noise-seeded evolution is often referred to as *spontaneous modulation instability* in contrast to the earlier case of *seeded-modulation instability* where a well-defined periodic perturbation is injected into the fiber. In the time domain, we see how the weak initial fluctuations are dramatically amplified and lead to the emergence of a noisy pulse train at 7 km that subsequently evolves chaotically. Simultaneously in the spectral domain, we observe how the noise that is not apparent at 1 km, has been significantly amplified within the MI gain curve (shown in red) at 7 km. We also observe the cascading effect that also occurs in the seeded case with the generation of higher-order sidebands, but now the cascade occurs for the entire band leading to a quasi-continuous spectrum that evolves into a characteristic triangular shape (when plotted on logarithmic scale) [55].

2.5 Breather formalism

As mentioned before, the NLSE has analytical solutions that can be obtained by IST, where the nonlinear partial differential equation is represented in a form of a compatibility condition of two linear differential equations. This is often done in the dimensionless coordinate system, which will also help us to classify the solutions later. The dimensionless NLSE is obtained by the change of variables $\xi = z\gamma P_0$, $\tau = T/\sqrt{|\beta_2|/(\gamma P_0)}$ and $A = P_0^{1/2}\psi$ yielding,

$$i \frac{\partial \psi}{\partial \xi} + \frac{1}{2} \frac{\partial^2 \psi}{\partial \tau^2} + |\psi|^2 \psi = 0. \quad (2.41)$$

Soon after the first solutions of the bright soliton and continuous wave cases obtained by IST by Zakharov & Shabat in 1972 [48], by using slightly different compatibility condition and a dressing method known as the Darboux transformation, Akhmediev *et al.* reported on new solutions of the NLSE [15].

These solutions were derived from a continuous wave solution and describe analytically the evolution of the weak perturbation amplified by MI discussed earlier. These particular solutions are now commonly referred to as Akhmediev breather (AB) [49]. Other solutions derived by different variations of the inverse scattering method were reported even before the AB solutions: the famous Peregrine soliton [56] and the Kuznetsov-Ma soliton [57] named after their founders. All of these solutions are part of the same one-parameter family of solutions classified as solitons on finite background, as the pulse structures lie on top of a constant background. The entire family of soliton on finite background is described by

$$\psi(\xi, \tau) = e^{i\xi} \left[1 + \frac{2(1-2a)\cosh(b\xi) + ib\sinh(b\xi)}{\sqrt{2a}\cos(\omega_a\tau) - \cosh(b\xi)} \right]. \quad (2.42)$$

The evolution is governed by a single parameter a , that defines the other parameters by $b = \sqrt{8a(1-2a)}$ and $\omega_a = 2\sqrt{1-2a}$ (we have used the subscript a to differentiate from angular frequency). The solutions $0 < a < 0.5$ correspond to ABs, taking the limit $a = 0.5$ corresponds to the Peregrine soliton, and values of $a > 0.5$ correspond to the Kuznetsov-Ma solitons. In addition to these, nonlinear superpositions of two of these solutions can be obtained by the Darboux transformation, that are referred to as collisions of breathers [49]. Examples of the AB, PS and KM-soliton evolution are shown in figure 2.11.

It should be noted that for any single soliton on a finite background (AB, Peregrine soliton, Kuznetsov-Ma), the highest normalized intensity value obtainable is 9, which occurs for the Peregrine soliton. However, by using Eq. 2.42 with $a > 0.5$ for the Kuznetsov-Ma solitons, one will obtain intensities above nine. This is due to the fact, that the form of Eq. 2.42 for the Kuznetsov-Ma soliton correspond to a different normalized form of the NLSE [49]. Using the proper normalization for the Kuznetsov-Ma soliton, one can show that its intensity is always below nine, and the only possible solutions above intensity nine are necessarily the superposition or collision of two of these solitons on a finite background. This point will be important later, when discussing some of the experimental results.

While the analytical was derived already in the 1980s, it is only recently that the potential of these results for experimental studies in optics was truly appreciated [19]. Using an intensity modulator to generate sidebands at frequency ω_a allows for exciting AB structures, and indeed early 2010 saw numerous experiments and studies reporting on the observation of the different analytical solutions of SFBs in optical fibers [20, 58–60].

Finally, we draw attention to the fact that the fundamental soliton of Eq. 2.36 is another analytical solution of the NLSE of Eq. 2.39. The main difference between the $N = 1$ soliton and AB is that that the ABs lie on top of a continuous wave background (the DC

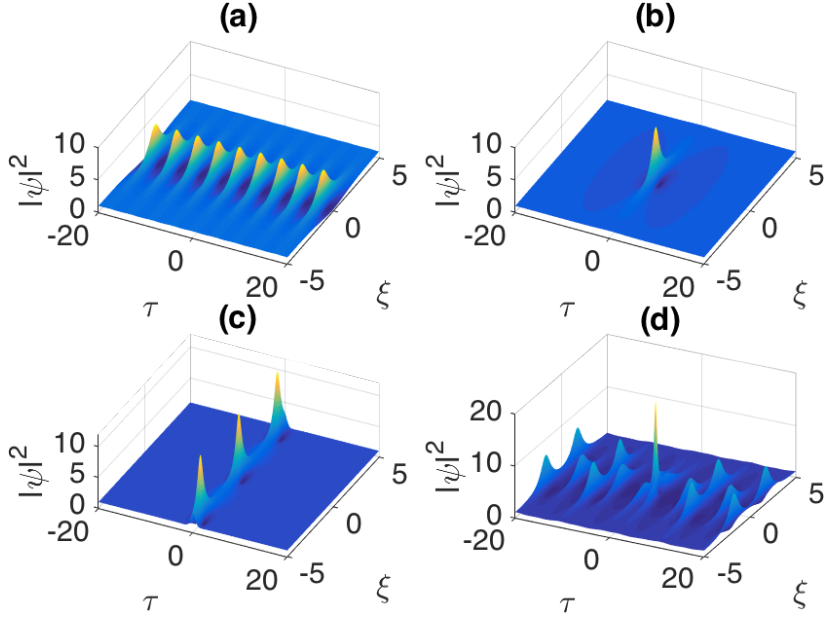


Figure 2.11: Examples of breather structures with various a -parameters. (a) AB with $a=0.25$, (b) Peregrine soliton with $a=0.5$, (c) Kuznetsov-Ma soliton with $a=0.7$ and (d) collision of two ABs with $a_1=0.25$ and $a_2=0.4$

component in the spectrum) whereas the bright soliton has no background radiation. Both of these solutions have their importance in understanding experimental results. Coarsely put, solitons on zero background (bright solitons) play an important role in experiments with pulsed laser sources while SFBs are the key to understanding continuous wave laser experiments. In practice, these two descriptions might need to be used simultaneously - this will be addressed later.

Section 3.2 will discuss in more detail the connection between these analytical/seeded structures with those emerging in spontaneous MI.

2.5.1 Rogue waves

One of the major interests for studying the NLSE and MI dynamics arises from trying to understand the formation of extremely high waves in the ocean that appear and disappear without any apparent signatures [61]. These rogue waves have been proposed as a possible candidate for some of the 100 ships sunk every year as reported by Allianz in 2013 [62]. Predictions of such events would be extremely desirable in order to save lives.

As deep ocean waves and optical fields in fibers are both governed by the NLSE, the possibility of doing simple laboratory experiments in optics for understanding rogue wave formation and transferring this knowledge to hydrodynamics has drawn significant attention [63].

The term rogue wave in optics was coined by Solli *et al.* in 2007, when they showed that the spectral intensities of the long wavelength edge of a supercontinuum generated in an optical fiber followed an “L-shape” statistical distribution, characteristic of extreme events

[64]. Several reports of rogue-like statistics in optics have subsequently been reported in laser resonators [65–67] and spatio-temporal dynamics [68, 69].

Classification of a wave as “rogue” is somewhat arbitrary, but a commonly agreed statistical definition of a rogue event in optics is defined by the pulse having an intensity twice I_{RW} as large as the intensity $I_{1/3}$ of the average intensity of the one third of the highest intensities in the data set. Mathematically this is usually expressed as the condition $I_{\text{RW}} \geq 2I_{1/3}$ and corresponds roughly to intensities larger than four standard deviations away from the mean [70].

Many of the rogue wave statistics observed in optical systems were systems whose dynamics are in fact not governed by the NLSE. Indeed, even the 2007 paper was actually studying the dynamics of supercontinuum generation in the GNLSE regime, where higher-order effects such as Raman scattering and higher-order dispersion need to be accounted for and the system is therefore not a direct analogy of the ocean case.

While studying the NLSE has its own specific motivation from a fundamental physics point of view, the noisy MI dynamics of the NLSE that triggers supercontinuum generation in the long pulse regime connect the two subjects together.

2.6 Supercontinuum generation

The GNLSE of Eq. 2.36 is a more general model applicable for pulses with durations down to the few-cycle limit (few femtoseconds). In general when the propagation distance exceeds significantly the nonlinear length $L_{\text{NL}} = 1/(\gamma P_0)$ higher-order effects kick in and the propagation dynamics become very complex. Analytical solutions cannot be used to understand the dynamics in this case and numerical simulations are needed in practice. The nonlinear dynamics can lead to extreme spectral broadening of the input spectrum along the propagation in the optical fiber, such that an input pulse with a few nanometer bandwidth can extend up to a thousand nanometers at the output of the fiber. This massive spectral broadening process is commonly referred to as supercontinuum (SC) generation [30, 71, 72].

SC generation generally involves all of the nonlinear processes discussed earlier, but often key processes can be isolated depending on the particular input pulse & fiber parameters. A coarse division of the different SC generation regimes by the pulse duration and dispersion regime of the fiber is given in table 2.1 below.

Table 2.1: Dominating effects in SC generation for different pulse durations and dispersion regimes.

	Short pulse	Long pulse
Anomalous	Soliton dynamics	Modulation instability
	Dispersive waves	Soliton dynamics
Normal	Self-phase modulation	Raman scattering
	Four-wave mixing	Four-wave mixing

The division between short and long pulses is somewhat arbitrary, but as a rule of thumb the division can be done around 500 fs duration. Pulses well below this duration can be considered short, whereas pulses exceeding few picosecond durations can be considered long. In the intermediate regime the dynamics are usually a mixture of long and short

pulse dynamics. The boundary is set by the particular fiber dispersion and nonlinearity and should be considered for each experimental setting individually.

Most of the nonlinear effects listed in table 2.1 have been introduced in section 2.2, but the concepts of solitons and dispersive waves are yet to be discussed. As they are key elements in achieving the broadest SC spectra and play an essential role in explaining some of the results of this thesis, we will next discuss these topics in more detail in the next sections.

2.6.1 Supercontinuum generation with long pulses

In the normal dispersion regime fundamental bright solitons are not supported and the input pulse will experience generation of new frequencies through stimulated Raman scattering with the generation of cascade of isolated spectral peaks separated by 13.2 THz, the Raman gain maximum. With sufficient power, SPM and XPM will also take place and can merge these peaks into a more quasi-continuous spectrum. If the initial pump is located relatively close to the ZDW, higher-order dispersion terms allow for phase-matching of FWM processes that can transfer energy to the anomalous dispersion regime [2]. Generally the spectral widths of SC generated in the normal dispersion regime are significantly smaller than in the anomalous dispersion regime or require significantly more power to reach a similar bandwidth. A simulated example of the above dynamics is shown in figure 2.12.

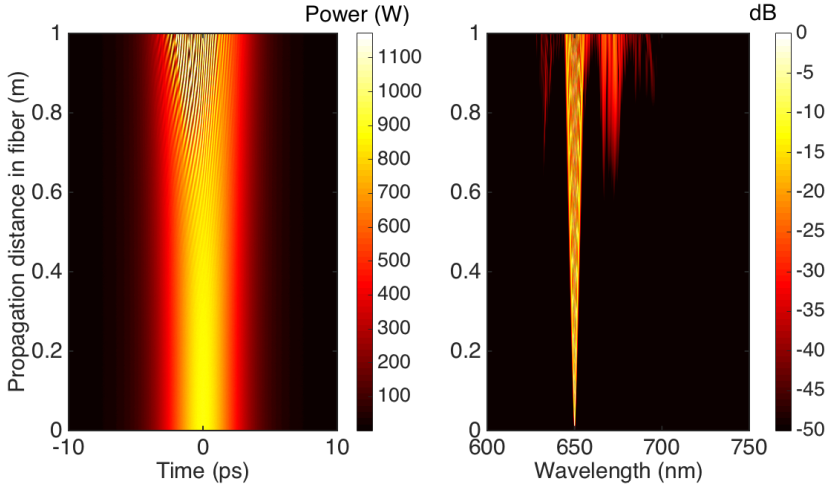


Figure 2.12: Evolution of a long pulse ($T_{\text{FWHM}} = 5$ ps, $P_p = 880$ W, $\lambda_0 = 650$ nm) in temporal and spectral domains in the normal dispersion regime of NL-PM-750 fiber ($\text{ZDW}_1 = 750$ nm, see Fig. 2.1 c). The central peak in spectrum undergoes some broadening due to SPM and at 0.7 m we see the Raman scattering peaks rising 13.2 THz away, causing modulation in the pulse temporal profile.

In the anomalous dispersion regime higher-order dispersion and SRS become less important and the initial dynamics can be understood on the basis of the NLSE analysis of section 2.4. For long pulses, the modulation period is set by the inverse of the MI gain maximum frequency $\tau_{\text{mod}} \approx 1/\Omega_M$ which is significantly shorter than the pulse duration such that, from the perspective of MI the pulse can be considered locally as a continuous wave. This can also be understood in the spectral domain, where long pulses

have narrow linewidths that do not overlap significantly with the MI gain curve. An example of simulated dynamics of a 5 ps pulse in the anomalous dispersion regime is shown in Fig. 2.13.

The initial broadening of the spectrum is associated with spontaneous MI seeded by noise, leading to noisy AB-like pulses appearing on top of the pulse envelope. The spectral broadening resulting from the cascaded FWM/MI will allow for higher-order dispersion and Raman effect to perturb these breather structures, decoupling them from the original pump pulse background. This allows them to evolve into individual fundamental sech-type solitons [73]. The fundamental solitons subsequently follow characteristics of soliton dynamics, generating dispersive waves and shifting towards longer wavelengths via RSFS. The result is a relatively flat spectrum that can extend over several hundreds of nanometers with generally a sharp peak corresponding to the residual of the pump pulse. It should be noted that variations in the spectrum from pulse to pulse are significant in this regime as the initial dynamics are seeded by spontaneous MI. This has dramatic effects on the stability and coherence of the SC as will be discussed in chapter 4.

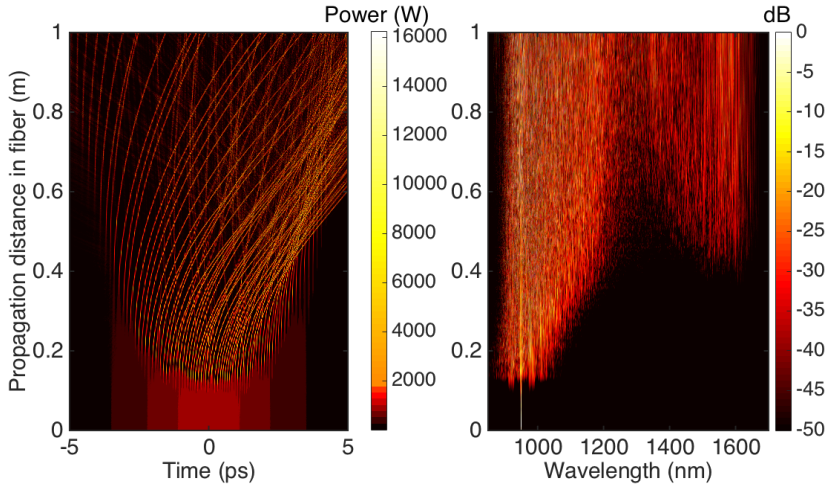


Figure 2.13: Evolution of a long pulse ($T_{\text{FWHM}} = 5$ ps, $P_p = 880$ W, $\lambda_0 = 950$ nm) in temporal and spectral domains in the anomalous dispersion regime of NL-PM-750 fiber ($\text{ZDW}_1 = 750$ nm, see Fig. 2.1 c). The dynamics start early at 0.15 m by MI sidebands growing from noise and causing AB structures to appear on the pulse envelope. At 0.25 m higher order perturbations change these AB structures into sech-solitons that start to undergo a Raman shift and at 0.5 m we observe the generation of several dispersive waves of these solitons on the other side of the 2nd ZDW of the fiber at 1260 nm.

2.6.2 Supercontinuum generation with short pulses

When pulse durations are around 100 fs and the pump lies in the **normal dispersion regime** the spectral broadening is dominated by SPM and the SC spectral width is largely determined by the pulse peak power. However, increasing the peak power does not increase the bandwidth indefinitely. The rapid spectral broadening due to SPM causes the pulse to spread out temporally due to increased dispersion and consequently the peak power drops rapidly, leading to weaker SPM and halting the spectral broadening. FWM effects can cause additional broadening near the ZDW, but spectral broadening in this regime is still moderate or weak. The benefit of this approach is however that the

generated SC has very little pulse to pulse fluctuations and is temporally coherent. These dynamics are illustrated in Fig. 2.14.

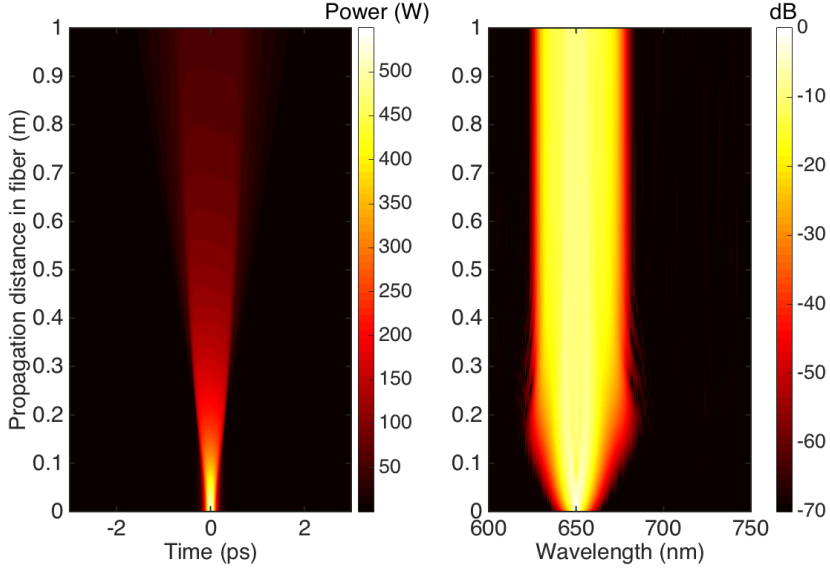


Figure 2.14: Evolution of a short pulse ($T_{\text{FWHM}} = 200$ fs, $P_p = 550$ W, $\lambda_0 = 650$ nm) in temporal and spectral domains in the normal dispersion regime of NL-PM-750 fiber ($Z_{\text{DW}_1} = 750$ nm, see Fig. 2.1 c). We observe an initial broadening of the spectrum due to SPM which is quickly halted by the increased dispersion decreasing the peak power, which can be observed clearly in the temporal profile of the pulse.

When pumping in **anomalous dispersion regime** with short pulses the following SC dynamics is a competition of soliton fission and MI. The dynamics are triggered by soliton fission of higher-order solitons followed by RSFS and dispersive wave generation. Generally, this soliton fission and subsequent soliton dynamics occur in a deterministic manner caused by higher-order dispersion and Raman effect such that the resulting SC is coherent. We show an example of simulated results for these dynamics in Fig. 2.15.

If the input pulse peak power is increased such that the input soliton order is larger than $N \approx 16$, the maximum of MI gain value increases and shifts away in frequency from the pump pulse [74]. MI will start competing with soliton fission during the initial stages of propagation in the fiber causing pulse to pulse fluctuations in the SC. Figure 2.16 demonstrates this, by showing three simulated spectra obtained by an input soliton order of $N = 23$ with parameters that are similar as the experiments for the incoherent SC presented in chapter 4.

Conclusions

In this chapter we have described the fundamental nonlinear phenomena that can occur when intense laser pulses propagate in nonlinear waveguides and fibers. Many of the phenomena discussed here will be useful when describing the experimental results presented in the following chapters. We have introduced the GNLSE and demonstrated its use in numerical modelling of pulse propagation in optical fibers for a very broad range of input conditions. We have also seen that for long pulses or continuous wave lasers the GNLSE

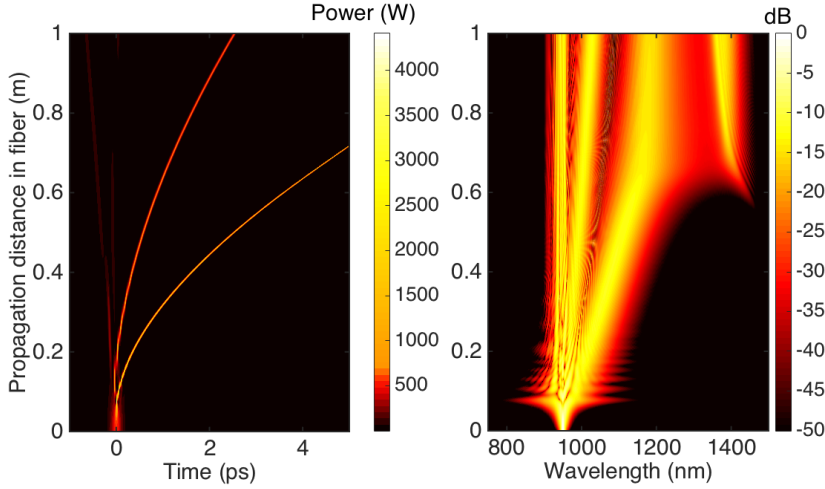


Figure 2.15: Evolution of a short pulse ($T_{\text{FWHM}} = 200$ fs, $P_p = 550$ W, $\lambda_0 = 950$ nm) in temporal and spectral domains in the anomalous dispersion regime of NL-PM-750 fiber (ZDW₁ = 750 nm, see Fig. 2.1 c). The dynamics start with a compression of the higher order soliton, after which soliton fission occurs due to Raman effect and higher order dispersion. We observe the RSFS of the solitons in both, temporal (curved trajectory) and spectral domains (continuous redshift on the long wavelength side) until the 1st ejected soliton is phase matched with the dispersive wave around the 2nd ZDW (1260 nm) and we observe a dispersive wave at around 1400 nm.

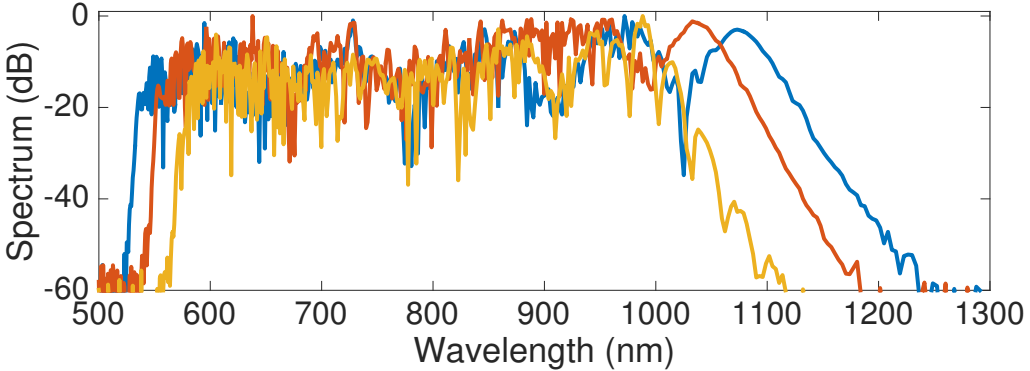


Figure 2.16: Simulated spectra of SC generated by an input pulse ($T_{\text{FWHM}} = 300$ fs, $P_p = 1200$ W, $\lambda_0 = 785$ nm) with one photon per mode noise in NL-PM-750 fiber. The high soliton order $N = 23$ means that noise-driven MI is dominating the SC generation process and the pulse-to-pulse fluctuations are large as seen here.

can be approximated by the NLSE, which allows for additional theoretical insight into several of the experiments reported in chapters 3 and 4.

As we will see in the following chapters, the nonlinear propagation dynamics described above can be significantly affected when noise is initially present on top of the input field, which in turn can cause massive fluctuations of the field at the output of the nonlinear waveguide or fiber. While such noise-seeded dynamics are straightforward to isolate in simulations, experimental detection systems are often limited to measuring the average

of these fluctuations such that simulations, theory and experimental results cannot be compared on individual realization basis. The experimental techniques developed in this thesis have been specifically designed to isolate, measure and possibly utilize the effects of these fluctuations in order to obtain a better understanding of the phenomena at hand and enable comparison with theoretical and numerical results.

3 Real time measurement of noise initiated dynamics

As we have seen at the end of the previous chapter nonlinear effects in optical fibers constitute to a rich variety of phenomena that can cause rapid fluctuations within the optical field and variations from pulse-to-pulse. These fluctuations can be practically unpredictable, caused by phenomena such as spontaneous modulation instability, that arises from quantum fluctuations, or more well-defined such as soliton fission in the absence of noise. This sensitivity to input conditions is a fundamental property of any nonlinear system. Two seemingly similar input conditions with unmeasurable variations can give rise to entirely different outputs, which is also referred to as deterministic chaos [75].

From a practical point of view this is an obvious problem, as no one wants to buy a laser that gives a randomly varying output power. Much of engineering effort is indeed spent on minimizing the unwanted nonlinear effects or finding possible stable *attractor* states of the nonlinear systems such as solitons in mode-locked lasers [76]. In order to understand and utilize the possibilities of these systems a significant amount of mathematical interest has concentrated on studies of nonlinear systems. To validate the mathematical models, experimental measurements are of course needed, or reversely, new experimental measurements can open up a pathway for theoreticians to model and understand physical systems more generally.

The standard measurements in optics are the measurement of the spectrum (or spectral envelope) or time varying power by a photodetector. An obvious problem in measuring the temporal behaviour of optical systems is the inherently rapid nature of the field occurring on timescales that render practically most electronical equipment unviable for use. Fastest photodetectors to date go down to tens picosecond response times, which are still unable to detect the small changes in the temporal shape of the shortest pulses.

Traditional spectrographs or spectrum analyzers can measure the spectra extremely accurately with a high dynamical range. However, the measurement times of these devices are usually on the order of some seconds to milliseconds (or even down to $100\mu\text{s}$ with modern line cameras). Such measurements do not allow for tracking for any rapid pulse-to-pulse changes in the field occurring at the MHz operating rates of modern lasers in a pump-probe setup for example. What's more, both of these techniques only measure the power (absolute value squared) of the light in the temporal or spectral domains respectively. The only way for complete understanding of the underlying physics can be made by single-shot measurements capable of acquiring continuous snapshots of the evolving nonlinear processes yielding the complex electric field information.

Based on the above discussion we can classify the limitations with optical measurements

into roughly three categories: (i) lack of temporal resolution down to the femtosecond scale, (ii) lack of single shot acquisition speeds up to MHz rates, and (iii) lack of information of the complex electric field phase. We will first review some of the techniques introduced to overcome one or two of these limitations.

Techniques with high temporal resolution

Streak cameras based on photoelectron emission and consecutive electrical streaking can have time resolutions down to few hundred fs. Combined with a spectrograph they can be simultaneously spectrally resolved yielding a direct spectrogram similar to XFROG detection by placing a CCD array at the output. Single shot acquisitions are therefore limited by the acquisition speed of the camera. In addition to this, the photoelectron conversion can be relatively inefficient, yielding often noisy data, with small signal to noise ratio for small pulse energies. Usually one is also left without the phase-information, even though a phase retrieval should be possible using computer algorithms.

For even higher temporal resolution, many indirect measurement methods such as FROG [23], SPIDER [24], dispersion scan [77] and their variants [78] have demonstrated with resolutions down to attosecond timescales [79] being able to resolve the direct fluctuations of the optical field. The benefit of these techniques is that they characterize the electric field completely i.e. they yield the envelope and phase allowing one to change between spectral and temporal domains at will by the Fourier transform and providing a more complete picture of the phenomenon in question. However, the common versions of any of these techniques average over multiple shots being therefore able to only resolve the possible coherent structures in the pulse train [80].

Single shot versions of the above techniques also exist [81–86] but are usually limited in the pulse complexity (time-bandwidth product) and might require temporal-to-spatial encoding of the pulse or multiple beam geometries that make experimental arrangements less trivial. Another drawback are the obtainable acquisition rates. The techniques often require cameras at the detection plane that are limited from hundreds of hertz to few kilohertz in acquisition speeds, which often means that the single shot events have to be triggered externally reducing their usability in studying the evolution of rapidly occurring dynamics.

Techniques with high acquisition rates

Late 1990s saw the development of a new single shot spectral measurement approach based on dispersive properties of optical fibers [27, 28]. The basic idea is to stretch temporally the input pulse spectral components enough by dispersion, so that different wavelength components can be measured at different time instants by a fast detector. With faster oscilloscopes, detectors and dispersion engineered fibers becoming more available this *dispersive Fourier transform* (DFT) technique evolved into maturity during 2000s [29]. The technique is also capable to acquisition rates up to hundreds of megahertz making it capable of resolving spectral dynamics truly in real time and allowing for measurements of underlying correlations in the systems [22, 87].

In addition to DFT, temporal magnification allows for similar rapid acquisition rates in the time domain [25]. The temporal resolution of the demonstrated magnification systems has been on the order of some hundreds of femtoseconds limited by distortions caused by higher order dispersion in the system. The resolution is similar to streak cameras but not capable of competing with FROG or similar techniques.

Both of these measurements yield only the spectral and temporal envelopes respectively the access to phase information has to be done by synchronized DFT and temporal magnification measurements complemented by phase-retrieval algorithms. As the combination of these techniques has the highest acquisition rate of any of the systems and it's capable of retrieving the complex electric fields of the rapidly evolving dynamics, we will discuss the theory and implementation of the techniques in more detail in the following section.

3.1 Spatio-temporal duality in optics

The concept of a temporal magnification by time lens was introduced in 1989 by Kolner & Nazarathy [26]. The idea was conceived by noticing the similarity of the equation governing the paraxial diffraction of a spatial beam profile $E(x, y, z, t)$ propagating to the z -direction and the equation governing dispersive light propagation of a laser pulse in the time-space coordinates [88]. More specifically, the first can be written as (following the notation of [25])

$$\frac{\partial E}{\partial z} = \frac{i}{2\beta} \nabla_t^2 E, \quad (3.1)$$

where $\nabla_t^2 = \partial^2/\partial x^2 + \partial^2/\partial y^2$ describes the diffraction of the transverse beam profile and $\beta = 2\pi n/\lambda$ is the propagation coefficient.

The equation for dispersive light propagation of pulses in time-space coordinates is obtained by assuming no nonlinearities ($\gamma = 0$) in the NLSE of Eq. 2.39 yielding:

$$\frac{\partial A}{\partial z} = -\frac{i\beta_2}{2} \frac{\partial^2 A}{\partial T^2}. \quad (3.2)$$

We see that purely diffractive propagation in free space is mathematically equivalent to a purely dispersive propagation of a laser pulse. This also leads to other interesting observations and analogues between the two equations.

If one considers the Kirchoff diffraction equations for a spatial beam profile in free space and in the far field (i.e. Fraunhofer diffraction) with the condition $z \gg \Delta x \beta$, where Δx is the transverse spread of the beam (also applies for Δy), one obtains the result, that the far field beam profile is the Fourier transform of the input beam profile [89]. Because of the mathematical equivalence of the two equations a similar result can be obtained for laser pulses in the time domain. Indeed, if the dispersion is strong enough, ($z \gg \Delta \tau / \beta_2$, where $\Delta \tau$ is the pulse duration) the pulse temporal envelope will evolve into its Fourier transform. This is the working principle of dispersive Fourier transform (DFT), and is illustrated in figure 3.1.

The spectrum can be then obtained by a direct measurement of the stretched temporal envelope with a fast photodetector and oscilloscope. The time to frequency mapping occurring in DFT by fiber of length z and a given GVD value is given by the simple relation

$$\omega = \omega_0 + \frac{T}{\beta_2 z}. \quad (3.3)$$

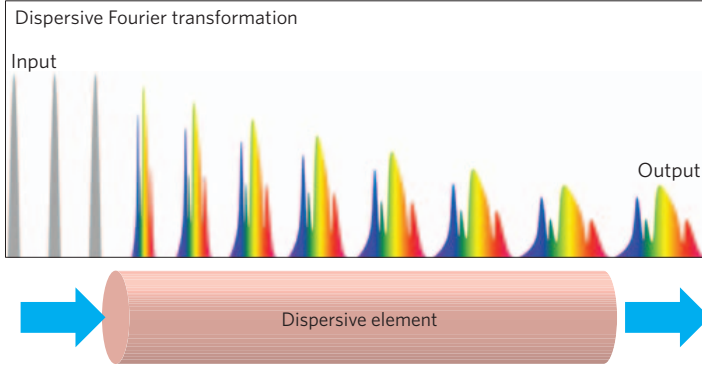


Figure 3.1: Principle of the dispersive Fourier transform (figure taken from [29]). A polychromatic laser pulse is injected into a dispersive material, such as an optical fiber, where dispersion spreads various spectral components in time. With sufficiently long propagation it can be shown that the pulse temporal envelope evolves to a replica of its spectrum.

A common method to induce the required dispersion is to use an optical fiber due to the low losses and long lengths available, but fiber Bragg gratings and free space gratings can be utilized as well [29]. One of the limitations of the DFT technique is, that often the required source needs to have a reasonable bandwidth, the dispersion needs to be high enough in order to separate different frequencies enough in time for photodetection. In practice this limits the measurements to pulsed sources, but new approaches have pushed this approach to kilohertz resolutions in optical frequency by replicating the signal in fiber loops and utilizing acousto-optic frequency shifters [90]. At the other extreme, higher order dispersion terms can cause distortions for spectrally broad pulses, though the third order dispersion effects can be corrected afterwards [91].

Time lens

Utilizing the space-time duality further, we consider the traditional geometrical optics approach of a circular thin lens, with a focal length f . When placed on the path of the beam, the lens will impose an approximately radial quadratic phase on the beam profile of the form [88]:

$$\phi(x, y) = \frac{\beta(x^2 + y^2)}{2f}. \quad (3.4)$$

The quadratic phase is just a result of the varying thickness of the lens: light rays passing through the center pass through thicker glass and have a larger phase delay compared to those passing at the edges of the lens. The electric field directly after the infinitely thin lens is obtained by a simple multiplication: $E_{lens}(r, t) = E_0(r, t) \cdot \exp(i\phi(x, y))$. In the temporal domain we can imagine analogously imposing a quadratic phase to the laser pulse of the form

$$\phi(T) = \frac{T^2}{2D_f}, \quad (3.5)$$

where D_f is the group delay dispersion (GDD) of the system, defined on the next page. Such a system would function as a time lens (TL), that (de)focuses a given laser pulse in time. In practice, such a quadratic phase in time can be imposed for example by electro-optical modulators [92], XPM/SPM [93] or FWM [94]. Especially the FWM approach in silicon waveguides has proven to be able to yield strong temporal lenses for ultrafast time scales at high repetition rates [25, 95]. The working principle of the FWM based time lens is as follows.

An ultrashort pump laser, $E_p(t)$, is propagated through a dispersive fiber D_p , where it acquires a temporal quadratic phase caused by dispersion. In the silicon waveguide this pump pulse is mixed with the signal pulse, $E_s(t)$. Due to dispersion engineering of the silicon waveguide, the pump and signal wavelengths are phase matched and a seeded degenerate FWM occurs, where two photons from the pump are converted to the signal and idler photons. In terms of electric field notation the generated idler field is of the form (neglecting the spatial dependence for simplicity) [1, 25]:

$$E_i(t) = \eta E_p(t)^2 E_s(t)^* = \eta A_{0,P}^2(t) e^{i2\phi_P(t)} A_{0,S}(t) e^{-i\phi_S(t)}. \quad (3.6)$$

Here the asterisk denotes complex conjugation and η is the conversion efficiency of the FWM process. The idler pulse can then be seen to be composed of the signal pulse with an additional quadratic phase transferred from the pump. The amplitude $A_p(t)$ is designed so, that the variations during the signal field are moderate and distortions due to this are minimized. After this mixing stage, the idler with the imparted quadratic phase is separated from the pump and signal fields by a long pass filter and injected into the output dispersive fiber D_2 to form the image.

Temporal magnification

Similar to a traditional lens used to form magnified images of small objects (magnifying glass) a time lens can form magnified images of the temporal pulses. This analogy is illustrated in figure 3.2.

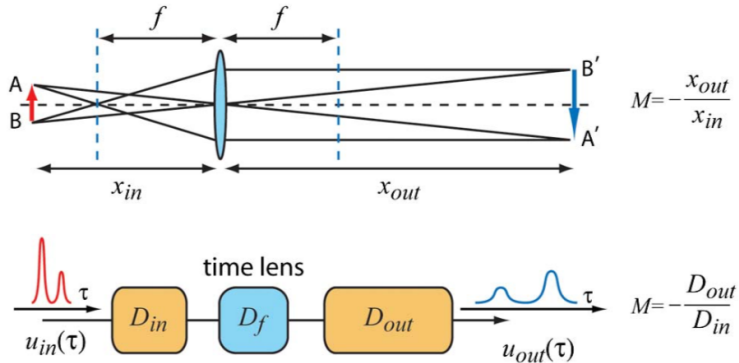


Figure 3.2: Analogue between the spatial and temporal imaging systems where a positive lens is used to magnify the object. Image taken from [25].

The properties of the time lens can be understood again with the help of the analogy. A spatial object at a distance x_{in} from the lens with focal length f will be formed at a

distance (according to the thin lens formula) $1/x_{out} = 1/f - 1/x_{in}$. This image of the object will have a magnification of $M = -x_{out}/x_{in}$.

In temporal imaging, the spatial diffractive propagation distances are replaced by the respective GDDs of the dispersive fibers, $D_i = \beta_{2,i}z_i$, where the index i refers to the respective GVD values and fiber lengths.

In order to form a temporally magnified image of a laser pulse propagating first through the fiber D_{in} followed by the lens D_f a fiber with GDD of $1/D_{out} = 1/D_f - 1/D_{in}$ has to be used. Similarly as in the spatial case, the original pulse will be magnified in time with a factor of $M = -D_{out}/D_{in}$. Magnification factors up to $M = 500$ have been reported with FWM based techniques [96]. A schematic of FWM time lens system is shown in Fig. 3.3.

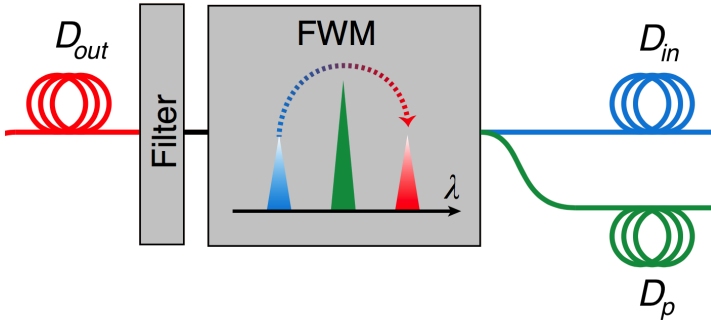


Figure 3.3: Working principle of the FWM based time lens.

In the experiments of this thesis, a commercial time lens system (PicoLuz UTM-1500) was used which is based on FWM on a silicon chip. The input, pump and output GDDs in the system were $D_{in} = 4.15$ ps/nm, $D_p = 2D_f = 8.19$ ps/nm (the factor of two is a consequence of the FWM pumping scheme [25]) and $D_{out} = 318$ ps/nm. The default magnification value of the system was $M = D_{in}/D_{out} = 76.4$, but an additional fiber patch could be inserted at the output to increase D_{out} in order to achieve magnification up to 123 times. The image quality is not degraded significantly by this additional module, because of the large magnification values that imply that the object lies near the focal point of the lens. This kind of GDD values usually require some hundreds of meters to few kilometers of optical fiber in the system. One practical issue often limiting this are the higher order dispersion terms that cause distortions with long pulses [25].

The temporal resolution of the magnification is set by the time lens aperture (i.e. the duration over which the quadratic phase can be applied), which is again analogous to the spatial counterpart. In FWM based systems the aperture is set by the pump pulse duration/bandwidth - the signal pulse bandwidth needs to fit within the time lens bandwidth in order to be imaged without distortions [95]. In our system the pump pulse has roughly 11 nm bandwidth and 300 fs input duration which is also the temporal resolution of the system. The measurement window duration (i.e. the duration of the stretched pump pulse over which the FWM can occur) is about 66 ps.

These are the working principles and key characteristics of the time lens system and DFT system used in the experiments of this thesis. We now proceed on to utilizing both of

these systems in experimental measurements of the spontaneous MI pulses and fiber laser modelocking dynamics.

3.2 Temporal breather structures in spontaneous modulation instability

Section 2.4 discussed the modulational instability of continuous wave and pulsed lasers with more than few picosecond durations. Examples of seeded MI were shown (Fig. 2.8) as well as spontaneous MI originating from noise (Fig. 2.10). The seeded cases were shown to be associated with the analytical solutions called Akhmediev breathers (Eq. 2.42), that are defined by the a -parameter, which is connected to the experimental frequency of the applied intensity modulation.

A paper in 2015 by Toenger *et al.* proposed the possibility of also interpreting the spontaneous MI dynamics with the help of ABs [21]. The numerical simulations of the NLSE (with a continuous wave input and weak random noise) in the paper showed that the structures in the (ξ, τ) -plane of the evolution show structures that are well approximated by the different AB solutions with varying a values.

While spontaneous MI has been known as an effect for quite a long time [8], the ultrafast nature of the chaotic pulses has prevented direct measurements of these in experiments. Most of the original experiments have either measured the average spectrum [8] or the time averaged autocorrelation [97] that are inherently unsuitable for measuring these randomly fluctuating pulses. More modern approaches have studied the single shot spectral dynamics with the DFT technique [22, 98].

While the spectral characteristics have their own interesting aspects, that will be discussed in more depth in the following section, they cannot directly yield the information of the pulse temporal shapes in order to compare with the analytical AB theory. A recent paper has also used a temporal magnification system in order to study the dynamics of highly noisy field evolution in an NLSE system [99], which belong to a different class of *integrable turbulence* [100] and are not directly comparable with the weak perturbation initiated MI dynamics. Paper I of the thesis addresses the experimental verification of the numerical simulations of weak noise initiated dynamics by using a temporal magnification system, and this will be also the scope of this chapter.

3.2.1 Experimental setup and characteristics of the system

To generate spontaneous MI from weak noise in the NLSE regime [100] we used a CW laser (Agilent 8194A) operated at $\lambda_0 = 1550$ nm that was phase-modulated with a pseudo-random bit sequence at 5 GS/s rate before amplification in an erbium-doped fiber amplifier (Keopsys C40-PB) to power level of $P_{\text{ave}} = |A|^2 = 700$ mW. The purpose of the phase modulation is to reduce SBS, that occurs with CW lasers and high powers [101, 102]. The single mode fiber used in experiments is 20 km in length and has low losses ($\alpha \approx 0.18$ dB/km) and a nonlinearity $\gamma = 0.0013$ (Wm) $^{-1}$. The dispersion curve is similar as in Fig. 2.1 (b) with a ZDW at 1300 nm. The low losses, anomalous dispersion at λ_0 and weak noise CW operation ensure pure NLSE driven MI dynamics in the experiments.

To illustrate the behavior of the system we begin by showing simulated results that match our experimental conditions for a CW laser with noise injected into a single mode fiber. Similar as before we plot the temporal and spectral 3.4 evolutions of the input field. Note,

that in order to compare with the AB theory, we use the normalized power and time units as defined in section 2.4. In addition to this we show the average spectral evolution over numerous simulations and the experimentally measured spectra, showing a good agreement.

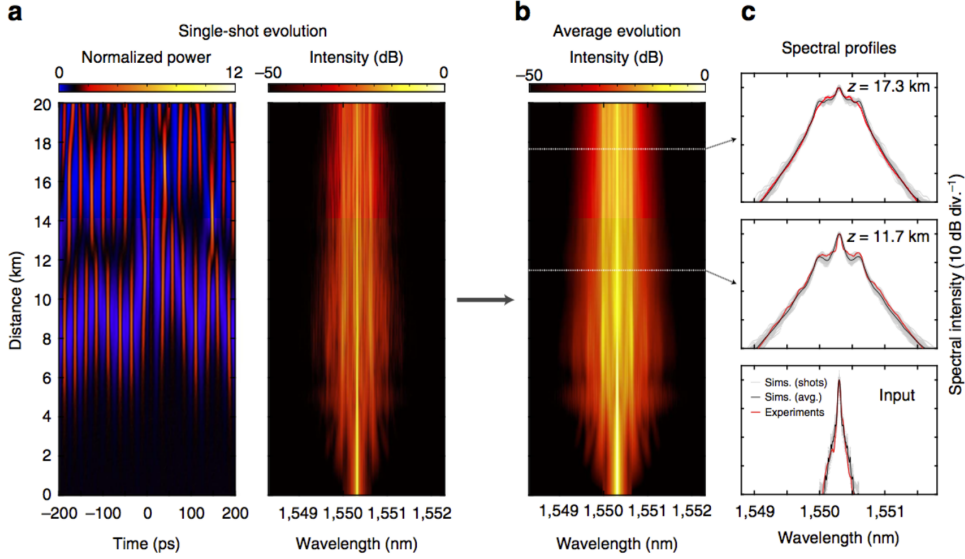


Figure 3.4: (a) Simulated evolution of spontaneous MI originating from noise in the temporal (left) and spectral (right) domains. (b) Evolution of the average spectrum over 5000 simulations and (c) selected average spectra at different distances compared with experimental average spectra.

We observe the amplification of noise in the spectral domain under the calculated MI gain curve, which spreads increasingly in spectrum by cascaded FWM. With further propagation the band structure disappears and a characteristic triangular shape of the logarithmic spectrum is obtained [55]. Simultaneously in the temporal domain, a pulse train with a period corresponding to the inverse of the gain maximum frequency $\tau = 1/\Omega_m \approx 25$ ps appears. The pulses have varying amplitudes and durations due to the noisy initial conditions. We see that the durations of the noisy pulses are on the order of 2-10 picoseconds, which is too short for direct measurement with a fast photodiode and an oscilloscope that have response times in the order of tens of picoseconds.

In order to overcome this problem, the UTM-1500 time lens system (specified in previous section) was used to magnify these breather structures by 76.4 times in order to make them measurable with a 38 GHz photodiode (NewFocus 1474-A) combined with 30 GHz real-time oscilloscope (LeCroy 845 Zi-A). Anritsu MS9710B optical spectrum analyzer was used to measure the average spectrum in parallel to the time lens system. Note that the pump laser of the time lens system is pulsed (100 MHz repetition rate), whereas the breather structures occur continuously. This means that we are able to take “snapshots” of the ABs at 10 ns intervals for 66 ps time windows that are set by the duration of the temporally broadened pump pulse. This allows to capture about 2-4 breathers within one measurement window. We collected 30,000 of these randomly varying breathers for statistical analysis. The full setup is shown in figure 3.5.

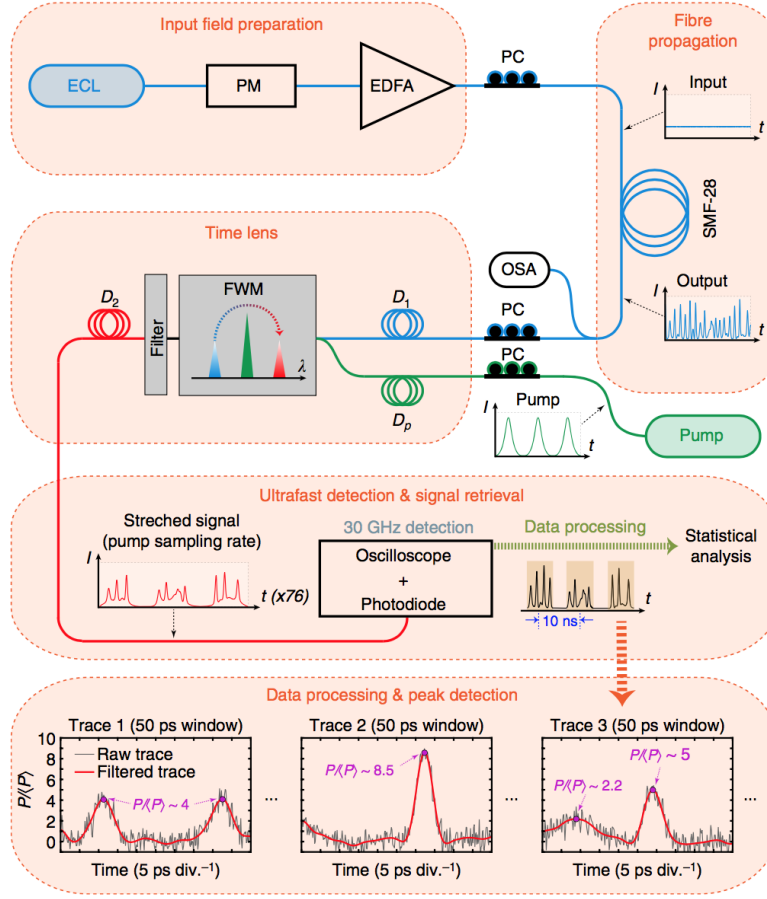


Figure 3.5: Experimental setup to generate and measure AB structures generated by spontaneous MI. The data processing inset demonstrates the effect of a 8 GHz bandwidth low-pass filter applied (red curves) on the measured data (black curve, see discussion below).

Data processing

Because of the pump pulse temporal shape, the time lens system causes small amplitude distortions within the time window relative to the pump pulse (see Eq. 3.6 and Fig. 3.6). These can be corrected with post processing the data. The amplitude distortion was measured by injecting CW laser with an equivalent power without any breather structures (i.e. no propagation in the 20 km SMF-28 fiber) into the time lens and measuring a corresponding background level $\langle P_0 \rangle$. By dividing the measured breather structures with the background a normalized peak power was obtained, that can be compared with AB theory.

In addition to correcting the amplitudes of the breathers we performed low-pass filtering of the sampling noise of the oscilloscope in order to determine the amplitudes and temporal durations of the breather pulses more reliably. The sampling noise occurs at the sampling rate of 12.5 ps extending to 40 GHz in the RF spectrum. We inspected manually several of the shortest breather structures observed in the data (that would correspond to broadest spectra) and found all to fall within an 8 GHz bandwidth. Thus an 8 GHz super-Gaussian

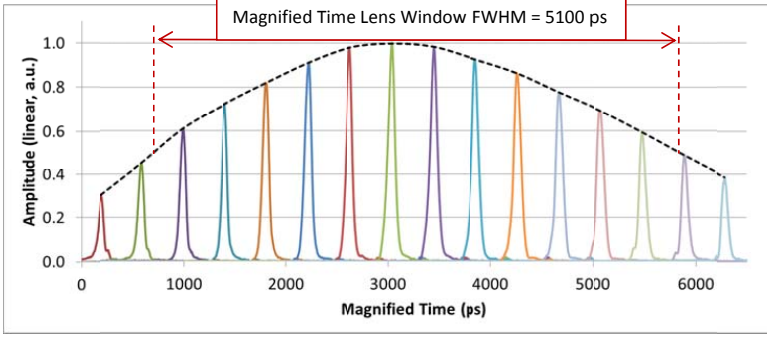


Figure 3.6: Manufacturer reported amplitude distortion of a test pulse that is delayed with respect to the pump pulse. The dashed line corresponds roughly to the pump pulse envelope square, $A_p(t)^2$ due to the FWM pumping scheme.

low-pass filter was chosen and applied on the data. Example of the filtering is shown in the bottom panel of figure 3.5.

3.2.2 Temporal breathers

In total we collected about 30,000 breather pulses in experiments for various fiber lengths varying from 7 km to 20 km. The key elements of the dynamics are illustrated with experimental data measured at propagation lengths of 11.7 km and 17.3 km that are compared with 50,000 peaks from simulations shown in Fig. 3.7 (a) and (b). The simulations used a noise level at -50 dB in the spectral domain, with random phase corresponding to our experimental conditions. Phase modulation was also included in the simulations for completeness, even though results were qualitatively the same with or without the phase modulation at propagation distances longer than the initial MI spectral broadening (≈ 7 km in Fig 3.4). In addition we collected the normalized peak powers of the temporal profiles at a given distance and plot these on a histogram in Fig. 3.7 (c) and (d) for 11.7 km and 17.3 km respectively.

We have also estimated the threshold for a rogue wave for the 17.3 km case according to the criterion of intensities above the average of the highest third of the waves i.e. $I_{RW} \geq 2I_{1/3}$. This is plotted as the vertical line in the histograms. At this distance the dynamics have evolved to their fully turbulent state, where the average spectrum has reached its triangular shape in the logarithmic scale and does not vary significantly upon propagation. The RW criterion in experiments is set at $I_{RW} = 9.2$ and roughly 0.3% of the events are above this threshold, which is in good agreement with our simulations and predicted values of 0.26% [103].

Note, that the original paper of Toenger *et al.* studying the dynamics numerically extracted the peak values from simulations in the whole two-dimensional (ξ, τ) -plane guaranteeing, that all of the breathers were measured at the peak of their evolution. Here, the collected values are not necessarily at their evolution maxima, which affects the statistics slightly and brings the rogue wave criterion to slightly lower values.

What's even more interesting, is that the rogue waves occur at intensities over 9, that is highest obtainable value for a single breather obtained by the Peregrine solution of Eq. 2.39 by setting $a = 0.5$. However, collisions of these breather structures can have

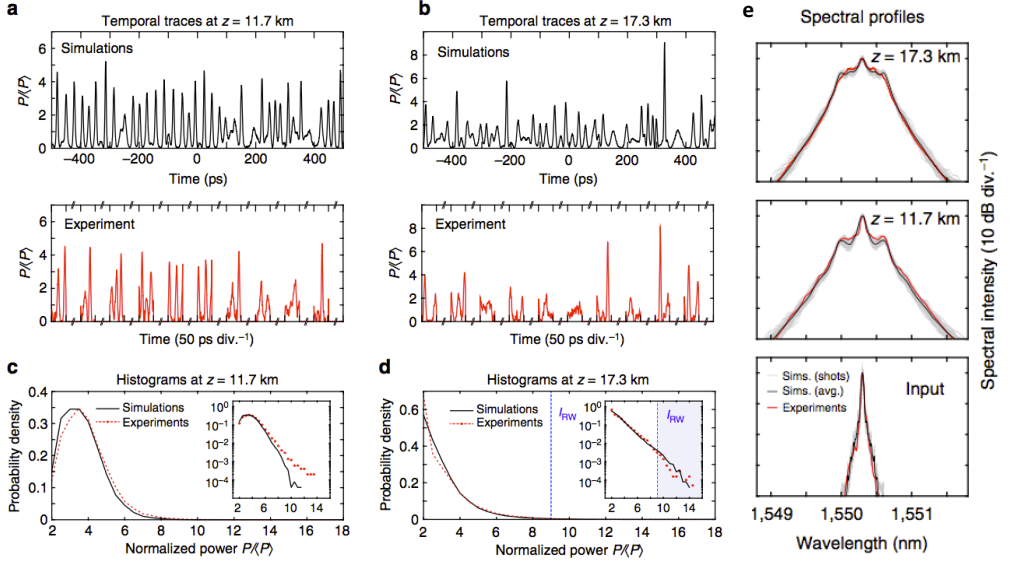


Figure 3.7: Experimental and simulated results for spontaneous MI in the fiber at (a) 11.7 km and (b) 17.3 km. Experimental results are cut in 50 ps windows due to the time lens pumping scheme sampling the breathers only at every 10 ns. Histograms of the normalized peak intensities are shown in (c) and (d) with the insets plotted in semilogarithmic scale. Average spectra measured by the OSA also compared with simulations are shown in (e) for various distances.

intensities exceeding 9 [49] and are responsible for practically all the rogue events observed in our experiments confirming earlier predictions [21, 61, 100].

To further verify the hypothesis, that ABs present a natural attractor state of the system, we extract the temporal durations corresponding to each measured peak intensity from both experiments and simulations and plot them on a scatter plot in figure 3.8.

We observe how the experimental and simulated results are closely packed around the analytical AB curve. The scatter arises from two factors: firstly it is difficult to extract reliably all the peak values from the noisy data algorithmically leading to some false peak value detection. The second and more significant factor is, that while the structures resemble closely the analytical AB structures, they still originate from noise with several other AB structures and linear waves affecting the overall shape of the waveform. This effect can be observed in figure 3.9 (b), where we compare the analytical solution of the Peregrine soliton with 10 pulses with similar intensities extracted from simulations. The remarkable resemblance to the analytical PS solution is a further manifestation of these structures being a natural basis on which to interpret the results. Furthermore in 3.9 (c) we fit a collision of two ABs to an extracted pulse with an intensity well above the Peregrine limit of nine.

All in all the obtained experimental results agree well with the predictions made by simulations showing that the ABs provide a kind of a basis on how to interpret the spontaneous MI results. This could provide insight into understanding noise driven mechanisms in nonlinear fiber optics and possibly oceanography, and coupled with the mathematical tools of IST could provide a pathway to predicting rogue waves and utilizing the complex dynamics in applications.

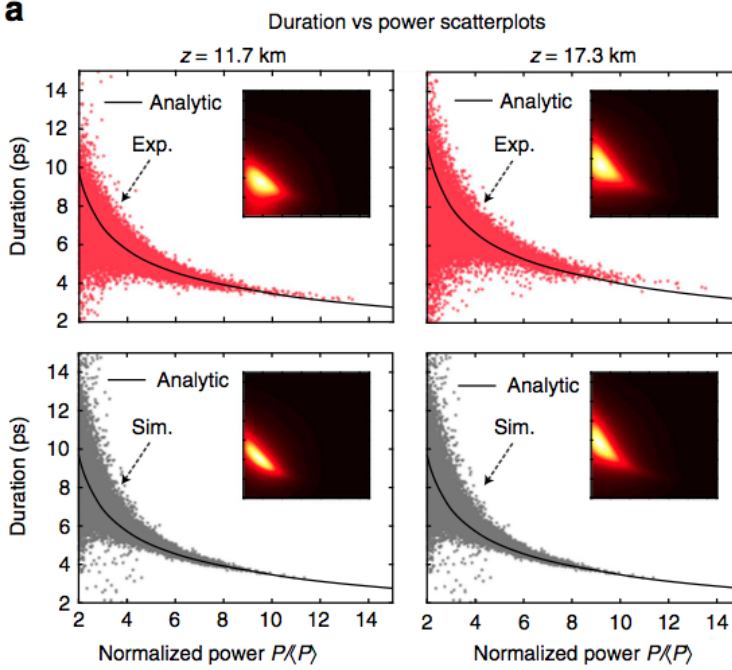


Figure 3.8: Scatter plots showing the extracted breather durations vs. normalized peak power for simulations (bottom) and experimental results (top) for the two propagation distances. In addition we have plotted the duration vs. peak power of the analytical AB structures and their collisions as the black curve. As the data points are densely packed, the false color plots in the insets show also a density map of the data points.

3.3 Spectral measurements of spontaneous modulation instability

The previous section demonstrated the direct characterization AB structures arising from noise in the time domain. Here, we approach the problem from a different angle and perform real-time measurements of noisy AB structures in the spectral domain. The complex spectrum and the electric field in the time domain are the two sides of the same coin. Knowledge of the signal in either domain provides all the necessary information and one can switch between the two domains using Fourier transform.

From an experimental viewpoint, this is not straightforward. Indeed, photodetectors measure the intensity and not the actual complex field. In other words, one measures the photocurrent $i(t)$ generated in optoelectronic circuits which is proportional to the time averaged intensity (power over surface area) of the incoming light, i.e. $i(t) \propto \langle |E(t)|^2 \rangle_T$ such that any information of the phase is lost. This holds true for both spectral and temporal domain measurements.

Even though it is extremely challenging to measure the complex field on a shot-to-shot basis, the sole intensity information still has remarkable use as shown in the previous section where measurements of the temporal intensities still enables to make important conclusions on breather dynamics. In general, single-shot spectra are more straightforward

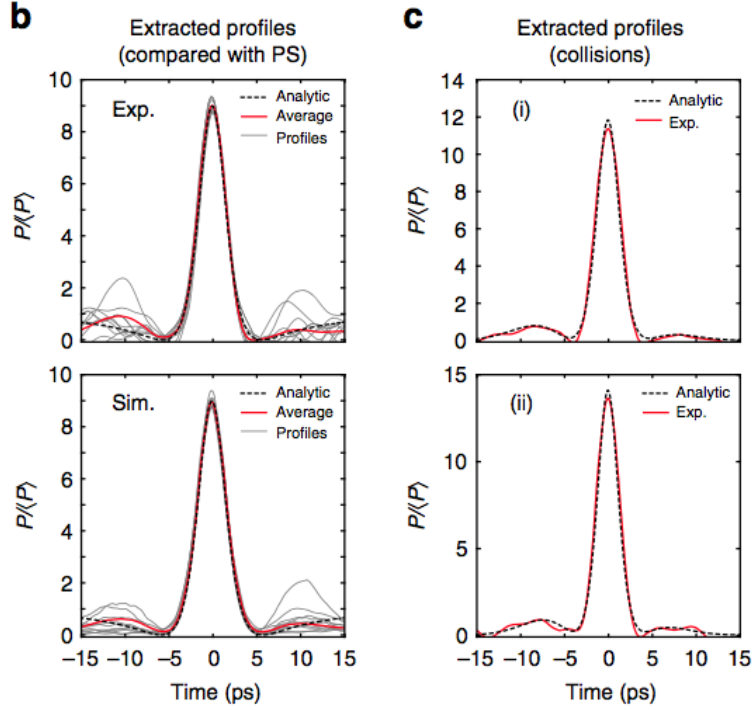


Figure 3.9: Scatter plots showing the extracted breather durations vs. normalized peak power for simulations (bottom) and experimental results (top) for the two propagation distances. In addition we have plotted the duration vs. peak power of the analytical AB structures and their collisions as the black curve. As the data points are densely packed, the false color plots in the insets show also a density map of the data points.

to measure and we may not have the access temporal data due to experimental limitations (e.g. no time lens available for the given wavelength or temporal resolution is limited).

Earlier studies have utilized the DFT technique to study the correlations in spontaneously generated MI spectra, demonstrating the capability of single shot measurements to reveal previously unobserved details in the dynamics and allows for statistical correlation analysis [22, 98]. These earlier studies were typically limited to a 20 dB dynamic range, set by the 8-bit digitization of oscilloscopes making it unable to capture the subtle features occurring at low intensities in the case of pure NLSE dynamics. Similar spectral correlation measurements have also been used to suggest the use of MI as a source of entangled photons in ultrafast quantum optics [104].

We next address the possibility of detecting rogue waves and AB collisions in the spectral domain. This is possible because the events with largest amplitude in the time-domain (or rogue waves) manifest themselves in the spectrum with a larger bandwidth below the -40 dB level. The results were obtained by introducing a new technique based on a mechanical streak camera, capable of 60 dB dynamic range single shot spectral measurements at a 150 kHz acquisition rate. The dynamic range is four orders of magnitude better than the standard DFT technique

As mentioned in section 2.4, aside from fundamental physics aspect, significant attention

has been drawn to MI due to the connection between oceanography, optics and rogue waves. One particularly interesting aspect is the possible prediction of these high intensity events from spectral measurements [39, 105].

The experimental setup is illustrated in Fig. 3.10. The experiments were performed using a Ti:Sapphire laser producing 2.9 ps pulse duration (FWHM, measured by an autocorrelator and assuming a transform limited sech^2 profile) operating at 80 MHz. An acousto-optic modulator placed after the laser output allowed to control the repetition rate between 10 kHz and 4 MHz, so that the output spectra are measurable with our mechanical streak camera. The pulses were then injected into 69 cm of PCF fiber in the anomalous dispersion regime at $\lambda_0 = 825$ nm. The peak power of the pulses was set to 200 W and GNLSE simulations were performed to verify that the dynamics with these parameters were nearly in the quasi-NLSE regime. Figure

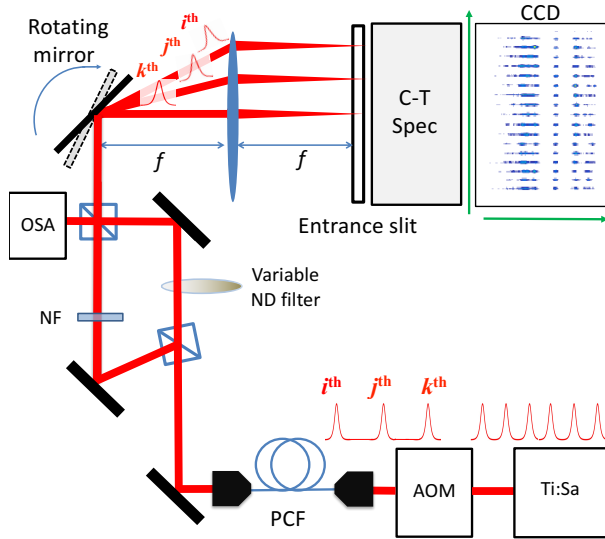


Figure 3.10: Experimental setup for the single shot spectrometer based on a mechanical streak camera principle. The lower part of the setup shows the imbalanced interferometer used to increase the effective dynamic range.

The MI broadened spectra were directed to a rotating mirror mounted on a galvanometer, deflecting consecutive pulses at different angles. The galvanometer was driven by a square wave with 120 Hz frequency and 30% duty cycle resulting in an angular speed of the mirror $\omega_{mir} \approx 26$ rad/s, equivalent to 240 rev/min. A positive lens was placed at one focal length distance ($f = 150$ mm) away from the deflection point. In this way the consecutive pulses propagate as parallel beams, and are focused at different heights of the input slit of a self-built Czerny-Turner spectrograph.

The spectrograph consisted of a 300 lines/mm grating with a 500 nm blaze. After the grating, a 50 mm achromatic doublet lens was used to focus the spectra onto an EMCCD camera (Andor Ixon 3) with 512x512 pixels of $(13 \mu\text{m})^2$ size. Consecutive pulses were recorded at every second row of the camera to avoid possible spatial overlap and a single image consisted of about 150 pulses. In total we collected about 3000 experimental spectra for statistical analysis.

The dynamic range of the single-shot spectral measurements is defined as the ratio of the smallest signal to the highest signal measurable at the same time. In our case this corresponds to the ratio of the noise level e_{noise}^- to the electron well-depth e_{max}^- of the camera, i.e. $10 \cdot \log_{10}(e_{noise}^-/e_{max}^-)$. As the image is digitized, the digitization levels should be designed to match the full well capacity. Typical digitizers vary usually between 12 and 16 bits. In the experiments reported here the camera had a full well depth of 180,000 electrons and 14-bit digitization depth, that limited the dynamic range to 42 dB assuming a single electron noise level. The camera was also thermo-electrically cooled to -80 °C and had a 5x pre-amplifier gain that reduced the noise values close to zero.

As this is very close to the -40 dB level needed to detect the spectral broadening occurring as a result of AB collisions, we further increased the dynamic range by an additional approach. The principle is based on measuring separately the strong central part of the spectral and the weak spectral wings with the 40 dB dynamic range and then combining them together. This is done using the setup in Fig. 3.10. The input spectra $S_i(\lambda)$ was split in two parts by a 50/50 beamsplitter. The first half was passed through an optical density 4 notch filter that attenuated the wavelength band at the center of $825 \text{ nm} \pm 20 \text{ nm}$ by 40 dB resulting in a spectrum of the form $\alpha_{NF}(\lambda) \cdot S_i(\lambda)$, where $\alpha_{NF}(\lambda)$ is the transmission of the wavelength dependent notch filter. The second part of the spectrum was passed through a variable neutral density filter attenuating the spectrum equally at all wavelengths resulting in a spectrum of the form $\alpha_{ND}S_i(\lambda)$. In addition to this the notch filter, the optical path length was extended by 6 cm in order to avoid any spectral interference effects between the central part of the spectra and the wings.

The two attenuated beams were then combined and the light was guided to the mechanical streak camera, which measured the spectrum $S_M(\lambda) = [\alpha_{ND} + \alpha_{NF}(\lambda)]S_i(\lambda) = f(\lambda)S_i(\lambda)$. Thus by adjusting the attenuation of the neutral density filter one can variably attenuate the central part of the spectrum and measure the full spectral data at a single line of the camera. This data can be used to obtain the unaltered original spectrum by a simple division by the combined attenuation function $f(\lambda)$. The attenuation function can be determined experimentally by measuring the average spectrum with and without the filter combination.

We verified the validity of this approach by measuring reference spectra by a separate OSA and the DFT measurement as show in Fig. 3.11 showing an excellent agreement. The discrepancies in the wings of the spectra between the OSA and our technique are attributed to the combined effect of the grating efficiency & camera quantum efficiency that both peak around 500 nm and drop towards the longer wavelengths.

Resolution and acquisition speed of the system

As for any spectrograph, the resolution is a trade-off with the maximum obtainable bandwidth. Our spectrograph had an output focal length of 50 mm that resulted in approximately 80 nm/mm linear dispersion at the focal plane and a 1 nm bandwidth per pixel. This allows to measure the full 300 nm bandwidth of the spontaneous MI with the 512 pixel grid.

The acquisition speed of the camera is set by the focal length of the input focal length lens, the camera vertical pixel spacing and the rotation speed of the mirror. This can be understood using a simple ABCD-matrix approach [106]. Writing the propagation from the rotating mirror to the thin lens and to the input slit of the spectrograph we obtain:

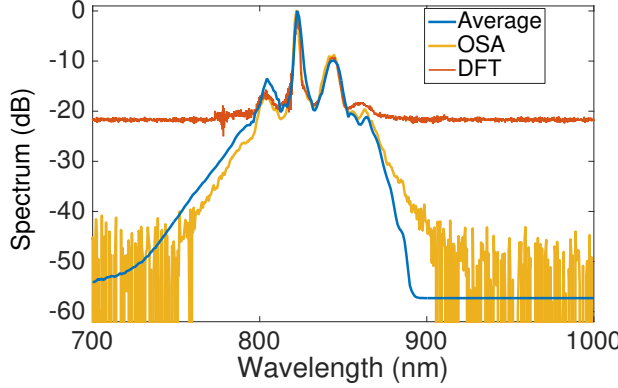


Figure 3.11: Comparison of the average spectra of the 3000 realizations of the mechanical streak camera (blue), reference measurement by OSA (yellow) and average of 1000 DFT pulses (red).

$$\begin{pmatrix} 1 & f \\ 0 & 1 \end{pmatrix} \begin{pmatrix} 1 & 0 \\ -\frac{1}{f} & 1 \end{pmatrix} \begin{pmatrix} 1 & f \\ 0 & 1 \end{pmatrix} = \begin{pmatrix} 0 & f \\ -\frac{1}{f} & 0 \end{pmatrix} \quad (3.7)$$

Multiplying the input vector $(y_{in}, \theta_{in})^T$ with the input beam height $y_{in} = 0$ (on the optical axis) and input beam angle θ_{in} we obtain the output beam height y_{out} as:

$$\begin{pmatrix} 0 & f \\ -\frac{1}{f} & 0 \end{pmatrix} \begin{pmatrix} y_{in} \\ \theta_{in} \end{pmatrix} = \begin{pmatrix} y_{out} \\ \theta_{out} \end{pmatrix} = \begin{pmatrix} f\theta_{in} \\ -\frac{1}{f}y_{in} \end{pmatrix} \quad (3.8)$$

The vertical separation between two consecutive pulses is $\Delta y = y_{out,1} - y_{out,2} = f\theta_1 - f\theta_2 = f\omega_{mir}\tau_{rep}$, where τ_{rep} is the repetition rate of the pulses and ω_{mir} is the mirror angular speed. This tells us, that one can scale up the acquisition speed straightforwardly by using a faster mirror and/or by increasing the input focal length distance.

In our experiments we have chosen the vertical spacing to be at least two times the pixel spacing to avoid any crosstalk with the pixel rows, i.e. $\Delta y = 2 \cdot 13\mu m = 26\mu m$. The focal length at the input was 150 mm and maximum repetition rate to keep the two pixel row spacing was found to be 152 kHz.

Thus increasing the acquisition speed to the few MHz level should be relatively straightforward by increasing the focal length or using faster rotating mirrors. Another alternative is to use multiple beam pass geometries as in reference [107].

3.3.1 Results

Figure 3.12 shows 3096 single shot spectra measured with the described in the previous section. The average is also shown where one can clearly observe the MI sidelobes. The false color plot shows a selection of 60 single-shot spectra measured on different rows of the camera.

We observe that the dynamics are not purely in the NLSE regime with higher order dispersion causing on average the generation of a dispersive wave seen in the spectrum

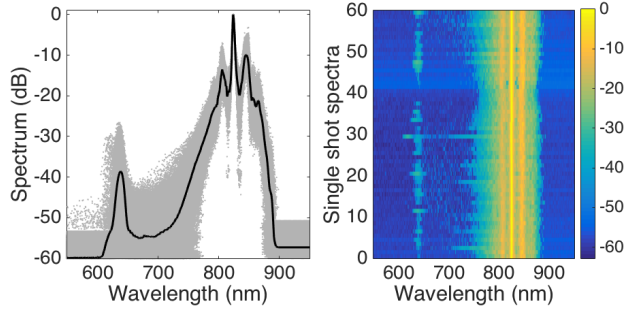


Figure 3.12: Left: 3096 single shot spectra (gray) with the average (black). Right: 60 spectra on different rows illustrating a spectral broadening most likely due to a breather collision on row 29.

at 630 nm. This can also be observed on the false color plot from the quasi continuous straight line around this wavelength on line 29. However we have verified using numerical simulations that the generation of DW does not fundamentally change the breather dynamics.

To confirm that breather collisions in spontaneous MI (with normalized $P_p > 9$) leads to broader spectra we ran 6000 numerical simulations using the GNLSE corresponding to experimental parameters. Two typical examples of simulation results in the spectral and temporal domains that correspond to (i) a collision with $P_p > 9$ and (ii) a non-collision case with $P_p < 9$ are illustrated in Fig. 3.13. We show for comparison two experimental spectra (bottom row), that display similar features to a collision and a non-collision case.

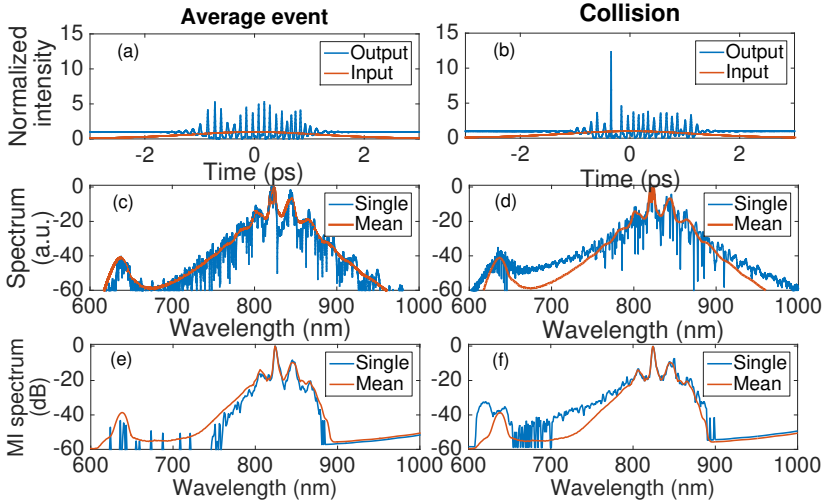


Figure 3.13: Left: Average event from simulations in the time domain (a) and spectral domain (c) compared with an experimental result (e). Right: Collision event from simulations in time domain (b) and spectral domain (d) and a similar broadening observed in experiments (f).

It is clear from inspection of the temporal and spectral plots that a collision exhibits a spectrum with larger bandwidth but also that this increase in bandwidths can only be seen below the -40 dB level.

All the 6000 numerical simulations were processed to compare the maximum normalized peak power observed in a single simulation (normalized to the input pulse profile [108]) peak and the corresponding -20 dB and -45 dB spectral widths. The results are shown in Fig. 3.14.

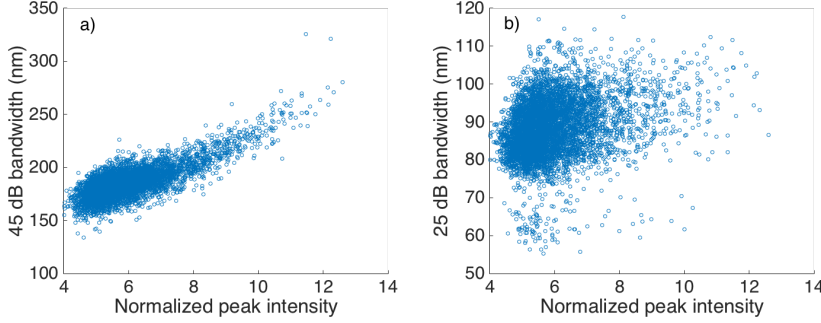


Figure 3.14: (a) 45 dB bandwidth vs. highest normalized peak in single realization in simulations showing a clear correlation. (b) 20 dB bandwidth vs. highest normalized peak in single realization in simulations with little to no correlation in the data.

It is clear upon inspection of Fig. 3.14 that there is no particular correlation between the -20 dB spectral width and an AB collision. On the other hand, when considering the -45 dB bandwidth one can observe partial correlation with a collision. The results can be understood from the fact, that while generally the highest intensity peak causes broadening at the spectral wings and therefore dominates the spectral features in the wings, the whole temporal structure does contribute to the spectrum and this is the cause for the scatter in the plots. We further checked that one can improve the correlation by measuring the bandwidth at an even lower level e.g. 60 dB. However, the generation of the dispersive waves in the experimentally accessible GNLSE regime causes anomalies in the spectral width arising from generation of dispersive wave such that the -60 dB bandwidth in this case not a mere reflection of an AB collision.

For this reason we then proceed with the possibility of reliably detecting collisions from the 45 dB bandwidth, which can be measured accurately in our experiments. Table 3.1 compares the percentage of collisions (with normalized intensity above nine) found in our 6000 simulations with the percentage that have 20% increase in the 45 dB bandwidth (compared to the mean) in simulations and in experiments. We see that the 20% increase in bandwidth results in a roughly similar percentage of estimated collisions as actual collisions in the simulations and also observed in the experiments. Of course in our experiments we do not measure the temporal profile in real time and cannot confirm that the percentage extracted from the number of spectra with a 20% increase in the -45 dB bandwidth are actually correct.

Due to the complex nature of the spectrum (causing also the scatter in fig. 3.14 a), this somewhat arbitrary 20% broadening condition chosen above will result in some false positives and false negatives in determining collisions above nine. These are tabulated in the confusion matrix of table 3.2.

Ignoring the correctly predicted low intensity cases, we get roughly a 60% likelihood of identifying a collision correctly out of rest of the cases which is only slightly better than a random prediction.

	Collisions	20% broadened
Sims	2.8%	2.7%
Expts	-	2.2%

Table 3.1: Percentage of collisions with normalized $P_p > 9$ and 20% broadened bandwidths at the 45 dB level. Collisions cannot be detected in the time domain in experiments and are therefore not reported.

	Predicted $P_p > 9$	Predicted $P_p < 9$
Actual $P_p > 9$	128	43
Actual $P_p < 9$	33	5796

Table 3.2: Confusion matrix for using the 20% broadened bandwidth for collision detection in simulations.

Collision detection in the pure NLSE regime

Clearly an unambiguous determination of breather collisions is not possible from our experimental data due to non-perfect correlation between the spectral bandwidth at -45 dB and the maximum peak power in the temporal domain. The coefficient of correlation can be increased by measuring the bandwidth at even larger dynamic range. However, this was not possible in our experiments due to the generation of dispersive waves. In order to confirm the possibility we show results from similar stochastic simulations done in the pure NLSE regime in Fig. 3.15 and compare the 45 dB, 20 dB bandwidths and the 60 dB bandwidth.

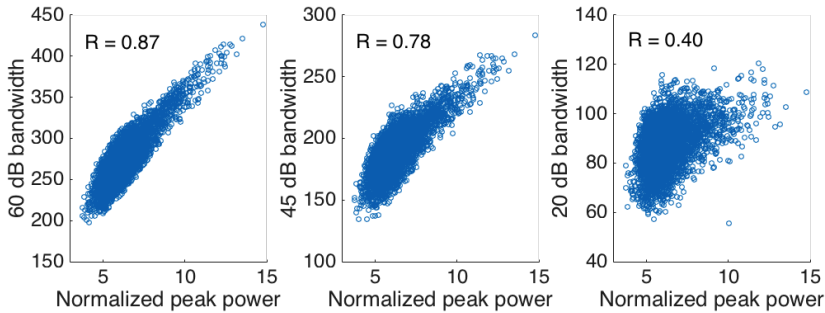


Figure 3.15: Normalized peak power vs bandwidths at various levels in the pure NLSE regime. We also show the Pearson's correlation coefficient R for each of the cases, with $R = 1$ denoting a perfect correlation and $R = 0$ noting no correlation.

We can see how the coefficient of linear correlation increases to $R=0.87$ in the 60 dB case. This increases our ability identify collisions from spectral data to 70% compared to the 60% obtained when using 45 dB bandwidth measurement. In principle our simulations would allow to go down to 80 dB level where even more reliable identification should be possible, but our experimental arrangement although allowing for a very high dynamic range is not able to capture the 80 dB bandwidth. Other prospects for increasing the reliability are based on novel machine learning algorithms. Preliminary testing has revealed the possibility of collision recognition from spectral data to be increased up to 80%.

3.4 Transient dynamics of fiber laser modelocking

The previous sections of this Chapter have focused on single shot measurements of nonlinear systems either in the temporal or in the spectral domain. In this section, we combine two single-shot techniques, the DFT and time lens, to study in real-time the complex dynamics occurring at megahertz repetition rates during the turn-on phase of a mode-locked fiber laser. The results of this experimental study are the subject of Publication II. Such spectro-temporal characterization allows to build a complete picture of the dynamics: using a phase-retrieval algorithm, one can obtain the information of the complex electric field allowing to determine the subtle differences in the physical processes on ultrafast time scales.

Passively mode-locked lasers represent one of the major advances in laser technology since the 1960s [109], enabling modern optical frequency combs and attosecond pulse generation. The first passively mode-locked lasers were based on saturable absorption in dye molecules and could reach pulse durations down to 27 fs under careful design [110, 111]. However, many of these lasers were inherently unstable and reliable pulse emission was difficult to achieve. In fact, the first ever reported mode-locking observation was made in a laser that was not working in a stable operation mode, but in an unstable Q-switched mode-locking regime [109, 110]. The next leap forward was made in the 1990s, with the invention of the Ti:Sapphire laser and discovery of the highly stable Kerr-lens mode-locking mechanism that could reduce the emitted pulse duration down to the few-cycle limit of femtosecond durations and allow for high peak power values [112]. However, cavity designs are relatively complex and the lasers rather bulky which may not be practical for all applications.

Mode-locking with the use of a semiconductor saturable absorber mirror (SESAM) was shortly reported after the Ti:Sapphire laser invention [113–115]. The SESAM approach allows for simplified cavity designs and much reduced low-footprint. SESAM-based lasers had originally stability issues, but the improvements in SESAM manufacturing have now mostly resolved these issues. Since the introduction of mode-locked lasers, the physics of the transition regime from the quasi-CW state to stable mode-locked operation has been widely investigated [116–118]. Several theoretical models have been proposed, including the now famous so-called Haus-master equation [119, 120]. This equation is in fact similar to the more general (and extensively studied) Ginzburg-Landau equation [121, 122], which is another generalization of the NLSE of equation 2.39 when gain dynamics are present in the modelled system. More specifically, the Ginzburg-Landau equation takes into account losses, gain and higher order nonlinearities (second and fourth powers of the field; not to be confused with delayed Raman effects and self-steepening of the GNLSE) and which describe what are referred to as *dissipative soliton dynamics* in contrast to the “passive” soliton dynamics of the GNLSE. The Ginzburg-Landau equation does not have general solutions and particular solutions can be found for a fixed set of relations between specific parameters of the equation. The propagation dynamics are then generally extremely complex and very rich.

Numerous experimental studies on the dynamics of passively mode-locked laser, including that of the transient regime, have been reported. These studies traditionally used fast photodetectors and/or averaging autocorrelation and spectral measurements [123–130]. While direct photodetection can generally provide an overall picture of the system dynamics they do not allow for capturing fast scale changes below some tens of picosecond due to the limited bandwidth of the detectors. On the other hand, autocorrelation can

provide information on sub-ps temporal structure but the inherent averaging over long time span prevents resolving changes occurring from one roundtrip to another in the laser cavity. More recent studies have exploited the potential of DFT for tracking changes occurring between subsequent roundtrips in the cavity during the mode-locking transition or unstable mode-locking operation [131–133]. In our work, we demonstrate for the first time how the combination of DFT measurements with that of a synchronized time lens allows for capturing dissipative soliton dynamics of the transient regime of a SESAM mode-locked fiber laser with sub-ps and sub-nm resolution, and which had not been resolved in previous experiments.

3.4.1 Experimental overview

The laser under study was a commercial femtosecond fiber laser (Pritel FFL-500) that produced 4.5 ps pulses at 1545 nm (characterized by an independent FROG measurement) with 20 MHz repetition rate. The laser has a net anomalous dispersion resulting in soliton-mode-locking achieved by a SESAM used at the other end of the linear cavity. A spectral filter placed in the cavity allows one to select the output pulse duration - here the filter bandwidth was chosen to be 3 nm. A schematic of the cavity is shown in Fig. 3.16.

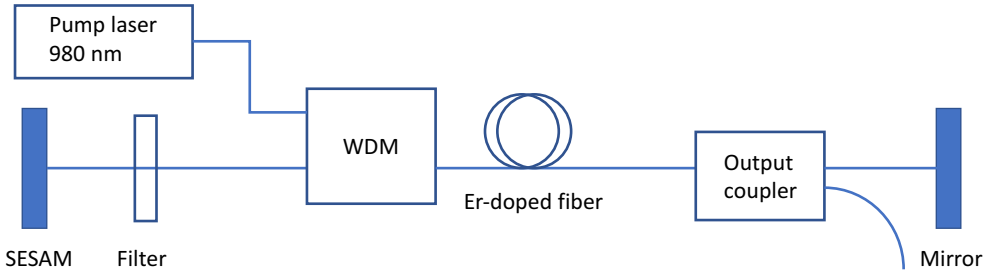


Figure 3.16: Schematic of the fiber laser cavity studied.

The experimental setup implemented to characterize the transient regime from the laser is shown in Fig. 3.17. The output of the fiber laser was split into two by a fiber beam splitter and the two outputs were connected to the real-time spectral and temporal measurement systems. For temporal detection we used the UTM-1500 time lens system described in section 3.1. For the DFT we utilized an 875 m long dispersion compensated fiber (Sumitomo Electric industries) with a total dispersion of $\beta_2 z = 133 \text{ ps}^2$. The output of the time lens was directed to a 13.5 GHz amplified photodetector (Miteq 135GE) and the output of the DFT to a 38 GHz amplified photodetector (NewFocus 1474 A). Both of these were connected to two channels of the same 30 GHz oscilloscope (80 GS/s, Lecroy 845 Zi-A).

Due to different physical path lengths, the spectral and temporal recorded signals from the DFT and time lens respectively were recorded with a time delay on the oscilloscope. In order to establish the one-to-one correspondence between the real-time spectral and temporal measurements, this delay was calibrated using a modulated CW laser operating at 1590 (square intensity modulation pattern at 50 MHz) that passed through both of the measurement systems. The operating wavelength was chosen that we can pass it through the time lens system without any upconversion needed. Triggering the oscilloscope on the CW laser being turned off, once can then determine the time difference from the falling edge of the modulation on both channels.

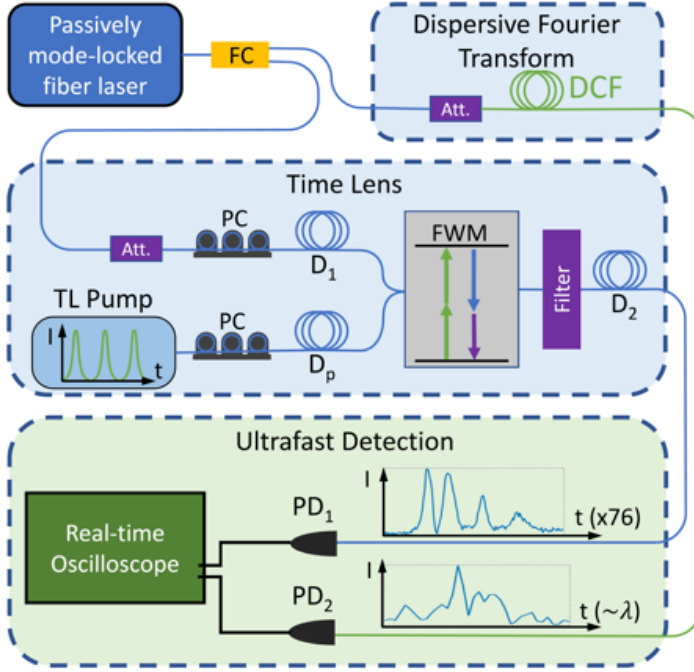


Figure 3.17: Experimental setup for simultaneous acquisition of real-time spectral and temporal information of a mode-locked fiber laser. Attenuators were used in order to minimize nonlinear effects in the DFT and TL systems. PC = polarization control, DCF = dispersion compensating fiber, FC = fiber coupler.

3.4.2 Phase retrieval

The potential of simultaneous measurement of the temporal and spectral envelopes can be fully appreciated when performing phase retrieval, allowing for the complete characterization of the underlying electric field and coherent structures in real time.

Phase retrieval was performed using a modified Gerchberg-Saxton algorithm (also referred to as iterative Fourier transform algorithm) [134, 135]. Originally developed for two-dimensional image phase retrieval, the Gerchberg-Saxton algorithm can also be applied in one dimension for time domain signals, provided the temporal and spectral intensity envelopes are known. Aside from few trivial ambiguities, the Gerchberg-Saxton algorithm performs relatively well despite the criticisms it has received [136]. However, these criticisms arose from the assumption that only the spectrum and autocorrelation data are available for the reconstruction. But, the precise knowledge of the temporal intensity envelope rather than that of the autocorrelation improves significantly the convergence and reliability of the algorithm.

The algorithm principle is illustrated on the flow chart of 3.18. It uses as an initial condition the measured temporal intensity $I_M(t)$ and a random phase $\phi_{\text{rand}}(t)$: $E_g(t) = \sqrt{I_M(t)}e^{i\phi_{\text{rand}}(t)}$ which is then Fourier transformed to the spectral domain to yield a corresponding initial guess for the spectral amplitude and phase $\mathcal{FT}[E_g(t)] = \sqrt{S(\omega)}e^{i\varphi(\omega)}$. In the next iteration, the calculated spectral phase is retained but the spectral amplitude is replaced with that experimentally measured, i.e. $\sqrt{S_M(\omega)}e^{i\varphi(\omega)}$. This spectral field is

then transformed back into the time domain to obtain $\sqrt{I(t)}e^{i\phi(t)}$, where one retains the calculated temporal phase but again replace the temporal amplitude with that obtained from measurements.

The convergence of the algorithm is quantified via the root mean square temporal intensity error, defined by $\epsilon_I = [\sum(I(t) - I_M(t))^2/N]^{1/2}$. The iterative procedure is repeated until the root mean square error between the measurements and retrieved intensity profiles becomes smaller than a target value (3×10^{-5} in our case). Convergence was improved by applying the measured temporal and spectral intensities only for values were well above the noise floor (-20 dB from the maximum). Elsewhere, the amplitudes were multiplied with a small constant value of 0.001 forcing them below the noise level. If the algorithm was found to stagnate (i.e. no change in the retrieval error before reaching the target value), a small additional random phase contribution was added. The reliability of the algorithm was tested with simulated pulses and by performing multiple retrievals on the same experimental data, which all converged to the same results (within the retrieval error).

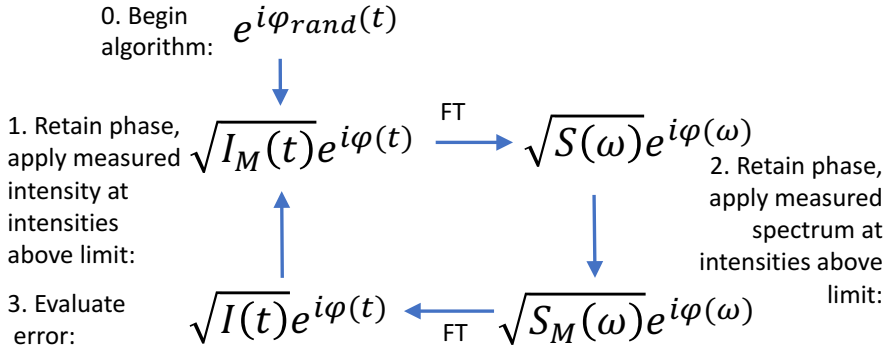


Figure 3.18: Flow chart of the one-dimensional Gerchberg-Saxton algorithm.

This algorithm was extensively tested with numerically-constructed pulses with properties similar to those seen in experiments, and typical results are shown in 3.19. These numerical tests were performed for: (a) a single pulse with moderate nonlinear phase from self-phase modulation (SPM); (b) a double pulse with different amplitudes and a π relative phase difference; (c) a triple pulse with different amplitudes and a π relative phase difference between adjacent pulses. For each case, we added 1% multiplicative noise to both the temporal and spectral intensity before running the phase retrieval algorithm.

The susceptibility of the algorithm to noise was also studied. For these results, we quantify the retrieval fidelity in terms of root mean square errors (rms) between the target numerical (known) intensity and phase and that which is retrieved, defined as ϵ_I above for the intensity and $\epsilon_\phi = [\sum(I(t)^2(\phi(t) - \phi_r(t))^2/N)]^{1/2} / [\sum(I^2(t))/N]$. Figure 3.20 (a) and (b) show how the rms phase and intensity errors vary with the level of multiplicative noise applied to the numerical test pulse with SPM. Even at higher levels of noise the phase retrieval algorithm still yields very good results. Indeed, figure 3.20 (c) and (d)

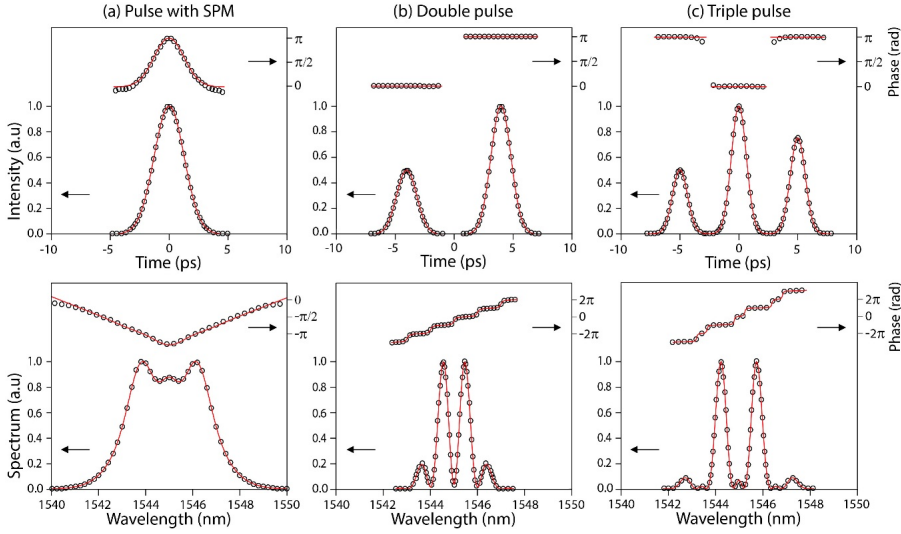


Figure 3.19: Examples of retrieved intensities and phases by the Gerchberg-Saxton-algorithm for three different cases: (a) a single pulse with moderate nonlinear phase from SPM; (b) a double pulse with different amplitudes and a π relative phase difference; (c) a triple pulse with different amplitudes and a π relative phase difference between adjacent pulses. The figures show (top) temporal and (bottom) spectral properties, comparing retrieved intensity and phase (open circles) with those of the target numerical pulses (red solid lines). Temporal and spectral intensities are referred to the left axis; temporal and spectral phases are referred to the right axis.

show retrieved temporal and spectral characteristics (in intensity and phase) for the case of 5% multiplicative noise. For higher levels of noise, as in experiments, algorithm convergence can be improved by applying the measured temporal and spectral constraints only where the measured intensities were well above the noise floor.

3.4.3 Results

In addition to the real time measurements, we complemented our results with standard measurements of the transition to mode-locking by the fast diode only by removing the fiber used for the DFT and limiting the oscilloscope effective bandwidth to 20 MHz. This allowed us to capture the overall behavior shown in Fig. 3.21 and corresponding to the full 100 ms transition period from the turn-on time to the stable mode-locking regime.

One can see how the recorded sequence shown in Fig. 3.21 (a) can be divided into two distinct Q-switched mode-locking (QML) regime and the stable mode-locked regime. During the initial QML regime, the laser generates multiple bursts of pulses for 200-300 roundtrips which eventually die out. Three of these QML bursts are shown in Fig. 3.21 (b). Within a QML burst, the photodetector shows pulses separated by 50 ns, corresponding to the cavity roundtrip time. These QML bursts start with scarce intervals (few milliseconds) and get denser the closer we get to the mode-locked regime (e.g. 70 microsecond interval shown in the figure). In the mode-locked regime (zoom in showed in Fig. 3.21 (c)) we observe a stable constant energy pulse train at the repetition rate of the laser. The increase in the occurring frequency of the QML bursts are attributed to

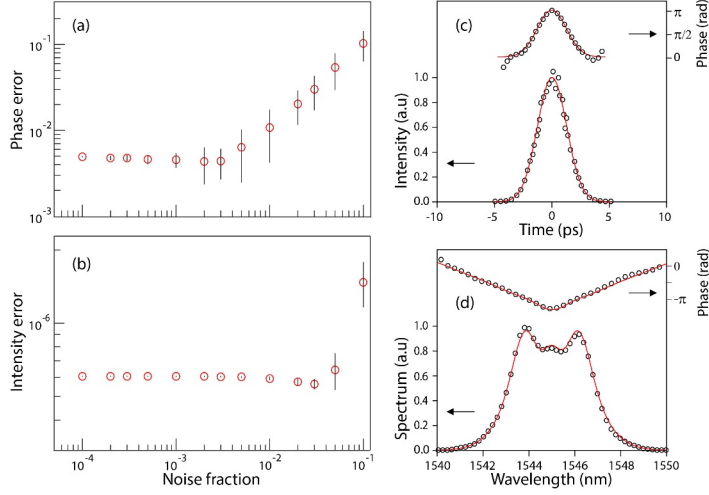


Figure 3.20: Results showing the dependence on multiplicative noise fraction of: (a) the phase error and (b) the intensity errors (defined in the text) between retrieved and target pulse after applying the Gerchberg-Saxton algorithm. The error bars show the standard deviation from repeated retrievals using different noise to highlight the reproducibility of the algorithm. The results in (c) and (d) show the retrieved temporal and spectral characteristics for a pulse with SPM and 5% noise.

the constantly increasing pump current once the laser is tuned on, which allows these bursts to occur more often as the overall energy in the cavity is increased. There are also significant energy variations within the QML bursts resulting from the interplay between the saturable absorber, the gain depletion and varying pump current. Aside from these energy variations, the fast photodetector simply cannot yield any additional information about any possible fine structure within the QML bursts. In order to get detailed insight into the dynamics of the QML bursts we recorded simultaneously their evolution over several hundreds round trips using the DFT and time lens. The time lens pump laser (at 100 MHz repetition rate) can only be synchronized to the Pritel laser in the stable mode-locked regime such that in order to measure the temporal intensity during the mode-locking transition the time lens was operated in free-running mode, where the pump pulses occasionally overlap with the Pritel pulses during the transition. This means that one cannot measure the full transition mode-locking period of 100 ms with the time lens (which would also be impossible due to memory constraints of the oscilloscope) as the pump pulses drift away from the signal pulses but rather measure the temporal intensity over short time intervals, nevertheless longer than the typical lifetime of a single QML burst. Note that the DFT has no such limitation (except for the oscilloscope memory constraint) and will capture all bursts during the transition and thus can serve as a control measurement.

Stable mode-locked regime

We first show a selection of real-time measurements corresponding to the stable mode-locking regime and to the onset of stable mode-locking when output pulses undergo periodic breathing as shown in Fig. 3.22 (a) and Fig. 3.22 (b), respectively.

In the case of stable mode-locking operation, one can observe a steady ≈ 5 ps pulse

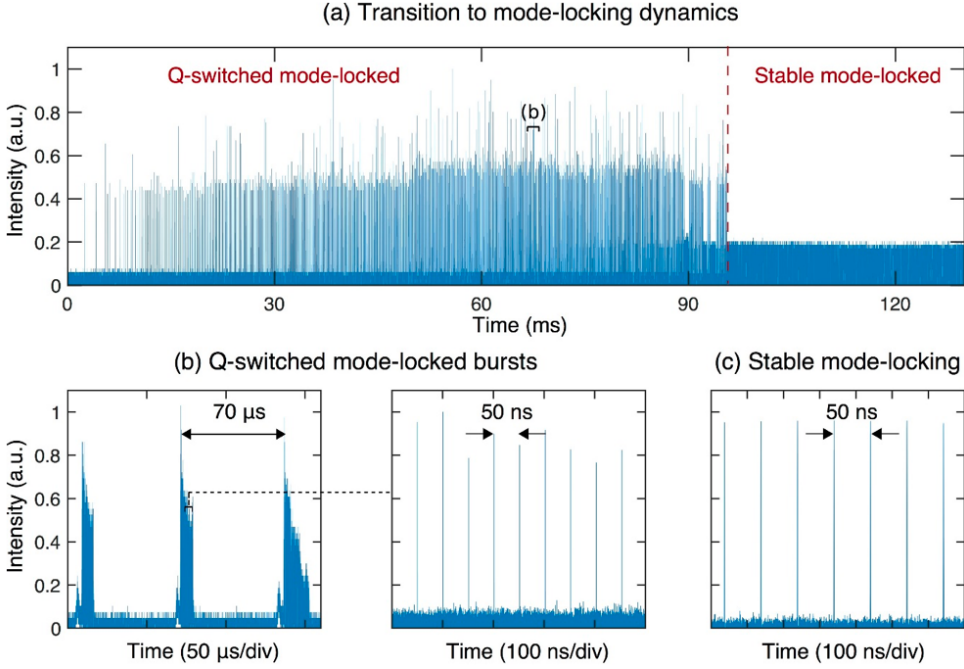


Figure 3.21: Full mode-lock transition when the laser is turned on measured by a bandwidth limited photodetector.

train from one roundtrip to another both in the spectral and temporal domains. This is confirmed when performing phase-retrieval using a modified Gerchberg-Saxton-algorithm [134] and yielding a nearly constant phase across the temporal profile of the output pulses indicating near transform limit.

At the onset of mode-locking, the pulse duration and energy oscillate periodically and the pulses have not quite reached the steady-state transform limited operation, as seen from the phase plots.

QML bursts

In order to capture the QML bursts at the different phases of the transition cycle, we used a two-stage triggering scheme on the oscilloscope. The first trigger was set by the DFT to identify the first QML burst. A variable hold-off time then used for the second trigger set from time lens channel. By varying the hold-off time, it is then possible to capture bursts at different stages of the transition regime. Independently of the precise occurrence within the transition cycle, the evolution of a single QMP burst was found to bear similar characteristic features: an initial high intensity pulse that breaks up into few sub-pulses (typically 2 to 4) that subsequently propagate independently or interact and eventually collapse. Figure 3.23 shows three typical examples of measured QMP burst evolution illustrating the richness of the dynamics observed on a short time scale.

Particular attention is drawn to the dissipative soliton interactions after the initial breakup dynamics and these can be classified into 3 groups as shown in Fig. 3.23 as: (a) non-interacting soliton triplet, (b) interacting soliton doublet with a third independent soliton and (c) interacting soliton doublet.

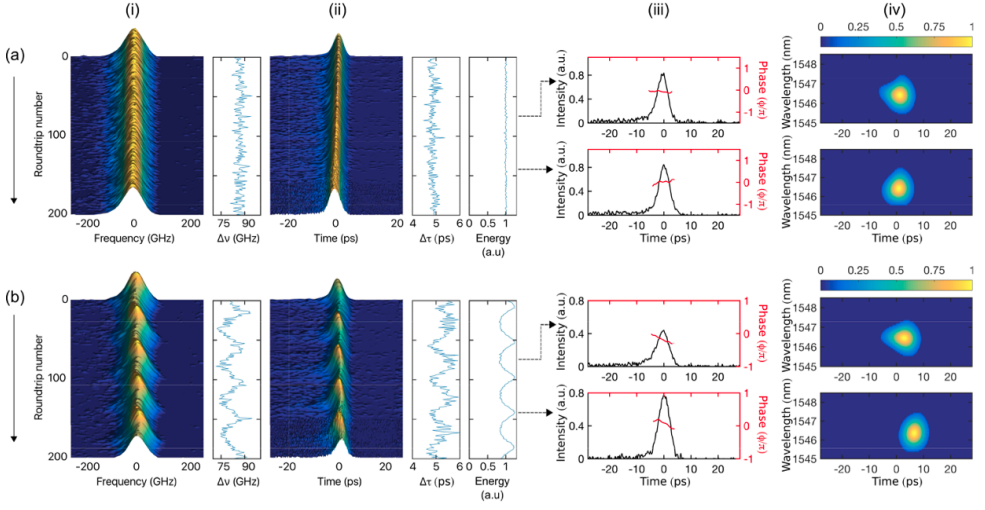


Figure 3.22: (a) Mode-locked state: (i) DFT data, (ii) TL data, (iii) phase retrieval at the indicated positions, (iv) spectrogram of the retrieved complex electric fields (b) Breathing of the mode-locked pulses just before mode-locking, the subfigures show the same data as in (a).

Cases (a) and (b) both show a soliton triplet emerging with the discrepancy that for case (a) the solitons propagate independently until they collapse, while for case (b) two of the solitons attract each other and collide. Inspecting the reconstructed spectrograms from the phase-retrieval procedure, one can notice that for the non-interacting case all of the three solitons have slightly different center wavelengths while interaction generally occurs when two of the solitons have the same center frequency. Furthermore, one can note that the leading and trailing solitons in the non-interacting case have a relative phase-difference of approximately π with respect to the center pulse. For the interacting soliton pair in the triplet the two colliding solitons have almost no relative phase-difference but both have approximately $\pi/2$ phase difference to the leading pulse. Similar features are observed for the soliton molecule of Fig. 3.23 (c): the two colliding solitons reside at the same center wavelength and have nearly zero relative phase-difference. These results are in good qualitative agreement with earlier theoretical studies studying soliton interaction in fiber laser cavities, where similar phase difference values have been reported to cause similar attraction and repulsion between multiple solitons [124, 125, 137, 138].

3.4.4 Complex eigenvalue spectra

The retrieved complex field allows us to perform a more detailed analysis using the inverse scattering transform to calculate the discrete “nonlinear Fourier transform” spectrum. Similar to a regular Fourier transform decomposing a waveform into a composition of sinusoidal waveforms, the nonlinear Fourier transform (NFT) decomposes the waveform into its underlying nonlinear content, yielding the “solitonic” content of the field [139]. The decomposition is performed by the IST method with respect to a particular Lax pair operator specified by the differential equation that governs the waveform evolution - which is the normalized NLSE of eq. 2.39 in this case. The complex NFT spectrum is symmetrical around the real-axis. It consists of a discrete part that remains unchanged with propagation and reflects the nonlinear content of the waveform such as solitons or cnoidal waves. The continuous part on the other hand varies with propagation and

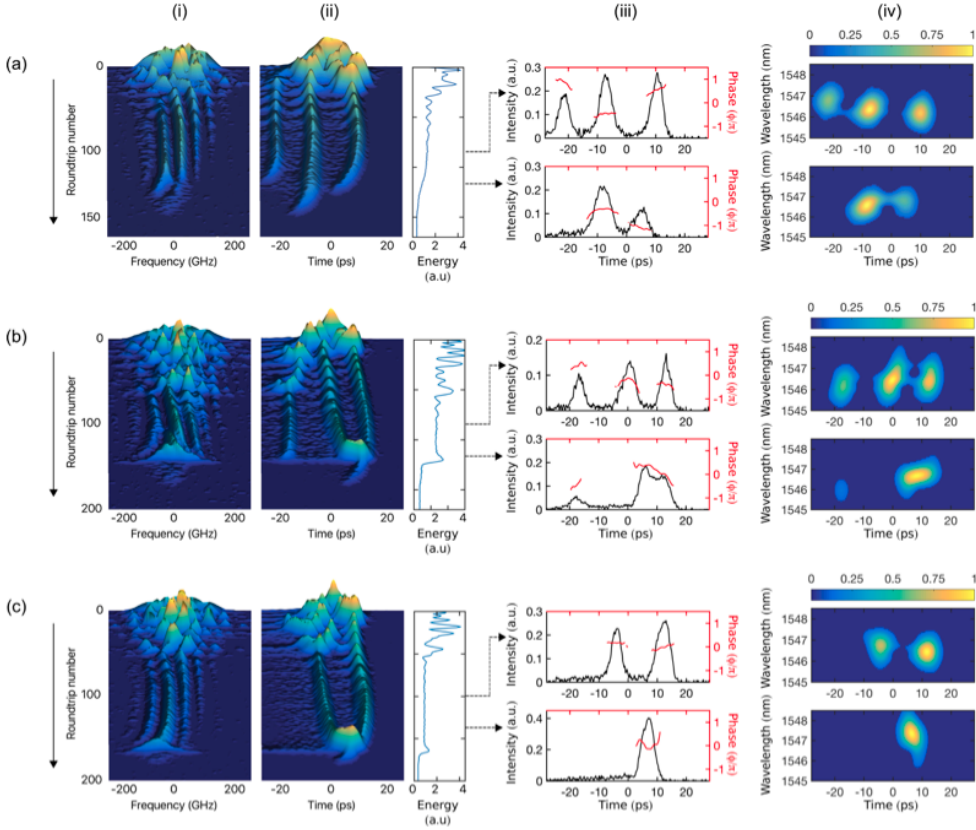


Figure 3.23: Three different QML bursts and their phase-retrieved pulse structure and spectrograms.

corresponds to the linear radiation component of the waveform. The discrete part of the NFT spectrum consists of complex eigenvalues ζ , while the continuous part is real.

Application of the nonlinear Fourier transform is in principle restricted to integrable nonlinear evolution equations such as the pure NLSE above. Thus, one must be cautious when using the IST to analyze the characteristics of a dissipative system, where one may expect deviation from integrability. In our study, the laser cavity consists of a large number of different fiber segments with multiple components such that it is (most likely) not integrable in the pure NLSE sense. The NFT is therefore not applied to the dynamical evolution of the field inside the laser cavity but to the field that exits the laser cavity through an SMF-28 fiber pigtail which then acts as a static NLSE emulator where the NFT transform can be applied. This allows us to identify coherent solitonic content of the field in the transient or stable operation regime. However, this analysis is only valid outside the laser cavity.

In order to calculate the discrete NFT spectra in the complex plane, we utilize the Fourier collocation method as described in [140]. It is first instructive to consider IST spectra corresponding to the particular analytic solutions of the NLSE shown in Fig. 3.24.

The discrete NFT spectrum of the fundamental sech-solution of the normalized NLS corresponds to a pair of purely imaginary eigenvalues $\text{Im}(\zeta) = 0.5i$, see Fig. 3.24 (a),

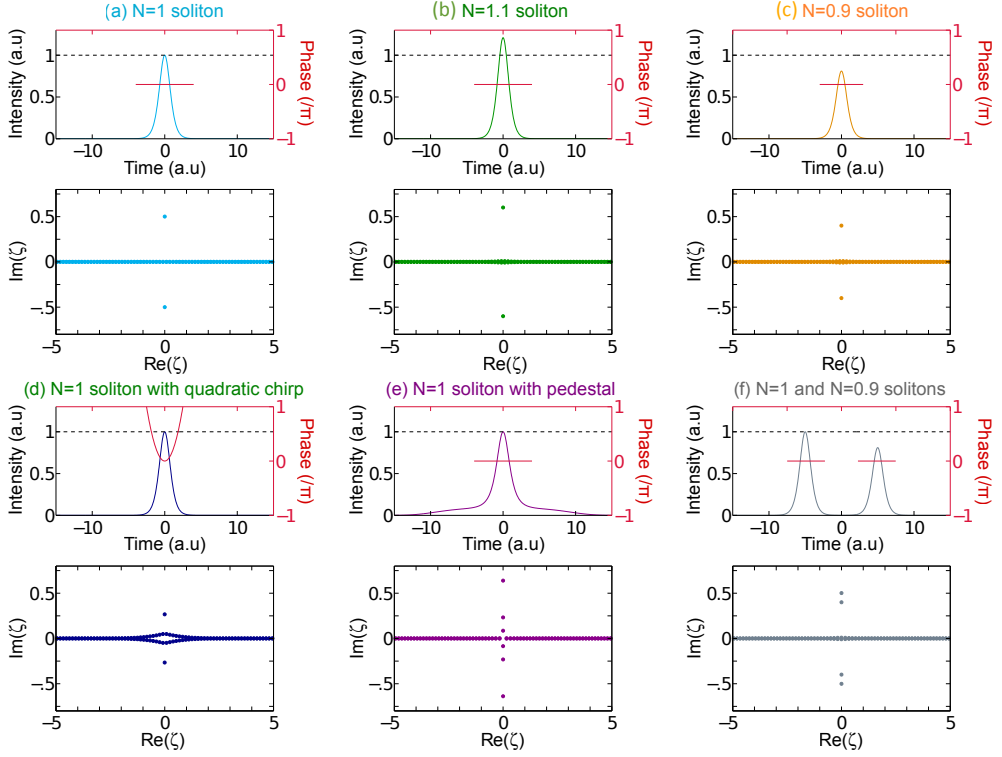


Figure 3.24: Results showing the nonlinear transform for typical pulse shapes. Fundamental sech-soliton with $N=1$ (a), $N = 1.1$ (b) and $N = 0.9$ (c) amplitude. (d) sech-soliton with quadratic chirp, (e) sech-soliton with residual pedestal and (e) two sech-solitons shifted in time with $N = 1$ and $N = 0.9$ amplitudes.

[141, 142]. This eigenspectrum can then be used as a reference to analyze other types of structure as shown in Fig. 3.24 (b-f) below. For example, preserving the functional sech-shape but increasing Fig. 3.24 (b) or decreasing Fig. 3.24 (c) in the input soliton number from $N = 1$ still yields purely imaginary eigenvalues but they are now shifted up ($N > 1$) or down ($N < 1$) with respect to the reference value $0.5i$ for $N = 1$. In the case of a chirped sech-pulse Fig. 3.24 (d), the energy corresponding to the solitonic part is reduced as compared to that of an ideal soliton (because the total energy is spread over a larger spectral bandwidth). This causes the eigenvalue to be reduced compared to the reference value $0.5i$ as well as to the appearance of a radiation part manifested as the “eye”-like structure around the zero point. For a pulse with a pedestal in Fig. 3.24 (e), the energy corresponding to the solitonic part is increased as compared to that of an ideal soliton resulting in multiple imaginary eigenvalues as well as a residual radiation component. In the case of a field composed of two sech-solutions with slightly different amplitudes and which are shifted in time Fig. 3.24 (f). The eigenspectrum in this case consists of two distinct eigenvalues on the imaginary axis associated with the presence of two distinct coherent soliton structures in the original field.

Finally, we inspect a more complex case with multiple solitons with relative velocity components. The NFT spectrum can also reveal the velocity components with respect to the time-frame of the NLSE solution, which appears as a non-zero real part of the

eigenvalue. This is shown in Fig. 3.25, where we show the NFT spectrum of three solitons with relative velocity components and one sech-pulse with an amplitude below the soliton limit i.e. $N < 0.5$. We observe the eigenvalue at $(0,0.5)$ corresponding to the first fundamental soliton. We also note the eigenvalue at $(2.5i,0.1)$, that is the soliton with the largest velocity mismatch. In addition to this, we observe two eigenvalues at $(-0.5i,0.5)$ and $(-0.5i,1.5)$ that correspond to the higher order $N = 2$ soliton with a relative velocity component. Indeed, any higher order soliton with an integer soliton number N will have N eigenvalues that have the same real value, but are separated by $1i$ [142]. On the contrary, we see no eigenvalues corresponding to the amplitude 0.4 soliton. This is to be expected, as we know from section 2.2.3 that these solutions do not possess enough energy to sustain soliton invariant-propagation and decay due to dispersion.

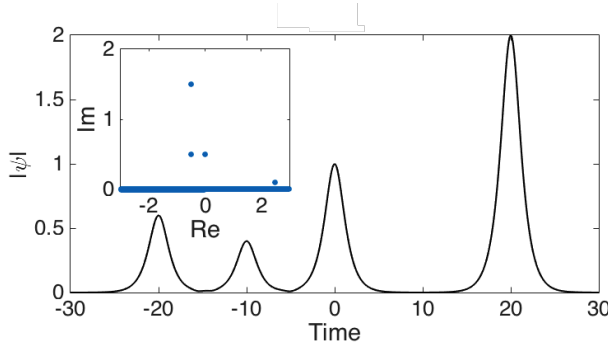


Figure 3.25: Discrete NFT spectrum of $\psi(t) = \text{sech}(t) + 2 \cdot \text{sech}(t - 20)e^{it} + 0.6 \cdot \text{sech}(t + 20)e^{-5it} + 0.4 \cdot \text{sech}(t + 10)e^{-2it}$. The time-dependent phases cause a shift in the center frequency of the pulse, which causes it to have a different relative velocity with respect to the NLSE time-frame. The weakest sech-pulse does not fulfill the soliton condition and thus it is not observed in the NFT spectrum.

These results illustrate how signatures of the solitonic content of coherent structures as well as deviations from the ideal hyperbolic-secant soliton solution of the NLS can be clearly identified from calculation of the discrete NFT spectrum. We applied the Fourier collocation method to calculate the NFT spectra for one of the QML-bursts occurring during the mode-locking transition and the result is shown in Fig. 3.26. The calculation of these eigenspectra is only possible because of the phase-retrieval allowed by the joint spectro-temporal measurements.

The energy of the pulses were normalized with respect to the stable mode-locked pulse, that was assumed to be a fundamental hyperbolic secant soliton. We observe, how the uppermost case shows roughly four distinct eigenvalues indicating the presence of the four solitons. This serves as a confirmation that these pulses arise from the nonlinearity in the system. The non-zero real parts reveal the relative velocity components that are likely to cause the collisions of the solitons in following round-trips. Some weak radiative waves are also observed in the nonlinear spectrum. Following the pulse evolution, we observe how the number of eigenvalues decreases from three to two, and finally one, in connection to the number of pulses observed in the temporal profiles.

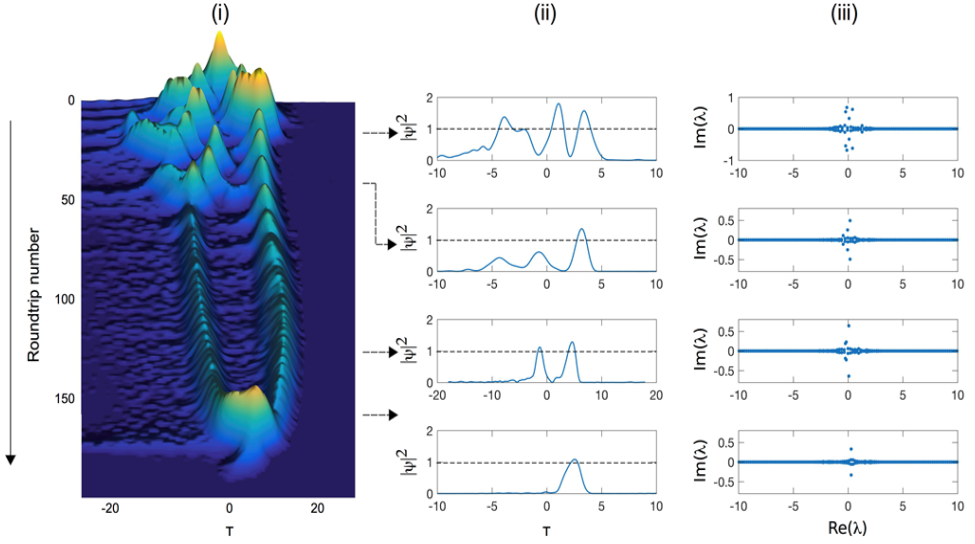


Figure 3.26: QML-burst (i) and the corresponding intensities (ii) and their NFT-eigenspectra (iii).

3.5 Conclusions

In this chapter, we have shown how single-shot measurement techniques can be conveniently used to obtain new insight into noise-driven nonlinear dynamics.

In particular, we have measured the characteristics of the stochastic pulse train arising from noise-seeded MI in spectral and temporal domains. The experimental results show excellent qualitative and quantitative correspondence between the experimentally measured structures and the Akhmediev breather solutions of the NLSE. This result is significant in providing evidence that the analytical breathers solutions of the NLSE provide a convenient framework with which to interpret the formation of locally coherent structures emerging from noisy input conditions.

Our results further confirm that the structures with the highest local intensity arise from the collision or nonlinear superposition of two or more breathers, and these collisions may then be interpreted as the rogue waves observed in a pure NLSE system. In another set of experiments that used a specifically developed single-shot mechanical streak camera, we have shown that the rogue events may be inferred from a spectral measurement of the field spectral bandwidth at the -40 dB level.

Combining real-time spectral and temporal measurements of the envelope of the electric field at the output of a passively mode-locked laser cavity operating in the transient regime, we have demonstrated the possibility for the first time to reconstruct the associated complex electric field (intensity and phase) and obtain insight in dissipative soliton dynamics that have never been observed experimentally before on such time scales. We have further shown how the knowledge of the complex electric field allows to identify solitonic structures via nonlinear Fourier transform. We anticipate that the high acquisition rate of the developed approach beyond the tens of MHz regime will foster new research into transient dynamics of nonlinear optical systems. Of course, there are

still some limitations in terms of wavelength range and bandwidth and research into expanding the technique capabilities in the near future is also expected.

4 Second order coherence measurement of supercontinuum

Supercontinuum generation in nonlinear fibers or waveguides has attracted significant attention because of their vast application potential both in fundamental or applied research. From a fundamental viewpoint, the generation of broadband supercontinuum sources allows for ultra precise frequency metrology and optical clocks that can exceed the precision of atomic clocks [33] or attosecond optical pulse generation and tracking the movement of electrons [34]. On the other hand, supercontinuum light sources can improve significantly the performances of optical imaging and sensing systems that require a broadband light source such as e.g. white light interferometry [143], optical coherence tomography [35] or broadband spectroscopy [144, 145].

Their coherence properties are central to the use of laser as light sources in optical systems. This also applies to supercontinuum generation and the required coherence properties depend on the particular application considered as illustrated in Fig. 4.1 [36]. More specifically, applications in frequency measurements and ultrashort pulse generation necessitate perfect stability and temporal coherence while optical imaging or sensing systems only requires perfect spatial coherence.

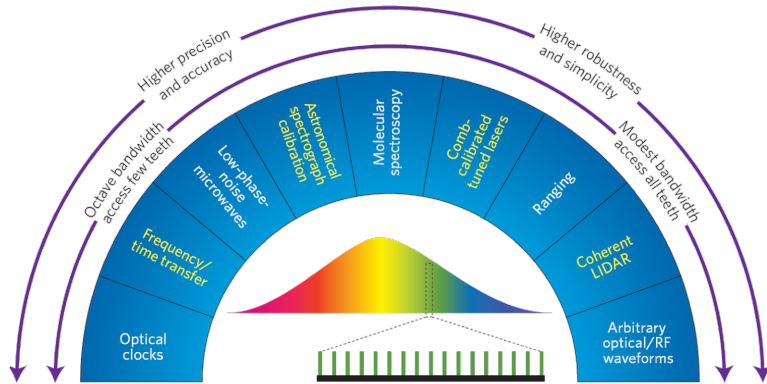


Figure 4.1: Required coherence/stability properties of the light source depending on the application [36].

In this Chapter, we first provide a brief overview of coherence theory and then move on to discuss the specifics of second order coherence properties of supercontinuum light from a theoretical and experimental viewpoint, as also reported in Publication III. The nonlinear dynamics leading to SC generation and which are directly linked to the resulting

coherence are discussed in section 2.6, and the reader is referred to this section for more details when needed.

4.1 Coherence theory

The first order degree of temporal and spatial coherence are related to the phase of the electric field. Specifically, temporal coherence is a measure of the electric field correlation at two different instants of time but in the same point in space. If the case of a perfectly monochromatic light source the electric field exhibits sinusoidal oscillations such that the electric field values at any arbitrary times are fully correlated and is therefore perfectly temporally coherent. In reality, light sources have a finite linewidth such that the evolution of the electric field can only be predicted over a finite time τ_c known as the *coherence time*. The physical meaning of the coherence time is the time interval over which the field correlation with a delayed replica of itself remains relatively high. For stationary light sources (defined in the next section), the coherence time is inversely proportional to the spectral bandwidth $\tau_c \propto 1/\Delta\nu$ [146] and is determined by the generating mechanism of the light: random photon emission from spontaneous emission in thermal sources such as sunlight is usually in the order of few femtoseconds [147] whereas continuous wave lasers based on stimulated emission of photons can have coherence times in the order of milliseconds.

Spatial coherence on the other hand compares the electric field complex amplitude at a given time instant but at two different spatial points in the propagating wavefront. Similarly to temporal coherence, if one can predict the field amplitude at a particular transverse position from another position, these are said to be mutually spatially coherent. One can define a *coherence area* as $A_c = \pi r_c^2$, which defines the average area over which the field values are correlated and where r_c represent the distance in the transverse plane beyond which the correlations drops significantly. For lasers, the coherence area corresponds roughly to the beam profile that can be several mm^2 , whereas for sunlight this is about $0.003\text{-}0.008 \text{ mm}^2$ [148, 149]. Supercontinuum light sources are mostly generated in a single mode fibers and are thus perfectly spatially coherent over the coherence area determined by the fiber core size [72, 150].

4.1.1 Coherence of non-stationary light

In the case of CW lasers, the emitted power is constant over time and their properties may be described as *stationary*. For stationary light sources such as CW lasers, the mean and the variance of the field amplitude remain constant independently of the chosen origin of time and measurement time. For pulsed sources this condition obviously does not hold, as the mean and variance of the field amplitude will depend on whether the origin of time coincides with a pulse or a time in between two pulses where the intensity drops to zero. Such sources are known as non-stationary light sources.

The temporal coherence of stationary light sources can be measured with a Michelson interferometer, where one arm is fixed and the other arm is scanned through various delays between the two replicas of the field. The measured power at the output will exhibit temporal interference fringes (or oscillations) as a function of the delay τ . The fringes visibility (peak-to-through variation) corresponds to the correlation function of the form:

$$\gamma^{(1)}(\tau) = \frac{\langle E^*(t)E(t+\tau) \rangle_T}{\langle |E(t)|^2 \rangle_T}. \quad (4.1)$$

Here the angle brackets denote a time average and the asterisk is the complex conjugate. This function is normalized with the average intensity (power) and varies between 0 (incoherent) and 1 (coherent). The coherence time is then defined from the width of this function.

In the case of non-stationary light sources, the coherence function above drops after a time inversely to the spectral bandwidth of the source but in contrast to stationary light sources, this drop arises from the zero intensity outside the pulse duration. This also means that the coherence function is in fact periodic with a periodicity corresponding to the repetition rate of the laser. This is because subsequent pulses emitted by a pulsed laser are generally correlated as they originate from the same pulse circulating within the cavity. The coherence time may then be seen as the time after which the local amplitude of the peaks in the correlation function has decreased significantly and this time usually corresponds to the linewidth of the individual modes of the cavity. The correlation function defined above may then not be perfectly adapted to describe the coherence of pulsed sources, and for non-stationary sources one rather computes the correlations between an ensemble of different realizations of the field corresponding to elementary time slots where pulses are emitted and the intensity is non-zero.

Second order coherence functions of non-stationary light

The more general *second order coherence function* applicable for both stationary and non-stationary sources in the time-domain is defined as:

$$\Gamma(\Delta t, \bar{t}) = \langle E^*(\bar{t} - \Delta t/2)E(\bar{t} + \Delta t/2) \rangle. \quad (4.2)$$

This function is also referred to as the mutual coherence function (MCF). Here the angle brackets denote an *ensemble average* and we have used the difference $\Delta t = t_1 - t_2$ and average $\bar{t} = (t_1 + t_2)/2$ coordinates as is common to use. A normalized version of this function can be obtained by dividing with the outer product of the average intensity $I(t) = |E(t)|^2$:

$$\gamma(\Delta t, \bar{t}) = \frac{\langle E^*(\bar{t} - \Delta t/2)E(\bar{t} + \Delta t/2) \rangle}{\sqrt{I(\bar{t} - \Delta t/2)I(\bar{t} + \Delta t/2)}}. \quad (4.3)$$

This normalization yields a more intuitive picture of the coherence properties as $0 \leq |\gamma(\Delta t, \bar{t})| \leq 1$, where 0 corresponds to completely incoherent light and 1 corresponds to coherent light.

It should be noted that Eq. 4.1 is actually a special case of Eq. 4.3: if one assumes that the field is stationary the ensemble average can be replaced by a time average and the MCF will only depend on one coordinate: the time difference Δt that can be linked with the delay τ in the Michelson interferometer [146].

Similarly, one can define the cross spectral density (CSD) function in the spectral domain in the average and difference coordinates,

$$W(\Delta\omega, \bar{\omega}) = \langle \tilde{E}^*(\bar{\omega} - \Delta\omega/2) \tilde{E}(\bar{\omega} + \Delta\omega/2) \rangle, \quad (4.4)$$

where the tilde $\tilde{E}(\omega)$ represents the Fourier transform of $E(t)$. Similarly to the MCF, the CSD can also be normalized with the average spectrum $S(\omega) = |\tilde{E}(\omega)|^2$,

$$\mu(\Delta\omega, \bar{\omega}) = \frac{\langle \tilde{E}^*(\bar{\omega} - \Delta\omega/2) \tilde{E}(\bar{\omega} + \Delta\omega/2) \rangle}{\sqrt{S(\bar{\omega} - \Delta\omega/2) S(\bar{\omega} + \Delta\omega/2)}}. \quad (4.5)$$

In the general case, both the MCF and CSF are two-dimensional complex valued functions that are symmetric about $\Delta t = 0$. If one uses the non-normalized forms, the two functions further form a two-dimensional Fourier transform pair [146].

To avoid confusion in terminology with other literature, it should be noted that the nomenclature used here follows that of Mandel & Wolf [146] when using the term second order coherence function and which treats the fields as classical. By definition, second order function refers to the case where the correlations of the field are studied with respect to two coordinates (e.g. the MCF is a two-time coordinate function). However, in quantum theory of optical coherence pioneered by Glauber, equation 4.3 defining the classical second order coherence function, is referred to as the first order coherence function [151], which can cause confusion. In quantum optics community the term second order coherence function is instead used when the intensity correlations of the field are measured:

$$\begin{aligned} g^{(2)}(\Delta t, \bar{t}) &= \frac{\langle E^*(\bar{t} - \Delta t/2) E^*(\bar{t} + \Delta t/2) E(\bar{t} - \Delta t/2) E(\bar{t} + \Delta t/2) \rangle}{\langle E(\bar{t} - \Delta t/2) \rangle \langle E(\bar{t} + \Delta t/2) \rangle} \\ &= \frac{\langle I(\bar{t} - \Delta t/2) I(\bar{t} + \Delta t/2) \rangle}{I(\bar{t} - \Delta t/2) I(\bar{t} + \Delta t/2)}. \end{aligned} \quad (4.6)$$

This equation has significant importance in analyzing non-classical light sources such as single photon emitters, but is beyond the scope of discussion of the thesis.

First order coherence functions of non-stationary light

Following the notation of Mandel & Wolf, we refer to Eq. 4.1 as a (classical) *first order coherence function*, as it depends only on one time coordinate in contrast to the general formulation of the MCF that depends on two coordinates. However, as discussed above, this equation holds only for stationary sources where the ensemble average can be replaced by a time average.

Interestingly, a similar first-order order coherence function can be formulated also for non-stationary/pulsed sources. This formulation has become popular due to the ease of measuring it experimentally - even though it holds no direct mathematical connection to the theoretical coherence functions defined earlier.

The idea is to measure the degree of correlation between consecutive pulses. The key experimental difference in contrast to measuring Eq. 4.1 in the Michelson interferometer experiment is to set the optical difference equal to a distance corresponding to the pulse repetition rate: $\Delta x = t_{rep}c/2$, where the factor of two arises from accounting for the roundtrip in the Michelson interferometer. This is visualized in figure 4.2 below.

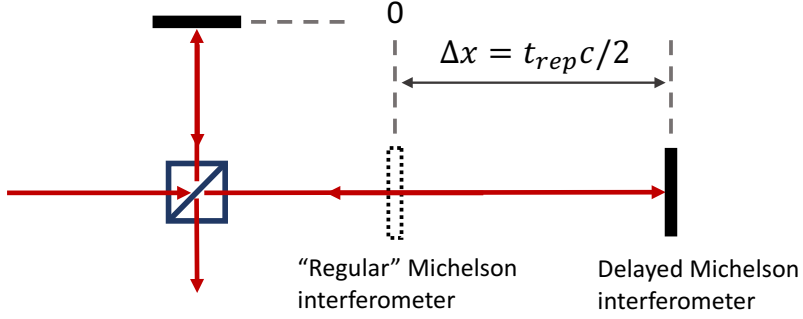


Figure 4.2: Traditional Michelson interferometer used for coherence measurements of stationary sources and the DMI used for non-stationary sources.

In such an experiment a stable, coherent source producing equivalent pulses from one to the other will interfere constructively resulting in an interference pattern at the output. In contrast, a pulse-to-pulse unstable source will wash out any observable interference as the phase difference between the pulses is random. If the interferometer was set to the regular Michelson configuration, an interference pattern would be observed in both cases as the pattern depends only on the phase difference set by the interferometer and not on pulse-to-pulse fluctuations.

In analogy with the first order coherence function for stationary light sources, one can define similar function for non-stationary light. Mathematically these are defined in the temporal and spectral domains as:

$$g_{12}^{(1)}(t) = \frac{\langle E_i^*(t) E_{i+1}(t) \rangle}{\langle |E(t)|^2 \rangle} \quad (4.7)$$

$$g_{12}^{(1)}(\omega) = \frac{\langle \tilde{E}_i^*(\omega) \tilde{E}_{i+1}(\omega) \rangle}{\langle |\tilde{E}(\omega)|^2 \rangle}. \quad (4.8)$$

Here, the ensemble averages are taken over consecutive pulse realizations i and $i + 1$ at identical times or frequencies. To distinguish from Eq. 4.1 we have used the subscript $_{12}$ to highlight the fact that the correlation is performed over two consecutive pulses. The reason that one defines the first order function also in the spectral domain is motivated by experimental restrictions. Measuring $g_{12}^{(1)}(t)$ is not often viable due to the ultrafast detection speeds that are unobtainable by direct means. Measurement of the first order spectral coherence function, however, is straightforward experimentally by a spectrometer placed at the output of a delayed Michelson interferometer. This can be understood by considering the spectrum measured at the output of the interferometer:

$$S_M(\omega) = \langle |\tilde{E}_i(\omega)|^2 + |\tilde{E}_{i+1}(\omega)|^2 + 2|\tilde{E}_i(\omega) \tilde{E}_{i+1}(\omega) e^{i\omega \Delta\tau}|^2 \rangle, \quad (4.9)$$

where $\Delta\tau$ is the relative delay between the two consecutive pulses in the delayed interferometer. The measured spectrum consists of the average spectrum $\langle |\tilde{E}_i(\omega)|^2 \rangle = \langle |\tilde{E}_j(\omega)|^2 \rangle$ modulated by a term depending on the delay that causes a spectral interference pattern. The visibility $V(\omega)$ (defined below) of the spectral interference pattern is directly linked with first order coherence function defined in the spectral domain [146]:

$$V(\omega) = \frac{S_{max}(\omega) - S_{min}(\omega)}{S_{max}(\omega) + S_{min}(\omega)} = |g_{12}^{(1)}(\omega)|. \quad (4.10)$$

Such spectral coherence function has thus become a standard coherence measure and particularly for SC sources [152–155].

4.2 Supercontinuum coherence measurement

While experimentally straightforward to implement and yielding an intuitive picture of the SC coherence properties, the first order coherence functions defined above is not as general as the MCF or CSD as it only allows for describing the stability of single frequency component between realizations and do not provide any measure of possible correlations between two different frequency (or temporal) components, which the MCF and CSD on the other hand permit to study. The first step towards unifying these two concepts was taken in 2010 when numerical studies showed that the MCF and CSD of supercontinuum could be separated into two distinct contributions called the *coherent square* (cs) and *quasi-stationary* (qs) line corresponding to the incoherent contributions. This separation was shown to hold true for a wide range of input conditions [156]. The separation into the two contributions is shown in Fig. 4.3. Another paper subsequently established a formal correspondence between the first-order spectral coherence function with the coherent square contribution of the CSD [157].

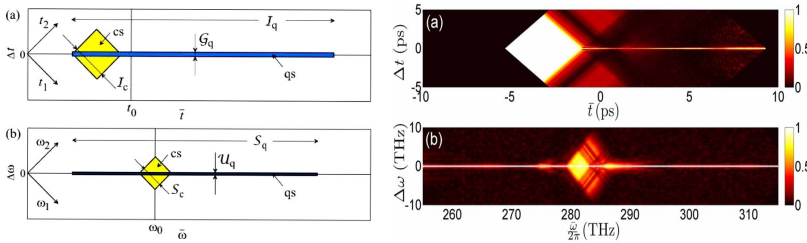


Figure 4.3: Left: schematic of the separation of the MCF (top) and CSD (bottom) to the cs- and qs-parts. Right: example simulations illustrating the validity of this theory. Image from [156].

It was further shown that the first order coherence function can be approximated very accurately as the ratio of the mean field squared to the mean spectrum

$$|g_{12}^{(1)}(\omega)| = \frac{|\langle \tilde{E}(\omega) \rangle|^2}{S(\omega)}. \quad (4.11)$$

The spectral coherence function is most sensitive to the shot-to-shot phase fluctuations of the SC source and completely random amplitude fluctuations at a given frequency one would still yield $|g_{12}^{(1)}(\omega)| = 0.75$ [150]. Intensity fluctuations are best measured with intensity correlation measurements of Eq. 4.6 on ultrafast time scales, which may be achieved using two-photon absorption of conventional photodetectors sensitive to the individual photon arrival times on femtosecond time scale [158].

An experimental scheme was suggested in [157] to measure the CSD and MCF based on separate measurements of the two contributions. Mathematically, the separation is a simple sum of the two contributions:

$$\begin{aligned}\mu(\Delta\omega, \bar{\omega}) &= \mu_{cs}(\Delta\omega, \bar{\omega}) + \mu_{qs}(\Delta\omega) \\ \gamma(\Delta t, \bar{t}) &= \gamma_{cs}(\Delta t, \bar{t}) + \gamma_{qs}(\Delta t).\end{aligned}\quad (4.12)$$

The average temporal intensity and average spectrum correspond to the diagonals of the MCF and CSD [146] and thus they also obey the partition into coherent and quasi-stationary contributions: $I(t) = \Gamma(t, t) = I_{cs}(t) + I_{qs}(t)$ and $S(\omega) = W(\omega, \omega) = S_{cs}(\omega) + S_{qs}(\omega)$.

The quasi-stationary contributions to the MCF and CSD can be obtained by Fourier transform of the corresponding quasi-stationary spectrum and intensity respectively normalized by the pulse energy E_0 :

$$\begin{aligned}\mu_{qs}(\Delta\omega) &= \frac{1}{2\pi E_0} \int_{-\infty}^{\infty} I_{qs}(\bar{t}) e^{i\Delta\omega\bar{t}} d\bar{t} \\ \gamma_{qs}(\Delta t) &= \frac{1}{E_0} \int_0^{\infty} S_{qs}(\bar{\omega}) e^{-i\Delta t\bar{\omega}} d\bar{\omega}.\end{aligned}\quad (4.13)$$

The coherent part of the CSD is linked with the first order coherence function of Eq. 4.8 [157]:

$$\mu_{cs}(\omega_1, \omega_2) = \sqrt{|g_{12}^{(1)}(\omega_1)| |g_{12}^{(1)}(\omega_2)|}.\quad (4.14)$$

Similarly the coherent part of the MCF may be associated with $|g_{12}^{(1)}(t)|$, which can be determined approximately by measuring the average spectrogram by XFROG and applying a spectral filter corresponding to the spectral coherence function. This procedure is illustrated in Fig. 4.4.

One can then obtain $I_{cs}(t)$ and $I_{qs}(t)$ by integrating the corresponding spectrograms over the frequency axis i.e. calculating the temporal margin when the reference pulse used for XFROG is short enough (see discussion of section 2.3). $S_{cs}(\omega)$ on the other hand can be obtained by a direct multiplication of the measured average spectrum by an optical spectrum analyzer with $|g_{12}^{(1)}(\omega)|$ and $S_{qs}(\omega)$ follows by subtracting the coherent contribution from the average spectrum. The CSD and MCF can therefore be determined by measuring (i) the spectrum and spectral interference in a delayed Michelson interferometer and (ii) the XFROG spectrogram using a short gate pulse. However, it is important to note that such XFROG filtering procedure in the spectral domain only provides an approximate measure of the coherent and quasi-stationary contributions. Indeed, if two pulses with varying degrees of coherence (one coherent and one incoherent) would have the same center frequency but occur at different times, the spectral coherence function would only measure the weighted average of coherence for these two. It would not be able reveal the true nature of the other pulse being coherent and other incoherent and this is why the filtering procedure is only approximate. An improved approach is proposed at the end of this chapter.

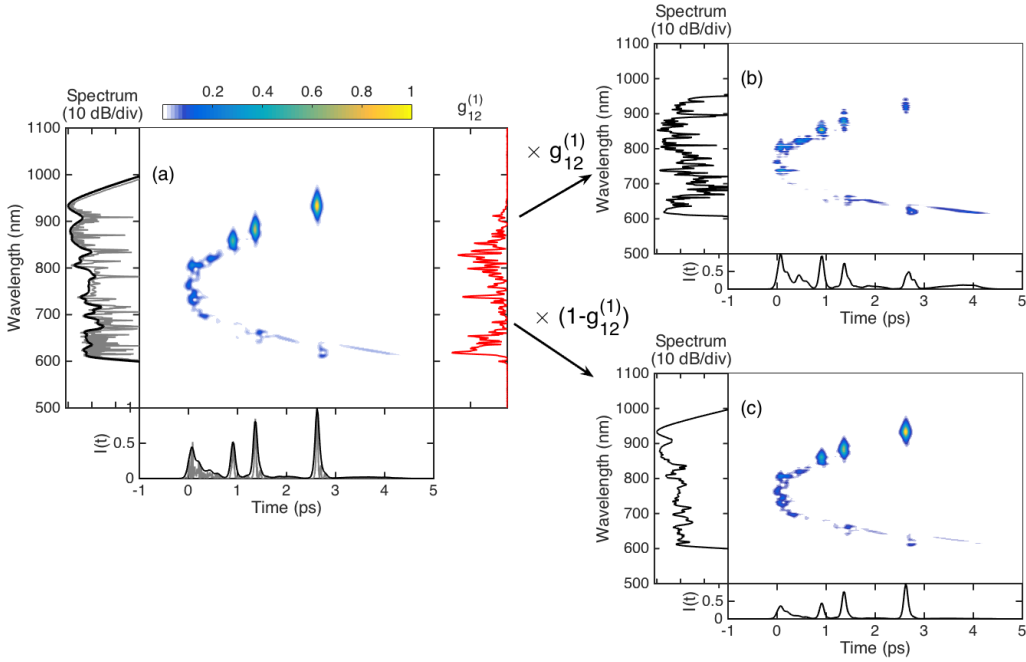


Figure 4.4: Filtering of the XFROG spectrogram with the coherence function. (a) Simulation of a partially coherent SC spectrogram with an XFROG gate pulse of 80 fs duration. The margins compare the actual spectral and temporal profiles (gray) to the XFROG margins (black), showing the convolution effect discussed before. (b) Coherent contribution of the spectrogram after filtering (multiplication) with the first order coherence function (shown in red). (c) Incoherent contribution of the spectrogram obtained by multiplying with $(1-g_{12}^{(1)})$.

4.3 Experimental results

The results presented in this section are reported in Publication III. Experiments were performed using a Ti:Sapphire laser at 785 nm producing nearly transform limited pulses with 72 fs duration (FWHM), characterized by a second harmonic generation FROG setup. These pulses were used as the reference pulse for the XFROG measurement. Part of the beam was extracted with a beamsplitter and injected into 69 cm of PCF fiber (NL-PM-750, Fig. 2.1). Before injection, the beam passed through a half-wave plate and polarizer combination to control the input pulse peak power and an optical isolator to avoid back reflections from the coupling lens. This broadened the input pulse further to 290 fs duration (characterized also by FROG).

The experimental setup is illustrated in figure 4.5. The generated SC at the fiber output was collimated with a microscope objective and guided either into a delayed Michelson interferometer or the XFROG setup using a flip mirror. The XFROG setup used a 1 mm thick beta-barium borate crystal rapidly dithered by a galvanometer in order to allow for efficient SFG phase-matching across the full SC bandwidth [159, 160].

As explained in section 2.6, the dynamics of SC generation in the short pulse & anomalous dispersion regimes are dominated by soliton effects. By controlling the input power/soliton order, we can vary the balance between soliton fission and MI during the initial stage of propagation in the fiber. As the first leads to fully deterministic and coherent dynamics

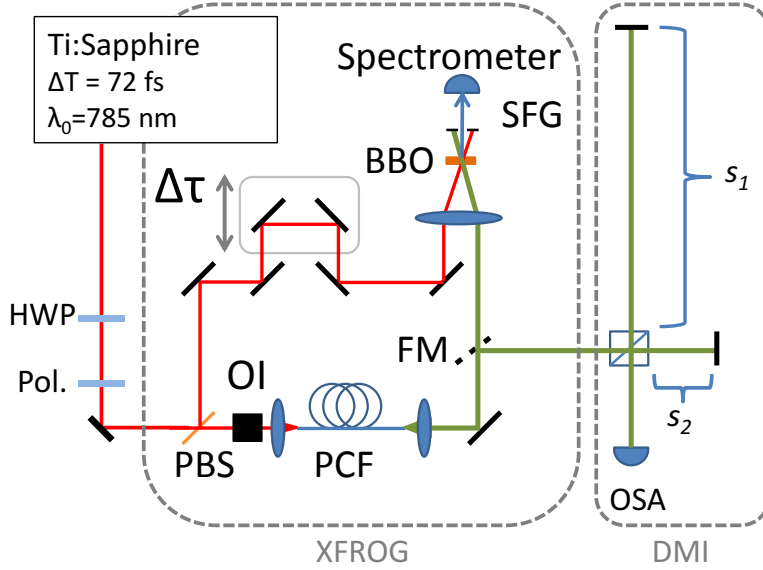


Figure 4.5: Experimental setup. PBS = pellicle beam splitter, HWP = half wave palte, Pol. = polarizer, OI = optical isolator, FM = flip mirror, BBO = beta barium borate, SFG = sum frequency generation, OSA = optical spectrum analyzer, PCF = photonic crystal fiber, DMI = delayed Michelson interferometer.

and the latter to fully random and incoherent dynamics, we can tune the coherence properties of the resulting SC simply by controlling the injected power. Measurement of the second-order coherence properties of SC light were performed for three cases from highly stable and coherent SC, to partially coherent and fully incoherent SC. The input peak powers and soliton orders corresponding to each of these cases are tabulated in table 4.1.

Table 4.1: Parameters for generating SC with varying coherence properties.

	Coherent	Partially coherent	Incoherent
P_p	70 W	360 W	820 W
N	6	15	23

The experimentally measured spectra and first order spectral functions are compared with those from numerical simulations of the GNLSE in Fig. 4.6.

We can see how the overall coherence drops when increasing the injected peak power with residual coherence only near the pump wavelength at the highest peak power. The coherence degradation can also be qualitatively observed in the average SC spectrum where the significant pulse-to-pulse fluctuations average out the fine structure in the spectrum. The dynamics of SC generation in the anomalous dispersion regime can be described in terms of soliton fission due to the higher order dispersion, dispersive wave generation and RSFS. In the case of relatively low peak power, the ejected solitons are shifted in the spectrum via the RSFS to the same wavelength from pulse to pulse and the average spectrum has thus a distinct fine structure. With increased soliton order/peak

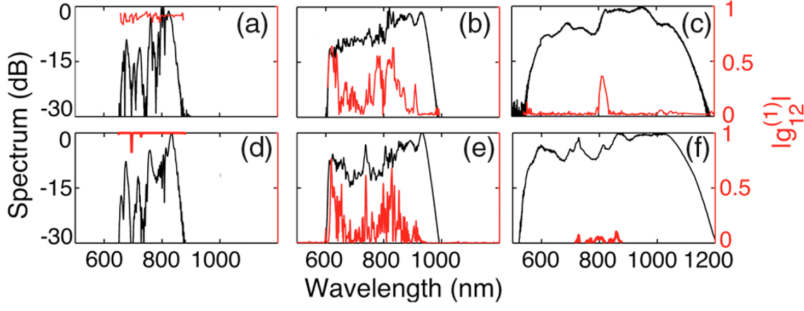


Figure 4.6: Top: Experimental spectra and first order coherence functions for (a) coherent, (b) partially coherent and (c) incoherent SC. Bottom: Corresponding simulated results.

power, noise amplification through MI perturbs the soliton fission process resulting in significant shot-to-shot fluctuations for the redshifting solitons and their corresponding dispersive waves. This is observed as a decreased fine structure (on the order of few nanometers) in the pulse spectrum for the partially coherent case, and the absence of any structure for the incoherent case.

The measured XFROG spectrograms for the three cases are shown in Fig. 4.7. We note that for the incoherent case when the bandwidth is largest, the angle dithering of the nonlinear crystal in the XFROG measurement is not sufficient to allow for phase-matching wavelengths above 1000 nm such that the agreement with the spectrum measured by the optical spectrum analyzer degrades for these wavelengths. The CSD and MCF were then reconstructed using the procedure described above. Comparison with numerical simulations for each of the three coherent, partially coherent, and incoherent cases is shown in Figs. 4.8 and 4.9.

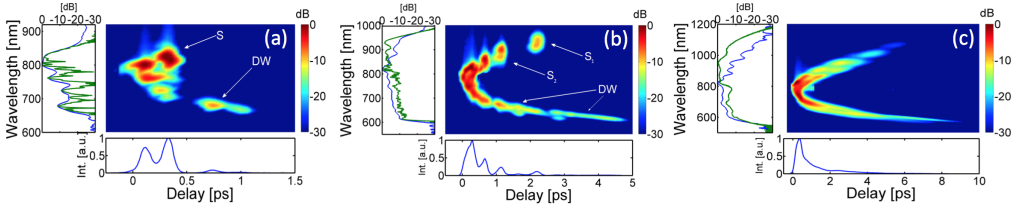


Figure 4.7: Experimentally measured spectrograms for the coherent (a), partially coherent (b) and incoherent (c) cases. We also show the integrated spectral and temporal margins. The spectral margins are compared with OSA average spectrum showing a good agreement. The S and DW correspond to solitons and their corresponding dispersive waves emitted during the soliton fission procedure.

We observe generally good agreement between the numerically simulated and experimental results. The overall coherence value in the coherent case is slightly less than 1 due to technical noise reducing the visibility of the interferometer fringes. The CSD functions agree generally very well for all cases and we observe how it reduces to the qs-line in the incoherent case, as shown in previous numerical studies. For the MCF we also see a good qualitative agreement with theory and simulations. The detail and contrast in the structure for the partially coherent case in Fig. 4.9 is lower than for the simulations. This is due to the fact that the retrieval of the coherent part of the MCF involves more

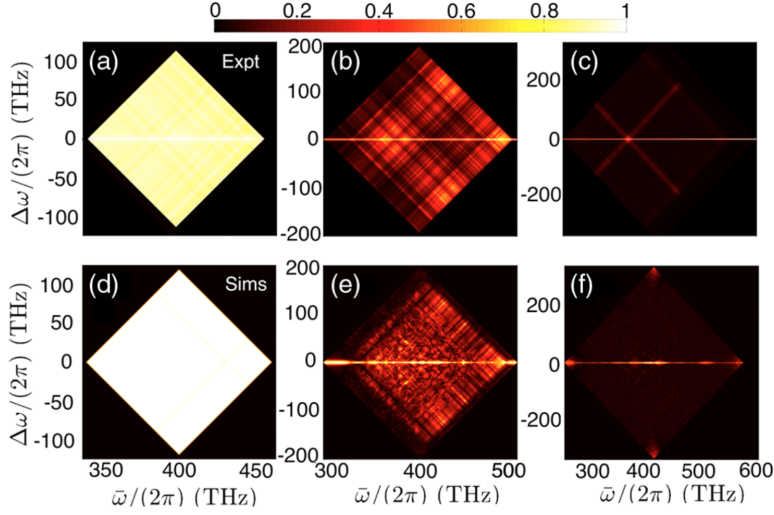


Figure 4.8: Experimentally measured CSD functions (top) for the three cases with varying coherence properties. Bottom shows the associated simulated CSD functions.

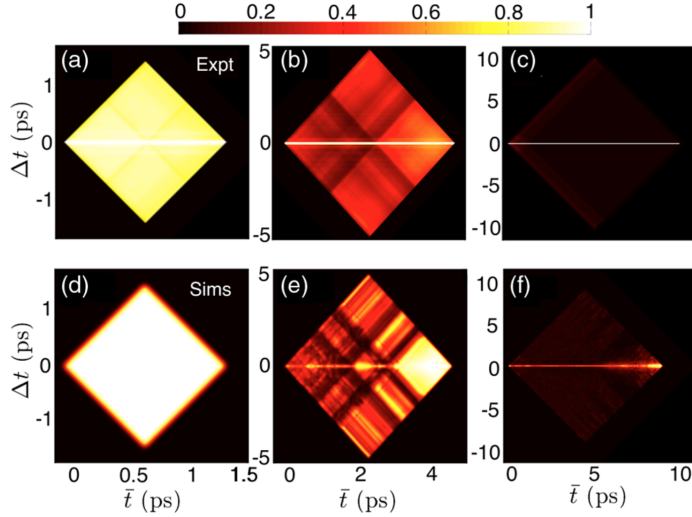


Figure 4.9: Experimentally measured MCF functions (top) for the three cases with varying coherence properties. Bottom shows the associated simulated MCF functions.

approximation due to the filtering procedure of the XFROG spectrogram as discussed above. Nevertheless, we can still see how the MCF also reduces to only the qs-contribution allowing to determine the coherence time from the width of the qs-part. The value of $\tau_c=3$ fs is comparable with that of sunlight, demonstrating how the SC in this regime of operation can be considered as a pulsed thermal source from the temporal coherence viewpoint yet with high spatial coherence.

4.4 Measuring the complex mean field

We devote the next section of this chapter to discussing a new possibility of determining the first order coherence function in time $g_{12}^{(1)}(t)$ for a more accurate measurement of the MCF, without the filtering procedure for the XFROG spectrogram described in the previous section. The proposed method also allows for measuring the spectrogram of the mean complex field which could be useful in other studies, where coherent contributions to the average measurements on ultrafast timescales would need to be recovered. The XFROG spectrogram of an electric field $E(t)$ is given by:

$$\begin{aligned} X(\tau, \omega) &= \left| \int_{-\infty}^{\infty} E(t)p(t+\tau)e^{-i\omega t} dt \right|^2 \\ &= |E(\tau, \omega)|^2 \end{aligned} \quad (4.15)$$

where τ represents the delay of the probe (or gate) pulse $p(t+\tau)$. The short notation $\int_{-\infty}^{\infty} E(t)p(t+\tau)e^{-i\omega t} dt = E(\tau, \omega)$ is referred to as the complex valued field spectrogram in what follows. The absolute value squared comes from the fact that we are measuring the spectrum. In practice one scans the discrete delay steps τ_i by a motorized stage and the spectrum is measured at each delay. Since the spectral measurement is done by a spectrometer integrating over milliseconds, one in fact measures the spectrum of many consecutive pulses at a given delay (assuming the gate pulse does not fluctuate). In other words, one measures the ensemble average of XFROG spectrograms *intensities*:

$$\begin{aligned} X_{ave}(\tau, \omega) &= \sum_{i=1}^N \left| \int_{-\infty}^{\infty} E_i(t)p(t+\tau)e^{-i\omega t} dt \right|^2 \\ &= \sum_{i=1}^N |E_i(\tau, \omega)|^2 = N \langle |E(\tau, \omega)|^2 \rangle. \end{aligned} \quad (4.16)$$

In the case of a perfectly coherent pulse train, Eqs. 4.15 and 4.16 are identical (averaging makes no difference). Clearly, for an unstable pulse train the measured spectrogram differs from that of individual pulses. Note also that in the latter case a phase retrieval algorithm will generally not converge as the measured average field does not actually correspond to a single physical electric field. Additional information may be obtained by combining two distinct XFROG measurements:

1. A standard average XFROG measurement $X_{ave}(\tau, \omega)$
2. An interference XFROG (IXFROG) measurement of two consecutive pulses with E-fields $E_i(t)$ and $E_{i+1}(t)$ that are superimposed in a delayed Michelson interferometer, and where one measures the average spectrogram given by: $X_{IX}(\tau, \omega) = N \langle \left| \int_{-\infty}^{\infty} [E_i(t) + E_{i+1}(t)]p(t+\tau)e^{-i\omega t} dt \right|^2 \rangle$.

The idea behind the IXFROG measurement can be described as follows. The coherent (shot-to-shot stable) temporal components of the complex pulse train will constructively interfere for all pairs $E_i(t) + E_{i+1}(t)$ resulting in an increased average field value at the output of interferometer. The incoherent (unstable) components on the other hand will

interfere destructively resulting in a decreased average field value. This means that the IXFROG spectrogram will then have comparatively higher intensities than the normal averaging spectrogram at the coherent components and lower intensities at the incoherent regions. By measuring comparing a standard XFROG measurement with the IXFROG one can then extract approximately the first order coherence functions both in the time domain $g_{12}(t)$ and in the frequency domain $g_{12}(\omega)$ as shown below.

From an experimental viewpoint both XFROG and IXFROG measurements can be performed using only a small modification of the setup in 4.5. One only needs to guide the output of the delayed Michelson interferometer measurement to the XFROG setup and perform two measurements: one with both interferometer arms open corresponding to the IXFROG and a second measurement by blocking the other interferometer arm to perform a standard XFROG measurement. Note that it is very important for the relative delay to be adjusted with micrometer precision in order for consecutive pulses to perfectly overlap temporally (simulations indicate a precision of 2 fs required).

Before giving more details on how to extract the coherence functions, it is instructive to rewrite the expression for the IXFROG spectrogram in a different form:

$$\begin{aligned} X_{IX}(\tau, \omega) &= \sum_{i=1}^N \left| \int_{-\infty}^{\infty} [E_i(t) + E_{i+1}(t)] p(t + \tau) e^{-i\omega t} dt \right|^2 \\ &= \sum_{i=1}^N \left| \int_{-\infty}^{\infty} E_i(t) p(t + \tau) e^{-i\omega t} dt \right. \\ &\quad \left. + \int_{-\infty}^{\infty} E_{i+1}(t) p(t + \tau) e^{-i\omega t} dt \right|^2 \end{aligned} \quad (4.17)$$

$$= \sum_{i=1}^N |E_i(\tau, \omega) + E_{i+1}(\tau, \omega)|^2 \quad (4.18)$$

$$\begin{aligned} &= \sum_{i=1}^N |E_i(\tau, \omega)|^2 + \sum_{i=1}^N |E_{i+1}(\tau, \omega)|^2 \\ &\quad + \sum_{i=1}^N [E_i(\tau, \omega) E_{i+1}^*(\tau, \omega) + E_i^*(\tau, \omega) E_{i+1}(\tau, \omega)]. \end{aligned} \quad (4.19)$$

Here, * denotes the complex conjugate. The first two sums of 4.18 correspond to the average spectrogram $X_{ave}(\tau, \omega)$ of Eq. 4.15 and the last term can be rewritten as:

$$\begin{aligned} &\sum_{i=1}^N [E_i(\tau, \omega) E_{i+1}^*(\tau, \omega) + E_i^*(\tau, \omega) E_{i+1}(\tau, \omega)] \\ &= \sum_{i \neq j}^N E_i(\tau, \omega) E_j^*(\tau, \omega) - \sum_{i \neq j, i \neq j \pm 1}^N E_i(\tau, \omega) E_j^*(\tau, \omega). \end{aligned} \quad (4.20)$$

Because realizations i and j are independent of each other, the two sums in Eq. 4.20 will be similar to each other as N grows large. The main difference is that the first sum has

$N^2 - N$ elements, whereas the second sum has $N^2 - 3N$ elements, which affects their overall amplitudes. One can then approximate Eq. 4.20 by

$$\begin{aligned}
 & \sum_{i \neq j}^N E_i(\tau, \omega) E_j^*(\tau, \omega) - \sum_{i \neq j, i \neq j \pm 1}^N E_i(\tau, \omega) E_j^*(\tau, \omega) \\
 & \approx \frac{N^2 - N - (N^2 - 3N)}{N^2 - N} \sum_{i \neq j}^N E_i(\tau, \omega) E_j^*(\tau, \omega) \\
 & = \frac{2}{N-1} \sum_{i \neq j}^N E_i(\tau, \omega) E_j^*(\tau, \omega). \tag{4.21}
 \end{aligned}$$

Using the binomial theorem, we get

$$\sum_{i \neq j}^N E_i(\tau, \omega) E_j^*(\tau, \omega) = \left| \sum_{i=1}^N E_i(\tau, \omega) \right|^2 - \sum_{i=1}^N |E_i(\tau, \omega)|^2 \tag{4.22}$$

and inserting Eqs. 4.21 and 4.22 into Eq. 4.19, one finally obtains

$$\begin{aligned}
 X_{IX}(\tau, \omega) &= 2X_{ave}(\tau, \omega) + \frac{2}{N-1} \left[\left| \sum_{i=1}^N E_i(\tau, \omega) \right|^2 - \sum_{i=1}^N |E_i(\tau, \omega)|^2 \right] \\
 &= 2N \langle |E_i(\tau, \omega)|^2 \rangle + \frac{2}{N-1} N^2 \langle |E_i(\tau, \omega)|^2 \rangle - \frac{2}{N-1} N \langle |E_i(\tau, \omega)|^2 \rangle \\
 &\approx 2N \langle |E_i(\tau, \omega)|^2 \rangle + 2N \langle |E_i(\tau, \omega)|^2 \rangle, \tag{4.23}
 \end{aligned}$$

where the last approximation holds for large N . The first term is the standard average spectrogram XFROG and the second term is the spectrogram of the *average complex field* $X_{mean}(\tau, \omega) = \left| \sum_{i=1}^N E_i(\tau, \omega) \right|^2 = \langle |NE(\tau, \omega)|^2 \rangle$ which contains the contributions of the coherent components of the field and can be obtained by subtraction of the two measured XFROG and IXFROG spectrograms

$$X_{mean}(\tau, \omega) \approx \frac{1}{2} X_{IX}(\tau, \omega) - X_{ave}(\tau, \omega). \tag{4.24}$$

We next apply the procedure described above to $N = 500$ numerically simulated realizations corresponding to the partially coherent case of section 4.3. Figure 4.10 (a) and (b) show the simulated XFROG and IXFROG spectrograms, respectively, and Fig. 4.10 (c) shows the result of their subtraction according to Eq. 4.24. One can clearly see the striking resemblance with the spectrogram of the mean field $X_{mean}(\tau, \omega)$ in Fig. 4.10 (d).

We next discuss how the first order coherence functions can be retrieved from the mean field spectrogram $X_{mean}(\tau, \omega)$. As discussed above, the first order functions can be written as Eq. 4.11 (to obtain the temporal function, just change the variable from ω to t). In order to obtain the mean electric field in the temporal domain, one should recall that the temporal margin of the spectrogram

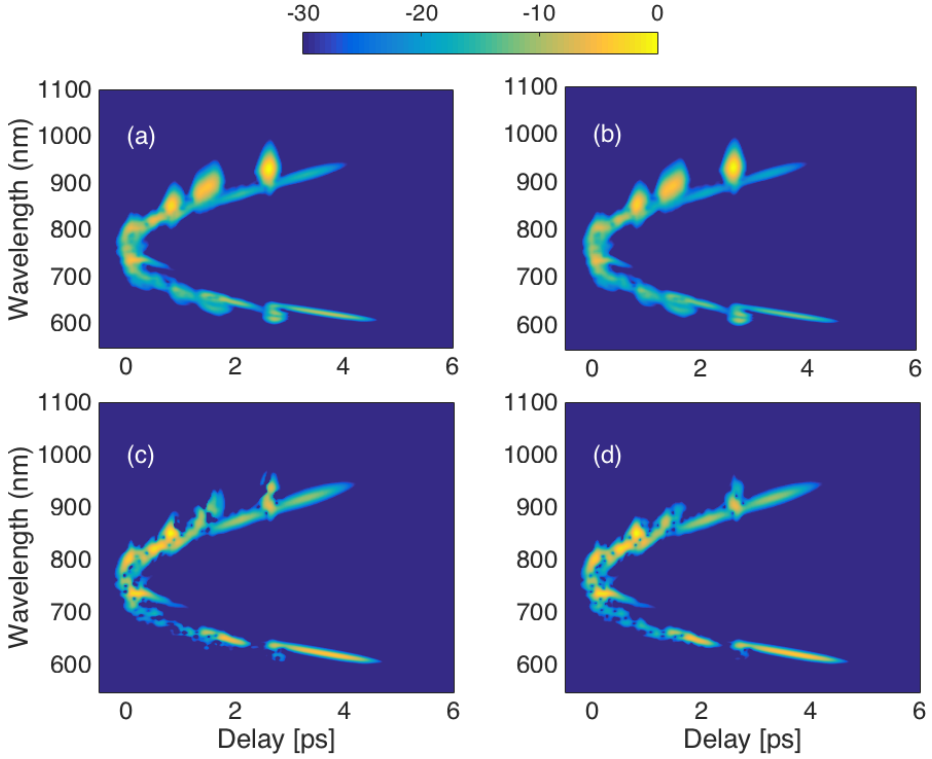


Figure 4.10: Numerically simulated spectrograms for the partially coherent SC of Figure 4.6 (b). (a) Interference XFROG (measurement 2) $X_{IX}(\tau, \omega)$, (b) Normal averaging intensity XFROG (measurement 1) $X_{ave}(\tau, \omega)$, (c) Difference of a and b, (d) mean field spectrogram $X_{mean}(\tau, \omega)$. The gate pulse has an 80 fs duration with 9 THz bandwidth at 785 nm. The color scale is in decibels.

$$I^{(M)}(\tau) = \int_{-\infty}^{\infty} X(\tau, \omega) d\omega. \quad (4.25)$$

is approximately equal to the temporal intensity of the unknown pulse $I(t) = |E(t)|^2$ if the gate pulse $p(t)$ used in experiments is sufficiently short. Thus, integrating over the frequency axis of the mean field spectrogram one obtains directly the intensity of the mean electric field in time $|E(t)|^2$. On the other hand, integrating over the frequency axis of the standard XFROG spectrogram one obtains the mean intensity of the pulse, and $g_{12}^{(1)}(t)$ is then the ratio of the two $|E(t)|^2/|E(t)|^2$.

One can apply the same approach in the spectral domain if the gate pulse bandwidth is narrower than the measured pulse bandwidth. Integrating over the temporal axis allows for obtaining the frequency margin of the mean field spectrogram and standard spectrogram, and the coherence function $g_{12}^{(1)}(\omega)$ can be retrieved.

Figure 4.11 compares the first order coherence functions in temporal and spectral domains from simulations calculated according to equation 4.11 (red lines) with the coherence functions calculated from the margins as explained above (blue lines).

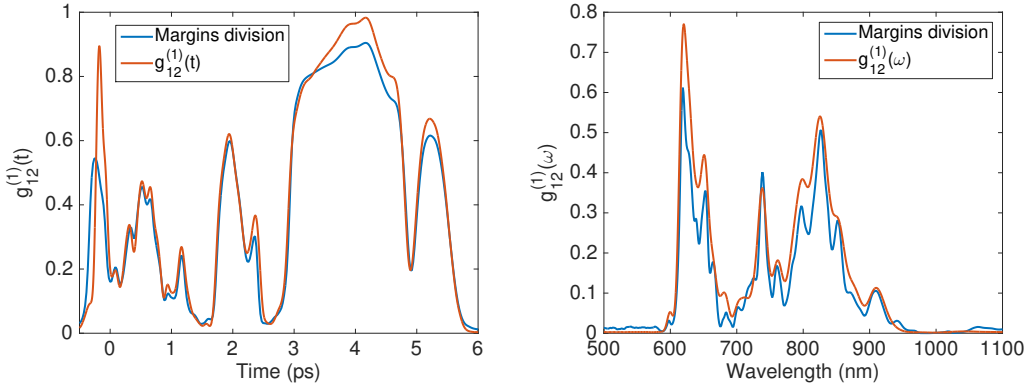


Figure 4.11: First order coherence functions in time (left) and spectral (right) domains in red. The exact functions from simulations are convolved with the gate pulse parameters ($P(\omega) = FT[p(t)]$) in the relevant domain. Blue curves show the coherence functions derived from the XFROG and IXFROG simulations.

We can observe extremely good agreement with the two, even though some residual discrepancies do exist due to the approximations in the derivation. This good agreement also holds promises for possible phase retrieval of the complex mean field that would allow for determination of the MCF and CSD complex parts. Because the method is general, it could be used in any ultrafast optical setup where the mean complex field characteristics may be required [80].

4.5 Conclusions

This chapter has presented an overview on the vast terminology and definitions of optical coherence theory. The connection between the theoretical second order coherence functions defined by Mandel & Wolf and the experimentally available first order coherence function for non-stationary sources (Eq. 4.8) was discussed. This connection was verified by the experiments presented in this chapter that presented the first measurements of the second order coherence functions for supercontinuum light sources. The results demonstrate how a supercontinuum can be considered a stable laser-like source or a nearly thermal light source depending on the experimental parameters, or it can operate in an intermediate stage where the coherent and thermal properties can be separated by the method.

The described method does have some uncertainty due to the filtering procedure used to retrieve the results. In order to improve the accuracy of the results, a new method was proposed based on two separate averaging XFROG measurements. Numerical results show an excellent agreement with the exact coherence functions and hold promise for improving these results even further and the possibility for applying it on any non-stationary source.

5 All-optical signal regeneration by supercontinuum generation

All-optical signal processing has been envisaged to be one of the key technologies to overcome the “capacity crunch” of ever-growing bandwidth needs for telecommunications [161]. This is because, in principle, all-optical signal processing does not require optical to electrical to optical conversion steps which are limited by the processing speed of the electronics. Various all-optical signal processing functionalities have already been demonstrated including e.g. optical delay lines and finite impulse filters [162, 163], optical time division multiplexing [164] and optical signal regeneration [165–167].

Signal regeneration is an important functionality where the original signal, that has been significantly impaired by noise or attenuation, is restored. Typically regeneration consists of three processes: (i) re-amplifying, (ii) reshaping and (iii) re-timing. A system that’s capable of doing all the functionalities is referred to as a 3R regenerator [161]. The difference of a 3R system to amplification only is illustrated in figure 5.1. Signal regeneration is thus directly linked to optical amplification and is important not only from the viewpoint of communications but also in sensing applications where weak amplitude signals for example in pump-probe spectroscopy experiments may be enhanced. Traditionally regeneration is performed electronically by first detecting the impaired signal and then re-transmitting it as an optical signal. Obviously the possibility of removing the electronic conversion step could increase the transmission speed of the system.

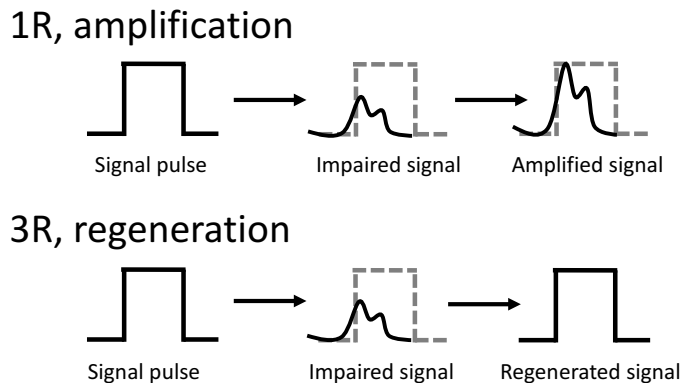


Figure 5.1: Difference of amplification only to full signal regeneration. The impaired signal is attenuated, distorted by noise and lags in time with respect to the original signal. A full 3R regeneration restores all of these properties, whereas an amplification only corrects for the attenuation.

Besides direct optical amplification by erbium-doped fiber amplifiers, signal regeneration may be achieved by taking advantage of the sensitivity of nonlinear systems to input fluctuations. The perfect example of such nonlinear system is an optical fiber where the weak amplitude fluctuations of an impaired signal can be enhanced as a result of the various nonlinear effects described in Chapter 2 of this thesis such as SPM [168] or Raman self-frequency shift [169]. Reported amplification factors using this approach could reach up to 20-fold, with a good reliability as these nonlinear processes are deterministic. Note, that these systems may not be full 3R regenerators, but often provide only amplitude and re-shaping functionalities without the capability of re-timing the signal all optically.

In Publication IV a technique capable of amplifying and re-shaping a weakly modulated signal by as much as 60 dB using the combination of all of the nonlinear processes contributing to SC generation is reported. This chapter starts by discussing the proof-of-principle measurements made by using few cycle pulses for coherent SC generation in Publication IV. The largest amplification factors are shown to occur in the short wavelengths region of the SC spectrum, as a result of soliton and dispersive wave dynamics. We also demonstrate the use of relaxed input pulse conditions using few hundred fs pump pulses in order to characterize the effect of the SC coherence on the quality of the regenerated signal, and in particular study in details how noise driven spontaneous MI can affect the signal regeneration fidelity.

5.1 Proof-of-principle measurements

A Ti:Sapphire laser producing 8 fs pulses at 790 nm with 76 MHz repetition was used for the experiments. The pulse train was amplitude modulated with a quartz based acousto-optic modulator (AOM) driven with a 4.6 MHz square wave. The input modulation depth was set to -75 dBc, and was measured from a reflection of the input from a glass plate directed to a 1 GHz silicon photodetector, which was connected to an oscilloscope. The amplitude modulated pulse train was then coupled into a PCF (NL-PM-750 of Fig. 2.1) by an aspheric lens and collimated by a microscope objective at the output. The collimated output was guided into a self-made Czerny-Turner spectrograph with 17.5 cm focal distance and 600 lines/mm grating. An avalanche photodiode (APD) (Hamamatsu, S8550) was placed at the spectrograph output such that an individual pixel of the array corresponded to a 10 nm bandwidth spectral channel. Three channels of the APD array were measured simultaneously by 1 GHz real-time oscilloscope and the fourth channel was used for the input modulation measurement. The oscilloscope recorded the spectral intensity variations over 1 ms time windows in order to fully capture the modulation pattern. The time traces of the oscilloscope were further processed by using the higher radio frequency harmonics (up to 5th harmonic) of the detected signal to increase the signal to noise ratio (up to the APD speed limit of 400 MHz) and a Takeda-algorithm [170]. The average spectrum of the SC was also monitored continuously in order to check that the coupling efficiency into the fiber did not change during the measurement. A schematic illustration of the setup is shown in Fig. 5.2.

The results in Fig. 5.3 (a) shows the input pulse spectrum and the SC spectrum where the three selected spectral channels chosen for the proof-of-principle measurements are highlighted. We also show a section of the time series of the input and output channels obtained applying the Takeda-algorithm (b,d,f,h) along with the corresponding RF spectra (c,e,g,i).

We observe a 60.5 dB amplification of the initial weak modulation at the spectral

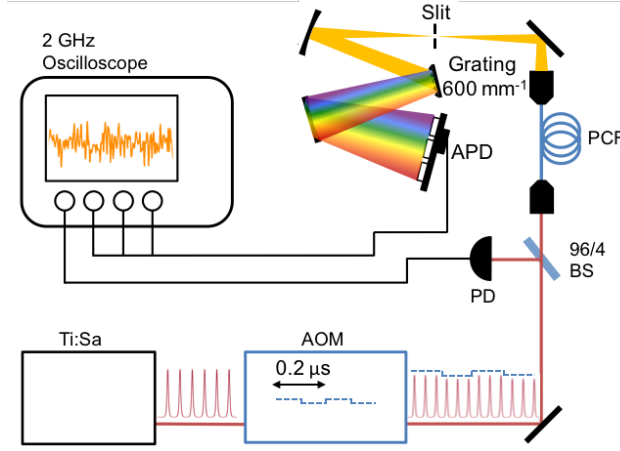


Figure 5.2: Schematic of the setup highlighting the key elements. Two different Ti:Sapphire lasers were used for the two sets of experiments presented here. Proof-of-principle measurements were made at $\lambda_0 = 790$ nm with 8 fs pulses and the coherence measurements with $\lambda_0 = 798$ nm with 190 fs pulse duration.

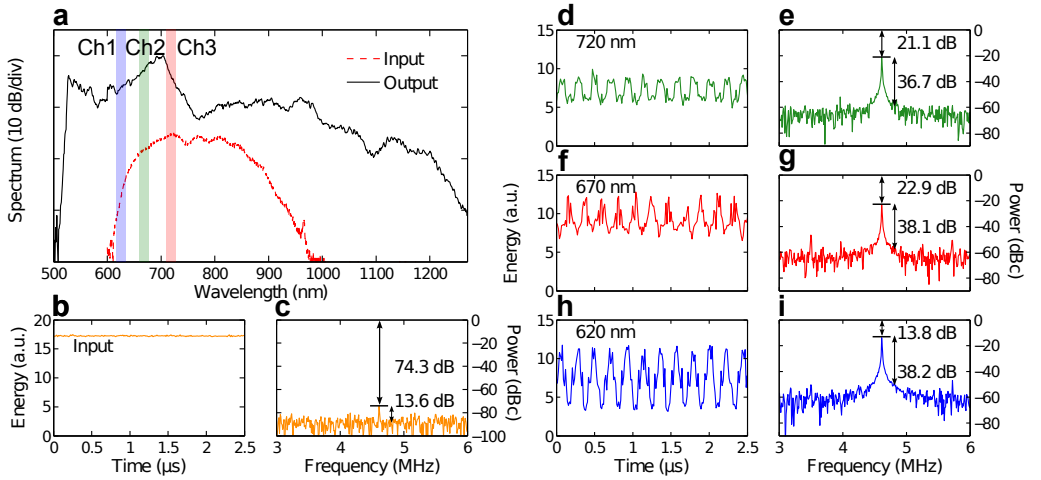


Figure 5.3: (a) Average spectrum of the input pulse and resulting SC. (b,c) Time series and RF spectrum of the input pulse train. (d,e) Time series and RF spectrum observed at 720 nm channel, (f,g) time series and RF spectrum observed at 670 nm channel, (h,i) time series and RF spectrum observed at 620 nm channel demonstrating 60 dB amplification.

channel centered at 620 nm wavelength. This particular spectral channel corresponds to the generation of a dispersive wave by solitons in the anomalous dispersion regime. Interestingly, we can also notice that the modulation pattern observed in different channels can be anti-correlated with each other (compare 670 nm and 620 nm), which allow for an increase in the signal regeneration capabilities (5 dB increase by using all of the three channels). One can also observe an increase in the noise floor at the spectral channels of lower amplitude associated with an increase in the shot noise level.

5.2 Physical mechanism of amplification

The physical mechanism of the weak modulation amplification can be understood from the coupling between solitons ejected from the fission process and subsequently generated dispersive waves. Specifically, in the anomalous dispersion regime, the dynamics of SC generation are triggered by higher-order soliton compression followed by fission into fundamental constituent solitons that will undergo RSFS and generate dispersive waves at the resonant wavelengths in the normal dispersion regime. Although the resonant energy transfer between the soliton and DW cease rapidly due to the loss of phase-matching, the high intensity soliton pulse can still locally modify the refractive index experienced by the DW via the Kerr effect trapping and causing additional blue-shift of the DW [171–173]. The amplitude modulation induces slight variations on the peak powers of the ejected solitons. The subsequent RSFS is very sensitive to these variations causing wavelength jitter of the soliton in the order of a few nanometers. As the DW generation process is highly dependent on the soliton parameters, this soliton wavelength jitter in turn translates into an even larger fluctuation of the DW wavelength and spectral energy [171], resulting in an effective amplification of the initial weak modulation applied at the fiber input. These dynamics are conveniently visualized in Fig. 5.4 (a) that shows a simulated spectrogram of the SC. In Fig. 5.4 (b), we show the spectrum of two solitons and their coupled DWs for two simulations for a 10 nm difference in the center wavelength of the solitons. This difference is roughly similar to the the jitter induced by the RSFS as a result of a change in input peak power corresponding to that between the minimum and maximum amplitude of the modulation in the experiments.

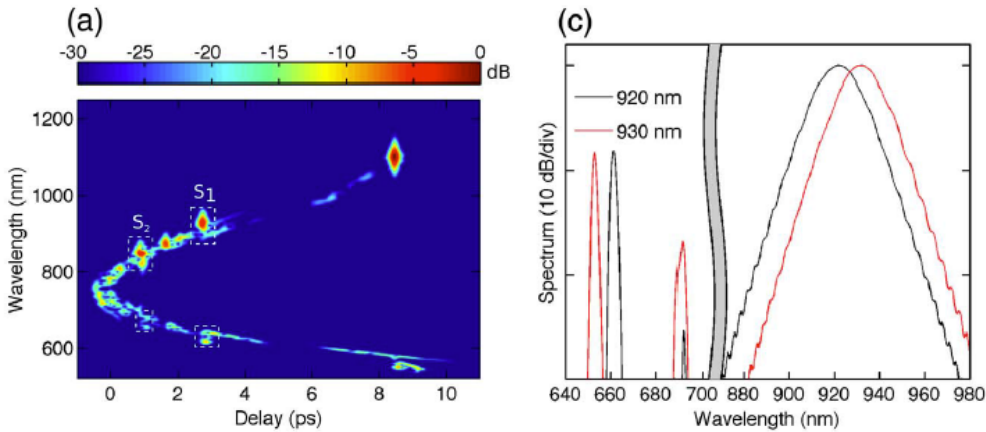


Figure 5.4: (a) Spectrogram of a single simulation of the SC generated with an 8 fs pulse. (b) Simulation of a soliton propagating at 920 nm and 930 nm and their corresponding dispersive waves that show dramatic change both in wavelength and energies as a result of the phase-matching sensitivity.

When a spectral channel corresponding approximately to the DW wavelength is selected by the spectrometer, one can observe a quasi on-off type modulation with very large amplitude. The robustness of this scheme obviously requires that the generated SC is coherent and the fluctuations in the resulting spectra are only caused by the amplitude modulation and not by fluctuations arising from noise driven effects such as MI.

5.3 Effect of supercontinuum coherence on signal amplification

In a second set of experiments, the input laser was changed to a Spectra Physics Tsunami operating at 798 nm with a pulse duration of 190 fs after the AOM that imposes the weak modulation with a 1.6 time-bandwidth product characterized by an SHG-FROG. With this setup, it is possible to adjust the peak power and therefore the input soliton order over a wide range of values resulting in SC with varying degrees of coherence similar to the cases in the chapter discussing SC coherence. In this way, one can tune the relative amount of stochastic spectral fluctuations caused by noise driven dynamics and study how much these affect the deterministic amplitude modulation amplification dynamics. The modulation speed of the AOM was set to 5 MHz and the modulation amplitude -60 dBc value. The SC coherence was measured with a separate delayed Michelson interferometer (see Chapter 4 on coherence). The measured amplification factors (blue bars) and coherence function (red line) are plotted together with the measured average spectrum in Fig. 5.5. The RF spectra and signal reconstruction of three particular channels highlighted in the spectrum by color bars are shown in Fig. 5.6 along with the input channel for reference. The amplification factor of the initial weak modulation amplitude is determined by subtracting the amplitude of the 5 MHz RF spectral peak of the spectral channel measured by the APD at the fiber output from the reference amplitude measured before the fiber.

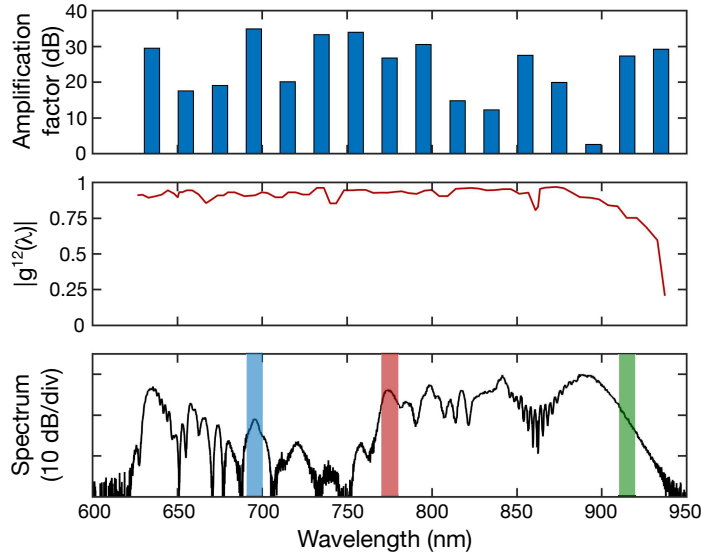


Figure 5.5: Coherent SC. **Up:** Coherence function (red) and amplification factors (blue), **Down:** Recorded SC spectrum with three spectral bins highlighted that are plotted in figure 5.6.

For lower input peak power, the coherence function shows a near unity value at all wavelengths indicating excellent phase-stability of the SC. In this case, we observe the largest amplification factor at the DW spectral location at around 695 nm, as described above from solitons-DW coupling dynamics. The reconstructed modulation pattern is also clearly visible in the temporal domain. Noise levels for this coherent SC case are very similar independently of the spectral channel selected, the spectral intensity levels and detection efficiency of the APD for a specific wavelength channel being the main contributors to the small fluctuations observed in the noise floor.

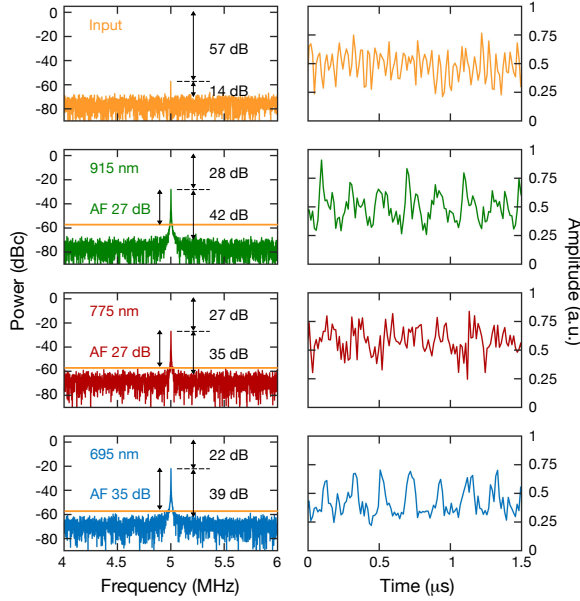


Figure 5.6: RF spectra and time domain reconstructions of the modulated signal for the coherent SC. The yellow line corresponds to the input pulse train while other colors correspond to the highlighted spectral bins in the spectrum.

When the input pulse peak power is increased a drop in the overall coherence is observed in agreement with previous studies on SC decoherence dynamics. Fine spectral features are smeared out in the average spectrum due to shot-to-shot fluctuations of the spectra caused by stochastic noise-seeded MI that competes with deterministic soliton dynamics.

Somewhat surprisingly, we measure amplification factor as large as 47 dB in the experiments (spectral channel at 640 nm) which is even larger than in the coherent case - again at the dispersive wave regime as shown in Fig. 5.8. The time domain reconstruction of the signal does not, however, show significantly more pronounced modulation than in the coherent case. This is due to the increased noise floor level that has jumped from around -66 dBc in the coherent case to -52 dBc. This drop in the signal to noise ratio can now be attributed to the dynamics of the SC generation itself rather than to the electrical detection noise. Spontaneous MI is causing random fluctuations in the output spectra that are observed as increased noise levels and reduce the efficiency of the signal regeneration method.

Finally the input peak power was increased such that the SC coherence function showed only residual coherence at around the pump residues and dispersive wave edge as shown in Fig. 5.9.

Measured amplification factors are similar to those in the coherent SC case, varying from 20 to 40 dB depending on the spectral channel. However, the noise floor is increased from the partially coherent case degrading so much the signal to noise ratio that the modulated signal is not clearly apparent in the time domain as shown in Fig. 5.10.

This increase in noise floor is attributed, similarly to the partially coherent case, to the increased influence of MI on the evolution dynamics causing unwanted jitter in the spectra. To further illustrate the effect of decoherence on the noise levels at different channels, we

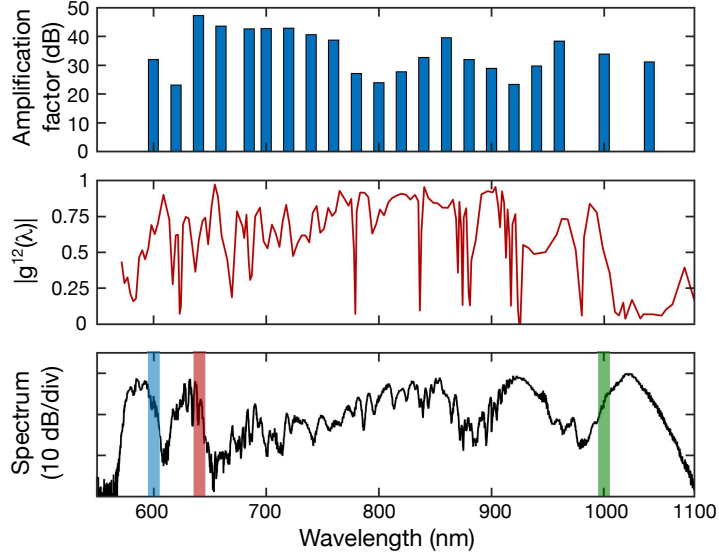


Figure 5.7: Partially coherent SC. **Up:** Coherence function (red) and amplification factors (blue), **Down:** Recorded SC spectrum with three spectral bins highlighted that are plotted in figure 5.8.

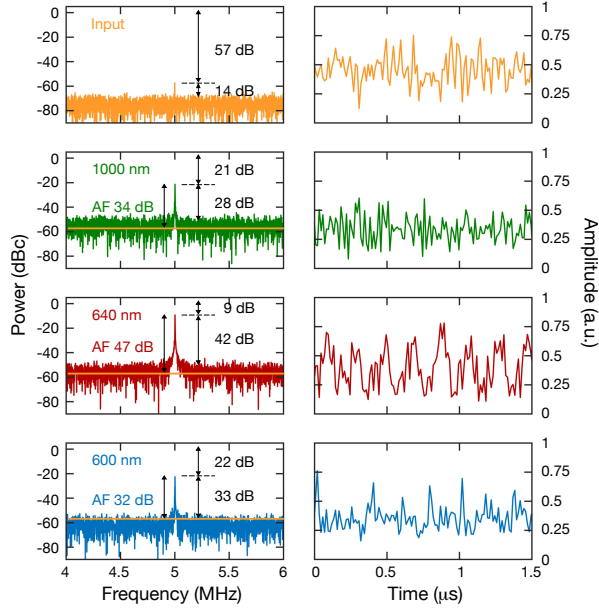


Figure 5.8: RF spectra and time domain reconstructions of the modulated signal for partially coherent SC. Yellow is the input pulse train and other colors correspond to the highlighted spectral bins in the spectrum

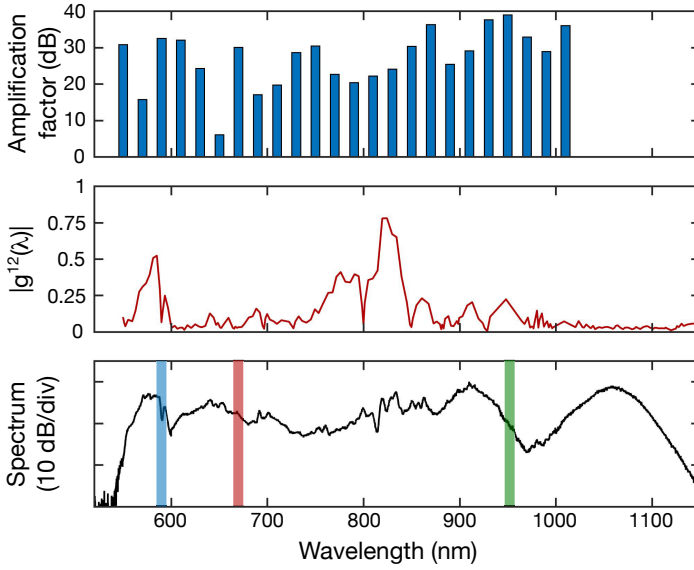


Figure 5.9: Incoherent SC. **Up:** Coherence function (red) and amplification factors (blue), **Down:** Recorded SC spectrum with three spectral bins highlighted that are plotted in figure 5.10. The amplification factors are plotted only until 1000 nm, where the APD response stops.

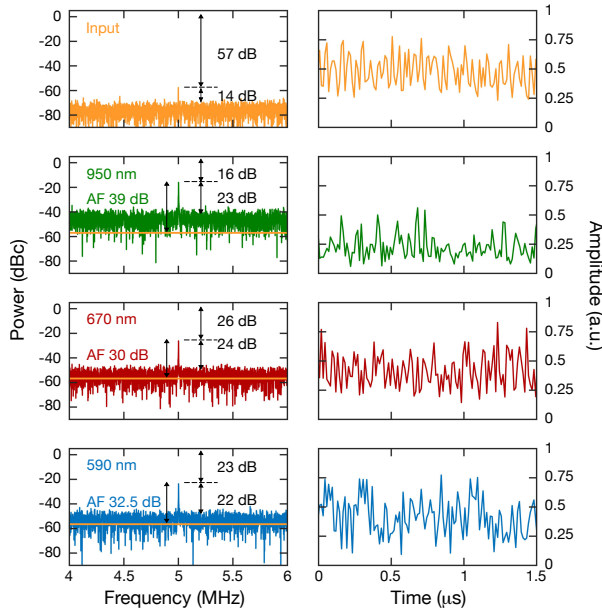


Figure 5.10: RF spectra and time domain reconstructions of the modulated signal for the incoherent SC. Yellow is the input pulse train and other colors correspond to the highlighted spectral bins in the spectrum

tabulate the measured highest, lowest and mean noise floors for all of the three cases in table 5.1.

Table 5.1: Measured noise floors for SC with varying coherence. The average is seen clearly to increase with the loss of coherence.

Case	Noise floor mean	Noise max	Noise min
Coherent	-71 dBc	-64 dBc	-83 dBc
Part. Coherent	-65 dBc	-57 dBc	-76 dBc
Incoherent	-57 dBc	-51 dBc	-73 dBc

There exists significant amounts of variance in the noise floors within any of the three cases due to the varying light levels and sensitivities as discussed above, but the trend observed in the average values is clear with decoherence being associated with significant increase in the noise floor and degrading the recovered modulation pattern.

5.4 Conclusions

An experimental method for amplifying and resolving weak amplitude modulations in a pulsed optical signal was demonstrated. The amplification mechanism was based on the sensitivity of supercontinuum generation process to input fluctuations. In particular, the numerical study shows that the soliton-dispersive wave coupling leads generally to the largest amplification values.

Additional experiments have also demonstrated that the need for few cycle pulses is not a necessary requirement for the proposed signal regeneration approach to work, as long as overall partial coherence of the SC can be maintained. The relaxed requirements on the pump source for signal amplification open up new venues for applications of the system in e.g. pump-probe systems requiring high sensitivity. Furthermore, advances in SC generation on chips with low powers could be used to decrease the peak powers required for applying the technique [174].

As a point of interest for possible future studies the reader's attention is drawn to the coherent case and the soliton peak at 900 nm, where one can recognize a very weak amplification of 3 dB. Although not shown in the current results, in some experiments negative amplification factors were observed in this wavelength range. A similar effect was observed also in the GNLSE simulations with modulated input power. This would correspond to a classical version of amplitude squeezing of the modulated signal [175] that could have applications for the opposite purpose of reducing experimental amplitude noise.

6 Summary and conclusions

Novel measurement methods on ultrafast timescales are paramount in allowing to form accurate pictures of the physics underlying ultrafast phenomena in Optics and Photonics. In this thesis, pre-existing and new techniques were modified or developed to measure with better precision and in real-time nonlinear dynamics that are susceptible to noise in optical fibers.

These measurements in the temporal domain have allowed us to confirm that the chaotic localized structures that emerge from noise in nonlinear Schrödinger equation governed systems can be well described by analytical breathers solutions. Measurements in the spectral domain on the other hand have revealed that temporal structures with high intensities are correlated with significant spectral broadening in the wings, providing an indirect approach for the characterization of extreme events. By combining real-time spectral and temporal measurements, we for the first time captured subtle dissipative soliton dynamics occurring during the transient period to mode-locking of an ultrafast laser. The fact that these allows for the full reconstruction of the complex electric field in real time permits further analysis of the underlying physics through the use of the nonlinear Fourier transform that yields the signature of fundamental nonlinear attractor states of the systems. Similar spectro-temporal real-time measurements performed on noise-induced modulation instability would also allow for retrieving the nonlinear phase of the electric field and computation of the nonlinear Fourier spectrum, that combined with state-of-the-art machine-learning algorithms could offer another possible pathway towards the prediction of extreme events.

We have also developed a new approach to characterize the coherence properties of broadband supercontinuum light sources. This is especially important because supercontinuum sources are finding an increasing number of applications for remote sensing and imaging, and the ability to determine accurately the fluctuations of the electric field arising from nonlinear amplification dynamics is thus needed. Moreover, the methodology introduced is actually not limited to the case of supercontinuum sources but can be applied to any non-stationary light source and could also be utilized to assess the correlations of the optical fields in pump-probe setup studying light-matter interactions.

Finally, we have exploited the extreme susceptibility of a nonlinear system in form of supercontinuum generation process to demonstrate a method for all-optical signal regeneration with sensitivity to the one part in million in fluctuations of the input field. This result illustrates the possibility of harnessing nonlinear system for practical applications - a feature that has been deemed non-practical for many decades. Furthermore, the rapidly evolving field of nonlinear Fourier transform and the measurement tools capable of capturing the chaotic fields have caused a widespread interest in academia and industry driving the progress towards for possible nonlinear communication systems.

All in all, with modern measurement techniques the properties of nonlinear systems can be finally understood better. This holds great promises for many practical applications in Optics and Photonics including telecommunications and laser design, but also for providing valuable knowledge to other domains of physics where nonlinear systems are governed by similar equations such as hydrodynamics, plasma physics and acoustics.

Bibliography

- [1] R. W. Boyd, ed., *Nonlinear Optics, 3rd Ed.* Academic Press, 2008.
- [2] G. P. Agrawal, *Nonlinear Fiber Optics*. Academic Press, 2013.
- [3] M. C. Cross and P. C. Hohenberg, “Pattern formation outside of equilibrium,” *Rev. Mod. Phys.*, vol. 65, pp. 851–1112, Jul 1993.
- [4] Y. S. Kivshar and M. Peyrard, “Modulational instabilities in discrete lattices,” *Phys. Rev. A*, vol. 46, pp. 3198–3205, Sep 1992.
- [5] R. Temam, ed., *Navier-Stokes Equations - Theory and Numerical Analysis*. AMS Chelsea Publishing, 2001.
- [6] M. Onorato, S. Residori, U. Bortolozzo, A. Montina, and F. T. Arecchi, “Rogue waves and their generating mechanisms in different physical contexts,” *Physics Reports*, vol. 528, no. 2, pp. 47–89, 2013.
- [7] K. E. Strecker, G. B. Partridge, A. G. Truscott, and R. G. Hulet, “Formation and propagation of matter-wave soliton trains,” *Nature*, vol. 417, pp. 150–153, 05 2002.
- [8] K. Tai, A. Hasegawa, and A. Tomita, “Observation of modulational instability in optical fibers,” *Physical Review Letters*, vol. 56, pp. 135–138, Jan 1986.
- [9] V. E. Zakharov and L. A. Ostrovsky, “Modulation instability: The beginning,” *Physica D: Nonlinear Phenomena*, vol. 238, pp. 540–548, 2009.
- [10] T. B. Benjamin and J. E. Feir, “The disintegration of wave trains on deep water. part i. theory,” *Journal of Fluid Mechanics*, vol. 27, pp. 417–430, 1967.
- [11] H. Bailung and Y. Nakamura, “Observation of modulational instability in a multi-component plasma with negative ions,” *Journal of Plasma Physics*, vol. 50, p. 231?242, Oct 1993.
- [12] T. Taniuti and H. Washimi, “Self-trapping and instability of hydromagnetic waves along the magnetic field in a cold plasma,” *Phys. Rev. Lett.*, vol. 21, pp. 209–212, Jul 1968.
- [13] W.-M. Liu, B. Wu, and Q. Niu, “Nonlinear effects in interference of bose-einstein condensates,” *Phys. Rev. Lett.*, vol. 84, pp. 2294–2297, Mar 2000.
- [14] V. M. Pérez-García, H. Michinel, and H. Herrero, “Bose-einstein solitons in highly asymmetric traps,” *Phys. Rev. A*, vol. 57, pp. 3837–3842, May 1998.

- [15] N. N. Akhmediev and V. Korneev, "Modulation instability and periodic solutions of the nonlinear schrodinger equation," *Theor. Math Phys. (USSR)*, vol. 69, pp. 1089–1093, 1986.
- [16] N. N. Akhmediev and V. I. Korneev, "Modulation instability and periodic solutions of the nonlinear Schrödinger equation," *Theoretical and Mathematical Physics*, vol. 69, no. 2, pp. 1089–1093, 1987.
- [17] C.-Y. Wang, P. L. Baldeck, Y. Budansky, and R. R. Alfano, "15-thz pulse generation arising from modulation instability oscillation in a colliding-pulse mode-locking dye laser," *Opt. Lett.*, vol. 14, pp. 497–499, May 1989.
- [18] A. Gouveia-Neto, M. Faldon, and J. Taylor, "Spectral and temporal study of the evolution from modulational instability to solitary wave," *Optics Communications*, vol. 69, no. 3, pp. 325 – 328, 1989.
- [19] J. M. Dudley, G. Genty, F. Dias, B. Kibler, and N. Akhmediev, "Modulation instability, Akhmediev breathers and continuous wave supercontinuum generation," *Optics Express*, vol. 17, pp. 21497–21508, Nov 2009.
- [20] K. Hammani, B. Wetzol, B. Kibler, J. Fatome, C. Finot, G. Millot, N. Akhmediev, and J. M. Dudley, "Spectral dynamics of modulation instability described using akhmediev breather theory," *Opt. Lett.*, vol. 36, pp. 2140–2142, Jun 2011.
- [21] S. Toenger, T. Godin, C. Billet, F. Dias, M. Erkintalo, G. Genty, and J. M. Dudley, "Emergent rogue wave structures and statistics in spontaneous modulation instability," *Scientific Reports*, vol. 5, p. 10380, 2015.
- [22] D. Solli, G. Herink, B. Jalali, and C. Ropers, "Fluctuations and correlations in modulation instability," *Nature Photonics*, vol. 6, no. 7, pp. 463–468, 2012.
- [23] R. Trebino, K. W. DeLong, D. N. Fittinghoff, J. N. Sweetser, M. A. Krumbügel, B. A. Richman, and D. J. Kane, "Measuring ultrashort laser pulses in the time-frequency domain using frequency-resolved optical gating," *Review of Scientific Instruments*, vol. 68, no. 9, pp. 3277–3295, 1997.
- [24] C. Iaconis and I. A. Walmsley, "Spectral phase interferometry for direct electric-field reconstruction of ultrashort optical pulses," *Opt. Lett.*, vol. 23, pp. 792–794, May 1998.
- [25] R. Salem, M. A. Foster, and A. L. Gaeta, "Application of space–time duality to ultrahigh-speed optical signal processing," *Adv. Opt. Photon.*, vol. 5, pp. 274–317, Sep 2013.
- [26] B. H. Kolner and M. Nazarathy, "Temporal imaging with a time lens," *Opt. Lett.*, vol. 14, pp. 630–632, Jun 1989.
- [27] Y. C. Tong, L. Y. Chan, and H. K. Tsang, "Fibre dispersion or pulse spectrum measurement using a sampling oscilloscope," *Electronics Letters*, vol. 33, pp. 983–985, May 1997.
- [28] P. V. Kelkar, F. Coppinger, A. S. Bhushan, and B. Jalali, "Time-domain optical sensing," *Electronics Letters*, vol. 35, pp. 1661–1662, Sep 1999.

- [29] K. Goda and B. Jalali, “Dispersive fourier transformation for fast continuous single-shot measurements,” *Nat Photon*, vol. 7, pp. 102–112, 02 2013.
- [30] R. R. Alfano and S. L. Shapiro, “Emission in the region 4000 to 7000 Å via four-photon coupling in glass,” *Phys. Rev. Lett.*, vol. 24, pp. 584–587, Mar 1970.
- [31] J. M. Dudley, G. Genty, and S. Coen, “Supercontinuum generation in photonic crystal fiber,” *Reviews of Modern Physics*, vol. 78, pp. 1135–1184, Oct 2006.
- [32] B. Zhou and M. Bache, “Invited article: Multiple-octave spanning high-energy mid-ir supercontinuum generation in bulk quadratic nonlinear crystals,” *APL Photonics*, vol. 1, no. 5, p. 050802, 2016.
- [33] T. Udem, R. Holzwarth, and T. W. Hansch, “Optical frequency metrology,” *Nature*, vol. 416, pp. 233–237, 03 2002.
- [34] M. T. Hassan, T. T. Luu, A. Moulet, O. Raskazovskaya, P. Zhokhov, M. Garg, N. Karpowicz, A. M. Zheltikov, V. Pervak, F. Krausz, and E. Goulielmakis, “Optical attosecond pulses and tracking the nonlinear response of bound electrons,” *Nature*, vol. 530, pp. 66–70, 02 2016.
- [35] L. Froehly and J. Météau, “Supercontinuum sources in optical coherence tomography: A state of the art and the application to scan-free time domain correlation techniques and depth dependant dispersion compensation,” *Optical Fiber Technology*, vol. 18, no. 5, pp. 411 – 419, 2012. Fiber Supercontinuum sources and their applications.
- [36] N. R. Newbury, “Searching for applications with a fine-tooth comb,” *Nat Photon*, vol. 5, pp. 186–188, 04 2011.
- [37] A. Ellis, J. Zhao, and D. Cotter, “Approaching the nonlinear shannon limit,” *Journal of Lightwave Technology*, vol. 28, pp. 423–433, 2010.
- [38] S. Birkholz, C. Brée, A. Demircan, and G. Steinmeyer, “Predictability of rogue events,” *Phys. Rev. Lett.*, vol. 114, p. 213901, May 2015.
- [39] N. Akhmediev, J. M. Soto-Crespo, A. Ankiewicz, and N. Devine, “Early detection of rogue waves in a chaotic wave field,” *Physics Letters A*, vol. 375, no. 33, pp. 2999 – 3001, 2011.
- [40] J. C. Maxwell, “A dynamical theory of the electromagnetic field,” *Phil. Trans. R. Soc. Lond.*, vol. 155, pp. 459–512, 01 1865.
- [41] P. S. Russell, “Photonic-crystal fibers,” *J. Lightwave Technol.*, vol. 24, pp. 4729–4749, Dec 2006.
- [42] L. G. Cohen, C. Lin, and W. G. French, “Tailoring zero chromatic dispersion into the 1.5-1.6 µm low-loss spectral region of single-mode fibres,” *Electronics Letters*, vol. 15, pp. 334–335, June 1979.
- [43] G. P. Agrawal, *Fiber-Optic Communication Systems*. John Wiley & Sons, 2002.
- [44] K. J. Blow and D. Wood, “Theoretical description of transient stimulated raman scattering in optical fibers,” *IEEE Journal of Quantum Electronics*, vol. 25, pp. 2665–2673, Dec 1989.

- [45] R. H. Stolen, J. P. Gordon, W. J. Tomlinson, and H. A. Haus, "Raman response function of silica-core fibers," *J. Opt. Soc. Am. B*, vol. 6, pp. 1159–1166, Jun 1989.
- [46] A. M. Weiner, J. P. Heritage, R. J. Hawkins, R. N. Thurston, E. M. Kirschner, D. E. Leaird, and W. J. Tomlinson, "Experimental observation of the fundamental dark soliton in optical fibers," *Phys. Rev. Lett.*, vol. 61, pp. 2445–2448, Nov 1988.
- [47] N. Akhmediev and M. Karlsson, "Cherenkov radiation emitted by solitons in optical fibers," *Phys. Rev. A*, vol. 51, pp. 2602–2607, Mar 1995.
- [48] V. Zakharov and A. Shabat, "Exact theory of two-dimensional self-focusing and one-dimensional self-modulation of waves in nonlinear media," *Journal of Experimental and Theoretical Physics*, vol. 34, pp. 62–69, 1972.
- [49] N. N. Akhmediev and A. Ankiewicz, *Solitons: Nonlinear Pulses and Beams*. Chapman & Hall, 1997.
- [50] M. J. Ablowitz and H. Segur, *Solitons and the inverse scattering transform*. Society for Industrial Mathematics, 1981.
- [51] J. Fermi, E. Pasta and S. Ulam, "Studies of nonlinear problems," *Los Alamos Scientific Laboratory report LA-1940*, vol. 6, 1 1955.
- [52] T. Dauxois, "Fermi, pasta, ulam, and a mysterious lady," *Physics Today*, vol. 6, 1 2008.
- [53] G. P. Agrawal, "Modulation instability induced by cross-phase modulation," *Phys. Rev. Lett.*, vol. 59, pp. 880–883, Aug 1987.
- [54] J. E. Rothenberg, "Modulational instability for normal dispersion," *Phys. Rev. A*, vol. 42, pp. 682–685, Jul 1990.
- [55] N. Akhmediev, A. Ankiewicz, J. Soto-Crespo, and J. Dudley, "Universal triangular spectra in parametrically-driven systems," *Physics Letters A*, vol. 375, no. 3, pp. 775 – 779, 2011.
- [56] D. Peregrine, "Water waves, nonlinear schrodinger equations and their solutions," *J. Aust. Math. Soc. B*, vol. 25, pp. 16–43, 1983.
- [57] Y. Ma, "Perturbed plane-wave solutions of the cubic schrodinger equation," *Stud. Appl. Math*, vol. 60, pp. 43–58, 1979.
- [58] B. Kibler, J. Fatome, C. Finot, G. Millot, F. Dias, G. Genty, N. Akhmediev, and J. M. Dudley, "The Peregrine soliton in nonlinear fibre optics," *Nature Physics*, vol. 6, no. 10, pp. 790–795, 2010.
- [59] B. Kibler, J. Fatome, C. Finot, G. Millot, G. Genty, B. Wetzal, N. Akhmediev, F. Dias, and J. M. Dudley, "Observation of Kuznetsov-Ma soliton dynamics in optical fibre," *Scientific Reports*, vol. 2, p. 463, June 2012.
- [60] B. Frisquet, B. Kibler, and G. Millot, "Collision of akhmediev breathers in nonlinear fiber optics," *Phys. Rev. X*, vol. 3, p. 041032, Dec 2013.
- [61] N. Akhmediev, J. M. Soto-Crespo, and A. Ankiewicz, "Extreme waves that appear from nowhere: on the nature of rogue waves," *Physics Letters A*, vol. 373, no. 25, pp. 2137–2145, 2009.

- [62] A. G. C. . Specialty, *Safety and Shipping Review 2014*. Allianz, 2014.
- [63] J. M. Dudley, F. Dias, M. Erkintalo, and G. Genty, “Instabilities, breathers and rogue waves in optics,” *Nature Photonics*, vol. 8, no. 10, pp. 755–764, 2014.
- [64] D. Solli, C. Ropers, P. Koonath, and B. Jalali, “Optical rogue waves,” *Nature*, vol. 450, no. 7172, pp. 1054–1057, 2007.
- [65] L. A. Lugiato and R. Lefever, “Spatial dissipative structures in passive optical systems,” *Phys. Rev. Lett.*, vol. 58, pp. 2209–2211, May 1987.
- [66] M. G. Kovalsky, A. A. Hnilo, and J. R. Tredicce, “Extreme events in the ti:sapphire laser,” *Opt. Lett.*, vol. 36, pp. 4449–4451, Nov 2011.
- [67] G. Huyet and J. R. Tredicce, “Spatio-temporal chaos in the transverse section of lasers,” *Physica D: Nonlinear Phenomena*, vol. 96, no. 1, pp. 209–214, 1996.
- [68] A. Mathis, L. Froehly, S. Toenger, F. Dias, G. Genty, and J. Dudley, “Caustics and rogue waves in an optical sea,” *Sci. Rep.*, vol. 5, no. 22, p. 12822, 2015.
- [69] F. T. Arecchi, G. Giacomelli, P. L. Ramazza, and S. Residori, “Experimental evidence of chaotic itinerancy and spatiotemporal chaos in optics,” *Phys. Rev. Lett.*, vol. 65, pp. 2531–2534, Nov 1990.
- [70] G. Z. Forristall, “On the statistical distribution of wave heights in a storm,” *Journal of Geophysical Research: Oceans*, vol. 83, no. C5, pp. 2353–2358, 1978.
- [71] R. R. Alfano, ed., *The Supercontinuum Laser Source, 1st Ed.* Springer-Verlag New York, 1989.
- [72] J. T. J. M. Dudley, ed., *Supercontinuum Generation in Optical Fibers*. Cambridge University Press, 2010.
- [73] C. Mahnke and F. Mitschke, “Possibility of an akhmediev breather decaying into solitons,” *Phys. Rev. A*, vol. 85, p. 033808, Mar 2012.
- [74] G. Genty and J. M. Dudley, “Route to coherent supercontinuum generation in the long pulse regime,” *IEEE Journal of Quantum Electronics*, vol. 45, pp. 1331–1335, Nov 2009.
- [75] M. W. Hirsch, S. Smale, and R. L. Devan, *Differential Equations, Dynamical Systems, and an Introduction to Chaos*. Elsevier, 2013.
- [76] K. Nozaki and N. Bekki, “Solitons as attractors of a forced dissipative nonlinear schrödinger equation,” *Physics Letters A*, vol. 102, no. 9, pp. 383 – 386, 1984.
- [77] M. Miranda, C. L. Arnold, T. Fordell, F. Silva, B. Alonso, R. Weigand, A. L’Huillier, and H. Crespo, “Characterization of broadband few-cycle laser pulses with the d-scan technique,” *Opt. Express*, vol. 20, pp. 18732–18743, Aug 2012.
- [78] I. A. Walmsley and C. Dorrer, “Characterization of ultrashort electromagnetic pulses,” *Adv. Opt. Photon.*, vol. 1, pp. 308–437, Apr 2009.
- [79] Y. Mairesse and F. Quéré, “Frequency-resolved optical gating for complete reconstruction of attosecond bursts,” *Phys. Rev. A*, vol. 71, p. 011401, Jan 2005.

- [80] C. Bourassin-Bouchet and M. E. Couprie, “Partially coherent ultrafast spectrography,” *Nat. Comm.*, vol. 6, pp. 6465 EP –, 03 2015.
- [81] D. French, C. Dorrer, and I. Jovanovic, “Two-beam spider for dual-pulse single-shot characterization,” *Opt. Lett.*, vol. 34, pp. 3415–3417, Nov 2009.
- [82] D. Fabris, W. Holgado, F. Silva, T. Witting, J. W. G. Tisch, and H. Crespo, “Single-shot implementation of dispersion-scan for the characterization of ultrashort laser pulses,” *Opt. Express*, vol. 23, pp. 32803–32808, Dec 2015.
- [83] T. C. Wong, M. Rhodes, and R. Trebino, “Single-shot measurement of the complete temporal intensity and phase of supercontinuum,” *Optica*, vol. 1, pp. 119–124, Aug 2014.
- [84] G. De Ninno, D. Gauthier, B. Mahieu, P. Ribič, E. Allaria, P. Cinquegrana, M. B. Danailov, A. Demidovich, E. Ferrari, L. Giannessi, G. Penco, P. Sigalotti, and M. Stupar, “Single-shot spectro-temporal characterization of xuv pulses from a seeded free-electron laser,” *Nat. Comm.*, vol. 6, pp. 8075 EP –, 08 2015.
- [85] E. A. Anashkina, V. N. Ginzburg, A. A. Kochetkov, I. V. Yakovlev, A. V. Kim, and E. A. Khazanov, “Single-shot laser pulse reconstruction based on self-phase modulated spectra measurements,” *Sci. Rep.*, vol. 6, pp. 33749 EP –, 09 2016.
- [86] P. Bowlan and R. Trebino, “Complete single-shot measurement of arbitrary nanosecond laser pulses in time,” *Opt. Express*, vol. 19, pp. 1367–1377, Jan 2011.
- [87] G. Herink, B. Jalali, C. Ropers, and D. R. Solli, “Resolving the build-up of femtosecond mode-locking with single-shot spectroscopy at 90 mhz frame rate,” *Nat Photon*, vol. 10, pp. 321–326, 05 2016.
- [88] B. H. Kolner, “Space-time duality and the theory of temporal imaging,” *IEEE Journal of Quantum Electronics*, vol. 30, pp. 1951–1963, Aug 1994.
- [89] E. Hecht, *Optics*. Addison-Wesley, 2002.
- [90] H. G. de Chatellus, L. R. Cortés, and J. A. na, “Optical real-time fourier transformation with kilohertz resolutions,” *Optica*, vol. 3, pp. 1–8, Jan 2016.
- [91] T. Godin, B. Wetzel, T. Sylvestre, L. Larger, A. Kudlinski, A. Mussot, A. B. Salem, M. Zghal, G. Genty, F. Dias, and J. M. Dudley, “Real time noise and wavelength correlations in octave-spanning supercontinuum generation,” *Opt. Express*, vol. 21, pp. 18452–18460, Jul 2013.
- [92] B. H. Kolner, “Active pulse compression using an integrated electro?optic phase modulator,” *Applied Physics Letters*, vol. 52, no. 14, pp. 1122–1124, 1988.
- [93] T. T. Ng, F. Parmigiani, M. Ibsen, Z. Zhang, P. Petropoulos, and D. J. Richardson, “Compensation of linear distortions by using xpm with parabolic pulses as a time lens,” *IEEE Photonics Technology Letters*, vol. 20, pp. 1097–1099, July 2008.
- [94] R. Salem, A. Foster, M.A .and Turner, D. F. Geraghty, M. Lipson, and A. L. Gaeta, “Optical time lens based on four-wave mixing on a silicon chip,” *Optics Letters*, vol. 33, no. 10, pp. 1047–1049, 2008.

- [95] M. A. Foster, R. Salem, D. F. Geraghty, A. C. Turner-Foster, M. Lipson, and A. L. Gaeta, "Silicon-chip-based ultrafast optical oscilloscope," *Nature*, vol. 456, pp. 81–84, 11 2008.
- [96] R. Salem, M. A. Foster, A. C. Turner-Foster, D. F. Geraghty, M. Lipson, and A. L. Gaeta, "High-speed optical sampling using a silicon-chip temporal magnifier," *Opt. Express*, vol. 17, pp. 4324–4329, Mar 2009.
- [97] A. Gouveia-Neto, M. Faldon, and J. Taylor, "Spectral and temporal study of the evolution from modulational instability to solitary wave," *Optics Communications*, vol. 69, no. 3, pp. 325–328, 1989.
- [98] B. Wetzal, A. Stefani, L. Larger, P. Lacourt, J. Merolla, T. Sylvestre, A. Kudlinski, A. Mussot, G. Genty, F. Dias, and J. Dudley, "Real-time full bandwidth measurement of spectral noise in supercontinuum generation," *Scientific Reports*, vol. 2, p. 882, 2012.
- [99] P. Suret, R. E. Koussaifi, A. Tikan, C. Evain, S. Randoux, C. Szwaj, and S. Bielawski, "Single-shot observation of optical rogue waves in integrable turbulence using time microscopy," *Nature Communications*, vol. 7, pp. 13136 EP –, 10 2016.
- [100] J. M. Soto-Crespo, N. Devine, and N. Akhmediev, "Integrable turbulence and rogue waves: Breathers or solitons?," *Phys. Rev. Lett.*, vol. 116, p. 103901, Mar 2016.
- [101] A. Hadjifotiou and G. A. Hill, "Suppression of stimulated brillouin backscattering by psk modulation for high-power optical transmission," *IEEE Proceedings J - Optoelectronics*, vol. 133, pp. 256–258, August 1986.
- [102] F. W. Willems, W. Muys, and J. S. Leong, "Simultaneous suppression of stimulated brillouin scattering and interferometric noise in externally modulated lightwave am-scm systems," *IEEE Photonics Technology Letters*, vol. 6, pp. 1476–1478, Dec 1994.
- [103] S. TOENGER, *Linear and Nonlinear Rogue Waves in Optical Systems*. Theses, Université de Franche-Comté, June 2016.
- [104] M. A. Finger, T. S. Iskhakov, N. Y. Joly, M. V. Chekhova, and P. S. J. Russell, "Raman-free, noble-gas-filled photonic-crystal fiber source for ultrafast, very bright twin-beam squeezed vacuum," *Phys. Rev. Lett.*, vol. 115, p. 143602, Sep 2015.
- [105] N. Akhmediev, A. Ankiewicz, J. Soto-Crespo, and J. M. Dudley, "Rogue wave early warning through spectral measurements?," *Physics Letters A*, vol. 375, no. 3, pp. 541 – 544, 2011.
- [106] O. Svelto, *Principles of Lasers*. Springer US, 2010.
- [107] C. Lai, D. Goosman, J. Wade, and R. Avara, "Design and field test of a galvanometer deflected streak camera," *Proc. Of 25th Int. Cong. on High Speed Photography and Photonics*, 2002.
- [108] M. Erkintalo, G. Genty, B. Wetzal, and J. Dudley, "Akhmediev breather evolution in optical fiber for realistic initial conditions," *Physics Letters A*, vol. 375, no. 19, pp. 2029 – 2034, 2011.

- [109] A. J. DeMaria, D. A. Stetser, and H. Heynau, "Self mode?locking of lasers with saturable absorbers," *Applied Physics Letters*, vol. 8, no. 7, pp. 174–176, 1966.
- [110] U. Keller, "Recent developments in compact ultrafast lasers," *Nature*, vol. 424, pp. 831–838, 08 2003.
- [111] J. Valdmann and R. Fork, "Design considerations for a femtosecond pulse laser balancing self phase modulation, group velocity dispersion, saturable absorption, and saturable gain," *IEEE Journal of Quantum Electronics*, vol. 22, pp. 112–118, Jan 1986.
- [112] D. E. Spence, P. N. Kean, and W. Sibbett, "60-fsec pulse generation from a self-mode-locked ti:sapphire laser," *Opt. Lett.*, vol. 16, pp. 42–44, Jan 1991.
- [113] M. Zirngibl, L. W. Stulz, J. Stone, J. Hugi, D. DiGiovanni, and P. B. Hansen, "1.2 ps pulses from passively mode-locked laser diode pumped er-doped fibre ring laser," *Electronics Letters*, vol. 27, pp. 1734–1735, Sept 1991.
- [114] U. Keller, D. A. B. Miller, G. D. Boyd, T. H. Chiu, J. F. Ferguson, and M. T. Asom, "Solid-state low-loss intracavity saturable absorber for nd:y:lf lasers: an antiresonant semiconductor fabry–perot saturable absorber," *Opt. Lett.*, vol. 17, pp. 505–507, Apr 1992.
- [115] W. H. Loh, D. Atkinson, P. R. Morkel, M. Hopkinson, A. Rivers, A. J. Seeds, and D. N. Payne, "All?solid?state subpicosecond passively mode locked erbium?doped fiber laser," *Applied Physics Letters*, vol. 63, no. 1, pp. 4–6, 1993.
- [116] E. P. Ippen, "Principles of passive mode locking," *Applied Physics B*, vol. 58, no. 3, pp. 159–170, 1994.
- [117] F. Krausz, M. E. Fermann, T. Brabec, P. F. Curley, M. Hofer, M. H. Ober, C. Spielmann, E. Wintner, and A. J. Schmidt, "Femtosecond solid-state lasers," *IEEE Journal of Quantum Electronics*, vol. 28, pp. 2097–2122, Oct 1992.
- [118] J. N. Kutz, B. C. Collings, K. Bergman, S. Tsuda, S. T. Cundiff, W. H. Knox, P. Holmes, and M. Weinstein, "Mode-locking pulse dynamics in a fiber laser with a saturable bragg reflector," *J. Opt. Soc. Am. B*, vol. 14, pp. 2681–2690, Oct 1997.
- [119] H. A. Haus, "Theory of mode locking with a fast saturable absorber," *Journal of Applied Physics*, vol. 46, no. 7, pp. 3049–3058, 1975.
- [120] H. A. Haus, J. G. Fujimoto, and E. P. Ippen, "Structures for additive pulse mode locking," *J. Opt. Soc. Am. B*, vol. 8, pp. 2068–2076, Oct 1991.
- [121] P. Grelu and N. Akhmediev, "Dissipative solitons for mode-locked lasers," *Nat Photon*, vol. 6, pp. 84–92, 02 2012.
- [122] I. S. Aranson and L. Kramer, "The world of the complex ginzburg-landau equation," *Rev. Mod. Phys.*, vol. 74, pp. 99–143, Feb 2002.
- [123] D. Abraham, R. Nagar, V. Mikhelashvili, and G. Eisenstein, "Transient dynamics in a self?starting passively mode?locked fiber?based soliton laser," *Applied Physics Letters*, vol. 63, no. 21, pp. 2857–2859, 1993.

- [124] D. Y. Tang, B. Zhao, L. M. Zhao, and H. Y. Tam, “Soliton interaction in a fiber ring laser,” *Phys. Rev. E*, vol. 72, p. 016616, Jul 2005.
- [125] P. Grelu, F. Belhache, F. Guty, and J.-M. Soto-Crespo, “Phase-locked soliton pairs in a stretched-pulse fiber laser,” *Opt. Lett.*, vol. 27, pp. 966–968, Jun 2002.
- [126] V. Roy, M. Olivier, and M. Piché, “Pulse interactions in the stretched-pulse fiber laser,” *Opt. Express*, vol. 13, pp. 9217–9223, Nov 2005.
- [127] P. Grelu and J. M. Soto-Crespo, “Multisoliton states and pulse fragmentation in a passively mode-locked fibre laser,” *Journal of Optics B: Quantum and Semiclassical Optics*, vol. 6, no. 5, p. S271, 2004.
- [128] A. Schlatter, S. C. Zeller, R. Grange, R. Paschotta, and U. Keller, “Pulse energy dynamics of passively mode-locked solid-state lasers above the q-switching threshold,” in *Advanced Solid-State Photonics*, p. TuB18, Optical Society of America, 2004.
- [129] M. B. Flynn, L. O’Faolain, and T. F. Krauss, “An experimental and numerical study of q-switched mode-locking in monolithic semiconductor diode lasers,” *IEEE Journal of Quantum Electronics*, vol. 40, pp. 1008–1013, Aug 2004.
- [130] C. Hönniger, R. Paschotta, F. Morier-Genoud, M. Moser, and U. Keller, “Q-switching stability limits of continuous-wave passive mode locking,” *Journal of the Optical Society of America B*, vol. 16, no. 1, pp. 46–56, 1999.
- [131] G. Herink, F. Kurtz, B. Jalali, D. R. Solli, and C. Ropers, “Real-time spectral interferometry probes the internal dynamics of femtosecond soliton molecules,” *Science*, vol. 356, no. 6333, pp. 50–54, 2017.
- [132] HerinkG., JalaliB., RopersC., and S. R., “Resolving the build-up of femtosecond mode-locking with single-shot spectroscopy at 90 mhz frame rate,” *Nat Photon*, vol. 10, pp. 321–326, 05 2016.
- [133] A. F. J. Runge, N. G. R. Broderick, and M. Erkintalo, “Observation of soliton explosions in a passively mode-locked fiber laser,” *Optica*, vol. 2, pp. 36–39, Jan 2015.
- [134] R. Gerchberg and W. Saxton, “A practical algorithm for the determination of the phase from image and diffraction plane pictures,” *Optik*, vol. 35, no. 35, p. 237, 1972.
- [135] J. R. Fienup, “Phase retrieval algorithms: a comparison,” *Appl. Opt.*, vol. 21, pp. 2758–2769, Aug 1982.
- [136] R. Trebino, *Frequency-Resolved Optical Gating: The Measurement of Ultrashort Laser Pulses*. Springer, 2000.
- [137] P. Grelu and N. Akhmediev, “Group interactions of dissipative solitons in a laser cavity: the case of $2+1$,” *Opt. Express*, vol. 12, pp. 3184–3189, Jul 2004.
- [138] N. N. Akhmediev, A. Ankiewicz, and J. M. Soto-Crespo, “Stable soliton pairs in optical transmission lines and fiber lasers,” *J. Opt. Soc. Am. B*, vol. 15, pp. 515–523, Feb 1998.

- [139] S. K. Turitsyn, J. E. Prilepsky, S. T. Le, S. Wahls, L. L. Frumin, M. Kamalian, and S. A. Derevyanko, “Nonlinear fourier transform for optical data processing and transmission: advances and perspectives,” *Optica*, vol. 4, pp. 307–322, Mar 2017.
- [140] J. Yang, *Nonlinear Waves in Integrable and Nonintegrable Systems*. Society for Industrial and Applied Mathematics, 2010.
- [141] S. Randoux, P. Suret, and G. El, “Inverse scattering transform analysis of rogue waves using local periodization procedure,” *Sci. Rep.*, vol. 6, pp. 29238 EP –, 07 2016.
- [142] A. Osborne, *Nonlinear Ocean Waves and the Inverse Scattering Transform*, vol. 97. Academic Press, 2010.
- [143] P. Ryczkowski, A. Nolvi, I. Kassamakov, G. Genty, and E. Hæggrström, “High-speed stroboscopic imaging with frequency-doubled supercontinuum,” *Opt. Lett.*, vol. 38, pp. 658–660, Mar 2013.
- [144] J. M. Langridge, T. Laurila, R. S. Watt, R. L. Jones, C. F. Kaminski, and J. Hult, “Cavity enhanced absorption spectroscopy of multiple trace gas species using a supercontinuum radiation source,” *Opt. Express*, vol. 16, pp. 10178–10188, Jul 2008.
- [145] K. Stelmaszczyk, M. Fechner, P. Rohwetter, M. Queißer, A. Czyżewski, T. Stacewicz, and L. Wöste, “Towards supercontinuum cavity ring-down spectroscopy,” *Applied Physics B*, vol. 94, no. 3, pp. 369–373, 2009.
- [146] L. Mandel and E. Wolf, *Optical Coherence and Quantum Optics*. Cambridge University Press, 1995.
- [147] A. Donges, “The coherence length of black-body radiation,” *European Journal of Physics*, vol. 19, no. 3, p. 245, 1998.
- [148] G. S. Agarwal, G. Gbur, and E. Wolf, “Coherence properties of sunlight,” *Opt. Lett.*, vol. 29, pp. 459–461, Mar 2004.
- [149] S. Divitt and L. Novotny, “Spatial coherence of sunlight and its implications for light management in photovoltaics,” *Optica*, vol. 2, pp. 95–103, Feb 2015.
- [150] T. Visser, *Progress in Optics*. San Diego, NETHERLANDS: Elsevier Science, 2016.
- [151] R. J. Glauber, “The quantum theory of optical coherence,” *Phys. Rev.*, vol. 130, pp. 2529–2539, Jun 1963.
- [152] J. M. Dudley and S. Coen, “Coherence properties of supercontinuum spectra generated in photonic crystal and tapered optical fibers,” *Opt. Lett.*, vol. 27, pp. 1180–1182, Jul 2002.
- [153] F. Lu and W. H. Knox, “Generation of a broadband continuum with high spectral coherence in tapered single-mode optical fibers,” *Opt. Express*, vol. 12, pp. 347–353, Jan 2004.
- [154] I. Zeylikovich, V. Kartazhev, and R. R. Alfano, “Spectral, temporal, and coherence properties of supercontinuum generation in microstructure fiber,” *J. Opt. Soc. Am. B*, vol. 22, pp. 1453–1460, Jul 2005.

- [155] X. Gu, M. Kimmel, A. P. Shreenath, R. Trebino, J. M. Dudley, S. Coen, and R. S. Windeler, "Experimental studies of the coherence of microstructure-fiber supercontinuum," *Opt. Express*, vol. 11, pp. 2697–2703, Oct 2003.
- [156] G. Genty, M. Surakka, J. Turunen, and A. T. Friberg, "Second-order coherence of supercontinuum light," *Opt. Lett.*, vol. 35, pp. 3057–3059, Sep 2010.
- [157] G. Genty, M. Surakka, J. Turunen, and A. T. Friberg, "Complete characterization of supercontinuum coherence," *J. Opt. Soc. Am. B*, vol. 28, pp. 2301–2309, Sep 2011.
- [158] F. Boitier, A. Godard, E. Rosencher, and C. Fabre, "Measuring photon bunching at ultrashort timescale by two-photon absorption in semiconductors," *Nat Phys*, vol. 5, pp. 267–270, 04 2009.
- [159] B. Tsermaa, B.-K. Yang, M.-W. Kim, and J.-S. Kim, "Characterization of supercontinuum and ultraviolet pulses by using xfrog," *J. Opt. Soc. Korea*, vol. 13, pp. 158–165, Mar 2009.
- [160] P. O'Shea, M. Kimmel, X. Gu, and R. Trebino, "Increased-bandwidth in ultrashort-pulse measurement using an angle-dithered nonlinear-optical crystal," *Opt. Express*, vol. 7, pp. 342–349, Nov 2000.
- [161] A. E. Willner, S. Khaleghi, M. R. Chitgarha, and O. F. Yilmaz, "All-optical signal processing," *J. Lightwave Technol.*, vol. 32, pp. 660–680, Feb 2014.
- [162] J. Sharping, Y. Okawachi, J. van Howe, C. Xu, Y. Wang, A. Willner, and A. Gaeta, "All-optical, wavelength and bandwidth preserving, pulse delay based on parametric wavelength conversion and dispersion," *Opt. Express*, vol. 13, pp. 7872–7877, Oct 2005.
- [163] S. Khaleghi, M. R. Chitgarha, O. F. Yilmaz, M. Tur, M. W. Haney, C. Langrock, M. M. Fejer, and A. E. Willner, "Experimental performance of a fully tunable complex-coefficient optical fir filter using wavelength conversion and chromatic dispersion," *Opt. Lett.*, vol. 37, pp. 3420–3422, Aug 2012.
- [164] B. J. Eggleton, B. Luther-Davies, and K. Richardson, "Chalcogenide photonics," *Nat Photon*, vol. 5, pp. 141–148, 03 2011.
- [165] O. Boyraz and B. Jalali, "Demonstration of 11db fiber-to-fiber gain in a silicon raman amplifier," *IEICE Electronics Express*, vol. 1, no. 14, pp. 429–434, 2004.
- [166] M. A. Foster, A. C. Turner, J. E. Sharping, B. S. Schmidt, M. Lipson, and A. L. Gaeta, "Broad-band optical parametric gain on a silicon photonic chip," *Nature*, vol. 441, pp. 960–963, 06 2006.
- [167] K. Croussore and G. Li, "Amplitude regeneration of rz-dpsk signal based on four wave mixing in fibre," *Electronics Letters*, vol. 43, pp. 177–178, 2007.
- [168] C. Finot and J. Fatome, "All-optical fiber-based ultrafast amplitude jitter magnifier," *Opt. Express*, vol. 18, pp. 18697–18702, Aug 2010.
- [169] C. H. Hage, B. Kibler, and C. Finot, "Fiber-based device for the detection of low-intensity fluctuations of ultrashort pulses," *Appl. Opt.*, vol. 51, pp. 949–953, Mar 2012.

- [170] M. Takeda, H. Ina, and S. Kobayashi, “Fourier-transform method of fringe-pattern analysis for computer-based topography and interferometry,” *J. Opt. Soc. Am.*, vol. 72, pp. 156–160, Jan 1982.
- [171] D. V. Skryabin and A. V. Yulin, “Theory of generation of new frequencies by mixing of solitons and dispersive waves in optical fibers,” *Phys. Rev. E*, vol. 72, p. 016619, Jul 2005.
- [172] T. G. Philbin, C. Kuklewicz, S. Robertson, S. Hill, F. König, and U. Leonhardt, “Fiber-optical analog of the event horizon,” *Science*, vol. 319, no. 5868, pp. 1367–1370, 2008.
- [173] K. E. Webb, M. Erkintalo, Y. Xu, N. G. R. Broderick, J. M. Dudley, G. Genty, and S. G. Murdoch, “Nonlinear optics of fibre event horizons,” *Nature Communications*, vol. 5, pp. 4969 EP –, 09 2014.
- [174] R. Halir, Y. Okawachi, J. S. Levy, M. A. Foster, M. Lipson, and A. L. Gaeta, “Ultrabroadband supercontinuum generation in a cmos-compatible platform,” *Opt. Lett.*, vol. 37, pp. 1685–1687, May 2012.
- [175] D. F. Walls, “Squeezed states of light,” *Nature*, vol. 306, pp. 141–146, 11 1983.

Publications

Publication I

Mikko Närhi, Benjamin Wetzel, Cyril Billet, Shanti Toenger, Thibaut Sylvestre, Jean-Marc Merolla, Roberto Morandotti, Frederic Dias, Goëry Genty, John M. Dudley

"Real-time measurements of spontaneous breathers and rogue wave events in optical fibre modulation instability"

Nature Communications, vol 7, no. 13675

DOI: 10.1038/ncomms13675

© 2016 Nature Publishing Group

ARTICLE

Received 8 Apr 2016 | Accepted 25 Oct 2016 | Published 19 Dec 2016

DOI: 10.1038/ncomms13675

OPEN

Real-time measurements of spontaneous breathers and rogue wave events in optical fibre modulation instability

Mikko Närhi¹, Benjamin Wetzel^{2,3}, Cyril Billet⁴, Shanti Toenger^{1,4}, Thibaut Sylvestre⁴, Jean-Marc Merolla⁴, Roberto Morandotti^{2,5,6}, Frederic Dias⁷, Goëry Genty¹ & John M. Dudley⁴

Modulation instability is a fundamental process of nonlinear science, leading to the unstable breakup of a constant amplitude solution of a physical system. There has been particular interest in studying modulation instability in the cubic nonlinear Schrödinger equation, a generic model for a host of nonlinear systems including superfluids, fibre optics, plasmas and Bose–Einstein condensates. Modulation instability is also a significant area of study in the context of understanding the emergence of high amplitude events that satisfy rogue wave statistical criteria. Here, exploiting advances in ultrafast optical metrology, we perform real-time measurements in an optical fibre system of the unstable breakup of a continuous wave field, simultaneously characterizing emergent modulation instability breather pulses and their associated statistics. Our results allow quantitative comparison between experiment, modelling and theory, and are expected to open new perspectives on studies of instability dynamics in physics.

¹Tampere University of Technology, Department of Physics, Optics Laboratory, FI-33101 Tampere, Finland. ²Institut National de la Recherche Scientifique (INRS), Centre EMT, Université du Québec, Varennes, Québec, Canada J3X 1S2. ³Department of Physics and Astronomy, School of Mathematical and Physical Sciences, University of Sussex, Sussex House, Falmer, Brighton BN1 9RH, UK. ⁴Institut FEMTO-ST, CNRS Université de Bourgogne Franche-Comté UMR 6174, 25030 Besançon, France. ⁵Institute of Fundamental and Frontier Sciences, University of Electronic Science and Technology of China, Chengdu 610054, China. ⁶National Research University of Information Technologies, Mechanics and Optics, St. Petersburg, Russia. ⁷School of Mathematics and Statistics, University College Dublin, Belfield, Dublin 4, Ireland. Correspondence and requests for materials should be addressed to J.M.D. (email: john.dudley@univ-fcomte.fr).

Dynamical instabilities are seen in many areas of physics, and their study has major applications in physics, chemistry, biology and the social sciences¹. An especially important class of instability is the ‘modulation instability’ (MI) which describes how low-amplitude noise on an initial wave of constant intensity can grow exponentially and induce a wide range of nonlinear dynamical behaviour. Although first seen in deep-water wave propagation described by the cubic nonlinear Schrödinger equation (NLSE) (where it was referred to as the Benjamin–Feir instability)², MI has attracted particularly widespread interest in optics and has been observed in a variety of nonlinear systems. The first observation of MI in optics was in optical fibre propagation described by the cubic NLSE^{3,4}, but other classes of related instabilities have since been reported in laser resonators and optical cavities^{5–10}, spatio-temporal dynamics^{11,12}, pattern formation^{13–17} and waveguides¹⁸.

Despite much research into more general manifestations of MI in optics, the cubic NLSE remains the canonical system of interest that illustrates the essential characteristics of the phenomenon^{19–21}. In addition, because the cubic NLSE describes pulse envelope propagation both in optical fibre and on the surface of deep water, there has been particular attention paid to the analogy between the instability growth dynamics in fibre optics and the formation of extreme rogue waves on the ocean^{22–24}. Indeed, although nonlinear noise amplification has been considered as a possible ocean rogue wave generation mechanism for some time^{25,26}, this possibility attracted renewed attention following experiments in optics where real-time measurements showed long-tailed statistics in the spectral intensity of an optical fibre supercontinuum²⁷. These experiments motivated significant wider interest in the statistical properties of random processes in optics, and subsequent studies have investigated long-tailed statistics in a variety of other optical systems²⁸, including those with only linear elements²⁹. It is important to stress, however, that the link between such ‘optical rogue waves’ and ocean waves remains an open question³⁰.

A significant feature of MI in the cubic NLSE arises from the fact that the low-amplitude noise on the initial conditions can be treated as a perturbation, allowing linear stability analysis to be used to derive the proper conditions for the excitation and growth of the instability. Moreover, beyond the initial phase of exponential instability growth, the MI dynamics lead to the generation of highly localized pulses that can be described in terms of analytic families of soliton on finite background or ‘breather’ solutions³¹. In fact, although these analytic solutions were known since the 1980s³², it is only very recently that advances in optical measurement technologies have actually permitted these solutions to be observed in experiments^{33–37}. However, these previous experiments were carried out in the regime of ‘induced MI,’ where a low-amplitude narrowband stable modulation on a continuous wave was used to stimulate the instability dynamics from a coherent seed⁴. Although highly significant from the perspective of confirming the analytic theory of breathers³¹, these experiments do not, however, model the scenario of the ‘spontaneous’ MI where breather-like rogue waves emerge from low-amplitude broadband noise. Yet, many numerical studies have shown that the analytic breather solutions of the NLSE can in fact also describe the localized structures emerging from spontaneous MI arising from a noisy continuous wave as initial condition^{24,38–40}.

A number of experiments studying spontaneous MI in cubic-NLSE systems have been carried out, but studies of irregular wave waves have focussed primarily on statistical measures, and have not considered wave envelope properties in detail^{26,41}. In optical fibre, the experiments have generally been limited to using

only time-averaged autocorrelation to characterize the unstable field envelope^{3,42}, although real-time measurements of the spectral fluctuations have been possible using dispersive Fourier transformation^{21,43}. Important recent experiments have reported the use of optical sampling⁴⁴ and a time-lens system⁴⁵ to study the evolution that arises from the propagation of an irregular high-contrast pulse train seed in an optical fibre^{46,47}. From a dynamical perspective, the absence of a significant continuous wave component in the initial conditions leads to a very different propagation regime from MI. The higher energy associated with these initial conditions leads to random background-free fundamental and higher-order soliton evolution^{40,48} whose intensity profile can reach locally extreme values, and where the central peak may be fitted with a Peregrine soliton (PS) structure^{46,47}. Although different from the regime of MI dynamics arising from low-amplitude broadband noise that we study here, this work shows how real-time optical techniques can be advantageously used to characterize the full field probability density⁴⁴ and intensity profiles⁴⁵ of background-free soliton time series.

In this paper, we report time-domain measurements of highly localized breathers generated from the spontaneous MI of a continuous wave (CW) field in a cubic NLSE optical fibre system. Using an integrated time-lens magnifier system^{49,50}, we capture in real time an extended series of transient high intensity breather pulses emerging from noise. The large data set allows quantitative comparison between measured statistics and those obtained from Monte Carlo NLSE simulations, and intensity envelope measurements confirm that the properties of the spontaneously generated breather profiles seen in experiment are in excellent agreement with analytic predictions. From a physical viewpoint, this agreement allows us to confirm experimentally that spontaneous MI can be interpreted in terms of breather solutions of the cubic NLSE, and by comparing peak-to-background ratios obtained from experiments with theory, we are also able to identify the most extreme events as corresponding to their collisions. Aside from representing a major advance in the experimental study of ultrafast MI, our results open up new possibilities for the study of other classes of nonlinear dynamical processes in optics.

Results

Numerical simulations of modulation instability dynamics. We first review the theory of MI and present numerical results showing the expected time-domain breather dynamics. The starting point is the cubic NLSE written in the notation of nonlinear fibre optics:

$$i\frac{\partial A}{\partial z} - \frac{1}{2}\beta_2\frac{\partial^2 A}{\partial T^2} + \gamma|A|^2A = 0. \quad (1)$$

Here $A(z, T)$ is the pulse envelope in a co-moving frame (at the envelope group velocity) and γ ($\text{W}^{-1}\text{m}^{-1}$) and β_2 (s^2m^{-1}) are the fibre nonlinear coefficient and group velocity dispersion respectively. The units of $A(z, T)$ are $\text{W}^{1/2}$, with $|A(z, T)|^2$ yielding instantaneous power. Note that the NLSE is derived assuming a perturbative expansion of the material nonlinear response which is fully justified at the power levels used in our experiment⁴.

Linear stability analysis assuming a low-amplitude modulation can be used to show that a constant-intensity wave of power P_0 is unstable when $\beta_2 < 0$, and the instability exhibits maximum gain at modulation frequency $\Omega = (2\gamma P_0 / |\beta_2|)^{1/2}$ (ref. 4). Figure 1 shows results from numerical simulations of the MI process with fibre parameters corresponding to our experiments at input wavelength of 1550.3 nm: $\beta_2 = -21.4 \times 10^{-27} \text{ s}^2 \text{ m}^{-1}$ and $\gamma = 1.3 \times 10^{-3} \text{ W}^{-1} \text{ m}^{-1}$. We simulate propagation in

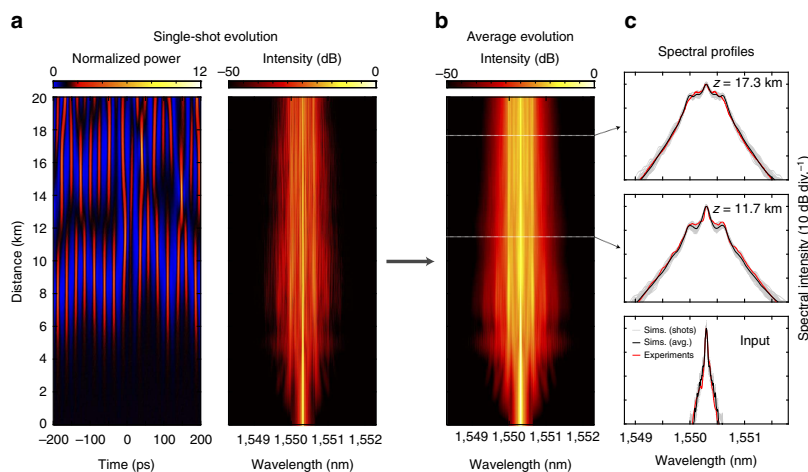


Figure 1 | Temporal and spectral evolution of modulation instability. (a) Single-shot simulations showing temporal and spectral evolution of spontaneous MI. (b) Evolution of the average spectrum calculated from an ensemble of 50 simulations. (c) compares the simulated average spectrum (black) with that measured experimentally (red) at the fibre input and after 11.7 and 17.3 km propagation as indicated. For each case in c, the superimposed grey curves also plot 50 individual realizations from the simulations to illustrate the degree of spectral fluctuation. For the chaotic temporal pulse train, we plot instantaneous pulse power normalized to background $P/\langle P \rangle$, whilst spectral plots are normalized to the input spectral intensity at 1550.3 nm.

km-lengths of fibre of a noisy continuous wave input field with $P_0 = 0.7$ W. The input noise model includes the effect of amplified spontaneous emission (ASE) and phase modulation in the initial conditions, but no forcing noise source during propagation (for example, spontaneous Raman scattering) was included. With narrowband initial conditions and our parameters, the intensity contrast on the input continuous wave is $< 5\%$ ensuring that we are in a low noise regime where the expected dynamics of cubic-NLSE MI can be clearly observed^{4,40}. Note also that simulations were performed with higher-order dispersive and nonlinear terms, but these effects were found to be negligible (see ‘Methods’ section).

Figure 1a plots typical simulation results showing field temporal and spectral evolution for a single numerical realization. The temporal evolution plot clearly reveals the emergence of distinct breather pulses from the injected continuous wave background as a result of MI, and we stress that it is precisely the intensity profiles of these (randomly evolving) structures that have never been measured before. We also note that although our simulations include loss to facilitate quantitative comparison with experiments, the expected NLSE breather growth and decay dynamics are very clearly observed. The associated spectral evolution shows the initial stage of MI sideband generation at frequency $\Omega/2\pi = 46.4$ GHz (≈ 0.37 nm) for $P_0 = 0.7$ W.

Performing multiple simulations for different random noise seeds (see ‘Methods’ section) allows us to plot the evolution of the average spectrum as shown in Fig. 1b. Figure 1c compares the computed average spectra from simulations (black) with experimentally measured spectra (red) at three propagation distances. The superimposed grey curves also plot 50 individual realizations from the simulations to illustrate the degree of spectral fluctuation observed. Note that for comparison with experiments, simulation results are convolved with the resolution response of the optical spectrum analyser (OSA) used in our setup (see ‘Methods’ section). There is excellent correspondence between the experimental and simulated average spectra, and we highlight in particular the agreement in the spectral wings over more than 30 dB. In this context, it is important to note that the particular ‘triangular’ nature of these wings (when viewed on a

semi-logarithmic scale) is a characteristic feature of the emergence of temporal breathers, and is an important confirmation that our experiments are being performed in the regime of MI in the cubic-NLSE^{20,35}.

Real-time measurement of emerging localized structures. To characterize these breathers experimentally, we used the setup in Fig. 2. A continuous wave 1550.3 nm external cavity laser (ECL) was phase modulated (to suppress Brillouin scattering^{33,51}) and amplified to $P_0 = 0.7$ W before injection in standard single-mode fibre in which the MI develops (see ‘Methods’ section). The figure also illustrates schematically the fact that the instability develops from an injected continuous wave as initial condition. At this power, simulations indicate that the unstable pulses have expected durations in the range 2–12 ps which we measured using the time-lens system described below⁵⁰.

When applied to a continuous wave field, the time-lens measurements yield distinct segments of the noisy pulse structure at a repetition rate of 100 MHz. After correcting for magnification, the physical (that is, demagnified) width of the measurement window was ~ 50 ps. For peak detection and analysis, we consider a smaller region of 25 ps at the centre of the measurement window, from which it is straightforward to extract intensity profiles of individual breather pulses. The digital oscilloscope used to record the traces introduces a low level of noise spanning the complete bandwidth of our detection system (out to 40 GHz) with a constant level and, to improve signal fidelity, we apply a frequency-domain numerical filter which allows us to more clearly identify the maxima and determine the temporal widths of the signal peaks (see ‘Methods’ section). Three subplots in Fig. 2 show both unfiltered raw data (black traces) and filtered data (red curves) for representative signals obtained from our experiments, illustrating how the filtering procedure is effective at allowing us to identify peak maxima. Note that during the peak detection process over the central 25 ps region of the measurement window, only peaks that showed distinct maxima and subsidiary minima were included in the statistical

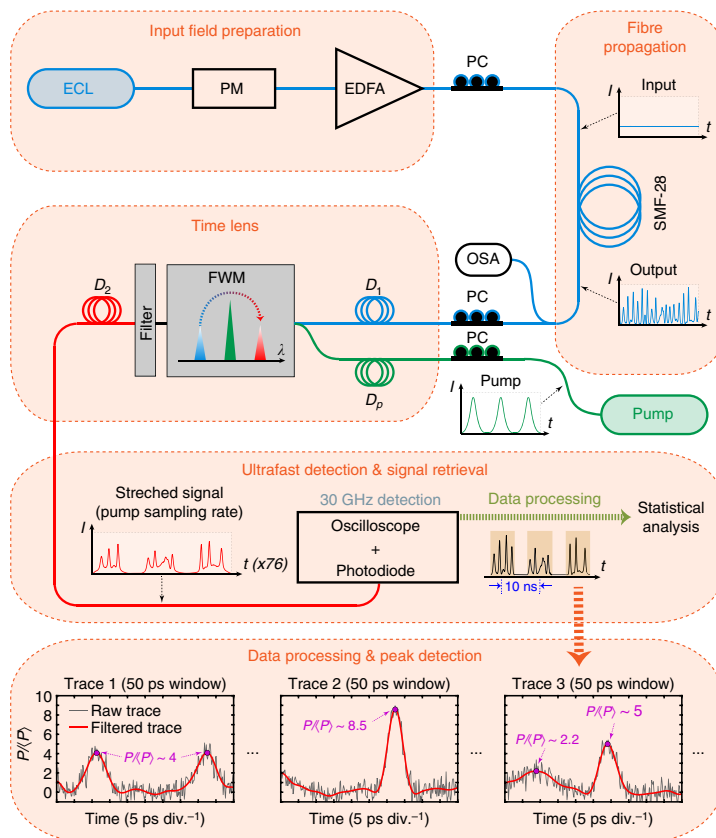


Figure 2 | Experimental setup. An external cavity laser (ECL) at 1550.3 nm is phase modulated (PM) and amplified in an erbium-doped fibre amplifier (EDFA) before injection in SMF-28 single-mode fibre. The input noisy continuous wave breaks up into a random breather train which is measured using an optical spectrum analyser (OSA) and a time-lens magnifier (PicoLuz UTM-1500). The time lens uses two dispersive propagation steps (D_1 and D_2), one on each side of an element that applies a quadratic temporal phase. In our experiments, the quadratic phase was applied from four wave mixing (FWM) with a linearly chirped pump pulse co-propagating in a silicon waveguide. The chirped pump pulses of duration ~ 90 ps are generated from a femtosecond pulse fibre laser at 100 MHz subsequently stretched through propagation in a fibre of dispersion D_p . Optimal fidelity in the time lens requires polarization control (PC) for the pump-signal FWM in the silicon waveguide. The wavelength-converted idler after FWM (with applied quadratic phase) is filtered before further propagation in segment D_2 . The overall temporal magnification is 76.4 such that the stretched replica of the input at the output of D_2 can be resolved using a 30 GHz bandwidth detection system (photodiode and ultrafast oscilloscope). The output signal takes the form of a sequence of noisy breather peaks separated by 10 ns. Note that the figure plots results over a timespan of 50 ps, but peak detection used only a 25 ps region of the measurement window. We also show three representative signals obtained from experiment (at 17.3 km propagation) plotting both unfiltered raw data (black traces), and data after filtering (see ‘Methods’ section) to remove instrumental noise (red curves).

analysis. See ‘Methods’ section for further details of the time-lens system.

Figure 3 compares experiment and simulation characterizing MI at two different fibre lengths of (a) 11.7 km and (b) 17.3 km. For each case we show a time series of intensity fluctuations obtained from simulations (top, black), and a section of a corresponding intensity time series from experiments (bottom, red). Although the experimental measurements are sampled at the repetition rate of the time-lens pump (indicated by the broken time axis), we see nonetheless good visual agreement in the general characteristics of the observed intensity fluctuations. These results complement those shown in the traces of Fig. 2 in illustrating the general features of a noisy MI field with random breathers. Note that while single isolated breathers can be observed in some instances, in many cases the pulse structure is more complex, but this is expected in the regime of spontaneous

MI where breathers generated from noise will overlap and merge³⁹.

Note that these results plot $P/\langle P \rangle$, the measured signal normalized with respect to the measured average background CW power at the fibre output, which facilitates comparison with expected analytic solutions, and which provides an important measure that can be used to infer details of the underlying dynamics^{24,38,39}. In particular, in the regime of MI in the cubic NLSE, the peak-to-background ratio $P/\langle P \rangle$ can be used to distinguish elementary breathers from collision events between breathers, because it is well-known that the highest possible peak-to-background of an elementary (single) breather is $P/\langle P \rangle = 9$ corresponding to the PS of the NLSE⁵². The only physical mechanism that can possibly yield a ratio $P/\langle P \rangle > 9$ is therefore a collision between elementary breathers³¹. This criterion to distinguish elementary breather

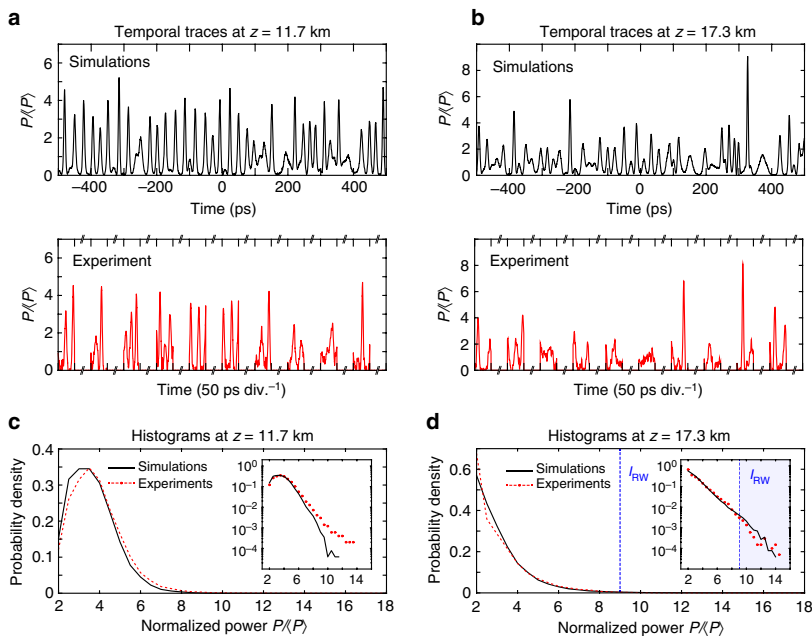


Figure 3 | Time lens results and histograms. Experimental results at (a) 11.7 km and (b) 17.3 km showing intensity profiles from simulations (top, black) and experiments (bottom, red) as indicated. Plotted intensities P are normalized with respect to the average output background power $\langle P \rangle$ and plotted against time after rescaling to account for the effect of magnification. The experimental results are shown for sequential measurement windows (note the broken axis between measurements). (c,d) Histograms of the peak intensities (shown as normalized probability density) from the chaotic pulse trains at 11.7 and 17.3 km respectively, comparing experiment (red) and simulation (black). The inset plots the histograms on semi-logarithmic axes. The calculated rogue wave intensity threshold (I_{RW}) is shown as a dashed blue line.

solutions from collision events has already been used in several works^{38,53}.

Statistical analysis. The statistics of these results are characterized by computing histograms of the peak intensities of the pulses seen in the time series³⁰. Figure 3 plots such histograms (equivalent probability density) comparing experiments (red) and simulations (black) for (c) 11.7 km and (d) 17.3 km propagation respectively. The inset plots use a semi-logarithmic axis. The histograms show clear qualitative differences with a distinct peak in the distribution for the 11.7 km case, and a near-exponential distribution at 17.3 km. This is consistent with the fact that 11.7 km is close to the first compression point of the MI evolution where more uniformity in pulse height might be expected. We also note that peaks with normalized powers exceeding the single breather PS limit of $P/\langle P \rangle = 9$ (ref. 31) are observed in both cases. Experiments and simulations at both fibre lengths match well up to this limit, and there is also very good agreement in Fig. 3d above the PS limit for 17.3 km propagation. The discrepancy in modelling the statistics above the PS limit in Fig. 3c is attributed to uncertainties in modelling the input noise; the effect of the initial conditions on the evolution is expected to be less important for longer distances when the dynamics are dominated by turbulence⁵⁴.

From these statistics, it is straightforward to calculate the rogue intensity threshold I_{RW} which defines the intensity above which events can be classified as rogue waves in the accepted statistical sense (see ‘Methods’ section). At the longest propagation distance of 17.3 km, when we are in a regime of turbulent dynamics, the blue dashed line in Fig. 3d shows the calculated value of $I_{RW} = 9.2$

from the experimental data, very close to the value of $I_{RW} = 9.1$ calculated from the simulation results. We also note that the fraction of events above I_{RW} can be readily calculated from experiment at $\sim 0.3\%$, a small fraction consistent with previous predictions for NLSE systems^{24,39}.

Note that with measurements made at a fixed fibre distance, the MI breather profiles are not necessarily characterized at their point of maximum intensity, but rather at various points along their longitudinal evolution. However, although the associated statistics will differ from those obtained considering peaks in a two-dimensional NLSE field³⁹, we can nonetheless draw an important conclusion about the physical nature of events that exceed the rogue wave threshold. In particular, since the calculated I_{RW} is very close to the limiting value of $P/\langle P \rangle = 9$ above which peaks in the MI field must necessarily arise from breather collisions (see above)³¹, this implies that the events classified as rogue waves in our data are associated with breather collisions. This is an important aspect of our study: the link between rogue wave events and breather collisions in the cubic NLSE has previously been made through numerical simulations^{24,39,40}, and our results allow us to confirm this experimentally.

Comparison with analytical breather theory. The time-lens measurements also permit quantitative comparison of the properties of the breather intensity profiles from experiments and those expected from theory. Firstly, for 30,000 distinct pulses in the time series, Fig. 4a plots the pulse duration (full-width at half-maximum (FWHM)) against the corresponding normalized peak power comparing experiment (top, red points) and simulation

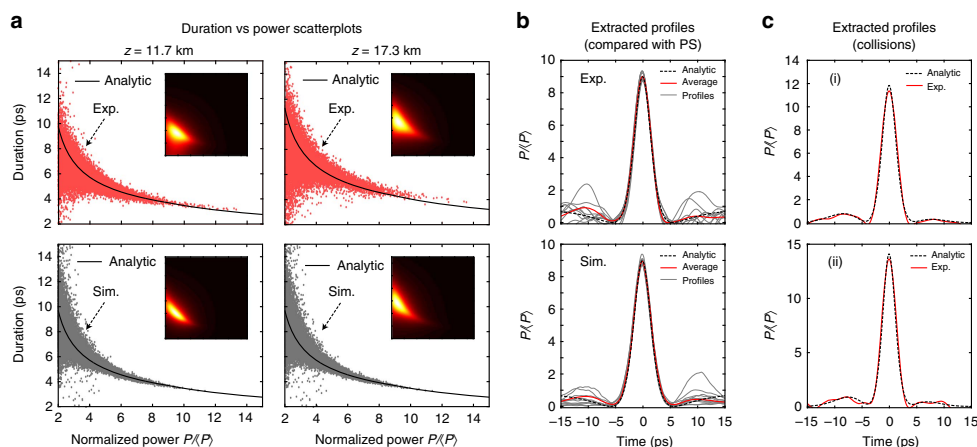


Figure 4 | Temporal properties of breathers. (a) Scatter plots of pulse duration against normalized power from experimental intensity profiles (top, red points) and simulation profiles (bottom, grey points) for 11.7 and 17.3 km propagation respectively, compared with theory (black line) in each case. The insets show the scatter plot converted to a false-color density map. (b) Results extracting 10 intensity profiles at 11.7 km with $P/\langle P \rangle \approx 9$ (grey lines) from experiment (top) and simulation (bottom). The average intensity profiles (red lines) are compared with the analytic PS (black dashed lines), showing excellent agreement over the central peak. (c) Two peaks of higher intensity (grey lines) with (i) $P/\langle P \rangle \approx 11.5$ and (ii) $P/\langle P \rangle \approx 13.5$. The dashed line in each case shows a higher-order breather fit.

(bottom, grey points) at two propagation distances as shown. As expected from a noise-driven process, there is significant scatter, but the results from experiment and simulation agree well, and both cluster strongly around the theoretical prediction relating duration to power based on the analytic properties of NLSE elementary breathers and their collisions (see ‘Methods’ section). (Because of the large number of points in the figure, the insets also show the scatter plot converted to a false-color density map.) These experimental results are important in confirming previous suggestions that the analytic predictions of the NLSE provide a natural basis with which to interpret the temporal structures in MI, even when stimulated from noise³⁹.

We can also compare the intensity profiles of the measured breather pulses with simulation and theory, and these results are presented in Fig. 4b,c. Firstly, from experimental and simulated data, we select intensity profiles with $P/\langle P \rangle \approx 9$ and a well-defined central peak with near 100% contrast (that is, zero intensity on either side of the central maxima). Figure 4b shows 10 such intensity profiles from experiment (top) and simulation (bottom). Although both cases show large fluctuations in the pulse structure in the wings (which is to be expected given that they emerge from noise), the central peaks overlap very closely. In addition, in the region of the central peak, the mean intensity profiles from experiment and simulation (red lines) are in excellent agreement with the analytic PS (black dashed lines) solution calculated for our parameters (see ‘Methods’ section). Note that when we measure at a fixed distance, the selection of peaks with $P/\langle P \rangle \approx 9$ will include not only ideal PSs at their maxima, but also some breather collision events with maximal intensity ≈ 9 . But we can attribute the excellent agreement with the PS profile due to its universal role in nonlinear dynamics that has been shown to also apply to a range of other propagation scenarios^{46,47}.

For structures with intensities $P/\langle P \rangle > 9$ arising from breather collisions, there is no simple analytic description. Nonetheless, it is possible to construct the theoretical profile of a breather collision using the Darboux transformation³¹. Two examples of experimentally measured collision profiles are shown in the grey lines in Fig. 4c for a normalized power of $P/\langle P \rangle \approx 11.5$ (top) and $P/\langle P \rangle \approx 13.5$ (bottom). Note that these are single-shot

measurements and not averages over an ensemble. In both cases we compare these results with theory by using the Darboux transformation to analytically construct a second-order breather solution (see ‘Methods’ section) and the construction is in excellent agreement with experiment. It is important to bear in mind that, in a noisy MI field, all the Fourier modes underneath the MI gain bandwidth are simultaneously excited such that the resulting evolution corresponds to the nonlinear superposition of the structures associated with these Fourier modes. This implies that the fit of a particular analytical breather (or collision thereof) can generally be performed only locally to a limited interval of the temporal field profile. To identify all the structures that are present in the random MI field generated in an integrable cubic NLSE system, a different approach consists in using the inverse scattering transform to compute the eigenvalue spectrum associated with a particular evolving field, allowing discrimination between particular structures that can emerge along propagation^{26,40,55}.

Discussion

There are several important conclusions to be drawn from this work. Firstly, our results show direct measurements of the ultrafast intensity profiles of optical breather structures emerging from noise-driven MI, and our measurements confirm analytical predictions made decades ago but never previously quantified in any physical system. We have been able to extract profiles of pulses satisfying criteria as statistical rogue waves, and our results have allowed us to associate these with collisions between elementary NLSE breathers. Our combined time domain, spectral and statistical characterization provides a comprehensive view of the underlying dynamics of MI and nonlinear breather formation that develop from the exponential amplification of broadband random noise in a cubic NLSE system.

Furthermore, these results complement the recent experimental study of transient intense structures that can emerge from a broadband input field corresponding to a random high-contrast pulse train⁴⁵, and whose evolution is naturally described in terms of random (background-free) higher-order soliton dynamics⁴⁰.

We anticipate that a detailed comparison between the long-term evolution and turbulence properties of these two regimes could provide additional insights into nonlinear propagation dynamics in optical fibres with noisy initial conditions.

Finally, we also note that our results highlight the intrinsic advantages of using advanced pulse metrology techniques in optics to continuously revisit and retest different scenarios in nonlinear optics. Our successful use of the time-lens approach to measure MI opens up possibilities in characterizing other optical systems displaying instabilities such as lasers with nonlinearity and feedback⁵⁶, or ultrafast lasers in which dissipative soliton evolution takes place⁵⁷. We expect that time-lens measurements will become a standard technique in allowing robust tests of theory and numerical modelling in many other dynamical systems in optics. We anticipate that the next important step towards a complete characterization and understanding of the dynamics of integrable nonlinear optical systems will be to access the complex amplitude associated with a given propagating field, which would then allow to unambiguously identify signatures of particular analytical structures using computational techniques such as, for example, the inverse scattering transform^{26,40,55}.

Methods

Numerical simulations. Although the NLSE equation (1) describes the qualitative MI dynamics very well for our experimental regime, for completeness in simulations, we used a generalized form of the NLSE including higher-order dispersion, inelastic Raman scattering, self-steepening and loss⁵⁸. Simulation parameters were: $\beta_2 = -21.4 \times 10^{-27} \text{ s}^2 \text{ m}^{-1}$, $\beta_3 = 1.2 \times 10^{-41} \text{ s}^3 \text{ m}^{-1}$, $\gamma = 1.3 \times 10^{-3} \text{ W}^{-1} \text{ m}^{-1}$, linear loss of 0.18 dB km^{-1} and 0.3 dB connector loss. Note that we checked using the generalized NLSE that there were negligible differences in simulations performed with and without the higher-order nonlinear terms, confirming the interpretation of our results in terms of cubic NLSE dynamics. In fact, experimental evidence for the negligible influence of higher-order dispersion and higher-order nonlinear effects is also seen in the symmetrical spectral broadening and linear spectral wings (on a semi-logarithmic scale) in Fig. 1. We also note that some effect of loss can be seen in simulations leading to a slight decrease in mean spectral bandwidth with propagation, but this has no effect on the qualitative growth and decay breather dynamics in the time domain.

Initial conditions used a continuous wave field of power $P_0 = 0.7 \text{ W}$ modified by phase modulation and with ASE noise to model the contribution from the erbium-doped fibre amplifier. The phase modulation is applied to suppress Brillouin scattering when using continuous wave excitation, and we used a standard technique⁵¹ with a $\sim \text{G bits}^{-1}$ pseudo-random bit sequence of $\pm \pi$ phase swings which was included in the simulations. The ASE noise was included through a spectral background of $\sim 50 \text{ dB}$ relative to the pump with random spectral phase. The spectral background level corresponded to that measured experimentally. The statistics of the MI spectral and temporal properties were obtained by Monte Carlo simulations to generate an ensemble of simulations using different random number seeds. The numerical ensemble yielded typically $\sim 50,000$ distinct intensity peaks from which a large number of distinct random peaks and a corresponding intensity histogram could be readily obtained for comparison with experiment.

Experimental setup. An ECL (Agilent 81949A) at 1550.3 nm was first phase-modulated using an electro-optic phase modulator driven by a pseudo-random bit sequence pattern generator (Tektronix AWG7122C) before amplification in an EDFA (Keopsys C40-PB) and coupling into single-mode fibre SMF-28. We performed initial experiments over a wide range of input powers ($0.3\text{--}1.2 \text{ W}$) but the evolution and breather characteristics were found to be qualitatively similar, and the results we present here at $P_0 = 0.7 \text{ W}$ are typical. An optical circulator was used to monitor Brillouin backscattered light which was always $< 5\%$ of the input power. Spectral measurements used an OSA (Anritsu OSA MS9710B) with 0.07 nm resolution.

The time lens used was a commercial Picoluz UTM-1500 system, similar to that described in ref. 50. Total accumulated dispersion for the input and output propagation steps was: $D_1 = 4.16 \text{ ps nm}^{-1} (-5.32 \times 10^{-24} \text{ s}^2)$ and $D_2 = 318 \text{ ps nm}^{-1} (-406 \times 10^{-24} \text{ s}^2)$ respectively, with magnification $|M| = D_2/D_1$. The temporal quadratic phase (to reproduce the effect of a thin lens) was imposed through four wave mixing from a pump pulse (100 MHz Menlo C-Fiber Sync and P100-EDFA) with linear chirp accumulated from propagation in a pre-chirping fibre segment D_p . The imaging condition for magnification is $2/D_p = 1/D_1 + 1/D_2$, so that the dispersion for the pump is around twice that of the signal input step. The time-lens output was detected with a 38 GHz photoreceiver (New Focus 1474-A) connected to a 30 GHz channel of a real-time oscilloscope (LeCroy 845 Zi-A 80 GS/s). Combining the electronic detection

bandwidth with the optical parameters of the time-lens yields an overall intrinsic demagnified temporal resolution of $< 300 \text{ fs}$ (ref. 50).

The measurement window in magnified time was $\approx 5 \text{ ns}$, and raw data traces are shown in Fig. 2 for a region of magnified time of 3.9 ns , corresponding to 50 ps in demagnified time. (Note that all results in Figs 3 and 4 are plotted against demagnified time.) For peak detection with improved signal-to-noise and to avoid any possibility of overlap between sequential records, we considered only the central 25 ps region (in demagnified time) of the measurement window. These measurements were then normalized to the mean background intensity to yield a peak-to-background ratio $P/\langle P \rangle$ for comparison with simulations. The mean background for normalization was obtained by measuring the time-lens output with a continuous wave signal at the same average power but with no SMF-28. This measurement was also verified by taking the average over a large number of the random MI pulse samples in the MI regime.

The digital oscilloscope used to record the traces introduces a low level of background noise ($\sim \text{mV}$) which can be seen on the unfiltered data (black traces) shown in Fig. 2. This broadband noise consists of fast fluctuations at the oscilloscope sampling interval of 12.5 ps extending up to a frequency of $2/12.5 \text{ ps} = 40 \text{ GHz}$ in a single sideband spectrum (limited by the sampling rate of the oscilloscope). This sampling noise was filtered in the Fourier domain with a sixth-order super-Gaussian low-pass filter with a 8 GHz FWHM bandwidth. After accounting for the effects of magnification, this yields an effective bandwidth of 610 GHz for resolving physical structures on the MI field. The appropriate bandwidth of the RF filter applied to reject unwanted noise was determined from the noise of the detection system both in the absence of any signal and when a narrowband CW field was directly measured. We further checked that the filtering operation did not distort pulse measurements by characterizing coherently seeded breather structures. The seeded breathers were generated from a modulated signal^{33,36,37} with various modulation periods leading to compressed structures with durations in the range $2\text{--}12 \text{ ps}$ similar to those observed in the spontaneous MI experiments, and which could be compared with ideal analytical breather solutions.

Inspection of the results in Fig. 2 reveals visually how the filtering procedure retains the overall peak structure very well when applied to experimental breather pulses. We also tested the effect of the filtering more quantitatively using simulated data of a spontaneous MI breather train to which sampling noise (as in experiment) was added numerically. We found that the intensity and temporal duration of the filtered peaks was within 5% of the original noise-free for breathers of duration greater than 3 ps duration, which in fact represents over 99% of the extracted peaks expected from simulations (see simulation results in Fig. 4). This testing of the filtering using numerical data also confirmed that artifacts such as ringing or peak asymmetry were not introduced by the procedure.

Fitting experimental data. The results in Fig. 4 plot temporal duration (FWHM) against normalized power $P/\langle P \rangle$ from an ensemble of $\sim 30,000$ distinct pulse profiles from experiments, and $\sim 50,000$ distinct pulse profiles from simulation. The theoretical curve shown in the figure is calculated from the known properties of the elementary Akhmediev breather for $P/\langle P \rangle < 9$ (refs 31,39) and for the second-order solution for $P/\langle P \rangle > 9$ corresponding to the in-phase collision between two elementary breathers constructed using the Darboux transformation technique³¹. Note that the theoretical curves plot duration against normalized power at the point of maximum temporal localization, but it is clear from Fig. 4 that the scattered points extracted from the random MI field cluster around the theoretical curve. The intensity I_{RW} indicated on the histograms describes a threshold criterion used to distinguish the small number of high intensity rogue wave events from the general population of intensity peaks. This is calculated from analysis of the statistics of the intensity peaks to determine the 'significant intensity' $I_{1/3}$ which is the mean intensity of the highest third of events. The rogue wave intensity threshold is then defined as $I_{\text{RW}} = 2I_{1/3}$, a criterion that is generally accepted as it can be calculated for any underlying probability distribution³⁰.

The detailed analytic breather profiles that are compared with experiments in Fig. 4b,c are based on well-known theory of NLSE breathers³¹. Figure 4b plots the analytic result for the PS⁵². Plotting the normalized intensity $I_{\text{PS}}(t) = P/\langle P \rangle$ against the physical time t , the analytic PS formula is $I_{\text{PS}}(t) = (1 - 4/(1 + 4\gamma P_0 t^2 / |\beta_2|))^{-2}$ where the parameters are as given above. Note there are no free parameters in the calculation of the PS profile which is compared with the experimental data. Also note that the experimental and simulation data in Fig. 4b show 10 randomly extracted peaks with maxima within 5% of the PS limit of $P/\langle P \rangle = 9$. The collision event in Fig. 4c was fitted using a three-parameter fit describing the analytic superposition of two elementary Akhmediev breathers³¹. Specifically, the temporal profile corresponding to the collision of two breathers can be fully described by the temporal periods of each breather train and their relative spatial (longitudinal) phase, and it is these parameters that were fitted using a least-squares method³¹. The fit in Fig. 4c (i) used two breather trains of periods 22.9 and 37.0 ps with longitudinal separation of 98.6 m and the fit in Fig. 4c (ii) used two breather trains of periods 27.1 and 30.5 ps with longitudinal separation of 19.7 m . We see remarkable agreement between the experimentally measured temporal profile of the extreme events and that of the second-order breather fit. We also emphasize that equally good fits are obtained for other events in the tail of the histograms of Fig. 3. These results provide clear evidence that: (i) the analytic AB

solutions of the NLSE provide an appropriate basis for describing the nature of localized structures that emerge from a chaotic MI field and (ii) the structures with highest intensity arise from the collision of elementary breathers. We stress that there is a fundamental difference between elementary and high-order breathers. An elementary breather corresponds to the exponential growth and decay of a weakly modulated continuous background with a single modulation frequency. On the other hand, a collision of breathers arises when two different elementary breather structures are simultaneously excited and their relative phase is such that the distances at which they reach maximum intensity closely coincide. A collision can thus also be seen as the nonlinear superposition of elementary breather structures.

Data availability. The data that support the findings of this study are available from the corresponding author upon request.

References

1. Scott, A. C. *The Nonlinear Universe: Chaos, Emergence, Life* (Springer, 2007).
2. Benjamin, T. B. & Feir, J. E. The disintegration of wave trains on deep water. Part 1. Theory. *J. Fluid Mech.* **27**, 417–430 (1967).
3. Tai, K., Hasegawa, A. & Tomita, A. Observation of modulational instability in optical fibers. *Phys. Rev. Lett.* **56**, 135–138 (1986).
4. Agrawal, G. P. *Nonlinear Fiber Optics* (Academic Press, 2013).
5. Lugiato, L. A. & Lefever, R. Spatial dissipative structures in passive optical systems. *Phys. Rev. Lett.* **58**, 2209–2211 (1987).
6. Tredicce, J. R. *et al.* Spatial and temporal instabilities in a CO₂ laser. *Phys. Rev. Lett.* **62**, 1274–1277 (1989).
7. Coates, A. B. *et al.* Dynamical transverse laser patterns. II. Experiments. *Phys. Rev. A* **49**, 1452–1466 (1994).
8. Vlaschenko, G. *et al.* Temporal dynamics of semiconductor lasers with optical feedback. *Phys. Rev. Lett.* **81**, 5536–5539 (1998).
9. Bonatto, C. *et al.* Deterministic optical rogue waves. *Phys. Rev. Lett.* **107**, 053901 (2011).
10. Kovalsky, M. G., Hnilo, A. A. & Tredicce, J. R. Extreme events in the Ti:sapphire laser. *Opt. Lett.* **36**, 4449–4451 (2011).
11. Arecchi, F. T., Giacomelli, G., Ramazza, P. L. & Residori, S. Experimental evidence of chaotic itinerancy and spatiotemporal chaos in optics. *Phys. Rev. Lett.* **65**, 2531–2534 (1990).
12. Huyet, G. & Tredicce, J. R. Spatio-temporal chaos in the transverse section of lasers. *Physica D* **96**, 209–214 (1996).
13. Arecchi, F. T., Boccaletti, S., Ramazza, P. L. & Residori, S. Transition from boundary- to bulk-controlled regimes in optical pattern formation. *Phys. Rev. Lett.* **70**, 2277–2280 (1993).
14. Staliunas, K., Šlekys, G. & Weiss, C. O. Nonlinear pattern formation in active optical systems: shocks, domains of tilted waves, and cross-roll patterns. *Phys. Rev. Lett.* **79**, 2658–2661 (1997).
15. Kip, D., Soljacic, M., Segev, M., Eugeniev, E. & Christodoulides, D. N. Modulation instability and pattern formation in spatially incoherent light beams. *Science* **290**, 495–498 (2000).
16. Schwartz, T., Carmon, T., Buljan, H. & Segev, M. Spontaneous pattern formation with incoherent white light. *Phys. Rev. Lett.* **93**, 223901 (2004).
17. Clerc, M. G., González-Cortés, G. & Wilson, M. Extreme events induced by spatiotemporal chaos in experimental optical patterns. *Opt. Lett.* **41**, 2711–2714 (2016).
18. Malendevich, R., Jankovic, L., Stegeman, G. & Aitchison, J. S. Spatial modulation instability in a Kerr slab waveguide. *Opt. Lett.* **26**, 1879–1881 (2001).
19. Zakharov, V. E. & Ostrovsky, L. A. Modulation instability: the beginning. *Physica D* **238**, 540–548 (2009).
20. Dudley, J. M., Genty, G., Dias, F., Kibler, B. & Akhmediev, N. Modulation instability, Akhmediev breathers and continuous wave supercontinuum generation. *Opt. Express* **17**, 21497–21508 (2009).
21. Solli, D., Herink, G., Jalali, B. & Ropers, C. Fluctuations and correlations in modulation instability. *Nat. Photonics* **6**, 463–468 (2012).
22. Dysthe, K. B. & Trulsen, K. Note on breather type solutions of the NLS as models for freak-waves. *Phys. Scr.* **T82**, 48–52 (1999).
23. Dyachenko, A. I. & Zakharov, V. E. Modulation instability of Stokes wave \rightarrow freak wave. *JETP Lett.* **81**, 255–259 (2005).
24. Akhmediev, N., Soto-Crespo, J. M. & Ankiewicz, A. Extreme waves that appear from nowhere: on the nature of rogue waves. *Phys. Lett. A* **373**, 2137–2145 (2009).
25. Kharif, C. & Pelinovsky, E. Physical mechanisms of the rogue wave phenomenon. *Eur. J. Mech. B/Fluids* **22**, 603–634 (2003).
26. Osborne, A. *Nonlinear Ocean Waves and the Inverse Scattering Transform* Vol. 97 (Academic Press, 2010).
27. Solli, D., Ropers, C., Koonath, P. & Jalali, B. Optical rogue waves. *Nature* **450**, 1054–1057 (2007).
28. Onorato, M., Residori, S., Bortolozzo, U., Montina, A. & Arecchi, F. T. Rogue waves and their generating mechanisms in different physical contexts. *Phys. Rep.* **528**, 47–89 (2013).
29. Höhmann, R., Kuhl, U., Stöckmann, H.-J., Kaplan, L. & Heller, E. J. Freak waves in the linear regime: a microwave study. *Phys. Rev. Lett.* **104**, 093901 (2010).
30. Dudley, J. M., Dias, F., Erkintalo, M. & Genty, G. Instabilities, breathers and rogue waves in optics. *Nat. Photonics* **8**, 755–764 (2014).
31. Akhmediev, N. N. & Ankiewicz, A. *Solitons: Nonlinear Pulses and Beams* (Chapman & Hall, 1997).
32. Akhmediev, N. N. & Korneev, V. I. Modulation instability and periodic solutions of the nonlinear Schrödinger equation. *Theor. Math. Phys.* **69**, 1089–1093 (1987).
33. Kibler, B. *et al.* The Peregrine soliton in nonlinear fibre optics. *Nat. Phys.* **6**, 790–795 (2010).
34. Hammani, K. *et al.* Peregrine soliton generation and breakup in standard telecommunications fiber. *Opt. Lett.* **36**, 112–114 (2011).
35. Hammani, K. *et al.* Spectral dynamics of modulation instability described using Akhmediev breather theory. *Opt. Lett.* **36**, 2140–2142 (2011).
36. Kibler, B. *et al.* Observation of Kuznetsov–Ma soliton dynamics in optical fibre. *Sci. Rep.* **2**, 463 (2012).
37. Kibler, B., Chabchoub, A., Gelash, A., Akhmediev, N. & Zakharov, V. Superregular breathers in optics and hydrodynamics: omnipresent modulation instability beyond simple periodicity. *Phys. Rev. X* **5**, 041026 (2015).
38. Akhmediev, N., Ankiewicz, A. & Soto-Crespo, J. M. Rogue waves and rational solutions of the nonlinear Schrödinger equation. *Phys. Rev. E* **80**, 026601 (2009).
39. Toenger, S. *et al.* Emergent rogue wave structures and statistics in spontaneous modulation instability. *Sci. Rep.* **5**, 10380 (2015).
40. Soto-Crespo, J., Devine, N. & Akhmediev, N. Integrable turbulence and rogue waves: breathers or solitons? *Phys. Rev. Lett.* **116**, 103901 (2016).
41. Onorato, M. *et al.* Observation of strongly non-Gaussian statistics for random sea surface gravity waves in wave flume experiments. *Phys. Rev. E* **70**, 067302 (2004).
42. Gouveia-Neto, A., Faldon, M. & Taylor, J. Spectral and temporal study of the evolution from modulational instability to solitary wave. *Opt. Commun.* **69**, 325–328 (1989).
43. Wetzel, B. *et al.* Real-time full bandwidth measurement of spectral noise in supercontinuum generation. *Sci. Rep.* **2**, 882 (2012).
44. Walczak, P., Randoux, S. & Suret, P. Optical rogue waves in integrable turbulence. *Phys. Rev. Lett.* **114**, 143903 (2015).
45. Suret, P. *et al.* Direct observation of rogue waves in optical turbulence using time microscopy. *Nat. Commun.* **7**, 13136 (2016).
46. Bertola, M. & Tovbis, A. Universality for the focusing nonlinear Schrödinger equation at the gradient catastrophe point: rational breathers and poles of the tritronquée solution to Painlevé I. *Commun. Pure Appl. Math.* **66**, 678–752 (2013).
47. Grimshaw, R. H. J. & Tovbis, A. Rogue waves: analytical predictions. *Proc. R. Soc. A* **469**, 20130094 (2013).
48. Turitsyn, S. K. & Derevyanko, S. A. Soliton-based discriminator of noncoherent optical pulses. *Phys. Rev. A* **78**, 063819 (2008).
49. Kolner, B. H. & Nazarathy, M. Temporal imaging with a time lens. *Opt. Lett.* **14**, 630–632 (1989).
50. Salem, R. *et al.* Optical time lens based on four-wave mixing on a silicon chip. *Opt. Lett.* **33**, 1047–1049 (2008).
51. Hadjifotiou, A. & Hill, G. A. Suppression of stimulated Brillouin backscattering by PSK modulation for high-power optical-transmission. *IEEE Proc. J.* **133**, 256–258 (1986).
52. Peregrine, D. H. Water waves, nonlinear Schrödinger equations and their solutions. *J. Aust. Math. Soc. Ser. B* **25**, 16–43 (1983).
53. Frisquet, B., Kibler, B. & Millot, G. Collision of Akhmediev breathers in nonlinear fiber optics. *Phys. Rev. X* **3**, 041032 (2013).
54. Wabnitz, S. & Wetzel, B. Instability and noise-induced thermalization of Fermi–Pasta–Ulam recurrence in the nonlinear Schrödinger equation. *Phys. Lett. A* **378**, 2750–2756 (2014).
55. Randoux, S., Suret, P. & El, G. Inverse scattering transform analysis of rogue waves using local periodization procedure. *Sci. Rep.* **6**, 29238 (2016).
56. Haken, H. *Synergetics: Introduction and Advanced Topics* (Springer-Verlag, 2004).
57. Grelu, P. & Akhmediev, N. Dissipative solitons for mode-locked lasers. *Nat. Photonics* **6**, 84–92 (2012).
58. Dudley, J. M., Genty, G. & Coen, S. Supercontinuum generation in photonic crystal fiber. *Rev. Mod. Phys.* **78**, 1135–1184 (2006).

Acknowledgements

This work was supported by the European Research Council (ERC) Advanced Grant ERC-2011-AdG-290562 MULTIWAVE and ERC-2013-PoC 632198-WAVEMEASUREMENT, the Agence Nationale de la Recherche (ANR OPTIROC ANR-12-BS04-0011) and the Region of Franche-Comté Project CORPS. B.W. acknowledges the support from the People Programme (Marie Curie Actions) of the European Unions FP7 Programme under REA grant agreement INCIPIT (PIOF-GA-2013-625466).

M.N. acknowledges the support of the Kaute Foundation. G.G. acknowledges the support from the Academy of Finland (Grants 267576 and 298463). R.M. acknowledges the support from NSERC through the Discovery and Accelerator Programs.

Author contributions

M.N., B.W., C.B., J.M.D. and G.G. performed the experiments with assistance and independent checking from J.-M.M., S.T. and T.S. Numerical simulations were carried out by M.N., B.W., J.M.D., G.G. and S.T. All authors contributed to interpreting the results obtained and to the writing and review of the final manuscript, with overall project supervision by F.D. and J.M.D.

Additional information

Competing financial interests: The authors declare no competing financial interests.

Reprints and permission information is available online at <http://npg.nature.com/reprintsandpermissions/>

How to cite this article: Närhi, M. *et al.* Real-time measurements of spontaneous breathers and rogue wave events in optical fibre modulation instability. *Nat. Commun.* 7, 13675 doi: 10.1038/ncomms13675 (2016).

Publisher's note: Springer Nature remains neutral with regard to jurisdictional claims in published maps and institutional affiliations.



This work is licensed under a Creative Commons Attribution 4.0 International License. The images or other third party material in this article are included in the article's Creative Commons license, unless indicated otherwise in the credit line; if the material is not included under the Creative Commons license, users will need to obtain permission from the license holder to reproduce the material. To view a copy of this license, visit <http://creativecommons.org/licenses/by/4.0/>

© The Author(s) 2016

Publication II

Piotr Ryczkowski, Mikko Närhi, Cyril Billet, Jean-Marc Merolla, Goëry Genty, John M. Dudley

"Real-time full field measurements reveal transient dissipative soliton dynamics in a mode-locked laser"

Available online at <http://arxiv.org/abs/1706.08571>

Publication III

Mikko Närhi, Jari Turunen, Ari T. Friberg, Goëry Genty

"Experimental Measurement of Second-Order Coherence of Supercontinuum"
Physical Review Letters, vol. 116, iss. 24, no. 243901

DOI: 10.1103/PhysRevLett.116.243901

© 2016 American Physical Society

Experimental Measurement of the Second-Order Coherence of Supercontinuum

Mikko Närhi,^{1,*} Jari Turunen,² Ari T. Friberg,² and Goëry Genty¹

¹*Department of Physics, Tampere University of Technology, P.O. Box 527, FI-33101 Tampere, Finland*

²*Institute of Photonics, University of Eastern Finland, P.O. Box 111, FI-80101 Joensuu, Finland*

(Received 22 September 2015; published 13 June 2016)

We measure experimentally the second-order coherence properties of supercontinuum generated in a photonic crystal fiber. Our approach is based on measuring separately the quasicohherent and quasistationary contributions to the cross-spectral density and mutual coherence functions using a combination of interferometric and nonlinear gating techniques. This allows us to introduce two-dimensional coherence spectrograms which provide a direct characterization and convenient visualization of the spectrotemporal coherence properties. The measured second-order coherence functions are in very good agreement with numerical simulations based on the generalized nonlinear Schrödinger equation. Our results pave the way towards the full experimental characterization of supercontinuum coherence properties. More generally, they provide a generic approach for the complete experimental measurement of the coherence of broadband sources.

DOI: 10.1103/PhysRevLett.116.243901

The physics of supercontinuum (SC) generation in optical fibers has been extensively studied in the past decade [1]. While the physics is now well understood, supercontinuum sources are finding an increasing number of applications ranging from frequency combs and confocal microscopy to optical coherence tomography or hyperspectral imaging. In principle, any powerful laser source can be used to create a SC. Yet, only SC spectra generated from femtosecond pump pulses possess the high phase stability and coherence required for applications in frequency metrology. Unstable incoherent SC spectra, on the other hand, are most suitable for applications where time-averaged measurements are important, as, e.g., in spectroscopy or imaging. Coherence then appears naturally as a critical parameter of SC light sources [2–6].

The spectral degree of “first-order” coherence characterizing the shot-to-shot phase stability at single frequencies [7] has now become the norm to evaluate the spectral coherence of SC. It can be measured using a polychromatic delayed Michelson interferometer (PDMI), where the visibility of the spectral interference fringes produced by two consecutive SC pulses directly corresponds to the coherence degree [8]. However, it was recently shown that this measure of spectral coherence gives only partial information, and that the two-time and two-frequency correlation functions of second-order coherence theory of nonstationary light provide a complete (up to second order in field variable) description of the temporal and spectral coherence of SC light [9,10]. This is because, unlike the first-order degree of coherence, the second-order cross-spectral density (CSD) and mutual coherence function (MCF) measure the correlation between two different frequencies and instants of time, respectively.

The experimental characterization of these second-order coherence functions requires the measurement of single-shot SC amplitude and phase. This is generally not possible due to current electronic limitations and, up to now, only time-integrated measurements corresponding to first-order degree of coherence have been successfully reported [6,11]. Here, using a combination of interferometry and cross-correlation frequency-resolved optical gating (XFROG) [12], we measure experimentally the second-order coherence functions of SC both in the time and frequency domains [10]. This allows us to access the true coherence time and coherence bandwidth of SC. The measurement procedure also enables us to generate the coherence spectrogram corresponding to the mean electric field, which directly links the spectral and temporal coherence properties. We further compare our experimental results with numerical simulations and find good agreement in all the cases investigated. Our results open the route towards modeling and optimizing SC-based optical systems where only the propagation of the second-order coherence functions is required to evaluate the system performance [13–15]. More generally, our experiments provide means to measure the complete coherence characteristics of broadband light sources, with access to the mean electric field, using only time-averaged measurements.

For nonstationary sources the second-order coherence properties are specified by the two-time MCF and two-frequency CSD functions. The normalized MCF and CSD expressed in average (\bar{t} , $\bar{\omega}$) and difference (Δt , $\Delta\omega$) coordinates are defined as

$$\gamma(\bar{t}, \Delta t) = \frac{\langle E^*(\bar{t} - \Delta t/2) E(\bar{t} + \Delta t/2) \rangle}{\sqrt{I(\bar{t} - \Delta t/2) I(\bar{t} + \Delta t/2)}}, \quad (1)$$

$$\mu(\bar{\omega}, \Delta\omega) = \frac{\langle \tilde{E}^*(\bar{\omega} - \Delta\omega/2) \tilde{E}(\bar{\omega} + \Delta\omega/2) \rangle}{\sqrt{S(\bar{\omega} - \Delta\omega/2) S(\bar{\omega} + \Delta\omega/2)}}, \quad (2)$$

where the angle brackets represent ensemble average over multiple SC electric field realizations $E(t)$ and the asterisk stands for the complex conjugate. $\tilde{E}(\omega)$ is the complex spectral representation of the electric field $E(t)$ obtained by Fourier transform. $I(t)$ and $S(\omega)$ are the mean temporal intensity and spectrum, respectively. These functions are bounded between zero and unity, the latter signifying complete correlation between frequencies and zero corresponding to no correlation. Note that Eqs. (1) and (2) do not form a two-dimensional Fourier transform pair, unlike their non-normalized form [13].

Recent numerical studies have shown that the MCF and CSD can approximately be separated into two distinct contributions—a quasicohherent square within which the spectral or temporal components are fully correlated and a quasistationary line representing the uncorrelated, noise-driven SC components [9,10]:

$$\gamma(\bar{t}, \Delta t) \approx \gamma_c(\bar{t}, \Delta t) + \gamma_q(\Delta t), \quad (3)$$

$$\mu(\bar{\omega}, \Delta\omega) \approx \mu_c(\bar{\omega}, \Delta\omega) + \mu_q(\Delta\omega), \quad (4)$$

where the subscripts c and q correspond to the coherent square and quasistationary line, respectively. From a physical point of view, the coherent square and quasistationary line represent the spectral or temporal interval within which the SC exhibits temporal and spectral coherence properties similar to those of a laser and a classical incoherent source, respectively. Because of the bandwidth limitations of currently available photodetectors, it is generally not possible to measure the shot-to-shot complex electric field of SC light and thus access directly the second-order correlation functions. Taking advantage of the separation of the coherence functions into a coherent and a quasistationary part, an indirect approach was suggested in Ref. [10]. Specifically, it was shown that the coherent contribution essentially corresponds to a cross product of one-argument first-order degrees of spectral coherence:

$$\begin{aligned} \mu_c(\bar{\omega}, \Delta\omega) &= \frac{\tilde{E}_c^*(\bar{\omega} - \Delta\omega/2) \tilde{E}_c(\bar{\omega} + \Delta\omega/2)}{\sqrt{S(\bar{\omega} - \Delta\omega/2) S(\bar{\omega} + \Delta\omega/2)}} \\ &\approx \sqrt{|g_{12}^{(1)}(\bar{\omega})| |g_{12}^{(1)}(\Delta\omega)|}, \end{aligned} \quad (5)$$

where $g_{12}^{(1)}(\omega) = \langle \tilde{E}_i^*(\omega) \tilde{E}_j(\omega) \rangle_{i \neq j} / \langle |\tilde{E}(\omega)|^2 \rangle$ is the first-order degree of spectral coherence [7]. Its absolute value can be obtained from the visibility of the spectral interference fringes measured from a PDMI.

The quasistationary part of the CSD, $\mu_q(\Delta\omega)$, can be inferred from the Fourier transform of the quasistationary intensity $I_q(t)$:

$$\mu_q(\Delta\omega) = \frac{1}{E_0} \int_{-\infty}^{\infty} I_q(\bar{t}) \exp(i\Delta\omega \bar{t}) d\bar{t}, \quad (6)$$

where $E_0 = (2\pi)^{-1} \int_{-\infty}^{\infty} I(t) dt$ is the total pulse energy. Measuring the XFROG trace allows us to access directly the quasistationary intensity $I_q(t)$ by filtering out the spectral components where interference fringes are observed in the PDMI and integrating over the filtered spectrum. Similarly, the coherent and quasistationary contributions of the MCF can be obtained from the first-order degree of spectral coherence and XFROG with appropriate filtering [10]. Hence, by measuring simultaneously the interference fringes in a PDMI and the corresponding XFROG trace, one can retrieve the experimental second-order coherence functions of SC light. Of course, it is important to bear in mind that the XFROG trace is the convolution of the actual SC complex field with the XFROG gate pulse, and a gate pulse with duration close to 100 fs generally yields a good compromise between temporal and spectral resolution. Note also that the functions are, in general, complex valued, and that only the absolute values are obtained by the procedure described above. However, the non-normalized CSD and MCF form a Fourier transform pair, which in principle allows for an approximate phase retrieval.

A schematic of our experimental arrangement is shown in Fig. 1. We used a Ti:sapphire laser (Spectra Physics Tsunami) at 785 nm producing pulses of 72 fs duration (FWHM) at 80 MHz repetition rate. An isolator placed after the laser to avoid any backreflection stretched the pulse duration to 290 fs. The pulses were then injected into a 69 cm polarization-maintaining photonic crystal fiber (NL-PM-750 from NKT Photonics). A polarizer and half-wave plate combination was applied to vary the input power. A pellicle beam splitter allowed us to extract a small fraction of the 72 fs pulses as the XFROG gate. A rapidly rotated

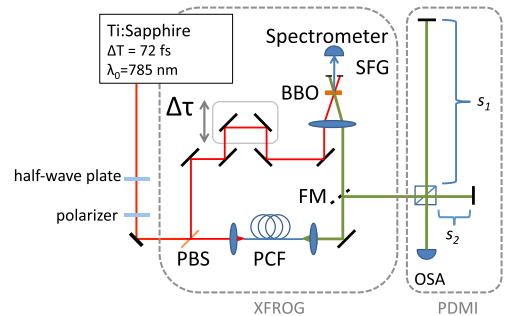


FIG. 1. Experimental setup. PBS, pellicle beam splitter; FM, flip mirror; BBO, beta-barium-borate nonlinear crystal used for SFG (sum-frequency generation); PCF, photonic crystal fiber; $\Delta\tau$, variable delay on a motorized stage; OI, optical isolator; OSA, optical spectrum analyzer.

1 mm thick beta-barium borate crystal was used in the XFROG to allow phase matching across the full SC bandwidth [16]. The grating spectrometer (Avantes AvaSpec-2048L) with adjustable integration time ensured that all the phase-matched signals were recorded during the crystal rotation. Second-harmonic generation FROG was performed to characterize the gate and input pulses.

The SC spectra generated for three different input peak powers are shown in Fig. 2 as black lines (top panels). For an input peak power of $P_p = 70$ W [Fig. 2(a)] the SC spectrum spans approximately 200 nm with a fine structure visible across the entire bandwidth. Such fine structure typically indicates high spectral degree of coherence, as confirmed by the measurement from the PDMI also shown in the figure (red solid lines). Indeed, we can see how the measured first-order coherence function $|g_{12}^{(1)}|$ shows uniform behavior over the full spectrum with values exceeding 0.9.

When the peak power is raised to 360 W [Fig. 2(c)], the SC bandwidth increases to 350 nm and some fine structure can still be observed but with a lower contrast than in the low peak-power case. The decrease in the spectral fine-structure contrast indicates a loss of coherence, as confirmed by the measured first-order spectral coherence function which drops below 0.5 at nearly every wavelength. For an input peak power of 820 W [Fig. 2(e)], the spectrum spans an octave from 550 to 1150 nm (-20 dB bandwidth) and the fine spectral structure is completely washed out, indicating large shot-to-shot fluctuations. The spectral coherence function is nearly 0 across the entire spectrum except around the pump where residual coherence can be observed. For comparison, we ran a series of 500 numerical simulations using the generalized nonlinear Schrödinger equation. We employed the fiber dispersion and nonlinear coefficients provided by the manufacturer, the experimentally measured Raman gain of silica, and a one photon per mode model for the noise implementation. The peak power was increased by 30% in the simulations as compared to the experiments to account for losses in the experimentally measured power. The simulation grid contained 2^{14} points spanning a range of 22 ps and resulting in a temporal and spectral resolution of 1 fs and 50 GHz, respectively.

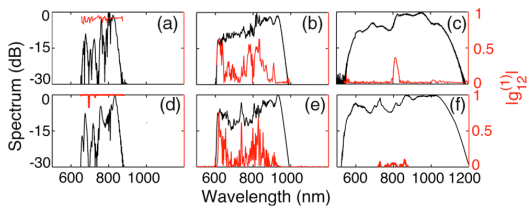


FIG. 2. Experimentally recorded SC spectra (black lines) and measured $|g_{12}^{(1)}|$ (red lines) for peak powers of (a) $P_p = 70$ W, (b) $P_p = 360$ W, and (c) $P_p = 820$ W. Corresponding numerical simulations are shown in (d)–(f).

The results are also shown in Fig. 2 (bottom panels). For all three cases, we see a very good agreement between the measured and simulated spectra on one hand and the spectral coherence functions on the other hand. We do notice small discrepancies, which we attribute to the uncertainty on the dispersion profile of the fiber.

We next proceed to the experimental reconstruction of the second-order coherence functions as described above. The experimentally reconstructed CSDs are plotted in the top panels of Fig. 3. For comparison, the numerically simulated CSDs from the ensemble of realizations are also shown (bottom panels). We observe again a very good agreement between experiments and simulations and, in particular, we see how the coherent square reduces and the quasistationary line becomes more pronounced as the peak power is increased.

The results can be explained in light of the SC dynamics. At a peak power of 70 W [Fig. 3(a)] the soliton order $N = 6$, such that the soliton fission process that leads to the broadband SC is seeded by the pump spectral components. The process is highly deterministic between the input and output, leading to nearly perfect coherence in the generated SC. In this case the CSD is simply a coherent square where spectral components are perfectly correlated. When the peak power is increased to 360 W [Fig. 3(c)], the soliton order $N = 15$, such that competition exists between deterministic soliton fission and stochastic modulation instability seeded from noise outside the pump spectral components which degrades the spectral correlations. The degradation is largest at the long wavelength edge where the peak power and the duration of the ejected solitons from the fission process fluctuate from shot to shot, translating into significant spectral jitter through the soliton self-frequency shift. On the other hand, the dispersive waves, which are emitted at the early stage of the fission

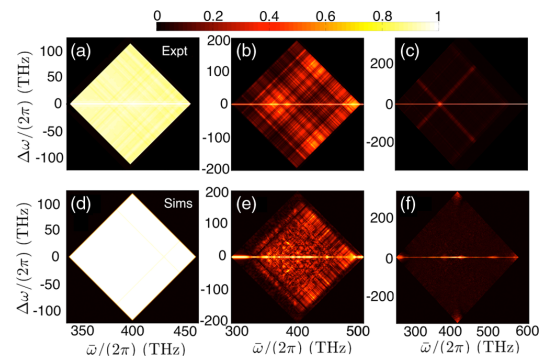


FIG. 3. Experimental (top) and simulated (bottom) CSDs for (a), (d) $P_p = 70$ W, (b), (e) $P_p = 360$ W, and (c), (f) $P_p = 820$ W. The numerical results were two-dimensionally convolved with a Gaussian (2 nm width) function to produce results with resolution comparable to that of our experiments.

process, are less affected by spectral jitter, especially because the fiber is too short for the long wavelength solitons to interact significantly with the dispersive waves through cross-phase modulation. The area of residual coherence in the central part of the spectrum corresponds to pump remain and solitons with low peak power having experienced a small frequency shift. It is interesting to note that the width of the quasistationary line of the simulated CSD is not exactly constant across the full spectrum unlike in the experimentally reconstructed CSD where the approach automatically leads to a constant width. This difference originates from the fact that the separation into a coherent and stationary part is least accurate in the partially coherent case [10]. The experimentally measured coherence bandwidth was found to be 0.9 THz, whereas in the simulations its average value integrated across the full spectrum is about 2.5 THz. For a peak power of 820 W [Fig. 3(e)], the initial stage of SC generation is triggered by noise-seeded modulation instability leading to stochastic variations at the fiber output and no correlations among the spectral components except around the pump remain due to residual coherent self-phase modulation in the initial stage. The CSD in this case thus reduces to a quasistationary line with a coherence bandwidth of 0.55 THz, in good agreement with the numerically simulated result of 1.2 THz.

The experimentally reconstructed and simulated MCFs are shown in Fig. 4. In general, the MCF reconstruction is less accurate than that of the CSD, when compared with the numerical simulations. This is due to the fact that the coherent part of the MCF is measured indirectly unlike for the CSD. Specifically, one frequency may generally consist of contributions from two different (but nearby) time instants of the SC, and filtering in the spectral domain

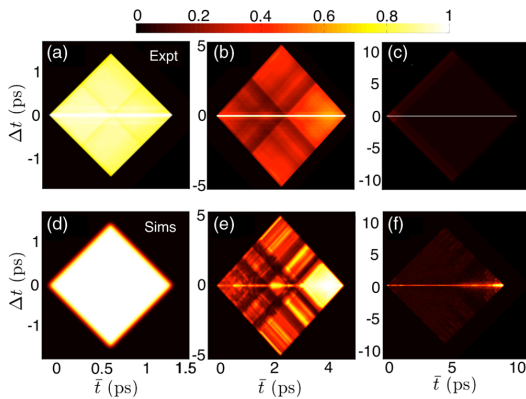


FIG. 4. Experimental (top panels) and simulated (bottom panels) MCFs for (a), (d) $P_p = 70$ W, (b), (e) $P_p = 360$ W, and (c), (f) $P_p = 820$ W. The numerical results were two-dimensionally convolved with a Gaussian (72 fs width) function to produce results with resolution comparable to that of our experiments.

can cause two time instants to have the same degree of coherence even though they actually may be somewhat different. At a low peak power [Fig. 4(a)], the MCF consists of only a coherent square with quasiperfect time correlations, consistent with the CSD and similar to what would be observed for a coherent broadband laser source. In the partially coherent case [Fig. 4(c)], the quasistationary line appears with an average coherence time of 6 fs. The coherent square is degraded, mostly around the solitonic components, while the time correlations are larger for the intensity of the dispersive wave components, as observed in the CSD measurements. Finally, for a large peak power [Fig. 4(e)], the MCF reduces to a quasistationary line with coherence time of 3 fs, corresponding precisely to the inverse spectral bandwidth of the SC in this case and indicating that the SC essentially behaves as a thermal source in terms of temporal coherence (the spatial coherence is still high).

The second-order coherence functions allow us to characterize, separately in the time and spectral domains, the coherence properties of a broadband light source. We illustrate in Fig. 5 how additional information can be obtained using the spectrogram of the mean electric field $\langle E(t) \rangle$. Whereas the mean spectrogram provides the average phase relationship between the spectral and temporal components, it does not furnish any quantitative information on their relative coherence. The spectrotemporal coherence, on the other hand, is fully described by the spectrogram of the mean field, which favors the coherent parts of the pulse due to constructive interference and conversely attenuates the incoherent parts. This quantity is not directly accessible experimentally; however, we demonstrate in Fig. 5 that by filtering the XFROG spectrogram with the spectral coherence function, one can generate “coherence” spectrograms, approximately corresponding to the spectrotemporal representation of the mean electric field and providing a clear spectrotemporal picture of the

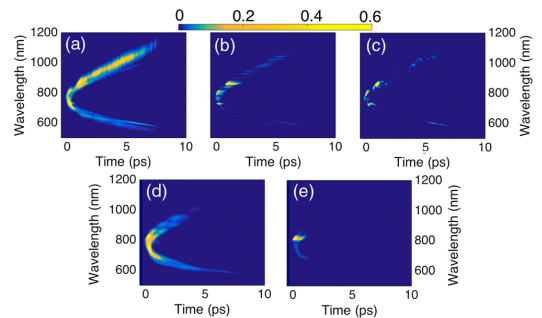


FIG. 5. Top row: Numerical simulations. (a) Average spectrogram, (b) coherence spectrogram obtained by filtering, and (c) spectrogram of the mean complex electric field. Bottom row: Experimental results. (d) Average spectrogram and (e) coherence spectrogram.

SC pulse coherence. We focus on the $P_p = 820$ W case, but the results can readily be extended to the other cases. One can see from the numerical simulations presented in Figs. 5(a)–5(c) how the trace obtained from the filtered spectrogram follows closely the spectrogram of the mean field, allowing us to unambiguously identify the spectrotemporal components of the SC that are carriers of high or low coherence. For comparison, the experimentally measured mean spectrogram and the retrieved coherence spectrogram are plotted in Figs. 5(d) and 5(e), respectively, showing good agreement with the numerical simulations. The coherence spectrogram conveniently reveals the spectrotemporal structure of the mean electric field corresponding to the distribution of the electric field that is coherent on average and thus can be recompressed or postprocessed. This is in contrast with a simple FROG or XFROG trace which does not provide information on the mean electric field.

In conclusion, we have measured the second-order coherence functions of SC light, which are the only quantities required to evaluate the performance of a SC source in an optical system. Our results permit us to measure the true coherence time and coherence bandwidth of SC and provide a generic experimental method for the full characterization of the coherence of nonstationary broadband sources. Finally, our experiments enable us to obtain a clear spectrotemporal picture of the coherence of broadband nonstationary light sources through the concept of a coherence spectrogram that approximately corresponds to the spectrogram of the mean electric field.

This work was supported by the Academy of Finland (Projects No. 267576 and No. 268480).

*Corresponding author.

mikko.narhi@tut.fi

- [1] J. M. Dudley, G. Genty, and S. Coen, *Rev. Mod. Phys.* **78**, 1135 (2006).
- [2] T. Udem, R. Holzwarth, and T. W. Hänsch, *Nature (London)* **416**, 233 (2002).
- [3] N. R. Newbury, *Nat. Photonics* **5**, 186 (2011).
- [4] I. Hartl, X. D. Li, C. Chudoba, R. K. Ghanta, T. H. Ko, J. G. Fujimoto, J. K. Ranka, and R. S. Windeler, *Opt. Lett.* **26**, 608 (2001).
- [5] B. Schenkel, R. Paschotta, and U. Keller, *J. Opt. Soc. Am. B* **22**, 687 (2005).
- [6] I. Zeylikovich, V. Kartazayev, and R. R. Alfano, *J. Opt. Soc. Am. B* **22**, 1453 (2005).
- [7] J. M. Dudley and S. Coen, *Opt. Lett.* **27**, 1180 (2002).
- [8] M. Bellini and T. W. Hänsch, *Opt. Lett.* **25**, 1049 (2000).
- [9] G. Genty, M. Surakka, J. Turunen, and A. T. Friberg, *Opt. Lett.* **35**, 3057 (2010).
- [10] G. Genty, M. Surakka, J. Turunen, and A. T. Friberg, *J. Opt. Soc. Am. B* **28**, 2301 (2011).
- [11] X. Gu, M. Kimmel, A. P. Shreenath, R. Trebino, J. M. Dudley, S. Coen, and R. S. Windeler, *Opt. Express* **11**, 2697 (2003).
- [12] J. Dudley, X. Gu, L. Xu, M. Kimmel, E. Zeek, P. O'Shea, R. Trebino, S. Coen, and R. Windeler, *Opt. Express* **10**, 1215 (2002).
- [13] L. Mandel and E. Wolf, *Optical Coherence and Quantum Optics* (Cambridge University Press, Cambridge, England, 1995).
- [14] M. Korhonen, A. T. Friberg, J. Turunen, and G. Genty, *J. Opt. Soc. Am. B* **30**, 21 (2013).
- [15] M. Erkintalo, M. Surakka, J. Turunen, A. T. Friberg, and G. Genty, *Opt. Lett.* **37**, 169 (2012).
- [16] P. O'Shea, M. Kimmel, X. Gu, and R. Trebino, *Opt. Express* **7**, 342 (2000).

Publication IV

Lasse Orsila, Johan Sand, Mikko Närhi, Günter Steinmeyer, Goëry Genty

"Supercontinuum generation as a signal amplifier"
Optica, vol. 2, iss. 8, no. 757

DOI: 10.1364/OPTICA.2.000757

© 2015 The Optical Society

Supercontinuum Generation as a Signal Amplifier

LASSE ORSILA¹, JOHAN SAND², MIKKO NÄRHI², GOËRY GENTY^{2,*}, AND GÜNTER STEINMEYER^{1,3}

¹Optoelectronics Research Centre, Tampere University of Technology, Korkeakoulunkatu 3, 33720 Tampere, Finland

²Department of Physics, Optics Laboratory, Tampere University of Technology, 33101 Tampere, Finland

³Max-Born-Institut für Nichtlineare Optik und Kurzzeitspektroskopie, Max-Born-Straße 2a, 12489 Berlin, Germany

*Corresponding author: goery.genty@tut.fi

Compiled November 7, 2017

Supercontinuum white-light generation in optical fibers is a process that is known for its extreme sensitivity towards fluctuations of the input pulses, giving rise to a strong amplification of input noise. Such noise amplification has been recognized as a detrimental effect that prevents compression of the broad white-light spectra into a few-cycle pulse. Here, we show that the same effect can be exploited to amplify and recover faint modulation signals to an extent that seems impossible with any electronic method. We experimentally demonstrate the deterministic amplification of faint amplitude modulation signals by up to 60 dB. As we show from numerical simulations, this amplification process arises from the interaction dynamics between solitons and dispersive radiation in the fiber. The resulting all-optic signal restoration provides a new photonic building block that enables signal processing at virtually unlimited processing speeds. © 2014 Optical Society of America

OCIS codes: (190.7110) Ultrafast nonlinear optics; (190.4370) Nonlinear optics, fibers; (070.7145) Ultrafast processing

<http://dx.doi.org/10.1364/optica.XX.XXXXXX>

1. INTRODUCTION

Optical supercontinuum (SC) generation has found widespread applications in spectroscopy [1], optical imaging [2], precision metrology [3, 4], and for measuring the carrier-envelope phase in attoscience [5]. Despite its complexity, the physical mechanism of SC generation in optical fibers has been extensively investigated over the past 15 years with various types of pumps sources [7, 8, 13] and fibers [9–11]. The dynamics are now very well understood [12] and arises from three key processes: group-velocity dispersion, Kerr nonlinearity, and stimulated Raman scattering. However, it has also been realized early on that the remarkable efficiency of fiber-based white-light sources comes with a caveat: a rapid loss of temporal and spectral coherence that can be particularly pronounced for pulses of 100 fs duration and above [12, 14]. This inherent limitation of SC generation arises from nonlinear noise-amplification dynamics which deteriorates the phase stability of the SC [15, 16]. Consequently, amplitude or phase variations induced by, e.g., amplified spontaneous emission in the pump laser may already cause substantial shot-to-shot variations in the output spectra of the fiber [14, 17, 18], which strongly limits or even thwarts their compression into a

short few-cycle pulse [19] and is responsible for the emergence of extreme-value statistics or rogue solitons in the infrared tail of the white-light continuum [17, 20]. While noise amplification in supercontinuum generation is well known and in particular for pulses with duration exceeding 100–150 fs [16, 21–24], it has so far only been considered as a nuisance and the actual potential for useful applications of this extreme sensitivity to noise has not been realized.

Here we propose and demonstrate that supercontinuum generation allows all-optical regeneration of faint modulation signals that are obscured by a strong carrier. This regeneration effect enables substantial enhancement of the obtainable signal-to-noise ratio, which exceeds capabilities of all-electronic signal restoration capabilities by orders of magnitude. Moreover, our scheme may help to overcome limitations of unavoidable shot noise and Johnson noise in the optoelectronic conversion process [25, 26]. Somewhat similar regeneration schemes have previously been demonstrated for telecommunication applications, which nevertheless address a different physical scenario of fully modulated signals that additionally experienced phase jitter [27, 28]. Specifically, we show that the coupling mechanism

between the long and short wavelength edges embedded within supercontinuum generation [12] induces changes in a few tens of nanometers wide spectral slices of the output pulse energy which follow input energy variations ΔI according to $(\Delta I)^N$ with a very high power N . This effect enables the enhancement of faint modulation signals relative to a strong carrier by up to 60 dB and comes with 25 dB signal-to-noise improvement. In order to reach such a high level of signal restoration, it is paramount to operate in a regime where a deterministic one-to-one correspondence between input signal and output signal is expected. This correspondence can be maintained up to pulse durations of 100 fs or more in the Ti:sapphire wavelength range. For longer durations, modulation instability can induce significant shot-to-shot fluctuations which then prevent the controlled amplification of the signal whereas noise signatures experience large amplification.

The paper is organized as follows. We first discuss the procedure for a proof-of-principle experiment, demonstrating the recovery of a faint modulation signal in the presence of a strong carrier. We compare our experimental results with numerical simulations, using sinusoidally amplitude-modulated sequences of input pulses. These simulations confirm nonlinear interaction of dispersive waves in the normal dispersion region and solitons in the anomalous dispersion region as the key process that provides the large amplification of the modulation signal. To obtain an understanding of the technical limitations of our method, we then conduct a detailed noise analysis, which identifies detection shot noise as the major limiting mechanism. Finally, we discuss the role of the coherence for our signal amplification process as well as for noise amplification and close with conclusions on possible applications.

2. EXPERIMENTS

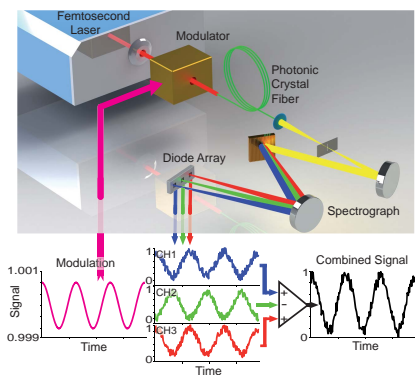


Fig. 1. Experimental set-up. A femtosecond laser beam receives a weak amplitude modulation by an acousto-optic modulator used in zero-order. This beam is launched into a photonic crystal fiber, and the output is spectrally dispersed in a spectrograph. Signals recorded at 35 nm wide wavelength channels show a strong enhancement of the modulation up to a factor 1000 in voltage (60 dB RF power). Suitably combining the wavelength channels leads to an even stronger signal enhancement.

Our experimental setup uses a commercial Ti:sapphire laser with a 76 MHz repetition rate and specified pulse duration of 6.5 fs, see Fig. 1. This duration ensures coherence between the input and output of the fiber, i.e., these conditions guarantee a one-to-one correspondence between phase and amplitude at the input and the output of the fiber. The beam was coupled

into 70 cm piece of polarization maintaining microstructured fiber (Thorlabs NL-PM-750). Coupling efficiency into the fiber is $\approx 25\%$ to 30% using a single aspheric lens.

In order to illustrate the high sensitivity of the energy in specific spectral bands to the input power, we performed a simple initial experiment. Using a digital single-lens reflex camera, we directly recorded the spectrally integrated projection of the diffracted output spectrum from the fiber while varying the input power, see Fig. 1 and movie sequence in the supplementary materials. The observed spectra that covers a range from 500 to 1000 nm essentially consist of a sequence of bright zones and dark fringes, and the position of the dark fringes varies in correlation with the measured total power. Inspecting the power in relatively narrow wavelength ranges, we find regions that are nearly perfectly correlated with the spectrally integrated power, but also others which are in anti-correlation. Note that the video recording provides an overview of the dynamics of the spectrum, but cannot be operated at the nanosecond exposure times that are necessary to resolve a MHz modulation. While the signal amplification is still rather modest in this initial experimental demonstration, the effect becomes much more prominent when switching to an avalanche photodiode array in the Fourier plane of a spectrograph which enables much higher spectral resolution at the laser repetition rate but is restricted to a small number of channels.

In this second set of experiments, the laser beam was focused into an acousto-optic modulator, where the optical pulse train experienced a weak amplitude modulation of about 75 dBc at 4.6 MHz. The frequency of 4.6 MHz was limited by the available amplitude modulator but the setup only relies on passive nonlinear effects and is thus, in principle, scalable to arbitrary speeds. The group delay dispersion of the modulator was compensated by 48 reflections off chirped mirrors. These chirped mirrors were arranged in 3 pairs with dispersion oscillations cancelling each other in each pair. The duration of the pulses at the fiber input was measured to be 8 fs. The pulses were not transform-limited due to residual third-order dispersion which was not compensated for. The generated supercontinuum spectrum is spectrally dispersed in a Czerny–Turner grating spectrograph with an avalanche photodiode array (APD, Hamamatsu S8550) located in its output plane. The spectrograph focal distance was 175 mm, and the 600 mm^{-1} diffraction grating resulted in a 9 nm/mm dispersion in the visible wavelength range. Given width and pitch of the individual APDs, we computed a bandwidth of 35 nm for the individual wavelength channels. Moreover, the array offers a total of 8 independent wavelength channels, which we could not fully exploit as we only had 4 oscilloscope channels available, one of which was reserved for digitization of the input transient. Each of the three measurement channels in the APD array was amplified with a separate transimpedance amplifier (Maxim MAX3665, 470 MHz bandwidth) with $20 \text{ k}\Omega$ gain. Detector noise-equivalent power was $10 \text{ fW}/\sqrt{\text{Hz}}$ with a 220 V reverse bias voltage on the APD. The spectral response range of the photo diode covers 300 – 1000 nm, with a peak quantum efficiency of 85% at 650 nm.

Signals were recorded by a digital storage oscilloscope with 5 GSa/s sampling rate and a 1 GHz analog bandwidth, using an 8 bit analog-to-digital converter. As the laser repetition rate was about 64 times lower than the sampling rate, this scenario allows for a resolution improvement of 3 bits, which translates into a noise floor of -105 dBc , effectively removing any dynamic range limitation of the oscilloscope. Aliasing artifacts were additionally suppressed by the use of analog 300 MHz lowpass filters. Given the choice of modulation frequency and electronic

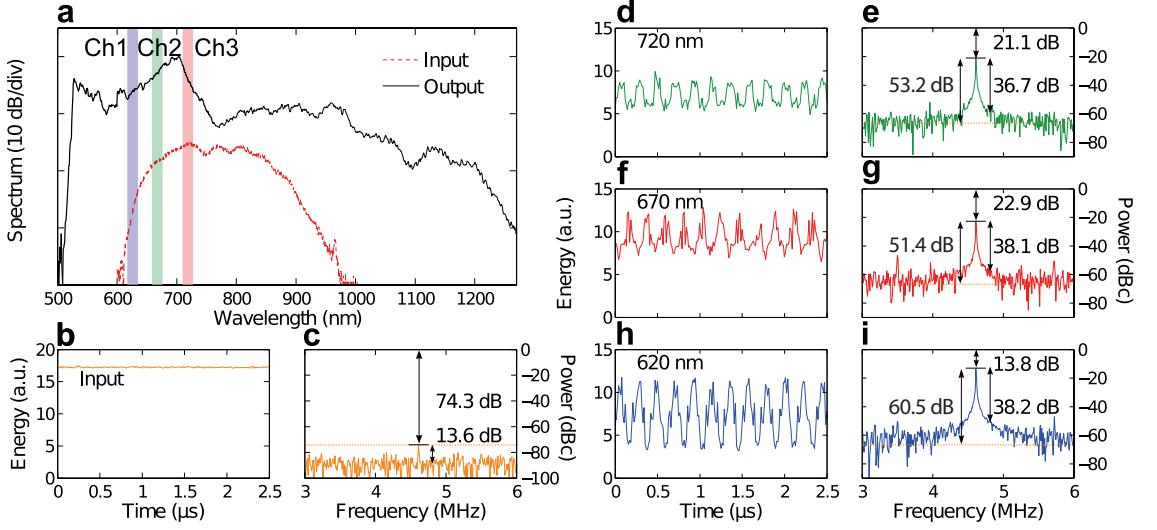


Fig. 2. Experimental results. a) Optical input and output spectra. b) and c) shows the time series and RF power recorded at the fiber input. This signal is limited by detection shot noise and excess noise of the avalanche photo diode. The right panels shows the time series and RF power recorded at the fiber output for the three different wavelength channels: d) and e) at 720 nm, f) and g) at 670 nm, h) and i) at 620 nm. Note the phase relation between the different wavelength channels, with f) being π out of phase relative to d) and h). Resolution bandwidth of all RF spectra: 10 kHz. Noise floor in d)-i) is caused by Johnson noise.

processing, the signal-to-noise ratio is expected to be dominated only by the number of detected photons per pulse and the resulting shot noise and by Johnson noise whereas other technical laser noise contributions are not expected to play any role here.

A small part of the modulated beam before the microstructured fiber was reflected with a thin glass plate into an avalanche photodiode in order to have a reference signal for the induced modulation. Detection of this signal was shot-noise limited. The reference and selected three bands of the supercontinuum pulse train were recorded simultaneously with the oscilloscope. Recorded pulse trains contained a few thousand to tens of thousands of modulation cycles. The detection was conducted both in the normal dispersion region (Fig. 2) as well as in the anomalous dispersion region of the microstructured fiber that had a specified zero dispersion wavelength at 750 nm. Both dispersion regions showed areas of the spectrum where the modulated signal seemed unaffected by the supercontinuum process, but then also areas where the signal was greatly enhanced. Here we restrict ourselves to the normal dispersion region, given that it showed higher signal amplification.

Experimental conditions ensured stability of the spectral shape and pulse energy of the laser output. However, our set-up did not include any means for stabilizing the power launched into the fiber. Longterm measurements indicate a drop of 10% on the timescale of one hour. In the experiments, we allowed the launched power to slowly drift and recorded a large number of individual time series of three APD channels and the reference detector. We noted average signal amplification values as well as their peak values.

Applying a faint 75 dBc (electrical) amplitude modulation with 4.6 MHz frequency to the pulses injected into the fiber, we find input power ranges where the modulation on a single output channel is enhanced by more than 60 dB compared to an integrated measurement before the fiber [Figs. 2(b-i)]. While the individual wavelength channels at the fiber output show

a clearly visible 4.6 MHz modulation, the spectrally integrated signal before the fiber only reveals presence of the modulation in the Fourier domain. Moreover, the central wavelength channel at 670 nm is clearly anti-correlated with the two other channels at 700 and 620 nm. Adding the measured signals of the correlated channels and subtracting the anti-correlated one results in a modulated signal that even shows an ≈ 65 dB signal enhancement. As the detected intensity levels in the spectrally resolved output are about three orders of magnitude smaller than in the input, we also see an increase of the noise background by approximately 30 dB. However, this increased noise level still enables a 30 dB signal-to-noise improvement in the combined signal. We observe similar results in the anomalous dispersion region, yet with a lower signal amplification of c.a. 10 dB.

3. THEORY AND NUMERICAL SIMULATIONS OF FIBER PROPAGATION

In our experiments, we exploit the sensitivity to the input peak power of supercontinuum (SC) generation with short pump pulses near the zero-dispersion wavelength of a highly nonlinear fiber. Prior to analyzing this process in detailed numerical simulations, let us first outline the mechanisms that lead to this pronounced input power dependence. The SC generation process consists of an initial stage of higher-order soliton compression followed by fission into fundamental solitons, with dispersive waves generated due to the presence of higher-order dispersion and stimulated Raman scattering [12]. Near-identical group velocities of soliton and dispersive wave provided, the large nonlinear potential represented by the soliton amplitude leads to a situation where dispersive waves are effectively trapped by the soliton [29]. Such soliton-dispersive wave dynamics have also been shown to be associated with transfer of energy to a frequency-shifted wave through a four-wave mixing process [30, 31].

If the power of the injected pump pulses is modulated by a

very weak signal, the resulting tiny variations in the power of the injected pulse transfer into wavelength jitter for the solitons ejected during the fission process. The power-dependent soliton jitter, although very modest on the order of few nm, dramatically affects the phase-matching condition for the four-wave mixing interaction, which, in turn, results in significant variations in the wavelength and energy of the frequency-shifted waves that appear “reflected” at the soliton boundary [31]. Furthermore, the dispersive waves and solitons may mutually affect each other by power dependent wavelength shifts [32], which further increases the sensitivity of the power-dependent shifting mechanism. These combined effects then translate into a very large amplification of the initial modulating signal when a narrow spectral bandwidth in the normal dispersion is filtered out from the supercontinuum. Note that this scenario is only possible for a SC generated under prevalent soliton dynamics and in a regime where a one-to-one correspondence between the input and output of the fiber holds.

We next analyze the experimental situation by conduction numerical simulations of the nonlinear fiber propagation, as shown in Fig. 3. These simulations employ the nonlinear Schrödinger equation with a standard split-step Fourier algorithm:

$$\begin{aligned} \frac{\partial A}{\partial z} - \sum_{k \geq 2} \frac{i^{k+1}}{k!} \beta_k \frac{\partial^k A}{\partial T^k} &= i\gamma \left(1 + \frac{i}{\omega_0} \frac{\partial}{\partial T} \right) \\ &\times \left(A \int_{-\infty}^{\infty} R(T') \times |A(z, T - T')|^2 dT' \right). \end{aligned} \quad (1)$$

Here $A(z, T)$ represents the envelope of the electric field in units of $W^{1/2}$ expressed in the frame of reference moving at the group-velocity of the pump at 785 nm. The constants β_k ($k \geq 2$) and γ are the Taylor-series expansion coefficients of the fiber dispersion and the nonlinear coefficient at the pump frequency ω_0 , respectively. The nonlinear response function $R(T) = (1 - f_R)\delta(T) + f_R h_R(T)$ includes both the instantaneous electronic and delayed Raman responses with $f_R = 0.18$ representing the Raman contribution. For $h_R(T)$ we use the experimentally measured fused silica Raman cross-section [12] as required for accurate modelling of broadband pulse propagation in optical fibers [33]. The parameters of the simulations correspond to that of the experiments. Specifically, we inject 8 fs pulses into 60 cm of a photonic crystal fiber. The fact that the fiber was polarization maintaining greatly simplifies numerical modeling. We chose a zero dispersion wavelength at 760 nm, i.e., slightly higher than specified as this value agrees best with previous comparisons between experiment and theory. This choice results in a SC that extends from 550 to 1100 nm as shown in Fig. 3. Note that, because the simulations do not include attenuation along the fiber, the length was adjusted to match the bandwidth of the experimental spectrum. The input pulses were modelled to include imperfections of the chirped mirrors present in the experimental setup, namely dispersion oscillations [34]. Amplitude and frequency of these oscillations were fitted to autocorrelation measurements to correctly account for a pedestal like background structure in the launched pulses. Broadband background noise in the form of one photon per frequency bin was added to the input field. Moreover, we included the effect of Raman noise and added it to the propagating field as well, although the latter effect was found negligible for the resulting RF modulation amplification.

We simulated the SC spectra generated by a pulse train of 4000 consecutive pulses with modulated peak power at a 4 MHz frequency (corresponding to a resolution bandwidth of 40 kHz

in the RF spectrum) and with amplitude modulation contrast of $10^{-3.4}$ (68 dB electrical) [see Fig. 3(c-d), top panels]. The results plotted in Fig. 3(a) shows how the very weak initial modulation of the input peak power is amplified by nearly 50 dB when detecting the energy fluctuations in wavelength channels with 10 nm bandwidth in the normal dispersion region [Fig. 3(c-d)], in very good agreement with the experiments. The mutual correlation between the different wavelength channels is also correctly reproduced.

In order to confirm the amplification mechanism, we plot the spectrogram representation of the SC generated by a single pulse in Fig. 4(a). We can clearly see how the spectral bands in the normal dispersion region where we observe large amplification of the initial modulation specifically corresponds to dispersive waves that are trapped by solitons as highlighted by the dashed lines. The amplitude of the periodic power-dependent spectral jitter of these solitons resulting from the weak initial modulation is on the order of few nm as shown in Fig. 4(b). This spectral jitter, in turn, induces a change in the trapped dispersive wave that may reach or exceed its bandwidth, as shown in Fig. 4(c). It is this dramatic change in the wavelength of the dispersive wave which is captured (or not) by the spectral filters and results in very large amplification of the initial modulation. Additional numerical simulations show that large amplification factors are obtained when the SC dynamics are self-seeded from the input pulse spectral components, which has been dubbed as the coherent regime previously [12]. This regime can be maintained for pulses up to 100 fs. Shorter pulses are, in principle, more favorable due to the smaller number of solitons ejected during the fission process, which serves to further increase the power-dependent jitter.

4. NOISE ANALYSIS

Our experiments indicate that the modulation signal is elevated by up to 60 dB relative to the carrier. We also observe a less pronounced increase of the noise floor, which still enables a substantial improvement of the signal-to-noise ratio. A physically intriguing question is the origin of this noise floor, whether it relates to technical limitations of the photodetectors or whether it has a quantum noise origin. In order to clarify this aspect, we carefully simulated all possible noise mechanisms as is explained in the following.

Photodetection underlies a series of noise mechanisms that define the attainable signal-to-noise ratio. Most prominently, these mechanisms include Johnson noise [26] and shot noise [25]. The latter is caused by the fact that measurements of optical pulse energies are quantized, with the detected photon number N following Poissonian statistics. Here it often proves limiting that only a small fraction of the available laser power can be converted into an electric current without destroying the photodetector. The uncertainty of an individual pulse energy measurement is given by \sqrt{N} , resulting in the best obtainable signal-to-noise (S/N) ratio of $1 : N^{-1/2}$ in the absence of Johnson noise and other technical noise sources. The obtainable S/N therefore increases with the square root of the detected photons. Johnson (or thermal) noise follows a Gaussian statistics that gives rise to voltage fluctuations of $\sqrt{4k_B T R}$ per root Hertz across the feedback resistor R of the transimpedance amplifier [26]. Other than shot noise, Johnson noise contribution is independent of signal levels. Here k_B is Boltzmann’s constant, and $T = 293$ K was assumed as the temperature. In combination, both these mechanisms limit our capabilities to detect a faint

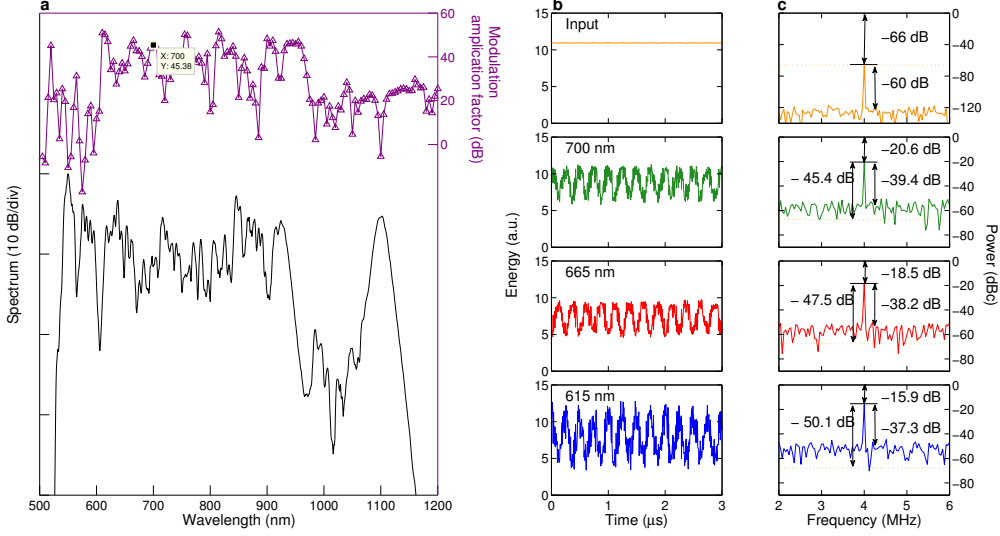


Fig. 3. Numerical simulations results. (a) signal amplification vs. wavelength with 10 nm bandwidth filters. (b) Supercontinuum mean spectrum. (c) and (d) show the modulated signal and corresponding RF power at the fiber input and output, respectively, for filters at the spectral locations indicated by the rectangles in (b). The pump pulse is at 790 nm with a peak power of 3.2 kW. The fiber length is 60 cm. Resolution bandwidth of simulated RF spectra: 40 kHz. Noise floor results from amplified spontaneous emission of the laser source and assumes no attenuation prior to detection in contrast with the experiments. Detection shot noise is not included.

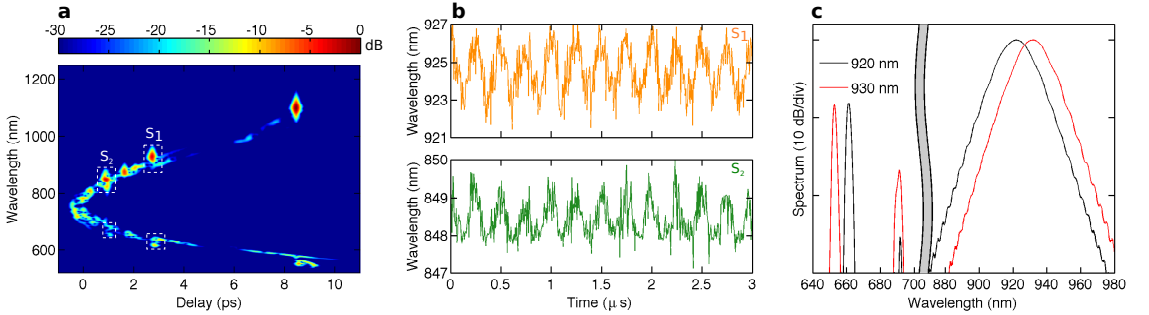


Fig. 4. (a) Single shot spectrogram representation of the simulated SC of Fig. 3. The solitons S1 and S2 and associated dispersive waves that play a central role in the signal amplification dynamics are highlighted by the dashed rectangles. The periodic wavelength jitter of the solitons as a result of the initial very weak peak power modulation is illustrated in (b). (c) Simple model that illustrates the dramatic change in the wavelength of a dispersive wave associated with its temporal reflection at a soliton boundary. The dispersive wave at 690 nm co-propagate with the soliton at a center wavelength of 920 nm (black) and 930 nm (red).

modulation signal. Figure 5 shows how shot-noise and Johnson noise affect the detection before and after the fiber in our signal amplification scheme. These simulations have been carefully adjusted to provide the exact same noise floor as was measured experimentally.

Our detection scheme relies on massive oversampling [35] of the signals acquired at $f_{sa} = 5 \text{ GSa/s}$ rate with 8 bit digitization. Numerical processing of the data allows for a maximum dynamic range increase by $\log_2(f_{sa}/f_{rep}) = 3 \text{ bit}$. The resulting effective 11 bit digitization shown as a gray curve in Fig. 5 pushes dynamic range limitations to below -105 dBc, i.e., substantially below the other noise sources in the photoelectric conversion. For completeness, we additionally included quantum noise estimations from the numerical simulations discussed below. These are shown as green lines in Fig. 5. The discrepancy between detection shot noise and amplified spontaneous

emission in Fig. 5(a) arises because only a small fraction of the available laser power can actually be converted in a photodiode without saturation or damage. The detection of this noise signature would require total photoelectric conversion near the watt level. Additionally, a dynamic range increase by an additional 4 bits is required, which seems out of reach for currently available fast photodiodes and high-speed analog-to-digital converters. Our estimations indicate that the obtainable signal-to-noise ratio of the input signal is limited by saturation of the photodiode and the resulting shot noise limit. In contrast, light levels after the fiber are much lower such that the detection of the modulation signal is not shot noise limited but rather it is the Johnson noise that dominates.

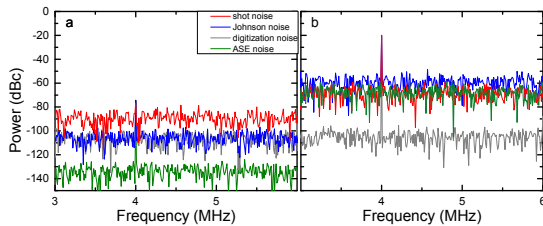


Fig. 5. Simulation of noise levels before and after photonic signal amplification. (a) Simulated noise levels as observed by the photo detector before launching the pulses into the fiber. (b) Same after photonic signal amplification. Red curves: shot noise limit [25] deduced from the square root of the number of detected photons per pulse. Blue curves: Johnson limit [26] deduced from the known transimpedance of both detectors (5 k Ω before and 20 k Ω after the fiber). Gray curves: digitization noise [35] as being caused by Poissonian noise in the least significant digit of an effective 11 bit digitization. Green curves: residual quantum noise contamination arising from amplified spontaneous emission inside the source laser (rescaled to 10 kHz resolution bandwidth from Fig. 3).

5. DISCUSSION

Our experimental results and numerical simulations have made it clear that the highly nonlinear soliton fission scenario results in spectra that may exhibit one or several pronounced dark fringes, in particular in the normal dispersion region. Variation of the input power leads to a spectral shift of these fringes. The strongest signal enhancement is observed for a detected spectral bandwidth smaller than the width of a dark fringe. In an ideal situation, the amplitude modulation of the input signal is adjusted to lead to a spectral shift of the dark fringe that exactly changes the detected power from near zero to the maximum possible. In our numerical simulations, we find signal enhancements of 50 dB, close to the best experimental observations, yet at narrower filter bandwidth than in the experiments. Even in this ideal situation of maximum signal amplification, spurious harmonics may appear.

It appears useful to analyze the behavior from a more general point of view, using the concept of a transfer function $E_{\text{out}} = f(E_{\text{in}})$ between input and output pulse energy, E_{in} and E_{out} , respectively. This is illustrated in Fig. 6, with a simulated input signal [Fig. 6(a,b)] being amplified via a linear transfer function [Fig. 6(c,d)] and under weakly nonlinear transfer [Fig. 6(e,f)]. In the latter case, harmonics of the modulation frequency appear in the output, and for multi-frequency driver signals, mixing products will appear. However, it can also be seen that the presence of these spurious harmonics does not strongly reduce the amplification of the modulation signal itself. This situation changes when the amplification process is completely overdriven [Fig. 6(g,h)]. Now the input modulation causes a spectral shift that is much larger than the spacing between the dark fringes, with a sinusoidal transfer function resulting in a multitude of harmonics that appear with comparable amplitude. Nevertheless, even this disadvantageous situation still enables some reduced signal amplification. All processes discussed so far have ensured coherence between input and output signal, with their explicitly assumed unambiguous functional dependence via the transfer function.

Finally, the concept of a transfer function may break down, and stochastic processes take over. This breakdown of the transfer function concept shows up as a white noise floor in the Fourier representation [Fig. 6(j)]. One possible source for such a contribution is a modulation instability or the spontaneous Raman effect in fibers. Stochastic processes further reduce signal amplification to the verge of usefulness, whereas noise amplifica-

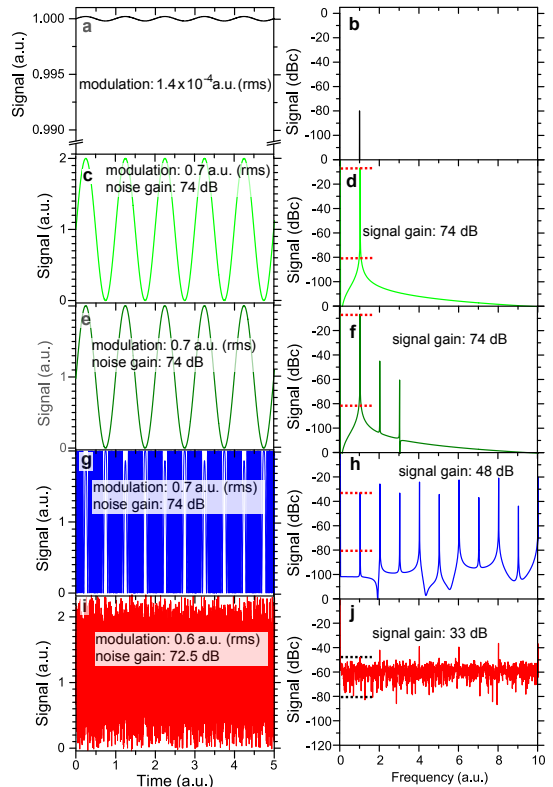


Fig. 6. Comparison of different nonlinear optical signal amplification scenarios. (a,c,e,g,i) Time domain signals. (b,d,f,h,j) Frequency domain representations. (a,b) Input signal with very weak -80 dB modulation. (c,d) Simulated ideal signal amplification. Transfer function: $f(x) = 0.5 \times 10^4(x - 0.9998)$, providing a linear one-to-one correspondence between input x and output $f(x)$. Both, the rms modulation and the modulation Fourier component are increased by 74 dB. (e,f) Same scenario with additional spurious nonlinearity, giving rise to modulation sidebands, but leaving noise and signal gains unaffected. (g,h) Oscillatory transfer function: $f(x) = 1 + \cos[50(0.5 \times 10^4(x - 0.9998))]$. rms modulation, i.e., noise gain is left unchanged, but signal gain reduces to 48 dB. (i,j) Same with additional stochastic noise contribution. Noise gain is slightly reduced to 72.5 dB; signal gain reduces to 33 dB. Signal-to-noise ratio of the modulation component is marginal.

tion still appears nearly undisturbed. These examples show that noise amplification may be easy to observe, yet typically such behavior cannot be exploited for the coherent amplification of an input signal. Moreover, the observation of relative intensity noise in the output channel also does not allow to conclude on an existing coherence of the nonlinear optical process.

6. CONCLUSIONS

At first glance, our findings may not appear overly surprising, given that similar noise amplification has been discussed before with lower amplification factors up to 30 dB [15, 16]. The latter experiments actually related relative intensity noise (RIN) of the supercontinuum to pump fluctuations, yet without investigating the phase relationship or coherence between input and output. Such noise amplification will appear regardless of a deterministic nature of the underlying processes. In fact, at pump pulse durations > 100 fs, our numerical simulations indicate that noise

amplification quickly degrades spectral and temporal coherence. In the absence of this coherence, noise amplification still appears while the modulation amplification factor that can be obtained may be reduced significantly. The demonstrated amplification of up to 60 dB therefore strongly contrasts the previously observed noise amplification scenarios. For a fixed wavelength interval in the output of the fiber, such favorably high amplification factors can only be seen for a narrow $\approx 10^{-4}$ W input power range. Nevertheless, our simulations indicate that signal amplification at 10–20 dB lower factors is actually a fairly robust phenomenon in a 100–200 nm wide dispersive wave region that co-propagates with solitons in the anomalous dispersion region. Outside this range, signal amplification factors are substantially lower. Our scheme can also tolerate larger changes in the input power and still amplify the modulated signal by 60 dB, but in this case such high gain value may be obtained for a different wavelength.

Moreover, to fully appreciate the observed improvements of the signal-to-noise ratios by up to 30 dB, it is useful to compute the photon fluences necessary to simply obtain the same enhancement via increase of the optical input power. In the case of shot-noise limited detection, a thousandfold increase of the input power would be necessary to measure a -70 dB signal 40 dB above the noise floor, which, in turn, would require 110 dB dynamic range as well as the total photoelectric conversion of about 100 mW of Ti:sapphire light. Such parameters pose a serious challenge for the dynamic range of available electronic test equipment [36] and are at the limit of high-power photodetector designs [37, 38]. Although all-optical regeneration for optical telecommunications can be conveniently achieved with simpler approaches, our scheme offer an important alternative whenever small modulations need to be recovered in a strong pulsed laser beam. In such a situation, we may be able to push detection limits by one or two orders of magnitude in intensity, which would greatly alleviate extremely sensitive pump-probe spectroscopy studies [39]. Other possible applications include high-sensitivity interferometry and sensitivity enhancement in the measurement of small induced refractive index changes.

ACKNOWLEDGMENTS

G. S. and G. G. gratefully acknowledge support by the Academy of Finland (project grants 128844, 130099 and 132279). The authors acknowledge fruitful discussions with John Dudley and Miro Erkintalo.

REFERENCES

1. R. R. Alfano *The supercontinuum laser source: fundamentals with updated references* 2nd edn (Springer, 2006).
2. K. Goda, K. K. Tsia, and B. Jalali, "Serial time-encoded amplified imaging for real-time observation of fast dynamic phenomena," *Nature* **458**, 1145–1149 (2009).
3. T. Udem, R. Holzwarth, and T. W. Hänsch, "Optical frequency metrology," *Nature* **416**, 233–237 (2002).
4. T. W. Hänsch, "Nobel Lecture: Passion for precision," *Rev. Mod. Phys.* **78**, 1297–1309 (2006).
5. M. Hentschel, R. Kienberger, C. Spielmann, G. A. Reider, N. Milosevic, T. Brabec, P. Corkum, U. P. Heinzmann, M. Drescher, and F. Krausz, "Attosecond metrology," *Nature* **414**, 509–513 (2001).
6. J. K. Ranka, R. S. Windeler, and A. J. Stentz, "Visible continuum generation in air-silica microstructure optical fibers with anomalous dispersion at 800 nm," *Opt. Lett.* **25**, 25–27 (2000).
7. S. Coen, A. Hing Lun Chau, R. Leonhardt, J. D. Harvey, J. C. Knight, W. J. Wadsworth, and P. St. J. Russell, "White-light supercontinuum generation with 60-ps pump pulses in a photonic crystal fiber," *Opt. Lett.* **26**, 1356–1358 (2001).
8. J. M. Dudley, L. Provino, N. Grossard, H. Maillotte, R. S. Windeler, B. J. Eggleston, and S. Coen, "Supercontinuum generation in air-silica microstructured

- fibers with nanosecond and femtosecond pulse pumping," *J. Opt. Soc. Am. B* **19**, 765–771 (2002).
9. W. J. Wadsworth, A. Ortigas-Blanch, J. C. Knight, T. A. Birks, T.-P. Martin Man, and P. St. J. Russell, "Supercontinuum generation in photonic crystal fibers and optical fiber tapers: a novel light source," *J. Opt. Soc. Am. B* **19**, 2148–2155 (2002).
10. A. K. Abeeluck, C. Headley, and C. G. Jorgensen, "High-power supercontinuum generation in highly nonlinear, dispersion-shifted fibers by use of a continuous-wave Raman fiber laser," *Opt. Lett.* **29**, 2163–2165 (2004).
11. T. Hori, J. Takayanagi, N. Nishizawa, and T. Goto, "Flatly broadened, wideband and low noise supercontinuum generation in highly nonlinear hybrid fiber," *Opt. Express* **12**, 317–324 (2004).
12. J. M. Dudley, G. Genty, and S. Coen, "Supercontinuum generation in photonic crystal fiber," *Rev. Mod. Phys.* **78**, 1135–1184 (2006).
13. J. K. Ranka, R. S. Windeler, and A. J. Stentz, "Visible continuum generation in air-silica microstructure optical fibers with anomalous dispersion at 800 nm," *Opt. Lett.* **25**, 25–27 (2000).
14. X. Gu, L. Xu, M. Kimmel, E. Zeek, P. O'Shea, A. P. Shreenath, R. Trebino, and R. S. Windeler, "Frequency-resolved optical gating and single-shot spectral measurements reveal fine structure in microstructure-fiber continuum," *Opt. Lett.* **27**, 1174–1176 (2002).
15. K. L. Corwin, N. R. Newbury, J. M. Dudley, S. Coen, S. A. Diddams, K. Weber, and R. S. Windeler, "Fundamental noise limitations to supercontinuum generation in microstructure fiber," *Phys. Rev. Lett.* **90**, 113904 (2003).
16. N. R. Newbury, B. R. Washburn, K. L. Corwin, and R. S. Windeler, "Noise amplification during supercontinuum generation in microstructure fiber," *Opt. Lett.* **28**, 944–946 (2003).
17. D. R. Solli, C. Ropers, P. Koonath, and B. Jalali, "Optical rogue waves," *Nature* **450**, 1054–1057 (2007).
18. T. Godin, B. Wetzel, T. Sylvestre, L. Larger, A. Kudlinski, A. Mussot, A. Ben Salem, M. Zghal, G. Genty, F. Dias, and J. M. Dudley, "Real time noise and wavelength correlations in octave-spanning supercontinuum generation," *Opt. Express* **21**, 18452–18460 (2013).
19. B. Schenkel, R. Paschotta, and U. Keller, "Pulse compression with supercontinuum generation in microstructure fibers," *J. Opt. Soc. Am. B* **22**, 687–693 (2005).
20. J. M. Dudley, F. Dias, M. Erkintalo, and G. Genty, "Instabilities, breathers and rogue waves in optics," *Nature Photon.* **8**, 755–764 (2014).
21. M. N. Islam, G. Sucha, I. Bar-Joseph, M. Wegener, J. P. Gordon, and D. S. Chemla, "Femtosecond distributed soliton spectrum in fibers," *J. Opt. Soc. Am. B* **6**, 1149–1158 (1989).
22. A. L. Gaeta, "Nonlinear propagation and continuum generation in microstructured optical fibers," *Opt. Lett.* **27**, 924–926 (2002).
23. M. H. Frosz, O. Bang, and A. Bjarklev, "Soliton collision and Raman gain regimes in continuous-wave pumped supercontinuum generation," *Opt. Express* **14**, 9391–9407 (2006).
24. M. Erkintalo, G. Genty, and J. M. Dudley, "Rogue-wave-like characteristics in femtosecond supercontinuum generation," *Opt. Lett.* **34**, 2468–2470 (2009).
25. F. Quinlan, T. M. Fortier, H. Jiang, A. Hati, C. Nelson, Y. Fu, J. C. Campbell, and S. A. Diddams, "Exploiting shot noise correlations in the photodetection of ultrashort optical pulse trains," *Nature Photon.* **7**, 290–293 (2013).
26. M. B. Gray, D. A. Shaddock, C. C. Harb, and H.-A. Bachor, "Photodetector designs for low-noise, broadband, and high-power applications," *Rev. Sci. Instrum.* **69**, 3755–3762 (1998).
27. R. Salem, M. A. Foster, A. C. Turner, D. F. Geraghty, M. Lipson, and A.-L. Gaeta, "Signal regeneration using low-power four-wave mixing on a silicon chip," *Nature Photon.* **2**, 35–38 (2008).
28. R. Slavik, F. Parmigiani, J. Kakande, C. Lundström, M. Sjödin, P. A. Andrekson, R. Weerasuriya, S. Sygletos, A. D. Ellis, L. Grüner-Nielsen, D. Jakobsen, S. Herström, R. Phelan, J. O'Gorman, A. Bogris, D. Syvridis, S. Dasgupta, P. Petropoulos, and D. J. Richardson, "All-optical phase and amplitude regenerator for next-generation telecommunications systems," *Nature Photon.* **4**, 690–695 (2010).
29. T. G. Philbin, C. Kuklewicz, S. Robertson, S. Hill, F. König, and U. Leonhardt, "Fiber-optical analog of the event horizon," *Science* **319**, 1367–1370 (2008).
30. A. V. Gorbach and D. V. Skryabin, "Light trapping in gravity-like potentials and expansion of supercontinuum spectra in photonic-crystal fibres," *Nature Photon.* **1**, 653–657 (2007).
31. K. E. Webb, M. Erkintalo, Y. Xu, N. G. R. Broderick, J. M. Dudley, G. Genty, and S. G. Murdoch, "Nonlinear optics of fibre event horizons," *Nature Comm.* **5**, 4969 (2014).
32. A. Demircan, S. Amirashvili, and G. Steinmeyer, "Controlling Light by Light with an Optical Event Horizon," *Phys. Rev. Lett.* **106**, 163901 (2011).
33. M. Erkintalo, G. Genty, B. Wetzel, and J. M. Dudley, "Limitations of the linear Raman gain approximation in modeling broadband nonlinear propagation in optical fibers," *Opt. Express* **18**, 25449–25460 (2010).
34. G. Steinmeyer, "Dispersion Oscillations in Ultrafast Phase Correction Devices," *IEEE J. Quantum Electron.* **39**, 1027–1034 (2003).
35. M. W. Hauser, "Principles of Oversampling A/D Conversion," *J. Audio Eng. Soc.* **39**, 1–26 (1981).
36. Agilent Technologies. Optimizing RF and Microwave Spectrum Analyzer Dynamic Range. *Application Note AN 1315*.
37. N. Uehara and K. Ueda, "Ultrahigh-frequency stabilization of a diode-pumped Nd:YAG laser with a high-power-acceptance photodetector," *Opt. Lett.* **19**, 728–730 (1994).

REFERENCES

38. N. Mio, M. Ando, G. Heinzel, and S. Moriwaki, "High-Power and Low-Noise Photodetector for Interferometric Gravitational Wave Detectors," *Jpn. J. Appl. Phys.* **40**, 426–427 (2001).
39. K. L. Hall, C. Lenz, E. P. Ippen, and G. Raybon, "Heterodyne pump-probe technique for time-domain studies of optical nonlinearities in waveguides," *Opt. Lett.* **17**, 874–876 (1992).

REFERENCES

Tampereen teknillinen yliopisto
PL 527
33101 Tampere

Tampere University of Technology
P.O.B. 527
FI-33101 Tampere, Finland

ISBN 978-952-15-4051-6
ISSN 1459-2045